

Doctoral Dissertation

博士論文

Evolution of Molecular Isotopic Ratios in the Low Mass Protostar L1527

(低質量原始星 L1527 における分子の同位体比の進化)

A Dissertation Submitted for Degree of Doctor of Philosophy

December 2018

平成 30 年 12 月博士（理学）申請

Department of Physics, Graduate School of Science,

The University of Tokyo

東京大学大学院理学系研究科

物理学専攻

Kento Yoshida

吉田 健人

ABSTRACT

Exploring chemical evolution from interstellar clouds to planetary systems is an important subject in astrophysics and astrochemistry, which could be directly related to the understanding of the material origin of the Solar System. One of the potential links between interstellar chemistry and planetary science is anomalies of molecular isotope ratios. It is known that molecular isotope ratios in interstellar clouds and protostellar cores can be much different from the elemental isotope ratio. For instance, deuterium fractionation into molecules is widely recognized, and has been used to study the chemical evolution of interstellar clouds. However, studies of the deuterium fractionation after the onset of star formation are limited, in contrast to those in prestellar cores. In addition, the isotope fractionation other than that of deuterium is not well investigated in prestellar and protostellar cores. Based on these backgrounds, this thesis presents the observational studies of the deuterium and carbon fractionation in the low-mass star-forming region L1527.

As the first step to understand the chemical evolution, it is important to reveal the chemical compositions of low-mass protostellar sources without any preconception. For this purpose, unbiased line survey observations in the millimeter-wave region toward the representative low-mass protostellar source L1527 have been conducted to reveal its whole chemical composition and isotope fractionations. 69 molecular species are identified in the 3-mm band, among which 27 species are carbon-chain species and their isomers, including their minor isotopologues. Comparison of the chemical composition of L1527 with those of other prototypical sources is discussed, and the drastic chemical diversity between sources is confirmed. In addition, various deuterated and ^{13}C -substituted species have successfully been detected, and the significant fractionation of isotopic species has been found in combination with the supplementary observations. Carbon-chain molecules such as CCH, HC_3N , $c\text{-C}_3\text{H}_2$ are diluted in ^{13}C , while CO, CN, and H_2CO have $^{12}\text{C}/^{13}\text{C}$ ratios similar to the elemental $^{12}\text{C}/^{13}\text{C}$ ratio of 60–70. This fractionation would originate from the isotope exchange reaction between C^+ and CO. Most of the deuterated species detected in this study show the D/H ratios of 0.02–0.07, while some species show very high fractionation (> 0.1).

In addition, the spatial distributions of H_2CO and CCH as well as their deuterated species in L1527 have been investigated with Atacama Millimeter/submillimeter Array (ALMA). The distributions of the normal species and deuterated species of these two species are found to be different: the deuterated species are deficient in the vicinity of the protostar where the normal species mainly reside ($r \sim 250$ au). Instead, the deuterated species are abundant in the outer

envelope at a distance of about 1000 au from the protostar. The D/H ratios are found to decrease with decreasing distance from the protostar along the protostellar envelope. This may originate from sublimation of whole ice mantles. D/H ratios preserved in the inner layers of the ice mantles are low, because a timescale of ice evolution is shorter than that of deuterium fractionation. Sublimation of such ice mantles contributes to the observed radial change in the deuterium fractionation of H_2CO . Similarly, the sublimation of CH_4 from dust grains is likely responsible for the decrease in the deuterium fractionation of CCH, which is produced from CH_4 in the gas phase.

These results provide us with a new insight into understanding the chemical evolution of the isotopic fractionation from protostellar cores to protoplanetary disks and eventually to planetary systems.

CONTENTS

LIST OF ABBREVIATIONS	8
1 Introduction	1
1.1 Formation of low-mass stars	2
1.2 Chemical evolution along star formation	3
1.2.1 Prestellar core	3
1.2.2 Protostellar core	7
1.3 Deuterium fractionation	9
1.3.1 Prestellar core	11
1.3.2 Protostellar core	12
1.4 Fractionation of ^{13}C species	13
1.5 Background of this thesis	14
1.6 Outline of this thesis	17
2 Observation Techniques	19
2.1 Single-dish telescope	19
2.1.1 Components	19
2.1.2 Switching mode	22
2.1.3 Calibration	22
2.2 Interferometer	24
2.2.1 Basic concepts	25
2.2.2 Imaging procedure	28
2.2.3 Calibration	30
2.3 Telescopes used in this thesis	31
2.3.1 Nobeyama 45-m telescope	31
2.3.2 IRAM 30-m telescope	32
2.3.3 Atacama Large Millimeter/submillimeter Array (ALMA)	32

3	Line survey observation toward L1527	34
3.1	Introduction	34
3.2	Observation	35
3.3	Results	39
3.3.1	Overall results	39
3.3.2	Column densities and rotational temperatures	41
3.4	Isotopic ratios	51
3.4.1	Deuterated species	51
3.4.2	^{13}C -substituted species	53
3.4.3	^{15}N -substituted species	56
3.5	Comparison with other sources	56
3.5.1	TMC-1	56
3.5.2	IRAS 16293-2422	58
4	Complementary study of the ^{13}C anomaly	64
4.1	c-C ₃ H ₂	64
4.1.1	Observations	65
4.1.2	Overall results	65
4.1.3	LTE analysis for c-C ₃ H ₂	66
4.1.4	LVG analysis for c-C ₃ H ₂	70
4.1.5	Discussion	70
4.2	H ₂ CO	77
4.2.1	Observation	78
4.2.2	Results	78
4.2.3	Observation toward the prestellar core L1544	79
4.3	Concluding remarks on the carbon fractionation	80
5	Mapping observation of deuterated species with ALMA	83
5.1	Introduction	83
5.2	Observation	84
5.3	H ₂ CO	85
5.3.1	Distributions	85
5.3.2	Column density and temperature of D ₂ CO	91

5.3.3	D/H ratios obtained with the ACA data	91
5.3.4	D/H ratios with the combined data	93
5.4	CCH	94
5.4.1	Distributions	94
5.4.2	D/H ratios	103
5.5	Discussion	105
5.5.1	Origin of the different distributions and the radial change of the deuterium fractionation	105
5.5.2	Comparison with the single-dish observations	106
5.5.3	Comparison with chemical models	107
5.6	Summary and Conclusion	107
6	Conclusion	110
6.1	Summary of this thesis	110
6.1.1	Overall chemical composition of L1527	110
6.1.2	Molecular $^{12}\text{C}/^{13}\text{C}$ ratios at a 1000 au scale	111
6.1.3	Molecular D/H ratios at a 1000 au scale	111
6.1.4	Distributions of deuterated species within 1000 au	112
6.2	Future prospects	112
6.2.1	Deuterated species	113
6.2.2	^{13}C species	114
Appendix		
A	Data of the line survey observation with NRO 45 m	125

LIST OF ABBREVIATIONS

ACA	Atacama Compact Array
AGB	Asymptotic Giant Branch
ALMA	Atacama Large Millimeter/submillimeter Array
AOS	Acousto-Optical radio Spectrometer
ASAI	Astrochemical Surveys At Iram
CASA	Common Astronomy Software Applications
CDMS	Cologne Database for Molecular Spectroscopy
COM	Complex Organic Molecule
DSB	Double Side Band
EMIR	Eight Mixer Receiver
ESO	European Southern Observatory
FTS	Fast Fourier Transform Spectrometer
FWHM	Full Width Half Maximum
HEMT	Hot Electron Mobility Transistor
IF	Intermediate Frequency
IRAM	Institut de Radioastronomie Millimétrique
IRAS	Infrared Astronomical Satellite
IRE	Infalling-Rotating Envelope
ISM	Interstellar Medium
JPL	Jet Propulsion Laboratory
LO	Local Oscillator
LSB	Lower Side Band
LSR	Local Standard of Rest
LTE	Local Thermodynamical Equilibrium
LVG	Large Velocity Gradient
NRO	Nobeyama Radio Observatory
PA	Position Angle
PdBI	Plateau de Bure Interferometer
PV	Position Velocity
RF	Radio Frequency
SAM45	Spectral Analysis Machine for the 45-m telescope
SED	Spectral Energy Distribution
SIS	Superconductor-Insulator-Superconductor
SSB	Single Side Band
TMC-1 (CP/MP)	Taurus Molecular Cloud-1 (Cyanopolyne Peak/Methanol Peak)
TP	Total Power
USB	Upper Side Band
UV	Ultraviolet
WCCC	Warm Carbon-Chain Chemistry

CHAPTER 1

INTRODUCTION

To understand how vast variety of materials are formed in space and how they are delivered to the Solar System is one of the most fundamental goals of modern science. One approach to answer this question is to study the molecular evolution along Solar-type star formation. Molecular synthesis begins in dense regions of the interstellar medium, so-called molecular clouds. Molecular clouds consist of gas and small dust grains made of silicate and carbonaceous materials. Dust grains, which typically comprise 1% of the cloud mass, attenuate the interstellar ultraviolet (UV) radiation so that molecules can survive for a relatively long time. The most abundant constituent is hydrogen molecules (H_2), whose typical density in molecular clouds ranges from 10^3 to 10^6 cm^{-3} . The most abundant molecule after H_2 is carbon monoxide (CO), which has a relative abundance of 10^{-4} to H_2 . Other molecules typically have the abundances as low as $\sim 10^{-7}$ relative to H_2 . Nevertheless, a rich molecular complexity is realized in molecular clouds.

So far, more than 200 molecular species have been detected mainly by radio astronomical observations of their rotational spectra (McGuire 2018). These species include not only diatomic molecules such as H_2 and CO, but also molecular ions (e.g., HCO^+ and N_2H^+), free radicals (e.g., OH and CCH), fundamental molecules which are common in the terrestrial environment (e.g., H_2O and CO_2), and saturated organic molecules (e.g., $(\text{CH}_3)_2\text{O}$ and HCOOCH_3). Molecules formed in molecular clouds are incorporated into ice mantles in protoplanetary disks and then finally may be inherited to planets and small bodies in protosolar systems. Recent radio and infrared observations revealed that comets have molecular compositions similar to those in cold molecular clouds (Mumma & Charnley 2011), although they significantly vary from comet to comet. Hence, chemical evolution along formation processes of Solar-type (low-mass) stars is of great importance to investigate how the interstellar matter was evolved into the Solar-System materials, and, ultimately, the origin of life. In this section, formation of low-mass stars and the chemical evolution during its process are briefly described.

1.1. Formation of low-mass stars

Star formation starts from gravitational contraction of a molecular cloud core, which is a dense part in interstellar clouds. A typical H_2 density of molecular cloud cores is higher than 10^4 cm^{-3} and the gas kinetic temperature is around 10 K (Benson & Myers 1989). Although diffuse interstellar clouds are under pressure equilibrium, some part of them starts collapsing to form molecular cloud cores and eventually stars at some point (Shu *et al.* 1986). Evolutionary stages of star formation are extensively studied by observations and numerical simulations (e.g., Benson & Myers 1989; Bergin & Tafalla 2007; Stahler *et al.* 1980). They are qualitatively classified into three phases as follows.

Prestellar core

Before the birth of a protostar, a molecular cloud core is often referred to as a prestellar core. Radiation cooling by spectral line emission of atoms and molecules and thermal emission from the dust keeps the core isothermal, resulting in a constant temperature of about 10 K during the collapse (Bonnor 1956; Alves, Lada, & Lada 2001). The timescale of the collapse is roughly comparable to the free fall time, $t_{\text{ff}} = \sqrt{3\pi/32G\rho_0}$, where G is the gravitational constant, and ρ_0 the initial cloud density. For the initial cloud density of 10^4 cm^{-3} , t_{ff} is 4×10^5 yr.

Protostar

As the density of a prestellar core increases, the dust continuum emission can be optically thick enough to prevent the radiation cooling, and the temperature and pressure in the central region of the core should start to rise. When the density of the prestellar core becomes as high as 10^{11} cm^{-3} , the core pressure becomes quasi-hydrostatic equilibrium with the self-gravity, which is called the first core. When the central temperature reaches 2000 K, dissociation of H_2 occurs. Endothermicity of the H_2 dissociation breaks the equilibrium and resumes gravitational contraction of the central region. The second core, a core composed of H plasma with quasi-hydrostatic equilibrium, is formed after the second collapse. These processes are predicted by numerical simulations (Larson 1969; Masunaga & Inutsuka 2000). Surrounding materials still remain in a flattened envelope, and they continue to accrete onto the protostar. Moreover, the bipolar outflows are developed perpendicular to the envelope (Bachiller 1996). The whole system including the protostar and the surroundings is called the protostellar core.

T-tauri star

After the envelope gas is dissipated by bipolar outflows and the accretion of the gas onto the protostar fades, the protostar is evolved into the phase called the T-tauri star. In this phase, the star is shining by releasing the gravitational energy. The heat produced in the central part of the star is delivered to the surface mainly by convection during the quasi-static contraction (Hayashi phase; Hayashi 1961). When the central temperature becomes high enough, the heat is transferred efficiently by thermal radiation. After the central temperature becomes higher than 10^7 K, nuclear fusion reactions start to occur. At this stage, the star reaches the main sequence. A protoplanetary disk, a parent body of a planetary system, is formed in the T-tauri star phase, when the envelope gas is almost dissipated.

Young stellar objects are classified into four classes (Class 0, I, II, and III) by using the slope of their radiation spectra (the spectral energy distribution; SED), $\alpha = d \log(\lambda F_\lambda) / d \log \lambda$ (e.g., Lada & Wilking 1984; Adams *et al.* 1987). For Classes I–III, the slope is derived from the infrared fluxes (classically 2.2 and 25 μm). Class I sources are deeply embedded and show a broader SED than that for a single black body because of the infrared excess caused by the envelope. Thus, these sources show α from 0 to 3. Class II sources show radiation from the photosphere and the circumstellar disk. The near infrared emission is dominant, and SED shows negative values of α from -2 to even 0 due to the infrared excess by the disk. Class III sources show negative values α from -3 to -2 , suggesting a single black body from the central star in the near infrared region with little excess circumstellar materials. Classes II and III correspond to the pre-main-sequence star, classical T-tauri star, and weak-line T-tauri star, respectively. An additional class, Class 0, was introduced by André *et al.* (1993) from submillimeter continuum observations, where stars in the earlier phase than Class I are classified. Its SED is well fitted by a black body of a low temperature, suggesting a thick envelope surrounding the central protostar. In this phase, the central star is growing through mass accretion from the envelope.

1.2. Chemical evolution along star formation

1.2.1. Prestellar core

In the course of star formation, the molecular compositions in the prestellar- and protostellar-core phases also evolve. It has been established that the chemical compositions are useful to trace the evolutionary stages of the cores.

In diffuse clouds where interstellar UV radiation can penetrate into the central region,

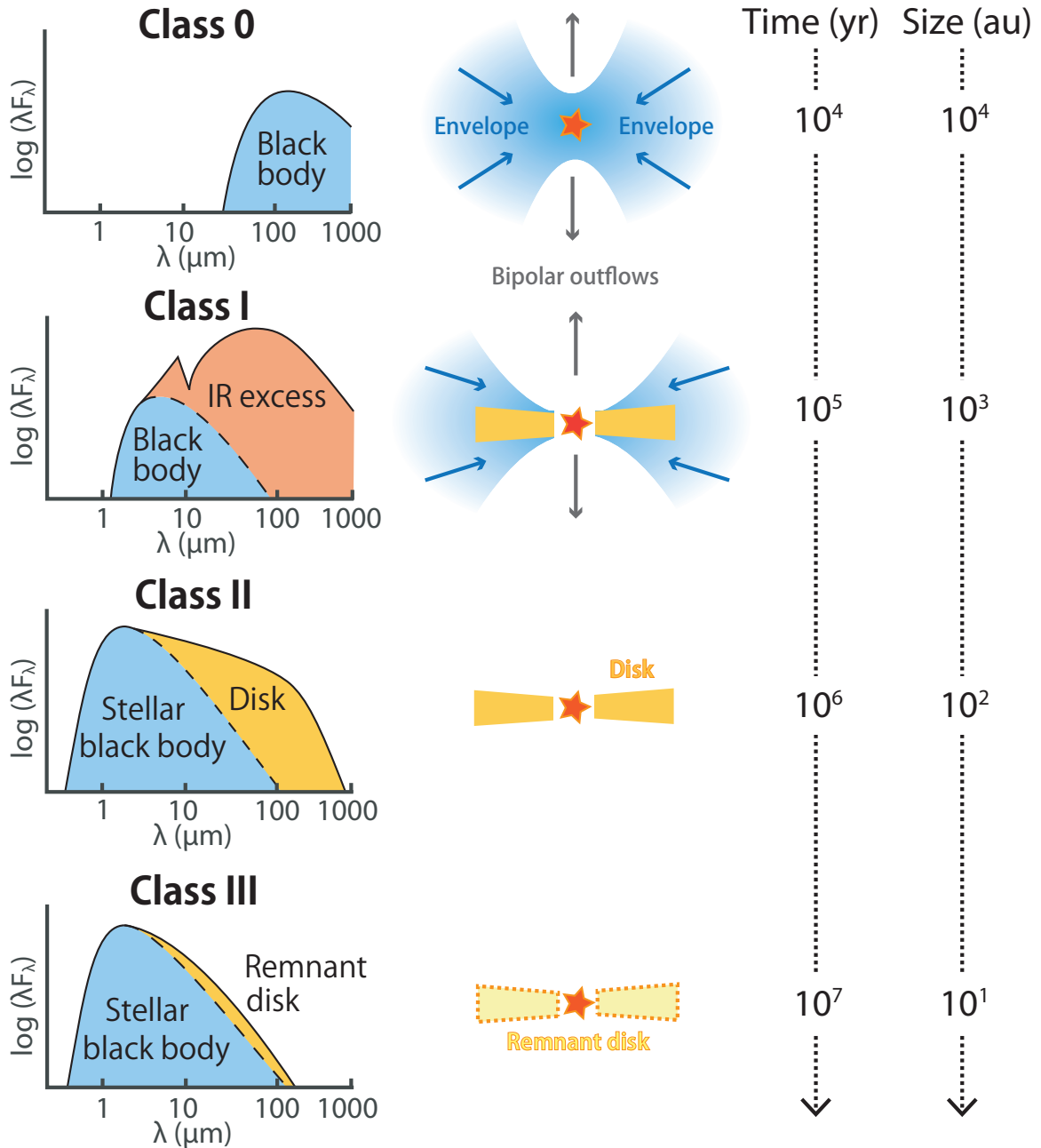


Figure 1.1: Classification of the evolutionary stages of low-mass protostars by infrared SED.

molecules are broken into atoms by photodissociation and atoms whose ionization potential is lower than that of H_2 (13.6 eV) are ionized (e.g., the carbon atom). After the density of the core becomes high enough to be shielded from the UV radiation, the ionized carbon atom is neutralized, and is then converted to CO through chemical reactions with O-bearing species. Because CO is stable, the gas-phase carbon is eventually locked up in CO. Carbon-chain molecules are efficiently formed in the early stage of the prestellar core when most of the carbon atoms have not been converted to CO. They are destroyed during the evolution of the prestellar core.

A pioneering work on the chemical evolution in molecular clouds was reported by Suzuki *et al.* (1992). They found a systematic chemical difference between prestellar cores and protostellar cores: carbon-chain molecules such as CCS and HC₃N are abundant in a chemically young phase, whereas N-bearing molecules such as NH₃ and N₂H⁺ are abundant in a chemically late phase associated with protostars. Such a systematic evolutionary trend of chemical compositions is caused, because the carbon-chain molecules are efficiently produced from C⁺ or the carbon atom in chemically young cores, whereas the timescale of the production of N-bearing species is relatively longer than that of carbon-chain molecules.

Another important phenomenon that has a substantial influence on the chemical evolution in the prestellar- and protostellar-cores is the ice formation on dust grains. Infrared observations toward prestellar- and protostellar-cores reveal that the dust grain is covered by ice, which is composed mainly of water as well as the fundamental molecular species such as CO, CO₂, and NH₃ (e.g., Gibb *et al.* 2004). The ices on the dust grains are formed by the adsorption of gas-phase species onto dust surfaces. Although the ice formed on the grain surface is rapidly destroyed by the UV radiation in diffuse clouds, it can survive in prestellar cores where the UV field is sufficiently attenuated by dust grains. The temperature during the prestellar-core phase is typically as low as 10 K, which is too low for the thermal desorption to take place. Hence, adsorbed species are usually kept frozen on ice surfaces and are accumulated to form thick ice mantles (Figure 1.2 (a)).

A time scale of the adsorption is approximately given as:

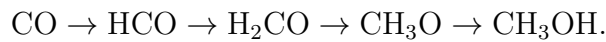
$$t_{\text{ads}} \sim 1 \times 10^6 \left(\frac{10^4 \text{ cm}^{-3}}{n_{\text{H}}} \right) \left(\frac{1.0}{S} \right) \left(\frac{0.1 \text{ } \mu\text{m}}{a} \right)^2, \quad (1.1)$$

where S is the sticking probability to the dust grains, a the grain radius, and n_{H} the number density of the H nuclei (Tielens 2005). As can be seen in this equation, the molecular depletion efficiently occurs at high density regions. The absence of molecules except for H₂ in the gas phase (the molecular depletion) was shown observationally by Caselli *et al.* (1999). They observed the C¹⁷O line toward the prestellar core L1544, and found that the abundance of CO decreases in the center of the core by comparing with the continuum map from the thermal emission of the dust grain.

The ice on dust grains is not just an absorber of gas-phase species, but also serves as formation sites of complex molecular species. Adsorbed atoms and molecules can move on the ice surfaces due to thermal diffusion and quantum tunneling. When an atom or a molecule encounters another species, they react with each other to form another molecular species (the so-

called Langmuir-Hinshelwood mechanism; e.g., Hasegawa *et al.* 1992). Unlike in the gas-phase, association reactions without dissociation (i.e., two-body reactions forming one product) can proceed efficiently on ice surfaces, because the surface can act as a third body for the reactions: the excess energy of the reactions can escape to the surface. Since the H atom is the lightest species, the reaction with the H atom (hydrogenation) efficiently occurs.

Because the gas-phase chemical composition changes in the course of the core evolution toward star formation, the species adsorbed on the ice and those formed via surface reactions on the ice also vary along the core evolution (Figure 1.2). Atoms such as O, C, and N are preferably depleted on the ice surfaces in the earlier stage of prestellar cores, where the atoms are not well converted to molecules in the gas phase. These atoms on the ices are hydrogenated to produce fundamental molecular species (e.g., H₂O, CH₄, and NH₃). On the other hand, CO is efficiently depleted in the later stage of the prestellar core, and is hydrogenated to form H₂CO and finally CH₃OH:



These species thus formed on the ice surface are usually kept frozen, although a small amount of them is sublimated via non-thermal processes such as reactive desorption (desorption due to the surplus energy of the two-body association reaction; Garrod *et al.* 2006) and photodesorption by cosmic-ray-induced UV photons (e.g., Prasad & Tarafdar 1983).

Such a chemical evolution in the gas phase and on the ices can be recognized as a systematic change in the chemical composition as a function of distance from the core center (or the protostar), as shown in Figure 1.3. The core edge has a diffuse-cloud-like environment, because it is less dense and exposed to the UV radiation. On the other hand, the core center is in

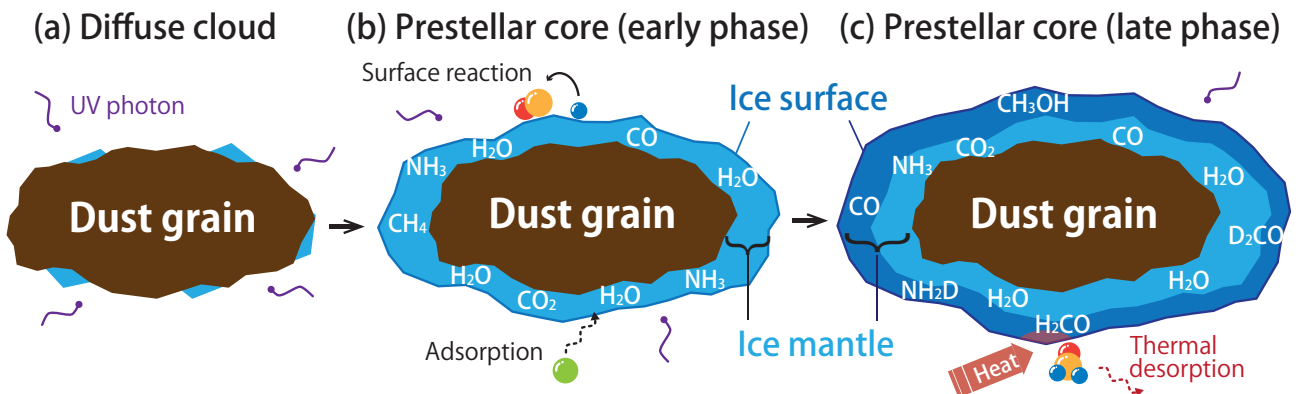


Figure 1.2: Schematic illustration of the evolution of ice mantle.

the more evolved stage due to the high density and low temperature. Indeed, the mapping observations of the CO isotopologues revealed that their emission is bright in the outer region but weak in the central region of the core, suggesting that CO is depleted only at the core center (Caselli *et al.* 1999; Bergin *et al.* 2002, Figure 1.4)

1.2.2. Protostellar core

The chemical composition of the ice mantle plays a crucial role in chemical processes in the protostellar-core phase. First, the gradual temperature rise of dust grains due to the protostellar heating stimulates the production of complex species on the ice surface, because the heavy molecules become mobile on the ice surface to react with each other (e.g., $\text{HCO} + \text{CH}_3\text{O} \rightarrow \text{HCOOCH}_3$; Garrod & Herbst 2006). Second, the molecules thus formed on the ice surface are released into the gas phase via thermal desorption. When the temperature reaches the desorption temperature of each species, a fraction of the molecules in the ice mantle sublimates. The remaining molecules trapped in water ice are released into the gas phase, when the water ice itself desorbs at around 100 K (the so-called volcano desorption; Collings *et al.* 2004). These characteristics are seen as a radial dependence of the chemical composition (Figure 1.3).

In the last decade, it has been established that the property of the prestellar core can provide a strong influence on the chemical composition of a protostellar core to be formed. This picture is based on the discovery of significant chemical diversity among low-mass proto-

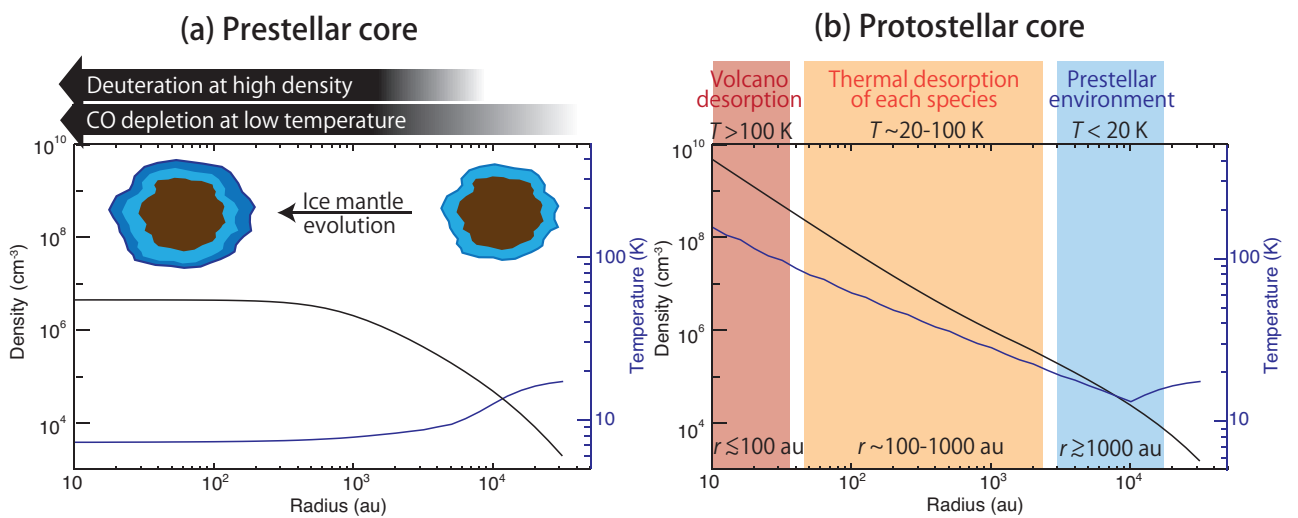


Figure 1.3: Radial difference of the chemical characteristics in prestellar- and protostellar-cores shown with their typical temperature and density profiles. The temperature and density profiles are taken from Taquet, Charnley, & Sipilä (2014).

stellar sources whose evolutionary stages are similar to one another (e.g., Sakai & Yamamoto 2013; Watanabe *et al.* 2012; Higuchi *et al.* 2018). One distinct case is hot corino chemistry characterized by rich saturated complex organic molecules (COMs) in a hot region around a protostar (e.g., Cazaux *et al.* 2003; Sakai *et al.* 2006; Öberg *et al.* 2011; Taquet *et al.* 2015; Codella *et al.* 2016). A representative hot corino source is IRAS 16293-2422 in Ophiuchus (e.g., Cazaux *et al.* 2003; Bottinelli *et al.* 2004; Kuan *et al.* 2004). Recent high spatial-resolution observations revealed that saturated COMs such as HCOOCH_3 , $(\text{CH}_3)_2\text{O}$, and even glycolaldehyde ($\text{CH}_2(\text{OH})\text{CHO}$) are abundant in the innermost part of the protostellar core having a temperature higher than 100 K (e.g., Jørgensen *et al.* 2012, 2016; Favre *et al.* 2014; Oya *et al.* 2016, 2018). On the other hand, the warm carbon-chain chemistry (WCCC) is characterized by high abundances of carbon-chain molecules and related species concentrated around a protostar (e.g., Sakai *et al.* 2008b, 2009a, 2010a; Hirota, Sakai & Yamamoto 2010). A prototypical source is IRAS 04368+2557 in L1527 in the Taurus molecular cloud. In WCCC, unsaturated hydrocarbons such as carbon-chain molecules and their isomers are efficiently produced in the gas phase, triggered by sublimation of CH_4 from the ice mantle in a lukewarm region around a protostar ($T \sim 25$ K and $r \sim 500$ au; one astronomical unit, 1 au, corresponds to the average distance between the Sun and Earth, 1.50×10^{11} m).

Hot corino chemistry and WCCC show exclusive nature: carbon-chain molecules are deficient in the hot corinos, while COMs are deficient in the WCCC sources (Figure 1.5; Sakai

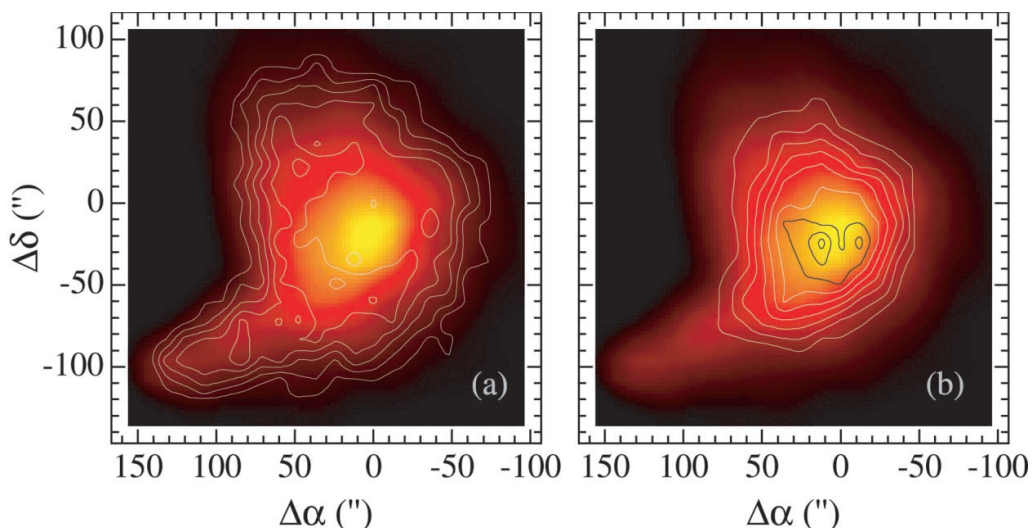


Figure 1.4: (a) The integrated intensity of the C^{18}O $J = 1-0$ line (contours) in the prestellar core B68 superposed on a map of visual extinction. The emission becomes weak at the core center where visual extinction is high. (b) The same as (a) but for N_2H^+ $J = 1-0$ line. Because N_2H^+ is destroyed mainly by CO, it is abundant in the core center where CO is deficient in the gas phase. Taken from Bergin *et al.* (2002).

et al. 2008b; Sakai & Yamamoto 2013; Lefloch *et al.* 2018). It is proposed that this chemical variation would originate from the duration time of the prestellar core phase after the shielding of the interstellar UV radiation from outside of the parent molecular cloud (Sakai *et al.* 2009a; Sakai & Yamamoto 2013). If the duration time is long enough for the gas-phase formation of CO from the C atom, CO is depleted onto dust grains rather than C, resulting in the formation of CH₃OH through a series of reactions with the H atom on the ice surface (e.g., Watanabe & Kouchi 2002; Soma *et al.* 2015). COMs are thought to be formed on the ice surfaces as in the case of CH₃OH, or by subsequent gas-phase reactions starting from sublimated CH₃OH (e.g., Garrod & Herbst 2006; Vasyunin & Herbst 2013; Balucani *et al.* 2015; Soma *et al.* 2018). On the other hand, if the duration time of the prestellar core phase is close to the free-fall time (i.e., the core collapse starts just after the UV shielding), the C atom still survives in the gas phase without being converted to CO, and can be depleted onto the ice surface. This situation leads to the efficient production of CH₄ on the ice surfaces by hydrogenation of the C atom. CH₄ thus formed triggers WCCC after its sublimation (Aikawa *et al.* 2008; Hassel *et al.* 2008). Thus, chemical diversity emerges in the gas phase, when molecules in dust mantles are released into the gas phase after the onset of star formation.

1.3. Deuterium fractionation

Molecular isotopic ratios can also vary along core evolution and star-formation processes, and can be used as an evolutionary tracer. A representative example is the deuterium fractionation. Almost all the molecules in cold interstellar clouds are enriched in deuterium in

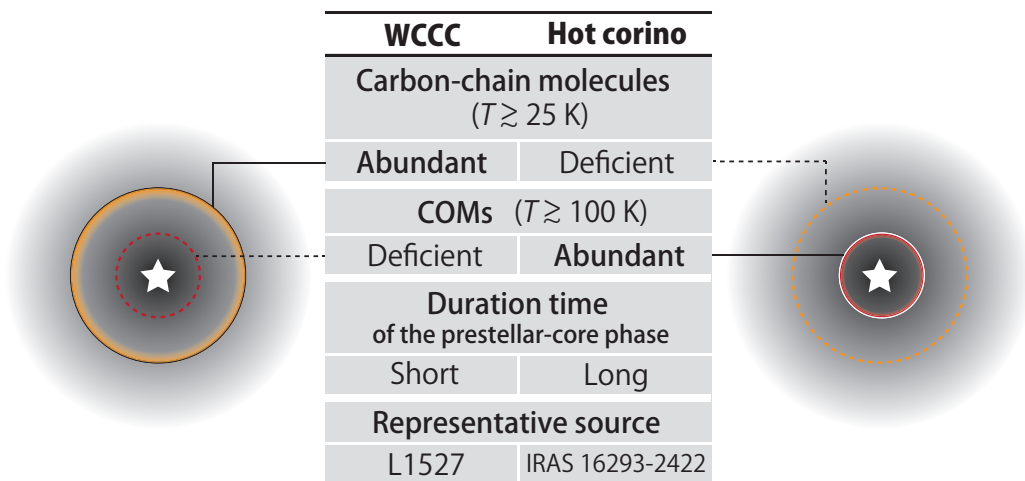


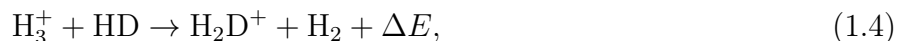
Figure 1.5: Comparison of WCCC and hot corino. Carbon-chain molecules are abundant in a lukewarm region near the protostar in the WCCC sources, whereas saturated COMs are abundant in the vicinity of the protostar in hot corino sources.

comparison with the cosmic D-to-H ratio of about 10^{-5} (Linsky 2003). Molecular D/H ratios are found to range from around 10^{-2} to even unity in some cases. This phenomenon is called deuterium fractionation, as deuterium is fractionated into molecules.

In molecular clouds, the main reservoirs of hydrogen and deuterium atoms are H_2 and HD, respectively. When a hydrogen molecule, H_2 , is ionized to H_2^+ by cosmic rays, it immediately reacts with another hydrogen atom to produce H_3^+ ion:



The H_3^+ ion stimulates the production of various molecules via proton transfer (Herbst & Klemperer 1973). Likewise, the deuterium fractionation is triggered by the reaction with H_3^+ and HD:



where $\Delta E = 230$ K (Gerlich *et al.* 2002). The abundance of H_2D^+ is significantly enhanced at low temperature conditions in prestellar cores (~ 10 K), because the backward reaction of (5.2) is unlikely to occur due to its endothermicity. Deuterium is then transferred to various molecules by reactions with other molecular species in the gas phase, e.g.,



In addition to the H_3^+ ion, CH_3^+ and C_2H_2^+ are also considered to contribute to the deuterium fractionation (Huntress 1977; Herbst *et al.* 1987). They react with HD fast enough to compete against electron recombination reactions:



where ΔE_1 and ΔE_2 are about 390 K and 550 K, respectively (Asvany *et al.* 2004; Herbst *et al.* 1987). Because the exothermicities are larger than that of the reaction of H_3^+ (5.2), CH_2D^+ and C_2HD^+ play an important role in the deuterium fractionation in a warmer environment (Roueff *et al.* 2007). In the following subsections, previous studies on the deuterium fractionation are

briefly summarized mainly from an observational point of view.

1.3.1. *Prestellar core*

Because a high deuterium fractionation is expected in a cold region, deuterated species have mainly been found by observations toward dark clouds in early days of radio astronomy: e.g., DCO⁺ (Hollis *et al.* 1976), DCN (Penzias *et al.* 1977), DNC (Godfrey *et al.* 1977), N₂D⁺ (Snyder *et al.* 1977), c-C₃HD (Gerin *et al.* 1987), and NH₂D (Turner *et al.* 1978).

In contrast, it has been recognized that the deuterium fractionation is less enhanced in warmer cores. Snell & Wootten (1979) found that the [DNC]/[HNC] ratio is strongly anti-correlated with the kinetic temperature of the cloud, based on the survey observations of sample sources with different kinetic temperatures (10–70 K). They estimated the exothermicity of the exchange reaction (5.2) to be 240 ± 60 K, verifying that exchange reactions between HD and molecular ions such as H₃⁺ and CH₃⁺ are responsible for the deuteration. The anti-correlation between the deuterium fractionation and the core temperature is also shown by many other studies (e.g., Schilke *et al.* 1992; Wilson *et al.* 1999).

The degree of the deuterium fractionation in the prestellar core phase does not depend solely on the temperature, but also on the density. The degree of the deuterium fractionation is found to be different from core to core (e.g., Howe *et al.* 1994; Saito *et al.* 2000; Crapsi *et al.* 2005), although the prestellar cores uniformly have a temperature of around 10 K (Benson & Myers 1989). An important phenomenon to account for this difference is the depletion of CO onto dust grains. As the core density increases to 10^5 – 10^6 cm⁻³, the timescale for CO depletion becomes much shorter than the dynamical timescale of prestellar cores, since the timescale for depletion of species onto dust grains is roughly estimated as t (year) $\sim 10^{10}/[n$ (cm⁻³)]. More than 90% of the CO molecules are reported to be frozen onto dust grains in prestellar cores (Caselli *et al.* 1999; Bacmann *et al.* 2003). Because CO is the main destroyer of the H₃⁺ ion, the CO depletion extends the lifetimes of H₃⁺ and its deuterated counterparts (H₂D⁺, D₂H⁺, and D₃⁺), leading to the heavy deuterium fractionation in various molecules. The trend of the higher deuterium fractionation for a higher degree of CO depletion is confirmed by observing many prestellar cores (e.g., Crapsi *et al.* 2005; Bacmann *et al.* 2003). The correlation between the CO depletion and the core density is also reported (Bacmann *et al.* 2002).

Since two important factors for the deuterium fractionation, namely, the low temperature and the heavy CO depletion, are fulfilled in the prestellar core phase, an extreme molecular deuteration is realized: even doubly and triply deuterated molecules have been detected

(e.g., D_2H^+ , $c\text{-C}_3\text{D}_2$, and ND_3 ; Vastel *et al.* 2004; Spezzano *et al.* 2013; Lis *et al.* 2002). The $[\text{ND}_3]/[\text{NH}_3]$ ratio is reported to be 8×10^{-4} , which corresponds to the D/H ratio higher than the elemental D/H ratio by 11 orders of magnitude (Lis *et al.* 2002). Such an extreme deuterium fractionation is reproduced by the chemical network calculations including the deuterated species such as H_2D^+ , D_2H^+ , and D_3^+ (Roberts *et al.* 2003).

The increase of the D/H ratio for the H_3^+ ion also enhances the atomic D/H ratio in the gas phase, because the dissociative recombination of H_2D^+ produces the deuterium atom:



The deuterium atoms thus produced are depleted onto the grain mantle and are used for the deuteration of the species on the ice, resulting in the enhancement of the molecular D/H ratios on the ice.

1.3.2. Protostellar core

In the protostellar core phase, the temperature rise after the onset of star formation has substantial influences on the deuterium fractionation. First, the deuterium fractionation no longer proceeds in the protostellar cores, because CO is released from dust grains ($T > 20$ K) and the temperature becomes high enough for the backward reaction of the reaction (5.2) to occur. Hence, the deuterium fractionation is expected to decrease along the protostellar evolution. This trend is indeed confirmed by the survey observations toward Class 0–I protostars in Perseus molecular cloud (Friesen *et al.* 2013; Imai *et al.* 2018). Second, the molecules formed on the grains are sublimated in the vicinity of the protostar ($r \sim 100$ au; $T \sim 100$ K), which could alter the chemical composition around the protostar. Since these sublimated molecules are formed on the dust grains during the prestellar-core phase, the D/H ratios are affected by the deuterium fractionation in the past prestellar-core era. Formaldehyde and methanol, which are the basic building-blocks of COMs, are found to have high D/H ratios in the protostellar cores (Parise *et al.* 2004, 2006; Roberts & Millar 2007)

However, the vast majority of observations to date were conducted with single-dish telescopes which cannot resolve the innermost vicinity of the protostar. A few interferometric observations recently revealed the deuterium fractionation of water and COMs in the innermost vicinity of the protostar with a radius of 100 au (e.g., Coutens *et al.* 2013; Persson *et al.* 2018; Jørgensen *et al.* 2018). Nevertheless, the deuterium fractionation in protostellar cores is

not well investigated by interferometers in terms of the chemical evolution from the prestellar cores. Since these interferometric observations focus on the innermost part, the results cannot directly be compared with that in the outer cold envelope which inherits the footprints of the parent prestellar core due to the ‘resolving-out’ problem of the interferometers (Section 2.2.2).

1.4. Fractionation of ^{13}C species

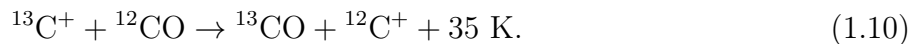
Recently, anomalies of the $^{12}\text{C}/^{13}\text{C}$ ratio for carbon-chain molecules have also been recognized in nearby cold and dense molecular clouds. Rotational spectral lines of the ^{13}C isotopic species of various molecules are now detectable with a reasonable observation time, thanks to recent developments of receiver and back-end technologies in radio astronomy. So far, spectral lines of the ^{13}C isotopic species of abundant molecules, whose main isotopologue (normal species) lines are optically thick, have widely been observed to derive the column density of the normal species accurately. In this case, the $^{12}\text{C}/^{13}\text{C}$ ratio of each species is usually assumed to be the same as the elemental $^{12}\text{C}/^{13}\text{C}$ ratio, which is 60–70 in the solar neighborhood (Lucas & Liszt 1998; Milam *et al.* 2005). On the other hand, some molecular species have been found to show two kinds of anomalies of the $^{12}\text{C}/^{13}\text{C}$ ratio: (1) different $^{12}\text{C}/^{13}\text{C}$ ratios for different carbon atoms in a single molecular species and (2) significantly high $^{12}\text{C}/^{13}\text{C}$ ratios for several carbon-chain molecules in comparison with the elemental $^{12}\text{C}/^{13}\text{C}$ ratio.

As for the former anomaly, Takano *et al.* (1998) reported the non-equivalent abundances of the three ^{13}C species of HC_3N toward the cold dark cloud TMC-1 (Cyanopolyne peak; CP). The abundance of the HCC^{13}CN is higher than that of H^{13}CCCN and HC^{13}CCN by a factor of 1.4. Sakai *et al.* (2007) also reported a large difference between the ^{13}CCS and C^{13}CS abundances toward TMC-1 (CP), the ratio of $[\text{C}^{13}\text{CS}]/[^{13}\text{CCS}]$ being 4.2. A similar non-equivalence of the ^{13}C isotopologues of a single molecular species is reported for CCH, C_3S , and C_4H (Sakai *et al.* 2010a, 2013). It is proposed that these non-equivalent abundances of the ^{13}C species reflect production pathways of each molecular species and/or originate from gas-phase reactions interchanging the ^{13}C position within a molecule (Sakai *et al.* 2010a; Furuya *et al.* 2011).

The second anomaly is that the $^{12}\text{C}/^{13}\text{C}$ ratios of some carbon-chain molecules are significantly higher than the elemental $^{12}\text{C}/^{13}\text{C}$ ratio (60–70) in the solar neighborhood, indicating that the ^{13}C isotope is diluted in these molecules. The most striking result is reported for CCH (Sakai *et al.* 2010a). The $[\text{CCH}]/[^{13}\text{CCH}]$ and $[\text{CCH}]/[\text{C}^{13}\text{CH}]$ ratios are higher than 250 and 170 toward TMC-1 (CP), respectively. High $^{12}\text{C}/^{13}\text{C}$ ratios are also seen in CCS, C_3S , and

C₄H. Such a dilution of the ¹³C isotopic species was theoretically predicted by Langer *et al.* (1984), and it was confirmed for some carbon-chain molecules by the above observations. On the other hand, Liszt & Ziurys (2012) reported the ¹²C/¹³C ratios of CS, HNC, and H₂CS to be in the range from 43 to 79 toward TMC-1 (CP), which is close to the elemental ¹²C/¹³C ratio. Hence, the degree of the ¹³C dilution seems dependent on molecular species, although its origin is still controversial.

According to Langer *et al.* (1984), the mechanism of the dilution of the ¹³C species is as follows. In dense molecular clouds, the main reservoir of ¹³C is ¹³CO, because CO is the most abundant carbon-bearing molecule. As carbon-chain molecules are produced by reactions starting from C⁺, their ¹³C species are formed by the reaction from ¹³C⁺. Although the ¹³C⁺ ion is produced from ¹³CO with the reactions of He⁺, as ¹²C⁺ from ¹²CO, ¹³C⁺ goes back to ¹³CO by the following isotope exchange reaction (Langer *et al.* 1984; Roueff *et al.* 2015):



This is the most important reaction for ¹³C⁺, because the reaction with H₂ is a very slow radiative association. The electron recombination is also much slower than the reaction with ¹²CO. This exchange reaction is exothermic (Watson, Anicich, & Huntress 1978), and hence, its backward reaction is slow at a low temperature. Then, the ¹²C⁺/¹³C⁺ ratio tends to be higher at a low temperature. The ¹³C species of various molecules produced from ¹³C⁺ thus become less abundant. After the proposal by Langer *et al.* (1984), Woods & Willacy (2009) and Furuya *et al.* (2011) also confirmed this trend by chemical model calculations.

1.5. Background of this thesis

So far, chemical evolution from molecular clouds to protostellar cores has almost been established, and now evolution to protoplanetary disks is being explored. However, there still exists a large missing link between chemistry of protostellar cores and that of protoplanetary disks (Figure 1.6). Since very complex chemical processes both in the gas phase and on dust grains would be expected from protostellar cores to planetary systems, it seems difficult to find a possible link between them only by focusing on molecular species. Namely, molecules found in protostellar cores are not always delivered to planetary systems as they are. One of the potential links between interstellar chemistry and planetary chemistry is anomaly of molecular isotope ratios. In the context of planetary science, the isotope anomaly is found in the small bodies in the Solar System, such as meteorites and comets. The deuterium fractionation has been found

in the so-called hot spots, which are micrometer-scale regions with isotope fractionations, in the carbonaceous meteorites ($D/H \sim 3 \times 10^{-3}$ at most; e.g., Busemann *et al.* 2009). The carbon isotope anomaly is also found (Floss *et al.* 2006). Although the $^{12}C/^{13}C$ anomaly in dust-forming zones of AGB stars (e.g., Milam *et al.* 2009; Kahane *et al.* 1992; Tomkin *et al.* 1976) is thought to mainly contribute to the anomaly in meteorites, the $^{12}C/^{13}C$ anomaly in cold molecular clouds may also be responsible. Hence, understanding the abundance anomaly of the molecular isotopic ratios and its evolution in star-forming regions is of particular importance to trace the material origin of the Solar System back to interstellar medium. It is however unclear whether the isotope fractionation found in meteorites is inherited from that formed in the very first stages of star formation (i.e., the prestellar- and protostellar-core phases) or is a product in a late stage of the protoplanetary-disk phase. One of the reasons is that the evolution of the isotope fractionation is not fully understood during the protostellar-core phase.

To investigate the evolution of isotope anomaly, two different approaches can be employed: one is a statistical approach, which reveals the systematic evolutionary trend of the isotopic ratios by observing many molecular cloud cores, and the other is a direct imaging of a particular core, which can probe the evolution from the outer surrounding envelope to the inner region near a newly born star. Although the evolution of deuterium fractionation is studied by the former approach (e.g., Hirota, Ikeda & Yamamoto 2001; Bacmann *et al.* 2003; Crapsi *et al.* 2005; Imai *et al.* 2018), the evolution of the deuterium fractionation within a protostellar core has not been well investigated due to the lack of the spatial resolution. As for the ^{13}C anomaly, it is not clear whether it is inherited from prestellar cores to protostellar cores, because only a limited number of sources has been investigated so far (the protostellar core L1527 and the

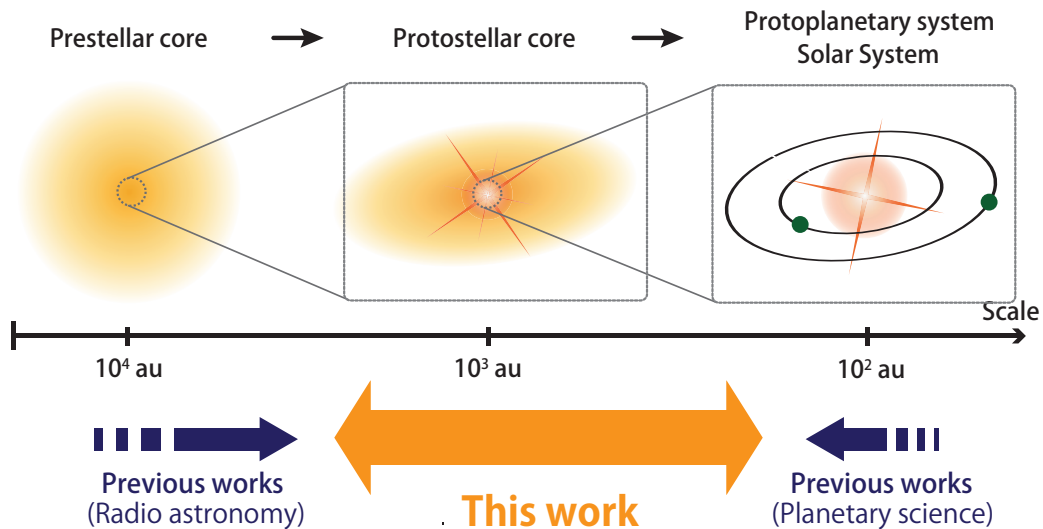


Figure 1.6: Schematic view of the evolution of a core and the approach of this thesis.

four prestellar cores; TMC-1, L1521E, L1521B, and L134N).

With this in mind, we investigated the isotope fractionation in the low-mass protostellar core L1527. We chose this source for the target source, because its physical and chemical characteristics have well been investigated so far. L1527, which was found as a heavily obscured infrared source (IRAS 04368+2557) by the *Infrared Astronomical Satellite (IRAS)* survey (Beichman *et al.* 1986), is located in one of the closest molecular clouds, the Taurus molecular cloud, at a distance of 140 pc ($1 \text{ pc} = 3.09 \times 10^{16} \text{ m}$; Torres *et al.* 2007). It is classified as an object in late Class 0 to early Class I phase (e.g., Motte & André 2001). Near-infrared observations revealed that the scattered light image shows bright bipolar outflow cavities in the east-west direction extending over $\sim 10^4$ au (Tobin *et al.* 2008, Figure 1.7 A). The molecular emissions of CO and its isotopologues (^{13}CO and C^{18}O) also show the outflow with a 10^4 -au scale (e.g., Bontemps *et al.* 1996; Zhou *et al.* 1996; Hogerheijde *et al.* 1998). On a smaller scale, Atacama Large Millimeter/submillimeter Array (ALMA) delineated the outflow traced by the CS emission within ~ 2000 au from the protostar, whose blueshifted and redshifted components are in the west and east side of the protostar, respectively (Oya *et al.* 2015). The protostellar envelope is also observed, and is found to have a flattened shape extending from north to south. A nearly edge-on configuration of the envelope enables us to directly probe the midplane of the envelope and the inner disk, making this source ideal for kinetic modelings.

Interferometric observations of CO isotopologues on a 2000-au scale showed the infalling motion of the envelope gas (Ohashi *et al.* 1997; Yen *et al.* 2013). On the other hand, observations of the ^{13}CO and C^{18}O ($J = 2-1$) lines on a 500-au scale suggest the existence of a Keplerian disk (Tobin *et al.* 2012; Ohashi *et al.* 2014, Figure 1.7 B). In addition, Sakai *et al.* (2014a,b) presented a clear infalling and rotating motion in the same envelope gas at a resolution of ~ 100 au with ALMA. The position-velocity diagram of $c\text{-C}_3\text{H}_2$ in the envelope gas shows the redshifted component on the southern side and the blueshifted one on the northern side, indicating a infalling motion (Figure 1.7 C, D, and E).

The peculiar chemical characteristic of this source is also well investigated mainly with the single-dish telescopes in the last decade. Sakai *et al.* (2008b) found that unsaturated carbon-chain molecules such as C_4H_2 and C_4H are abundant in L1527, which were thought to be deficient in protostellar cores due to the deficiency of the carbon atom that could produce carbon-chain molecules. The rotational temperatures derived for the carbon-chain molecules suggest that they mainly reside in a warm region. In addition, mapping observations showed that the carbon-chain molecules are concentrated within ~ 1000 au from the protostar (Sakai

et al. 2010a). Hence, the carbon-chain molecules exist mainly in a warm and dense region in L1527 rather than in the outer cold envelope where the prestellar-core environment remains. It is proposed that these carbon-chain molecules are efficiently produced from CH₄ sublimated from the ice mantle (WCCC; Sakai *et al.* 2008b; Sakai & Yamamoto 2013).

Recently, the chemical structure of L1527 at a disk scale (~ 100 au) is investigated with ALMA. Sakai *et al.* (2014a,b) presented a drastic change in chemical compositions across the centrifugal barrier of the infalling-rotating envelope (IRE) at the radius of 100 au. CCH and CS mainly reside in the IRE outward of the centrifugal barrier, whereas SO and probably CH₃OH are enhanced at the centrifugal barrier and may survive in the disk (Figure 1.7 C). The H₂CO emission traces both the IRE and the disk component. van't Hoff *et al.* (2018) reported that the Keplerian disk is warm enough for CO to be present in the gas phase, based on the ALMA observations of ¹³CO, C¹⁸O, and N₂D⁺ with a subarcsecond-resolution observation. However, the isotope fractionation in this source is not fully investigated. We therefore studied the ¹³C anomaly and the deuterium fractionation in this source with the single-dish telescope and ALMA, respectively.

1.6. Outline of this thesis

In this thesis, the isotopic fractionations in L1527 are studied by radio astronomical observations. The outline of this thesis is as follows: In Chapter 2, the general description of radio telescopes and observation techniques are briefly summarized. In Chapter 3, the overall chemical composition of L1527 is revealed by the spectral line survey observation with the Nobeyama 45-m telescope in the 3-mm band. The isotopic fractionations found in this survey are presented. Complementary studies of the ¹³C anomaly conducted with the IRAM 30-m telescope are discussed in Chapter 4. In Chapter 5, the mapping observations of deuterated species with ALMA are conducted to investigate the evolution of the deuterium fractionation in L1527. Finally, Chapter 6 concludes the thesis, and presents the future prospects.

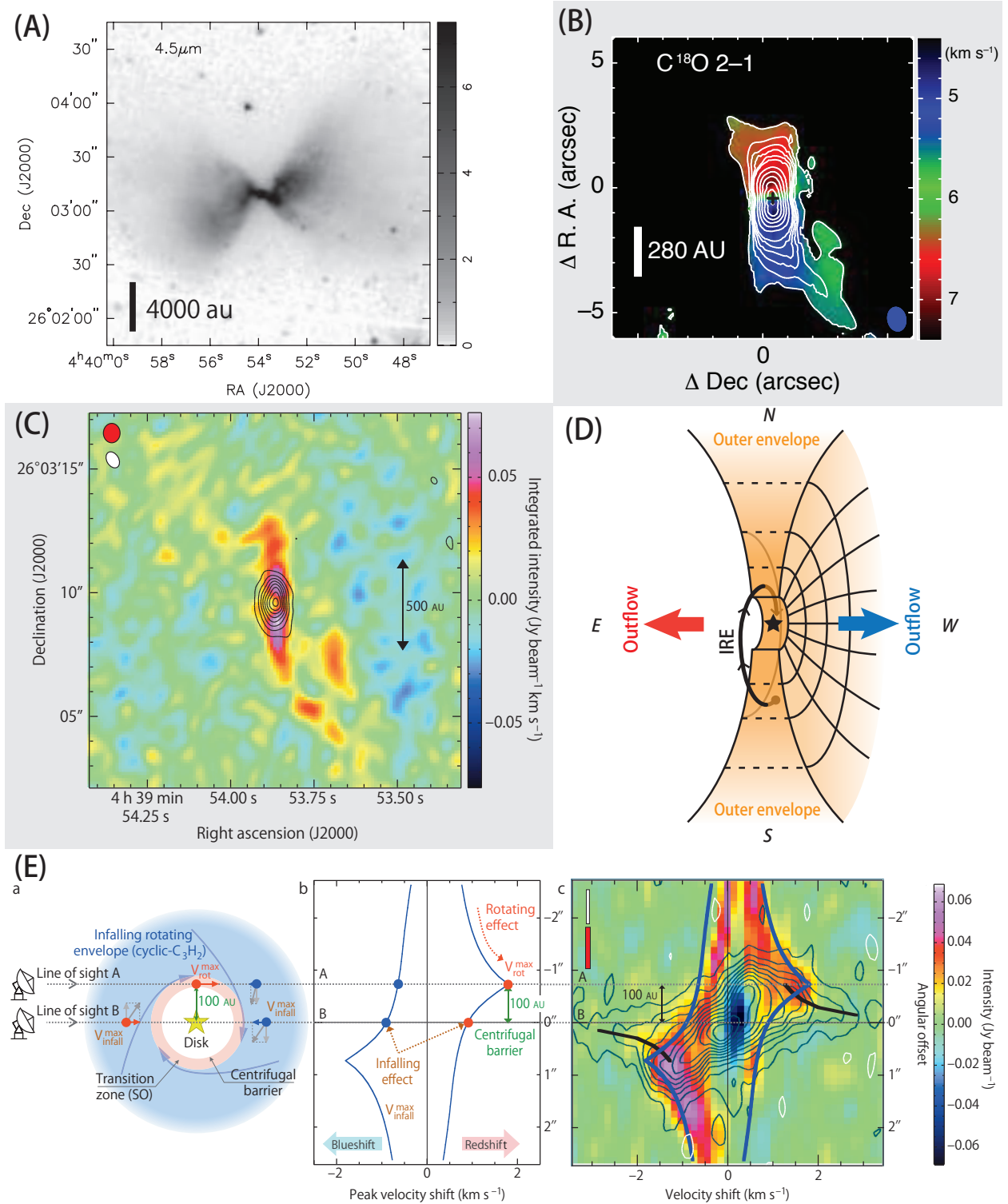


Figure 1.7: (A) Infrared image ($4.5 \mu\text{m}$) of L1527 by Tobin *et al.* (2008). (B) The integrated intensity (moment 0; contours) and intensity-weighted mean velocity maps (moment 1; color) of C^{18}O ($J = 2-1$) by Ohashi *et al.* (2014). (C) The integrated intensity maps of $c\text{-C}_3\text{H}_2$ ($5_{23}-4_{32}$; color) and SO ($N = 8-7$, $J = 7-6$; contours) lines by Sakai *et al.* (2014a). (D) Schematic illustration of the geometry of L1527. (E) a. Schematic illustration of the IRE. b. Maximum velocity shift calculated from the model for the edge-on geometry. c. Position-velocity diagrams of $c\text{-C}_3\text{H}_2$ ($5_{23}-4_{32}$; color) and SO ($N = 8-7$, $J = 7-6$; contours) along the midplane of the envelope. Blue and black lines denote the maximum velocity shifts of the infalling-rotating and Keplerian motion, respectively. Taken from Sakai *et al.* (2014a).

CHAPTER 2

OBSERVATION TECHNIQUES

Because the molecular clouds are extremely cold (typically 10 K), molecules existing there only emit a radio wave in a rotational transition. Molecular rotational lines have been detected by ground-based radio telescopes since 1960s (e.g., Cheung *et al.* 1968). Telescopes used for radio-wave observations are classified into two categories: single-dish telescopes and radio interferometers. Single-dish telescopes are composed of a single aperture antenna, and have been used for astronomical observations since 1930s. Interferometers are collections of telescopes that can produce images having much better angular resolutions than a single aperture, by using the aperture synthesis technique developed by Ryle through the 1950s and 1960s (e.g., Ryle & Neville 1962). To date, a hundred or more of radio telescopes have been used for astronomical purposes. The essential parts of their features and the instruments used in this thesis are briefly described in this chapter.

2.1. Single-dish telescope

2.1.1. Components

The simplest radio telescope is a single aperture antenna to collect the faint emission from astronomical objects. It consists of three components, as described below. A schematic illustration of radio telescopes is shown in Figure 2.1.

Antenna

Radio emission from astronomical objects is collected by a main reflector of the telescope, which is usually an antenna with a paraboloidal shape. A Cassegrain optics, in which a primary reflector dish aims at a smaller convex secondary reflector, is often employed. The surface of the main reflector needs to have an accuracy much better than the observing wavelength λ (typically less than $\lambda/10$ at least). It is difficult to maintain the surface of a large aperture antenna because of a gravitational deformation. To overcome this difficulty, the main reflector is usually designed by the homologous deformation technique: the main reflector deforms depending on the elevation angle so that it can keep the paraboloidal shape. Although the focal position and length change when the main reflector deforms, they are appropriately adjusted by changing

the position of the secondary reflector.

Front end

The electromagnetic signals collected by the antenna, which is called radio frequency (RF) signal, are fed into a receiver. Since a low-noise amplifier is not available for millimeter and submillimeter wavelengths, the signals are first converted to the intermediate frequency (IF) of a few GHz. For this purpose, a heterodyne mixer receiver is usually employed, which down-converts the frequency of the signal by the heterodyne mixing with the local oscillator (LO). As a nonlinear mixer device, a superconductor-insulator-superconductor (SIS) mixer, which consists of a very thin insulator layer (AlO_x) sandwiched by two superconductor layers (Nb), is widely employed. The tunneling current between the two superconductors realizes the nonlinear response.

Given that the RF signal V_{RF} and LO signal V_{LO} are written as

$$V_{\text{RF}}(t) = V_1 \cos(2\pi\nu_{\text{RF}}t + \phi_{\text{RF}}), \quad (2.1)$$

$$V_{\text{LO}}(t) = V_0 \cos(2\pi\nu_{\text{LO}}t + \phi_{\text{LO}}), \quad (2.2)$$

the output after mixing, $V_{\text{IF}}(t)$, can be obtained as

$$\begin{aligned} V_{\text{IF}}(t) &= [V_{\text{RF}}(t) + V_{\text{LO}}(t)]^2 \\ &= \frac{V_1^2}{2} \cos(4\pi\nu_{\text{RF}}t + 2\phi_{\text{RF}}) + \frac{V_0^2}{2} \cos(4\pi\nu_{\text{LO}}t + 2\phi_{\text{LO}}) \\ &\quad + V_1V_0 \cos [2\pi(\nu_{\text{RF}} + \nu_{\text{LO}})t + (\phi_{\text{RF}} + \phi_{\text{LO}})] \\ &\quad + V_1V_0 \cos [2\pi(\nu_{\text{RF}} - \nu_{\text{LO}})t + (\phi_{\text{RF}} - \phi_{\text{LO}})]. \end{aligned} \quad (2.3)$$

Here, we assume the nonlinear output as the square of the input signal for simplicity. By the use of an appropriate bandpass filter, one can obtain the down-converted signal (IF signal) with the frequency $\nu_{\text{IF}} = |\nu_{\text{RF}} - \nu_{\text{LO}}|$ (the last term in equation 2.3). The IF frequency is usually around 4–12 GHz. For the given IF frequency, the output IF signal includes information on two RF frequencies, $\nu_{\text{LO}} \pm \nu_{\text{IF}}$. $\nu_{\text{LO}} + \nu_{\text{IF}}$ is called the upper side band (USB), and $\nu_{\text{LO}} - \nu_{\text{IF}}$ is the lower side band (LSB). Processing the signal without separating USB and LSB is called the double side band (DSB) method, while using either USB or LSB is the single side band (SSB) method. Most observatories now employ the two single side band (2SB) method, which can separate one sideband from the other and obtain both USB and LSB signals simultaneously by using two mixers. In this scheme, the unwanted signal, which is not completely filtered out

from one side band, can be detected in the other side band. In case of imperfect separation of the side bands, an *'image line'* feature can be seen due to this effect, when the other side band (image band) covers a frequency of an emission line.

The IF signal thus obtained is amplified by an IF amplifier chain to the level necessary for the spectrometer. For the first amplification, high electron mobility transistor (HEMT) is generally used.

Back end

The amplified IF signal is fed to a radio spectrometer. A digital spectrometer using an autocorrelator is the most popular back-end. The IF signal is first digitized by a fast AD converter, followed by the autocorrelation as a function of the delay time. The spectrum is obtained by the Fourier transformation of the autocorrelation function. An acousto-optical spectrometer (AOS) is another type of the spectrometer frequently used, based on the diffraction of light by ultrasonic waves. The IF signal is induced into a piezoelectric transducer to generate an acoustic wave in a crystal. This acoustic wave diffracts an irradiated laser beam according to the amplitude and wavelength of the acoustic wave in the crystal. Thus, the direction of the diffracted light corresponds to the frequency. By measuring the diffracted light by CCD devices, the spectrum is obtained.

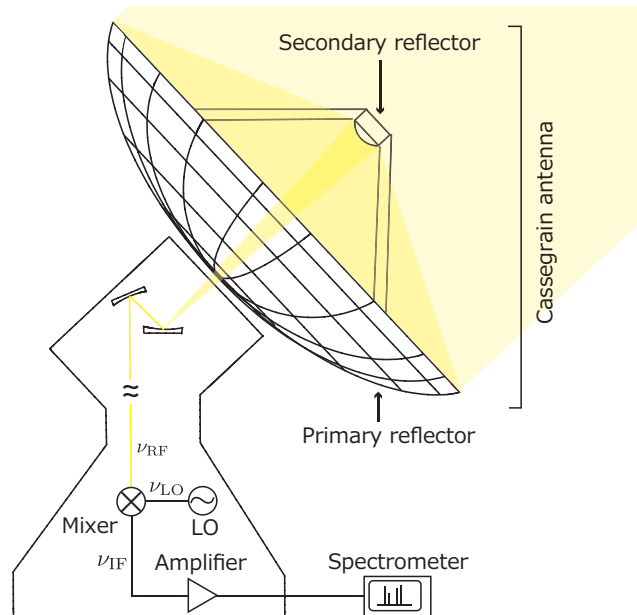


Figure 2.1: A schematic illustration of the observing system.

2.1.2. *Switching mode*

To eliminate atmospheric effects appeared on the spectrum, the switching procedure is employed. Here, we briefly describe three observation modes used in our observations.

Position switching mode

In this mode, the telescope alternately observes two positions: an ON position, namely, the source position, and an OFF position, a reference position which is free from emission. The integration time of the OFF position and that of ON position are usually set to be the same. The spectrum is obtained by subtracting the spectrum of the OFF position from that of the ON position (Figure 2.2). The OFF position should be close to the ON position to minimize the atmospheric variation between the two directions.

Frequency switching mode

In this mode, the telescope alternately observes two different frequency ranges toward the target source. The spectrum with the targeted frequency range is obtained at the first period, and that with the slightly shifted frequency range at the second period. The final spectrum is obtained by mutual subtraction. The observing efficiency is higher than that of the position switching mode, because no overhead time for driving the telescope is needed. On the other hand, the ripples of the baseline are likely to appear to some extent. This technique can therefore be applied to sources whose line emissions have a narrow linewidth so that the lines are less affected by the ripples.

Wobbler switching mode

This mode also switches the ON and OFF positions alternately as the position switching mode, but by wobbling the secondary reflector. This mode can achieve a higher observing efficiency than the position switching mode, because the overhead time for driving the main reflector is not necessary. On the other hand, caution must be taken for spatially extended sources, because the beam throw by the wobbler is fixed to a certain small angle. Therefore this mode is not appropriate for extended sources.

2.1.3. *Calibration*

A calibration procedure is needed to translate the output voltage from the spectrometer into the intrinsic brightness temperature of the target source, because observed signal suffers

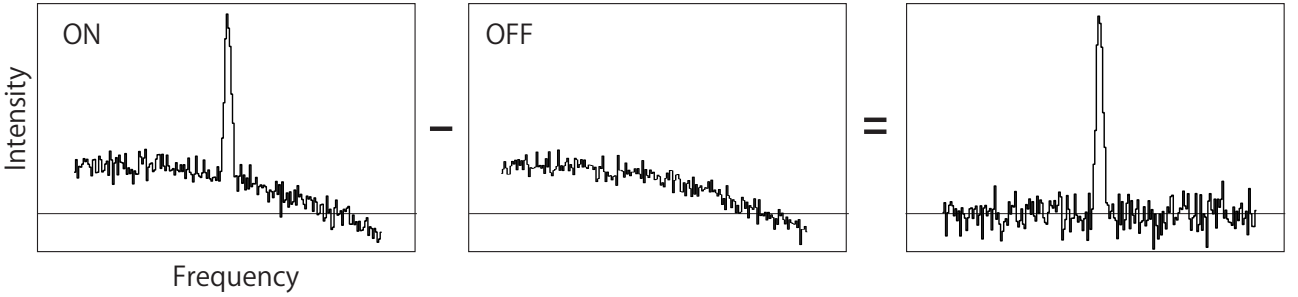
from gain variations of the telescope system and the atmospheric attenuation. The chopper wheel method is usually employed for this calibration (Ulich & Haars 1976). The power received at the source position can be written as

$$P_{\text{on}} = Gk [T_{\text{A}} + (1 - \eta_f)T_{\text{amb}} + \eta_f T_{\text{atm}}(1 - e^{-\tau}) + T_{\text{RX}}], \quad (2.4)$$

where G is the gain, k the Boltzmann constant, T_{A} the antenna temperature, η_f the forward efficiency, T_{amb} the room temperature, T_{atm} the atmospheric temperature, τ the optical depth of the atmosphere, and T_{RX} the receiver noise temperature¹. The forward efficiency represents the fraction of the signal fed into the receiver in the total signals that the antenna receives. Because the antenna temperature T_{A} suffers from the atmospheric extinction and the feed loss, the true antenna temperature T_{A}^* is written as

$$T_{\text{A}}^* = \frac{T_{\text{A}}}{\eta_f e^{-\tau}}. \quad (2.5)$$

Position switching mode / Wobbler switching mode



Frequency switching mode

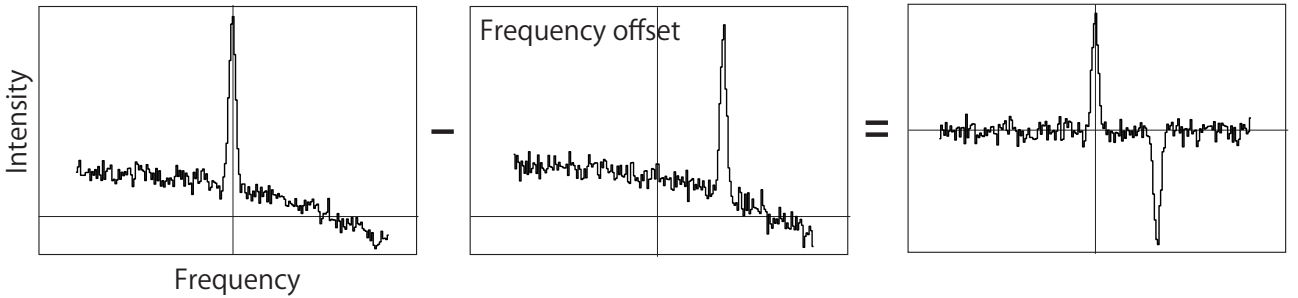


Figure 2.2: The procedures of each observing mode.

¹Intensity is usually represented in units of temperature in radio astronomy, which corresponds to the black body temperature giving the intensity under the assumption of the Rayleigh-Jeans approximation.

The power at the off position is written as

$$P_{\text{off}} = Gk [(1 - \eta_f)T_{\text{amb}} + \eta_f T_{\text{atm}}(1 - e^{-\tau}) + T_{\text{RX}}]. \quad (2.6)$$

For calibration, the reference power is measured with an absorber inserted to the optical path during the receiver:

$$P_{\text{abs}} = Gk (T_{\text{amb}} + T_{\text{RX}}). \quad (2.7)$$

Here, the corrected temperature T_C is defined as:

$$T_C = \frac{P_{\text{on}} - P_{\text{off}}}{P_{\text{abs}} - P_{\text{off}}} T_{\text{amb}} = \frac{T_{\text{amb}} T_A}{\eta_f [T_{\text{amb}} - T_{\text{atm}}(1 - e^{-\tau})]}. \quad (2.8)$$

When the temperature of the absorber is assumed to be the same as the atmospheric temperature, the corrected temperature T_C is equal to the antenna temperature T_A^* . This is the simplest method, because one can derive the antenna temperature without knowing η_f and τ . For a more elaborate approach, η_f and τ are determined by measuring another calibration power using a cold load. In this method, an atmospheric model is used to assume T_{atm} .

The derived source antenna temperature T_A^* does not represent the brightness temperature of the source, because the loss at the antenna is not included. The efficiency of the antenna is usually provided by the observatory, which is derived from the observations of standard sources whose absolute flux is already known, such as planets and quasars. The main beam efficiency is often used, and is defined by the power received by the main beam of the telescope divided by the power expected for the perfect aperture. The main beam brightness temperature, T_{mb} , is obtained by dividing the antenna temperature (T_A^*) by the main beam efficiency (η_{mb}).

2.2. Interferometer

A weakness of single-dish telescopes is that the spatial resolution is relatively coarse. It is roughly represented as $1.2\lambda/D$ (λ and D is the observed wavelength and the antenna aperture, respectively). For instance, the angular resolution of the Nobeyama 45-m telescope is $16''$ at 100 GHz, which corresponds to a linear scale of 2200 au in the Taurus molecular cloud ($d = 140$ pc). An interferometer is a technique to overcome this difficulty, which is an array of antennas that work together to form a single telescope. The angular resolution of an interferometer can be comparable to that of a telescope with an aperture equal to the maximum separation between

the antennas.

2.2.1. Basic concepts

Signals obtained with the each antenna are transferred to a correlator after the time delay to the other telescopes is compensated. In the correlator, the cross-correlation between two signals from different antennas is calculated. This provides spatial information on the target source, because the signals arriving from separated points of the source center arrive at slightly different times at each antenna. A separation from the source center of $\boldsymbol{\sigma} = (l, m)$ generates a time delay of $\Delta\tau = \mathbf{D} \cdot \boldsymbol{\sigma}/c$, which will be detected as a difference of the phase between antennas, $\Delta\phi = 2\pi(ul + vm)$. u and v are called spatial frequencies, as expressed by $(u, v) = (D_x \cos \theta/\lambda, D_y \cos \theta/\lambda)$, where D_x and D_y are the x - and y -components of the vector between two antennas, \mathbf{D} , respectively, and θ is the angle between \mathbf{D} and the vector from the telescope to the source, \mathbf{s}_0 (Figure 2.3). The cross-power spectrum, which is obtained by the Fourier transform of the cross correlation, can be expressed as a function of spatial frequencies. This is called visibility, which is a product of two-dimensional inverse Fourier transforms of the source brightness distribution on the sky. Hence, the intensity distribution of the source is derived by Fourier transform of the obtained visibility in the uv -plane to the lm -plane.

Here, a more detailed explanation of the above description is presented. An antenna receives an electromagnetic signal $\mathcal{E}_1(t)$, which is written by using a frequency- and angle-dependent amplitude $E(\mathbf{s}, \nu)$ as

$$\mathcal{E}_1(t) = \iint E(\mathbf{s}, \nu) e^{2\pi i \nu t} d\nu d\Omega. \quad (2.9)$$

The source intensity distribution as a function of frequency, $I(\mathbf{s}, \nu) = |E(\mathbf{s}, \nu)|^2$, is the final product to be obtained. The Fourier transform of $\mathcal{E}_1(t)$ yields the amplitude integrated over the solid angle:

$$\hat{\mathcal{E}}_1(\nu) = \mathcal{F}[\mathcal{E}_1(t)] = \int \mathcal{E}_1(t) e^{-2\pi i \nu t} dt \quad (2.10)$$

$$= \iiint E(\mathbf{s}, \nu') e^{2\pi i (\nu' - \nu) t} dt d\nu' d\Omega \quad (2.11)$$

$$= \iint d\nu' \delta(\nu - \nu') E(\mathbf{s}, \nu') d\Omega \quad (2.12)$$

$$= \int E(\mathbf{s}, \nu) d\Omega. \quad (2.13)$$

The other antenna receives the signal with a geometrical time delay $\tau_g = \mathbf{D} \cdot \mathbf{s}/c$. When a

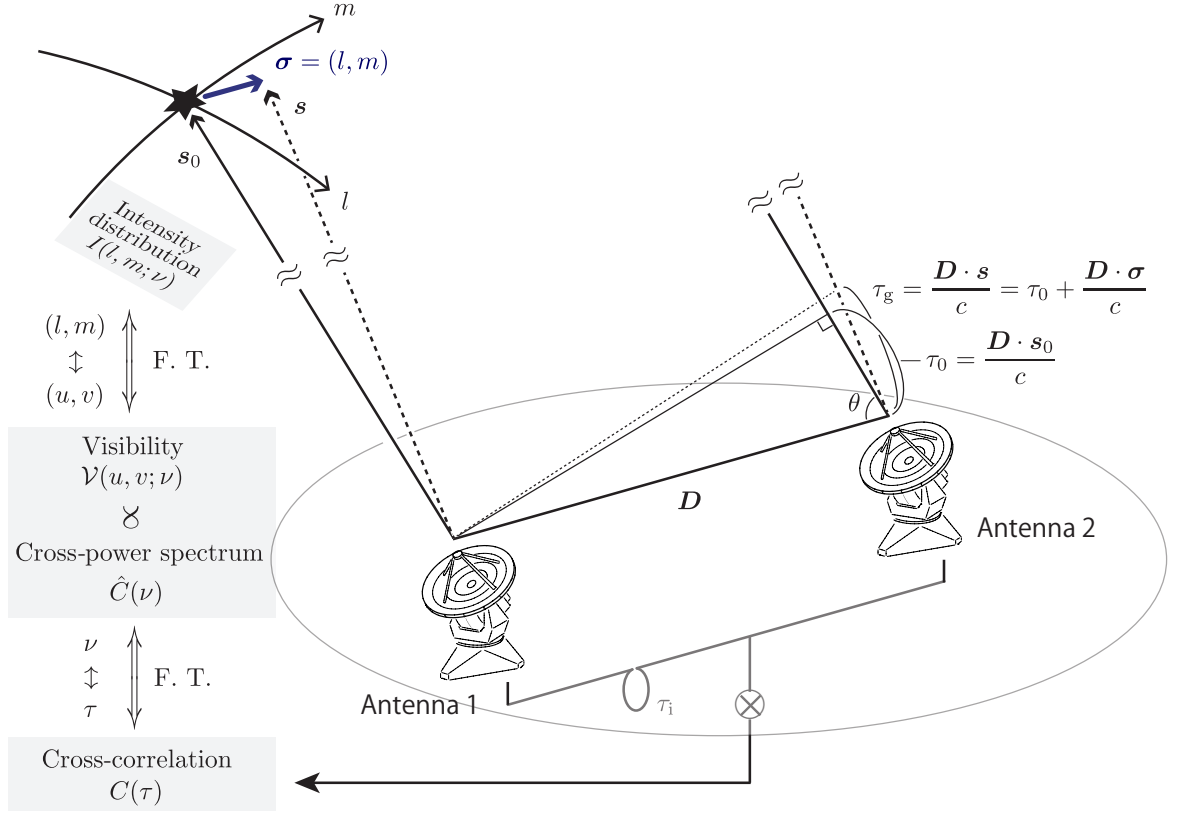


Figure 2.3: Schematic illustration of the concept of interferometers.

correction of the delay (τ_i) is applied to the antenna, the received signal is written as

$$\mathcal{E}_2(t) = \iint E(\mathbf{s}, \nu) e^{2\pi i \nu (t - \tau_g + \tau_i)} d\nu d\Omega, \quad (2.14)$$

$$\hat{\mathcal{E}}_2(\nu) = e^{-2\pi i \nu (\tau_g - \tau_i)} \int E(\mathbf{s}, \nu) d\Omega. \quad (2.15)$$

The interferometer outputs the correlation function of the two signals as a function of the delay time τ :

$$C(\tau) = (\mathcal{E}_1 * \mathcal{E}_2^*)(\tau) = \int \mathcal{E}_1(t) \mathcal{E}_2^*(t + \tau) dt, \quad (2.16)$$

where $(f * g)(\tau)$ denotes the convolution of f and g . The cross-power spectrum $\hat{C}(\nu)$ can be obtained by the Fourier transform of the correlation function:

$$\hat{C}(\nu) = \mathcal{F}[C(\tau)] = \int C(\tau) e^{-2\pi i \nu \tau} d\tau. \quad (2.17)$$

Because the Fourier transform of the convolution of the two functions f and g is the product

of the Fourier transforms of the two functions,

$$\mathcal{F}[f * g] = \mathcal{F}[f] \mathcal{F}[g], \quad (2.18)$$

the cross power spectrum can be obtained as follows:

$$\hat{C}(\nu) = \mathcal{F}[\mathcal{E}_1] \mathcal{F}[\mathcal{E}_2^*] \quad (2.19)$$

$$= \iint E(\mathbf{s}', \nu) E^*(\mathbf{s}, \nu) e^{2\pi i \nu (\tau_g - \tau_i)} d\Omega' d\Omega \quad (2.20)$$

$$= \int |E(\mathbf{s}, \nu)|^2 e^{2\pi i \nu (\tau_g - \tau_i)} d\Omega \quad (2.21)$$

$$= \int I(\mathbf{s}, \nu) e^{2\pi i \nu (\tau_g - \tau_i)} d\Omega \quad (2.22)$$

$$= \int I(\mathbf{s}, \nu) \exp \left[2\pi i \nu \left(\frac{\mathbf{D} \cdot \mathbf{s}}{c} - \tau_i \right) \right] d\Omega. \quad (2.23)$$

Here, we assume that the emissions from the different directions are incoherent, because they arise from independent processes. The derivation of the equation (2.21) from the equation (2.20) is based on this assumption.

Now, a convenient coordinate system is introduced to simplify the equation (2.23). The origin of coordinates is chosen at the source center. The source intensity distribution is expressed as $I(\boldsymbol{\sigma}, \nu)$, where $\boldsymbol{\sigma} = (l, m)$ is the vector from the source center (Figure 2.3). The equation (2.23) is expressed as:

$$\hat{C}(\nu) = \exp \left[2\pi i \nu \left(\frac{\mathbf{D} \cdot \mathbf{s}_0}{c} - \tau_i \right) \right] \int I(\boldsymbol{\sigma}, \nu) \exp \left(2\pi i \nu \frac{\mathbf{D} \cdot \boldsymbol{\sigma}}{c} \right) d\boldsymbol{\sigma} \quad (2.24)$$

$$= \exp \left[2\pi i \nu \left(\frac{\mathbf{D} \cdot \mathbf{s}_0}{c} - \tau_i \right) \right] \iint I(l, m; \nu) e^{2\pi i (ul + vm)} dl dm. \quad (2.25)$$

The exponential factor extracted from the integral denotes the phase of $\hat{C}(\nu)$, which can be compensated by appropriately choosing the time delay τ_i . The integral part is called the visibility,

$$\mathcal{V}(u, v; \nu) = \iint I(l, m; \nu) e^{2\pi i (ul + vm)} dl dm = \mathcal{F}^{-1} [I(l, m; \nu)]. \quad (2.26)$$

By the Fourier transform of the visibility, we obtain the source intensity distribution,

$$I(l, m; \nu) = \mathcal{F}[\mathcal{V}(u, v; \nu)] = \iint \mathcal{V}(u, v; \nu) e^{-2\pi i (ul + vm)} du dv. \quad (2.27)$$

2.2.2. Imaging procedure

In interferometric observations we obtain the visibility function, which is a function of (u, v) determined by the antenna baseline \mathbf{D} and the target direction \mathbf{s} . Although we need a complete visibility in the uv -plane to get the true intensity distribution $I(l, m; \nu)$, the measured visibility is limited to certain points in the uv -plane, because information obtained by a pair of antennas corresponds to one component in the uv -plane. To sample as many points in the uv -plane as possible, the antennas are configured so as to have as many different baselines (distances between two antennas) as possible. In addition, observing at different times can improve the sampling, because the rotation of the earth changes the projected baseline. The obtained Fourier component of the intensity distribution in the uv -plane is called (u, v) coverage $\mathcal{U}(u, v)$ (Figure 2.4). The observed visibility by the array, $\hat{\mathcal{V}}(u, v; \nu)$, is expressed by using the true visibility $\mathcal{V}(u, v; \nu)$ as $\hat{\mathcal{V}}(u, v; \nu) = \mathcal{U}(u, v)\mathcal{V}(u, v; \nu)$. The Fourier transform of the observed visibility can be written as:

$$\hat{I}(l, m; \nu) = \mathcal{F} [\hat{\mathcal{V}}(u, v; \nu)] = \mathcal{F} [\mathcal{U}(u, v)] * \mathcal{F} [\mathcal{V}(u, v; \nu)] \quad (2.28)$$

$$= B(l, m) * I(l, m; \nu), \quad (2.29)$$

where $B(l, m) = \mathcal{F} [\mathcal{U}(u, v)]$ is called the synthesized beam. The obtained intensity distribution $\hat{I}(l, m; \nu)$, the so-called dirty map, is the convolution of the true intensity distribution with the synthesized beam. An incomplete sampling in the uv -plane produces ghost emission/absorption features in an image, so-called side lobes. Some techniques to improve the quality of the obtained image are developed as briefly explained below.

Weighting

A weighting function can be multiplied to the visibility in order to change the effective beam shape and the side lobe level. There are two types of weighting: density weighting and uv -tapering.

Density weighting Density weighting is the method to weight the visibility data according to the density of (u, v) points in the uv -plane. The uniform weight is a weight inversely proportional to the sampling density. Because the change in the baseline length due to the earth rotation is larger for longer baselines than shorter ones, lower spatial frequencies are sampled more often than the higher ones. Hence, the uniform weighting gives higher weight to higher spatial frequencies, resulting in a higher angular resolution but a worse side-lobe level. On the contrary, the natural weighting scheme gives equal weight to

all samples, suppressing the side lobes and the angular resolution. Briggs or robust weighting creates an image between natural and uniform weighting (Briggs 1995). A tunable parameter, robustness, defines a noise level.

uv-tapering Tapering scheme applies a Gaussian weight $\mathcal{G}(u, v) = \exp[-(u^2 + v^2)/2\sigma^2]$ to the visibility data. This puts lower weight on the high spatial-frequency data, and suppresses artifacts arising from them. An extended source can well be depicted. This scheme is usually applied in combination with the density weighting.

Deconvolution

A procedure that eliminates the effect arising from the incompleteness of (u, v) coverage and reconstructs the intensity distributions is usually applied to the dirty image (Figure 2.4). Since the dirty map is the convolution of the true intensity distribution and the synthesized beam, this procedure is called deconvolution. One popular method of the deconvolution is called CLEAN (Högbom 1974). The CLEAN method reproduces the intensity distribution $I(l, m; \nu)$ as a set of point sources $\tilde{I}(l, m; \nu) = \sum I_i \delta(l_i, m_i)$. First, the intensity peak of the dirty image is found, and it is assumed to be a real emission ($I_1 \delta(l_1, m_1)$) in the image. Then a dirty image of this peak emission is created, and is subtracted from the original dirty map. Then, the intensity peak of the residual image is assumed to be a real emission ($I_2 \delta(l_2, m_2)$). This process is iterated to determine $I_i \delta(l_i, m_i)$ until the peak of the residual image becomes lower than the specified threshold value. Because the side lobe components can be significantly eliminated, this method is widely used in radio interferometric observations.

Here we note an important caveat on incomplete sampling in the uv -plane, the ‘*resolving-out*’ effect. Given an idealized square source with a shape of $I(l, m; \nu) = I_0$ for $|l| < \theta_0$, $|m| < \theta_0$ and otherwise $I(l, m; \nu) = 0$, the visibility is obtained as:

$$\mathcal{V}(u, v; \nu) = 4I_0\theta_0^2 \frac{\sin(2\pi\theta_0 u)}{2\pi\theta_0 u} \frac{\sin(2\pi\theta_0 v)}{2\pi\theta_0 v}. \quad (2.30)$$

Therefore, the visibility function goes almost zero, when the spatial frequencies u and v are larger than $1/2\theta_0$. Since the spatial frequencies can be written as D/λ , the visibility function becomes almost zero if $\theta_0 \gtrsim \lambda/2D$, where D is the baseline length. This means that a pair of antennas with a baseline of D has no sensitivity to a sufficiently extended source that satisfies $\theta_0 \gtrsim \lambda/2D$. Interferometers therefore miss information on large angular scales. This is called the ‘*resolving-out*’ effect (See Appendix in Wilner & Welch (1994) for a detailed discussion). The largest angular scale for which an array has a sensitivity is determined by the minimum

baseline in the array. Another array with a shorter spacing (baseline) is needed to observe an extended source larger than the largest angular scale. ALMA has three types of array according to the target (Section 2.3.3).

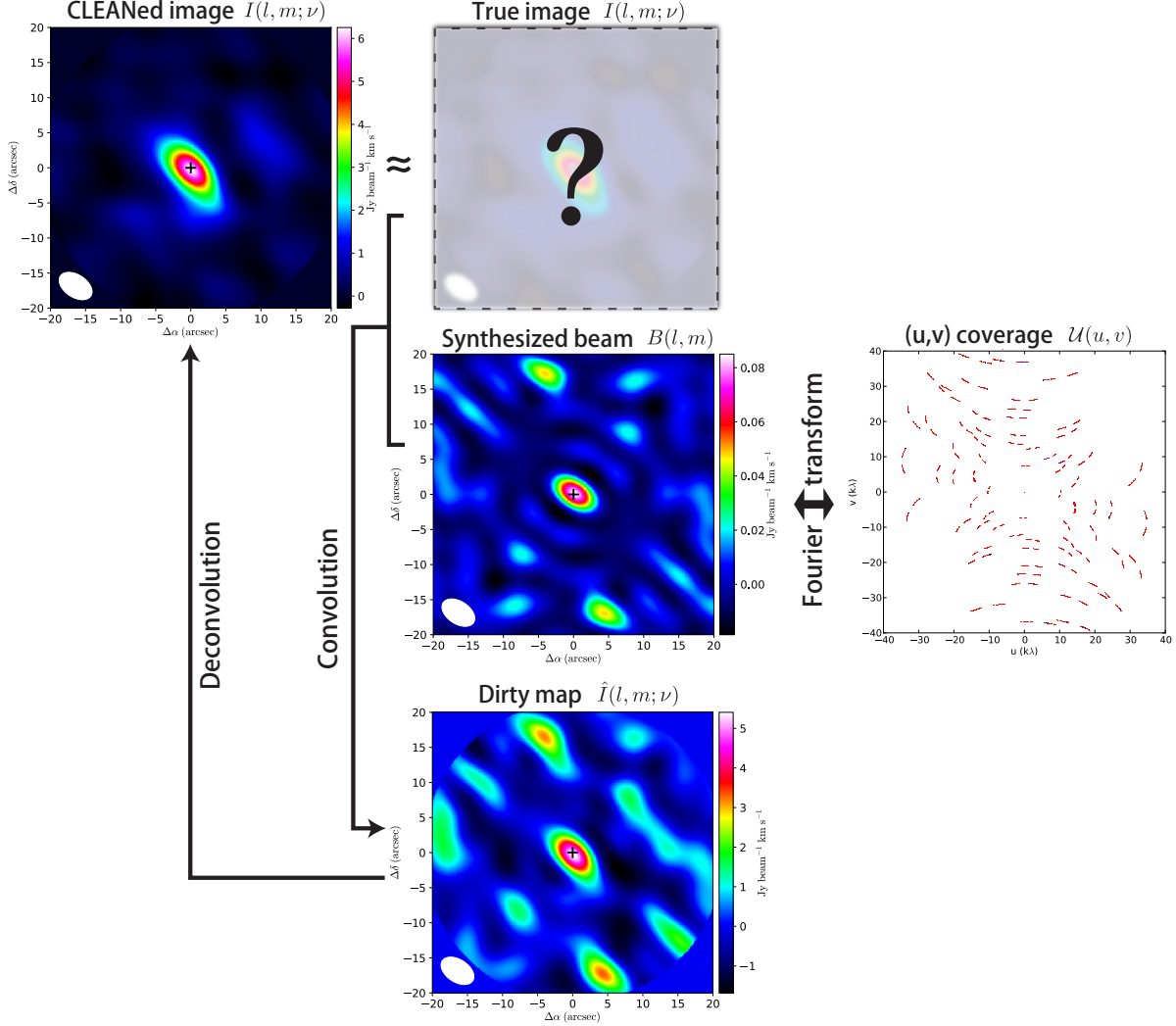


Figure 2.4: Relations between images of the $\text{H}_2\text{CO } 5_{15}-4_{14}$ line in L1527 observed with the ALMA ACA array. (Right column) The (u, v) coverage $\mathcal{U}(u, v)$. (Center column) The dirty map ($\hat{I}(l, m; \nu)$; bottom) is the convolution of the unknown true intensity image ($I(l, m; \nu)$; top) and the synthesized beam ($B(l, m)$; center) which is the Fourier transform of the (u, v) coverage. (Left column) The CLEANed image $\tilde{I}(l, m; \nu)$ is created by the deconvolution method to reproduce the true image. The white ellipse shows the synthesized beam size.

2.2.3. Calibration

The absolute flux and phase of the observed visibility are not always correct due to the atmospheric and instrumental effects. Thus, calibrations are needed to obtain a true visibility.

The calibration procedures consist of several steps as follows.

Bandpass calibration The output response from the telescope has a frequency dependence, which arises from the instrumental effects such as the intrinsic response from receivers and the attenuation by cables, and the atmospheric effects such as delay offsets and atmospheric lines. The bandpass calibration is a procedure to calibrate such a frequency response of amplitude and phase. A strong point continuum source such as quasars is observed to calibrate so as that the phase is zero and the amplitude is constant.

Phase calibration The observed visibility suffers from the atmospheric and instrumental time delay caused in each antenna, which results in a temporal fluctuation of phase. To calibrate this fluctuation, a strong point source is observed every several minutes. Quasars are often used as the phase calibrators, because their visibility can be modeled and the spatial size is sufficiently small.

Gain calibration The observed visibility also suffers from the temporal fluctuation of amplitude. Therefore, the amplitude of the phase calibrator is also measured in each phase calibration to correct the amplitude fluctuation.

Flux calibration To derive the absolute amplitude of the target source, a scaling factor to the observed amplitude of the phase calibrator is measured by observing the source whose flux density is already known. Solar System bodies such as planets and satellites as well as quasars are often used as flux calibrators. This calibration is done by the observatory.

2.3. Telescopes used in this thesis

2.3.1. Nobeyama 45-m telescope

Nobeyama 45-m telescope (hereafter referred to as NRO 45 m) is operated by Nobeyama Radio Observatory (NRO), which is a branch of the National Astronomical Observatory, National Institutes of Natural Science, Japan. The telescope is located at a latitude and a longitude of (35°56'40".9 N, 138°28'21".2 E) and at the altitude of 1,350 m. The main reflector has a diameter of 45 m, which is one of the largest millimeter-wave telescopes in the world. The position switching mode is employed for spectral line observations. The frequency coverage is from 20 GHz to 116 GHz, which can be observed with several receivers. A single load chopper wheel method is employed for the intensity calibration. As back-ends, a bank of AOSs and autocorrelators can be used. Because the beam efficiency can fluctuate depending on the wind

and telescope conditions, the intensity scale is usually calibrated by using the intensity of a strong line observed simultaneously, whose accurate intensity is already measured under good observing conditions.

2.3.2. IRAM 30-m telescope

IRAM 30-m telescope (hereafter referred to as IRAM 30 m) is operated by Institut de Radioastronomie Millimétrique (IRAM), which is founded by the French Centre National de la Recherche Scientifique, the German Max-Planck-Gesellschaft, and the Spanish Instituto Geografico Nacional. The telescope is located at the Pico Veleta near Granada, Spain, and the latitude, longitude, and altitude is ($37^{\circ}4'6''.29$ N, $3^{\circ}23'55''.51$ W) and 2,850 m, respectively.

It is equipped with a series of heterodyne receivers at the 3-, 2-, 1.3-, and 0.9-mm bands (80–350 GHz). Spectral line observations can be conducted by the frequency-, position-, and wobbler-switching modes. The intensity calibration is done with the chopper wheel method with the ambient and cold (liq. N₂) temperature loads.

2.3.3. Atacama Large Millimeter/submillimeter Array (ALMA)

ALMA consists of an array of fifty 12-m antennas (the 12-m array), with baselines ranging from 15 m up to 16 km, located on the Chajnantor plateau at the altitude of 5,000 m in Chile. Its high elevation and low humidity can minimize noise and signal attenuation due to earth atmosphere. In addition to the 12-m array, the Atacama Compact Array (ACA), composed of twelve 7-m antennas and four 12-m antennas, can also be used to image large scale structures that are not well sampled by the 12-m array. The four 12-m antennas (total power (TP) array) provide spatial information with spacings from 0 m to 12 m by autocorrelations. The 7-m array samples baselines from 8 m to 40 m, bridging the baseline sampling gap between the 12-m array and the TP array.

The ALMA front-end accommodates up to 10 different receiver bands. The bands available in the latest operations range from Band 3, starting at 84 GHz, to Band 10, ending at 950 GHz, to cover almost all the atmospheric windows.

The array has much higher sensitivity and higher resolution than conventional radio telescopes. The baseline can be extended to 16 km, enabling us to image at an angular resolution as high as 0.02 arcsec, which is smaller than other previous interferometers by about 1–2 orders of magnitude (Figure 2.6). The state-of-the-art receivers and back-end technologies realize ob-

servations with much higher sensitivity than earlier single-dish telescopes and interferometers roughly by two orders of magnitude.



Figure 2.5: Telescopes used in this thesis. (Left) NRO 45 m, (center) IRAM 30 m (*credit: IRAM*), (right) ALMA (*credit: Clem & Adri Bacri-Normier (wingsforscience.com)/ESO*)

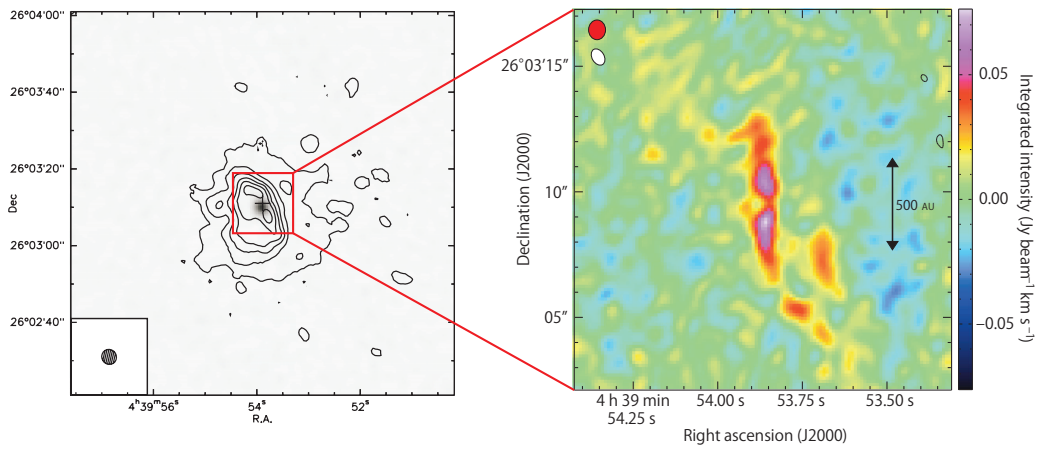


Figure 2.6: Comparison of angular resolutions with ALMA and the earlier interferometer (PdBI). The left panel shows the $c\text{-C}_3\text{H}_2$ $4_{32}\text{-}4_{23}$ line in L1527 observed with the PdBI interferometer and the right panel shows the $c\text{-C}_3\text{H}_2$ $5_{23}\text{-}4_{32}$ line in L1527 observed with ALMA. ALMA realizes much higher angular resolutions. Adopted from Sakai *et al.* (2010a) and Sakai *et al.* (2014a).

CHAPTER 3

LINE SURVEY OBSERVATION TOWARD L1527

3.1. Introduction

A detailed understanding of the origin and the fate of the chemical diversity described in Chapter 1 is of great interest for astrochemistry in relation to the material origin of the Solar System. As the first step toward this goal, it is important to reveal the chemical compositions of representative low-mass protostellar sources in an unbiased way. Although spectral line survey observations toward the hot corino source IRAS 16293-2422 have been conducted not only with single-dish telescopes but also with interferometers (Caux *et al.* 2011; Jørgensen *et al.* 2016; Ligterink *et al.* 2017), no spectral line survey observations toward WCCC sources have been reported except for that recently published by Lefloch *et al.* (2018) (See below). With this in mind, we conducted the unbiased spectral line survey toward the prototypical WCCC source L1527 in the 3-mm band with NRO 45 m, as part of the legacy project of Nobeyama Radio Observatory. Here, we report the whole result of the survey. The presence of highly unsaturated hydrocarbons is the most characteristic feature of interstellar chemistry. Hence, revealing the whole chemical composition of the WCCC source and its comparison with those of other sources such as prestellar cores showing cold carbon-chain chemistry (e.g., TMC-1 (CP); Kaifu *et al.* 2004) will give us valuable information on formation of these molecules in space.

As an independent study, a similar spectral line survey observation toward this source was also carried out with the IRAM 30-m telescope, as part of the ASAI (Astrochemical Surveys At Iram) program, whose brief summary result has recently been reported (Lefloch *et al.* 2018). However, detailed data exploitation has not been presented. The ASAI survey almost covers the frequency range of our survey in the 3-mm band with a larger beam size by a factor of 1.5. Nevertheless, independent spectral line surveys with different telescopes are always important for the fundamental sources such as L1527, because they give opportunities to confirm the consistency of the results, and also provide additional information such as the source sizes by taking advantage of the different beam sizes. Here, we report the results of our spectral line survey with NRO 45-m.

3.2. Observation

The spectral line survey observations of L1527 were carried out with NRO 45 m during the seasons from 2006 to 2012. The frequency range was from 79.8 GHz to 116.8 GHz. The observed position was $(\alpha_{2000}, \delta_{2000}) = (04^{\text{h}}42^{\text{m}}35^{\text{s}}.9, 25^{\circ}53'23''.3)$, which is the position of the protostar (Sakai *et al.* 2008b). In this observation, we used the SIS mixer receivers, S80 and S100, simultaneously from 2006 to 2008, while we employed the dual-polarization side-band-separating (2SB) SIS receiver T100H/V (Nakajima *et al.* 2008) from 2009 to 2012. The system temperatures varied from 250 to 350 K in the former and from 150 to 250 K in the latter. The intensity scale was calibrated by using the chopper-wheel method, and the calibration uncertainty is estimated to be better than 20%. The telescope pointing was checked once every 1 to 1.5 hour by observing the nearby SiO maser sources (NML-Tau and Ori-KL). The pointing accuracy was ensured to be better than 6". The main-beam efficiency (η_{mb}) at 86 GHz was 0.43 from 2006 to 2008, 0.49 in 2009, and 0.42 from 2010 to 2012, as reported on the NRO website. The antenna temperature (T_{A}^*) is converted to the main-beam brightness temperature (T_{mb}) by $T_{\text{mb}} = T_{\text{A}}^*/\eta_{\text{mb}}$. The beam size was 19" at 86 GHz and 15" at 110 GHz. A position switching mode with the off-position $(\alpha_{2000}, \delta_{2000}) = (04^{\text{h}}42^{\text{m}}35^{\text{s}}.9, 25^{\circ}53'23''.3)$, which is free from the emission of CO isotopologue lines, was employed in all the observations.

Before 2010, a bank of acousto-optical radio spectrometers (AOSs), whose bandwidth, resolution, and channel spacing are 250 MHz, 250 kHz, and 125 kHz, respectively, were used. In 2011-2012, a bank of autocorrelators, SAM45 (Spectral Analysis Machine for the 45-m telescope), whose bandwidth, resolution, and channel spacing were set to be 1 GHz, 244 kHz, and 244 kHz, respectively, was employed. The frequency resolution corresponds to the velocity resolution of $\sim 0.8 \text{ km s}^{-1}$ at 90 GHz. This resolution is higher than the typical line width in this source ($\sim 0.5\text{--}0.8 \text{ km s}^{-1}$). Nevertheless, this resolution was chosen to cover the whole 3 mm band within the limited observation time. Although the lines are partly frequency-diluted, the integrated intensity is reliable.

In addition to the observations in the 3-mm band, a supplementary observation was conducted in the 4-mm band with NRO 45-m from February to April 2012. This observation mainly aims at investigating the deuterium fractionation of some fundamental molecular species. Thus, only selected lines were observed. The side-band-separating (2SB) SIS mixer receiver T70H/V was used as the front end with a typical system noise temperature of 200–300 K. The back-end was SAM45, whose resolution was set to be 60.1 kHz. The beam size was 22" at 75 GHz. The main-beam efficiency at 75 GHz was 0.45.

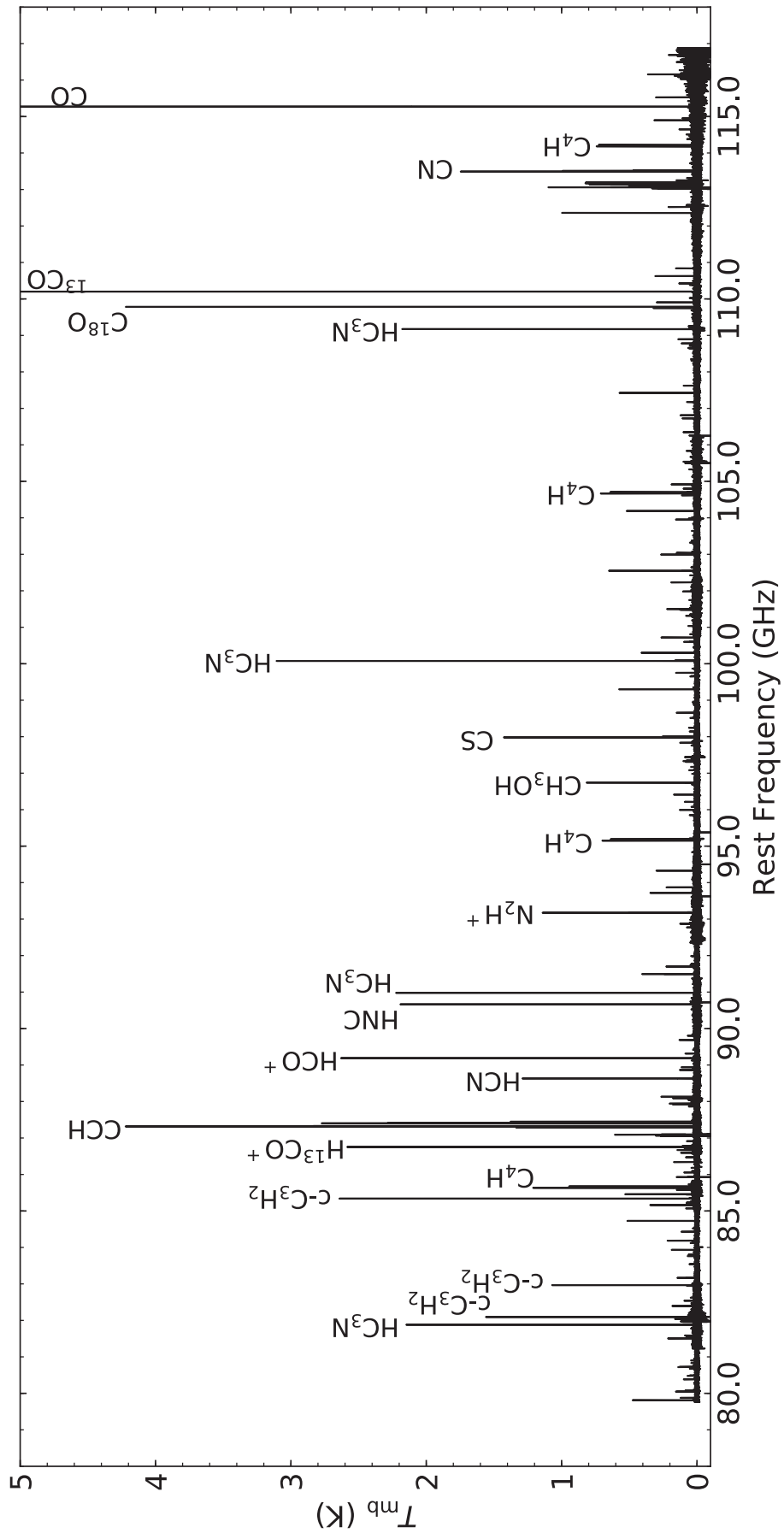


Figure 3.1: The overall spectrum of L1527 in the 3-mm band. Lines of some representative molecular species are indicated.

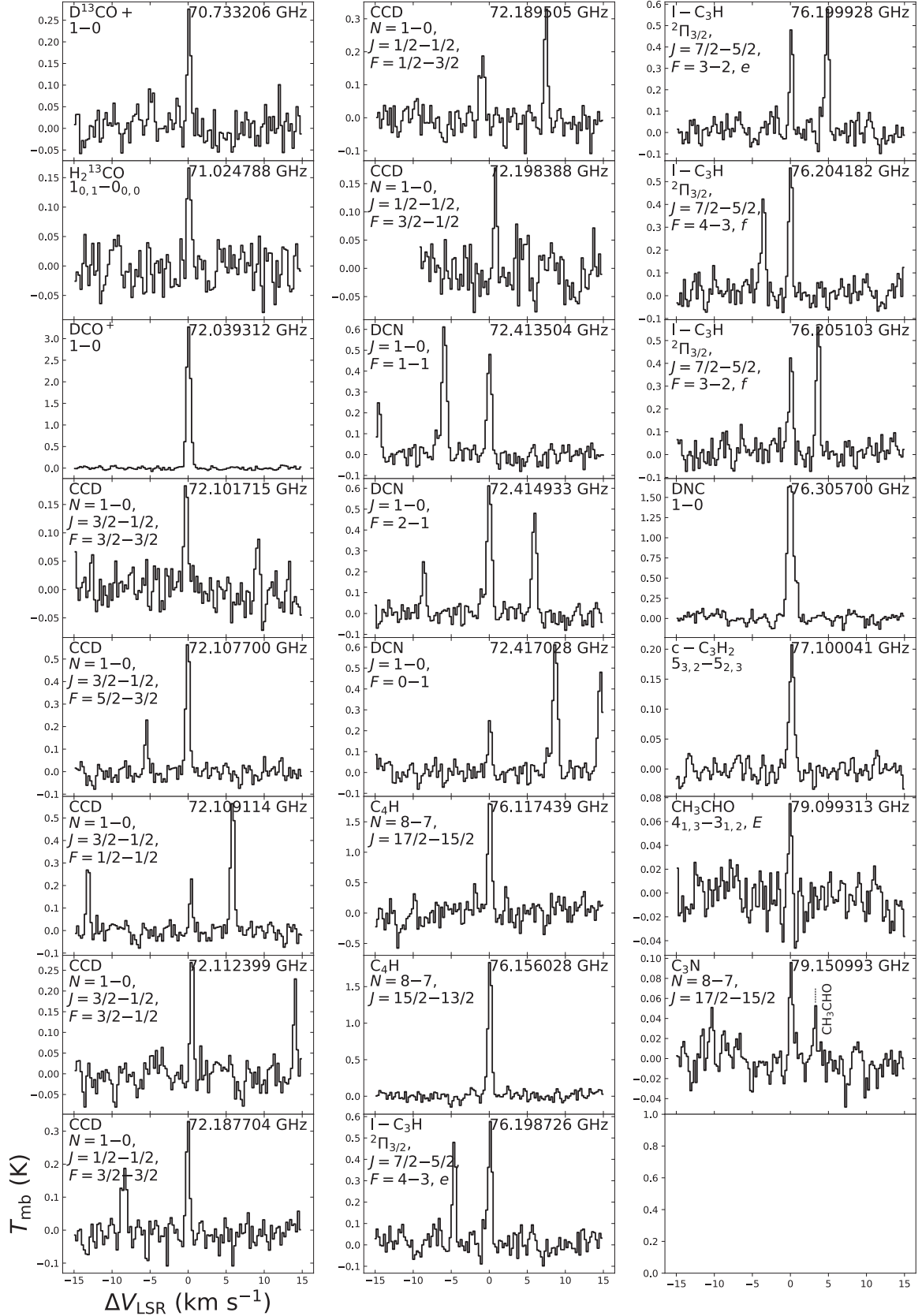


Figure 3.2: Individual spectral line profiles of molecules detected in the 70 GHz band. ΔV_{LSR} denotes the velocity shift from the V_{LSR} of 5.85 km s^{-1} of L1527. The $N = 1-0$ lines of N_2D^+ are shown in Figure 3.3.

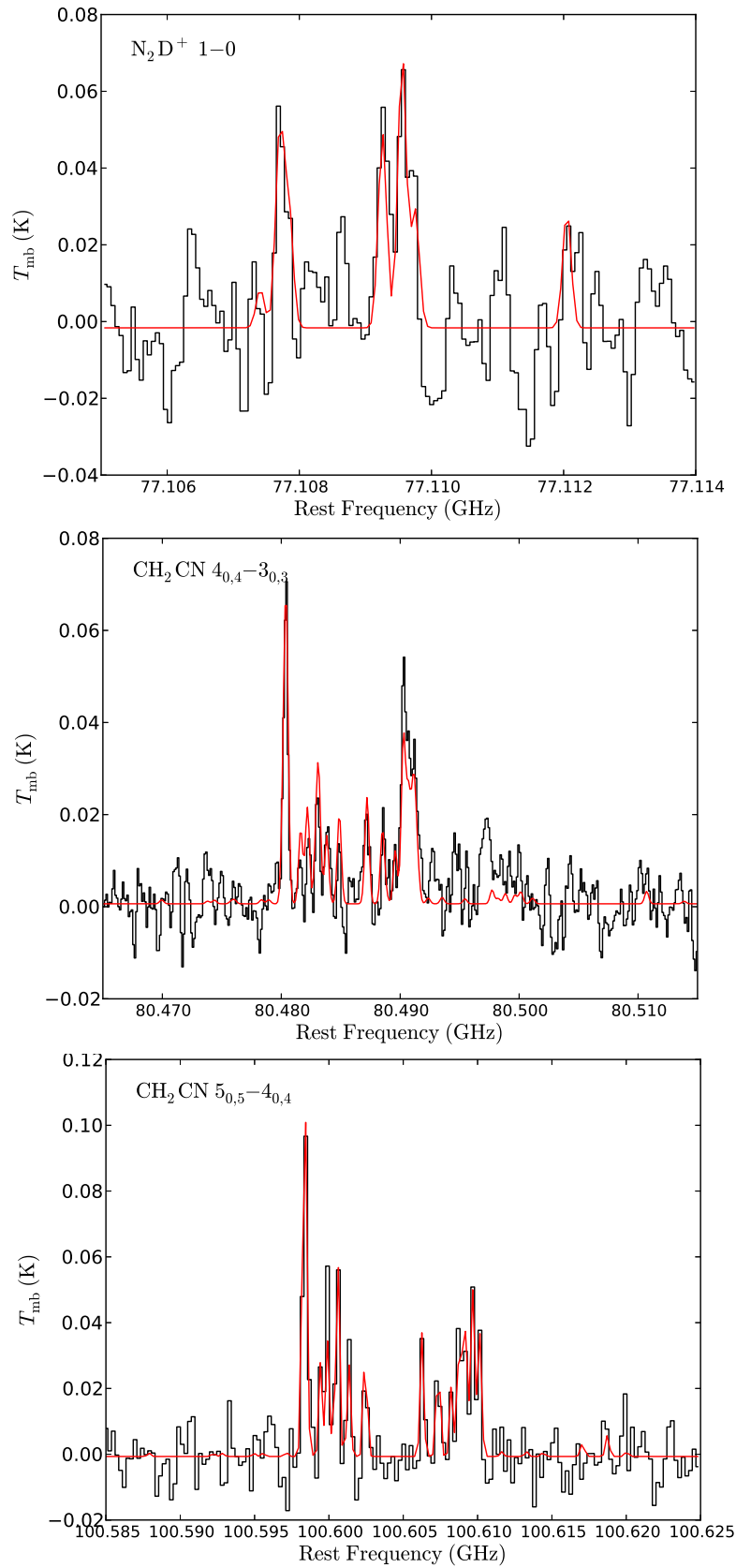


Figure 3.3: The hyperfine components of N_2D^+ and CH_2CN . The results of the multiple Gaussian fitting are also shown in red.

3.3. Results

3.3.1. Overall results

Figure 3.1 is an overview of the observed spectrum in the 3-mm band, while its zoomed view is shown in Appendix (Figure A.1). Figure 3.2 shows the spectra of the supplementary observation in the 70-GHz band. Typically, the rms noise at the native spectral resolution ranges from 5 to 15 mK in T_{mb} in the 3-mm band. This rms noise level is similar to or even better than that of the spectral line survey toward the outflow shocked region L1157 B1, which was also conducted with NRO 45-m as part of the legacy project of Nobeyama Radio Observatory (Sugimura *et al.* 2011; Yamaguchi *et al.* 2012). The detected lines are identified on the basis of spectral line databases, the Cologne Database for Molecular Spectroscopy managed by University of Cologne (CDMS; Müller *et al.* 2001, 2005) and the Submillimeter, Millimeter, and Microwave Spectral Line Catalog provided by Jet Propulsion Laboratory (JPL; Pickett *et al.* 1998). A line detection criterion is that the peak intensity of the line exceeds four times the rms noise level at its expected frequency. In total, 243 emission lines and one absorption line (CH₃OH 3_{1,3}-4_{1,4}, A⁺ at 107.01 GHz) are detected in the frequency range from 79.8 to 116.9 GHz (Figures 3.1 and A.1). Hence, the line density is 6.5 GHz⁻¹ with this sensitivity. From the detected emission lines, 69 molecular species are identified in the 3- and 4-mm bands, among which 37 species are isotopologues. These numbers are higher than those of L1157 B1 (line density: 3.4 GHz⁻¹, detected species: 47 species including 15 isotopologues). This clearly shows chemical complexity of L1527. The detected molecules are summarized in Table 3.1.

In this survey, c-C₃D is detected for the first time in interstellar clouds. Although c-C₃D is detected with the signal-to-noise (S/N) ratio higher than 4σ , the velocity resolution is not high enough to determine the line parameters by Gaussian fits. C₂O, C₃S, C₆H, HCNO, HCO₂⁺, C₄D, C₂H₃CN, and CH₂DOH are tentatively detected with the S/N ratio higher than 3σ . In addition, CC¹³CCH, l-C₃D and CH₃CCD are also tentatively detected, because multiple lines are marginally seen. Among the tentatively detected species in this survey, the detections of C₆H, HCNO, HCO₂⁺, C₄D, and l-C₃D have already been reported by the higher sensitivity observations (Sakai *et al.* 2007; Marcelino *et al.* 2009; Sakai *et al.* 2008c, 2009b).

For unidentified lines with the S/N ratio higher than 4σ , we carefully inspect whether they are also detected in the ASAI survey, and find that none of them have corresponding features in the ASAI data. Most of the unidentified lines that appear only in this survey are likely spurious lines, which are mainly caused in the AD converters of the autocorrelators during the period of our observations. Significant features of such spurious lines are shown in some panels of

Table 3.1: Molecules detected in this observation.

Carbon-chain molecules and the isomers
CCH, ^{13}CCH , C^{13}CH , CCD, C_2O^a , CCS, C_3O , C_3N , l- C_3H , l- C_3D^a , c- C_3H , c- C_3D , c- C_3H_2 , c- $^{13}\text{CCCH}_2$, c- $\text{CC}^{13}\text{CH}_2$, c- C_3HD , c- C_3D_2 , l- C_3H_2 , C_3S^a , CH_3CCH , CH_2DCCH , CH_3CCD^a , HCCNC, HC_3N , DC_3N , H^{13}CCCN , HC^{13}CCN , HCC^{13}CN , C_4H , C_4D^a , $\text{CC}^{13}\text{CCH}^a$, C_4H_2 , C_5H , HC_5N , C_6H^a
Complex organic molecules
CH_3OH , CH_2DOH^a , CH_3CHO , c- $\text{H}_2\text{C}_3\text{O}$, HCCCHO, $\text{C}_2\text{H}_3\text{CN}^a$
Other species
CO, ^{13}CO , C^{18}O , C^{17}O , $^{13}\text{C}^{18}\text{O}$, CS, C^{34}S , C^{33}S , CN, ^{13}CN , C^{15}N , SO, HNC, HN^{13}C , H^{15}NC , DNC, HCN, H^{13}CN , HC^{15}N , DCN, N_2H^+ , N_2D^+ , HCO^+ , H^{13}CO^+ , HC^{18}O^+ , DCO^+ , D^{13}CO^+ HCS^+ , HCO, HNCO, NH_2D , H_2^{13}CO , D_2CO , H_2CS , HDCS, CH_2CN , CH_2CO , CHDCO, $\text{HCO}_2^+{}^a$, HCNO^a
^a Tentative detection

Figure A.1. In the frequency range observed only with NRO 45 m, 2 lines are unidentified, and they should be verified in future observations. The intensity, line-of-sight velocity and FWHM line width of the detected lines are determined by a single Gaussian fit. If the line profile is blended with multiple lines such as nearby hyperfine components, multiple Gaussian functions are employed to determine the line parameters. For the hyperfine components of N_2D^+ and CH_2CN , we assume that the line width and the line-of-sight velocity are identical among all the components, and that the intensities are proportional to the line strengths, because the hyperfine splittings are too small to fit them independently (Figure 3.3). Tables A.1 and A.2 in Appendix present lists of the line parameters of the identified molecular lines including tentatively detected ones and unidentified lines. Note that some of the hyperfine components of CCD show significant offsets in ΔV_{LSR} (Table A.2). This is probably because of insufficient accuracy of the rest frequencies listed in CDMS. V_{LSR} denotes the velocity of the source in the local standard-of-rest frame (LSR), which is about 5.85 km s^{-1} for L1527.

As listed in Table 3.1, 27 species are carbon-chain species and their isomers. For saturated molecules, the most fundamental species, CH_3OH and CH_3CHO , which are found in many cold

prestellar cores (e.g., Kaifu *et al.* 2004; Vastel *et al.* 2014; Soma *et al.* 2018), are detected. However, larger complex organic molecules such as $(\text{CH}_3)_2\text{O}$ and HCOOCH_3 are not detected in this survey, while spectral lines of these species are detected in the 3-mm band with peak intensities of a few 10 mK or stronger toward the hot corino sources such as IRAS 16293-2422 and NGC1333 IRAS4A (e.g., Caux *et al.* 2011; Bottinelli *et al.* 2004). A deficiency of complex organic molecules in L1527 was also reported on the basis of high sensitivity observations (Sakai *et al.* 2008a).

3.3.2. Column densities and rotational temperatures

In this observation, multiple transition lines with different upper-state energies are detected for many species. Assuming a local thermodynamic equilibrium (LTE) condition, we determine the rotational temperature and the beam-averaged column density for each species by using the least-squares method with the following formula:

$$T_{\text{b}} = \frac{h\nu}{k} \left[\frac{1}{\exp(h\nu/kT_{\text{rot}}) - 1} - \frac{1}{\exp(h\nu/kT_{\text{bg}}) - 1} \right] (1 - e^{-\tau}), \quad (3.1)$$

and

$$\tau = \frac{8\pi^3 S \mu^2}{3h\Delta\nu U(T_{\text{rot}})} \left[\exp\left(\frac{h\nu}{kT_{\text{rot}}}\right) - 1 \right] \exp\left(-\frac{E_{\text{u}}}{kT_{\text{rot}}}\right) N, \quad (3.2)$$

where T_{b} is the brightness temperature, h the Planck constant, ν the transition frequency, k the Boltzmann constant, T_{rot} the rotational temperature, T_{bg} the cosmic microwave background temperature of 2.7 K, τ the optical depth, S the line strength, μ the dipole moment, $\Delta\nu$ the line width at half maximum, $U(T_{\text{rot}})$ the partition function, E_{u} the upper state energy, and N the total column density.

The partition function is numerically calculated from energies and degeneracies of the rotational levels, which are taken from the spectroscopy databases CDMS and JPL. The beam-filling factor is not included for simplicity. This assumption is reasonable especially for carbon-chain molecules, because distributions of carbon-chain molecules such as CCH and C_4H are reported to be extended over $20''$ – $40''$ (Sakai *et al.* 2010a), which is comparable to or larger than the typical beam size of the observation ($\sim 20''$). Uncertainties of the derived column densities include the rms noise, the fitting error, and the intensity calibration uncertainty of 20%. Table 3.3 shows the column densities and the rotational temperatures derived by the above analysis. The large uncertainty for C_3N originates from large scattering of the data due

to the poor S/N ratios.

For molecules for which only one transition line or multiple lines with almost the same upper-state energies are detected, the column densities are derived under the LTE assumption with the excitation temperatures of 10 K and 15 K. The range of the excitation temperature is chosen on the basis of the rotational temperatures derived for other molecules in the above analysis. The column densities thus evaluated are summarized in Table 3.4. A change in the temperature by 5 K does not result in a substantial change in the column density ($\sim 20\%$ or less for most of the species). Optical depths of the lines are also listed in Table 5. Most of them are less than 1. Hence, the column densities are reasonably estimated. An exception is the HCCNC case. The column density of HCCNC changes by a factor of 2 between 10 K and 15 K. This is likely due to the relatively high upper-state energy of the detected line ($J = 10-9$; $E_u = 26$ K). Moreover, if we employ the $J = 9-8$ line ($E_u = 21$ K) tentatively detected with the 3σ confidence level, the column density is derived to be about a half of that from the $J = 10-9$ line, assuming the excitation temperature of 10 K or 15 K. The column density of HCCNC therefore has a relatively large uncertainty.

It should be noted that some molecules having an extended distribution might have the excitation temperature lower than 10 K, because of contributions from less dense and colder parts. However, the excitation temperature of 5 K does not cause a substantial change in the column density ($\sim 20\%$ or less) and the optical depth (0.4 or less) for most of the species. For DNC and H^{13}CO^+ , the column densities would become ~ 2 times higher and optical depths become ~ 2 , if the excitation temperature were 5 K.

The low excitation temperature indicates that the emissions are not truly in the LTE condition, but are sub-thermally excited. To examine whether LTE is a good approximation for this observation, we compare the derived column densities with those obtained with the non-LTE radiative transfer code RADEX (van der Tak *et al.* 2007). Simple molecules such as C^{18}O , CS, SO, HC^{15}N , H^{13}CN , HC^{18}O^+ , CH_3OH , and CCH are examined, for which the collisional cross sections are available. The collisional rate coefficients are taken from Yang *et al.* (2010) for C^{18}O , Lique, Spielfiedel, & Cernicharo (2006) for CS and SO, Flower (1999) for HC^{18}O^+ , Green & Thaddeus (1974) for HC^{15}N and H^{13}CN , Spielfiedel *et al.* (2012) for CCH, and Rabli & Flower (2010) for CH_3OH . As summarized in Table 3.2, the column densities derived by RADEX and those derived by the LTE analysis agree within the error over a range of $n(\text{H}_2) = 3 \times 10^5 - 3 \times 10^6 \text{ cm}^{-3}$ and $T_k = 10-30$ K except for CS. The difference in the column density of CS is about a factor of 2, but it does not change the conclusion of the discussion

in Section 3.5 (see Figures 3.4 and 3.5). Larger molecules tend to exist in the denser part of the cloud, and hence, the non-LTE effect could be smaller than the above cases. The non-LTE effect on isotopic ratios is also negligible, because uncertainties of the derived column densities are mostly caused by assumptions of temperature and H₂ density, and their effects are canceled out in the ratios. Thus, we employ the results obtained with LTE in the following analysis and discussions.

The spectral lines of CO, ¹³CO, CS, HCO⁺, HCN, and HNC are optically thick, judging from the isotopologue lines. Hence, the column densities of these molecules shown in Table 3.4 are derived from the isotopologue lines, assuming the following isotopic ratios in the local interstellar matter (ISM): ¹²C/¹³C= 60, ¹⁶O/¹⁸O= 560, and ³²S/³⁴S= 22 (Lucas & Liszt 1998; Wilson & Rood 1994; Chin *et al.* 1996). As discussed later (Section 3.4.2), the ¹²C/¹³C ratios of carbon-chain molecules are higher than the local ISM value. However, we here employ the standard values for the above fundamental species. Although the optical depths of C¹⁸O and H¹³CO⁺ lines are moderate, the derived column densities are consistent with those derived from the C¹⁷O, ¹³C¹⁸O, and HC¹⁸O⁺ lines (¹⁸O/¹⁷O= 3.2; Wilson & Rood 1994).

For molecules having the ortho and para species due to symmetry, they are analyzed separately under the assumption of the same rotational temperatures, if the lines of both species are detected. Free parameters for the fit are the total column density, the rotational temperature, and the ortho-to-para ratio. For l-C₃H₂, c-C₃H₂, C₄H₂, and CH₂CO, the ortho-to-para ratios are derived to be 2.81 ± 0.14 , 2.2 ± 0.3 , 3.2 ± 0.2 , and 3.2 ± 1.2 , respectively. c-C₃H₂ shows lower ortho-to-para ratio than 3, probably because an optically-thick ortho line is used for the evaluation (See Chapter 3.5.2). For molecules of which only ortho lines are detected, we assume the statistical ortho-to-para ratios: 3 for H₂¹³CO, H₂CS, NH₂D, c-H₂C₃O, c-¹³CCCH₂, and CH₂CN, and 2 for D₂CO and c-C₃D₂. For CH₃CCH and CH₃CN, the *A* and *E* states caused by the internal rotation are analyzed separately under the assumption of the identical rotational temperature. The *A*/*E* ratios are derived to be 0.98 ± 0.14 and 1.07 ± 0.02 for CH₃CCH and CH₃CN, respectively. For CH₃CHO and CH₃OH, the *A*/*E* ratio is assumed to be 1, because only one line of the *A* state is detected. The column densities shown in Tables 3.3 and 3.4 represent the total column densities. The error of the column density of NH₂D is large because of the poor S/N ratio of the detected line.

We derive the upper limit to the column densities for important undetected species, OCS, HCOOCH₃, and (CH₃)₂O, to compare them with those derived in IRAS 16293-2422. A spectral line for which the highest S/N ratio is expected in the observed frequency range (i.e., $J = 7-6$

at 85.14 GHz for OCS, $4_{14}-3_{13}$ EE at 99.32 GHz for $(\text{CH}_3)_2\text{O}$, and $9_{09}-8_{08}$ A at 100.68 GHz for HCOOCH_3) is used for the evaluation for each species. The 3σ upper limit is derived from the rms noise under the assumption of the line width of 1.0 km s^{-1} , as shown in Table 3.4.

In order to derive the beam-averaged fractional abundances of molecules relative to H_2 ($X = N/N(\text{H}_2)$), we evaluate the beam-averaged column density of H_2 , $N(\text{H}_2)$, from the C^{17}O data. The $N(\text{H}_2)$ value is derived to be $(8.2 \pm 1.6) \times 10^{22} \text{ cm}^{-2}$ by assuming the rotational temperature of 15 K and the $N(\text{C}^{17}\text{O})/N(\text{H}_2)$ ratio of 2.6×10^{-8} (Jørgensen, Schöier & van Dishoeck 2002). Note that this ratio is derived from the C^{17}O and dust continuum observations, and is lower than the ratio reported by Frerking, Langer, & Wilson (1982) in which the canonical $N(\text{C}^{17}\text{O})/N(\text{H}_2)$ ratio without depletion is discussed. The fractional abundances of molecules are listed in Table 3.5. Here, we adopt the column densities derived with the excitation temperature of 15 K for the species listed in Table 3.4.

Table 3.2. Comparison of column densities derived by the non-LTE and LTE analysis.

Molecule	N (cm $^{-2}$)	
	Non-LTE	LTE ^a
C ¹⁸ O	$(0.7\text{--}1.0)\times 10^{16}$	$7.1(18)\times 10^{15}$
CS	$(1.4\text{--}2.0)\times 10^{13}$	$3.4(7)\times 10^{13}$
SO	$(4.0\text{--}6.5)\times 10^{12}$	$1.1(9)\times 10^{13}$
HC ¹⁸ O ⁺	$(3.5\text{--}7.5)\times 10^{11}$	$5.7(11)\times 10^{11}$
HC ¹⁵ N	$(1.5\text{--}2.6)\times 10^{11}$	$2.6(5)\times 10^{11}$
H ¹³ CN	$(0.7\text{--}1.4)\times 10^{11}$	$1.1(2)\times 10^{11}$
CCH ^b	$(1.2\text{--}2.2)\times 10^{15}$	$1.5(3)\times 10^{15}$
CH ₃ OH ^c	$(2.3\text{--}3.4)\times 10^{13}$	$2.3(10)\times 10^{13}$

Note. — The H₂ density and the kinetic temperature are set to be $3\times 10^5\text{--}3\times 10^6$ cm $^{-3}$ and 10–30 K, respectively.

^aThe numbers in parentheses represent the errors in units of the last significant digits. For molecules listed in Table 3.4, the column density derived with $T_{\text{rot}} = 15$ K is shown.

^bTwo optically-thin hyperfine components are used.

^cThe H₂ density is restricted to $3\times 10^5\text{--}1\times 10^6$ cm $^{-3}$ to reproduce the absorption feature of the $3_{1,3}\text{--}4_{1,4}$, A⁺ line.

Table 3.3. Derived column densities, rotational temperatures, and optical depths of the lines used for the evaluation.

Molecule	N (cm ⁻²)	T_{rot} (K)	τ range ^a
SO	$1.1(9) \times 10^{13}$	6(2)	< 0.21
CCS	$6(2) \times 10^{12}$	6.1(8)	< 0.066
C ₃ O	$1.8(11) \times 10^{11}$	11(5)	< 0.034
C ₃ N	$6(7) \times 10^{11}$	11(9)	< 0.009
l-C ₃ H	$3.5(2) \times 10^{12}$	11.5(12)	< 0.067
c-C ₃ H	$1.4(5) \times 10^{13}$	15(6)	< 0.034
c-C ₃ H ₂	$4.4(5) \times 10^{13}$	8.9(6)	< 0.83
c- ¹³ CCCH ₂	$2.18(16) \times 10^{11}$	8.9 (fix) ^b	< 0.013
c-CC ¹³ CH ₂	$1.07(16) \times 10^{12}$	8.9 (fix) ^b	< 0.058
c-C ₃ HD	$1.9(2) \times 10^{12}$	8.9 (fix) ^b	< 0.11
c-C ₃ D ₂	$2.2(8) \times 10^{11}$	8.9 (fix) ^b	0.006
l-C ₃ H ₂	$1.23(7) \times 10^{12}$	9.2(8)	< 0.049
C ₄ H	$2.32(12) \times 10^{14}$	12.3(4)	< 0.26
C ₄ H ₂	$1.9(2) \times 10^{12}$	12.7(11)	< 0.017
C ₅ H	$5.3(11) \times 10^{11}$	33(26)	< 0.002
HC ₃ N	$1.22(6) \times 10^{13}$	25(4)	< 0.16
H ¹³ CCCN	$1.4(4) \times 10^{11}$	25 (fix) ^b	< 0.002
HC ¹³ CCN	$2.4(3) \times 10^{11}$	25 (fix) ^b	< 0.0028
HCC ¹³ CN	$2.5(8) \times 10^{11}$	25 (fix) ^b	< 0.003
DC ₃ N	$4.7(12) \times 10^{11}$	25 (fix) ^b	< 0.015
HC ₅ N	$2.4(18) \times 10^{12}$	22(7)	< 0.005
CH ₃ CCH	$7.0(6) \times 10^{13}$	14.2(15)	< 0.070
CH ₂ DCCH	$9.83(13) \times 10^{12}$	14.2 (fix) ^b	< 0.008
CH ₃ OH	$2.3(10) \times 10^{13}$	13(8)	< 0.030
CH ₃ CN	$2.54(15) \times 10^{11}$	21(2)	< 0.005
CH ₂ CN	$2.2(4) \times 10^{12}$	8.6(19)	< 0.010
CH ₂ CO	$7(3) \times 10^{12}$	27(23)	< 0.008
HCCCHO	$2.4(3) \times 10^{12}$	16(13)	< 0.004

Note. — The numbers in parentheses represent the errors in units of the last significant digits.

^aThe range of the optical depths of the lines used in the analysis.

^bThe rotational temperature is assumed to be the same as that derived for the normal species.

Table 3.4. Derived column densities and optical depths of the lines used for the evaluation.

Molecule	$T_{\text{rot}} = 10 \text{ K}$		$T_{\text{rot}} = 15 \text{ K}$	
	$N \text{ (cm}^{-2}\text{)}$	$\tau \text{ range}$	$N \text{ (cm}^{-2}\text{)}$	$\tau \text{ range}$
CO	$(4.4(16) \times 10^{18})^{\text{a}}$	–	$(4.0(10) \times 10^{18})^{\text{a}}$	–
^{13}CO	$(5.1(13) \times 10^{16})^{\text{b}}$	–	$(5.9(15) \times 10^{16})^{\text{b}}$	–
C^{18}O	$8(3) \times 10^{15}$	1.07	$7.1(18) \times 10^{15}$	0.48
C^{17}O	$1.90(4) \times 10^{15}$	< 0.16	$2.1(4) \times 10^{15}$	< 0.088
$^{13}\text{C}^{18}\text{O}$	$9(2) \times 10^{13}$	0.011	$1.1(3) \times 10^{14}$	0.007
CS	$(3.1(6) \times 10^{13})^{\text{c}}$	–	$(3.4(7) \times 10^{13})^{\text{c}}$	–
C^{34}S	$1.4(3) \times 10^{12}$	0.025	$1.6(3) \times 10^{12}$	0.014
C^{33}S	$2.1(6) \times 10^{11}$	0.007	$2.3(7) \times 10^{11}$	0.004
CN ^d	$2.3(3) \times 10^{14}$	< 0.090	$2.6(5) \times 10^{14}$	< 0.051
^{13}CN	$3.7(7) \times 10^{12}$	< 0.018	$4.2(8) \times 10^{12}$	< 0.011
C^{15}N	$10(3) \times 10^{11}$	0.007	$1.1(2) \times 10^{12}$	0.004
HCO ⁺	$(2.9(7) \times 10^{14})^{\text{d}}$	–	$(3.1(7) \times 10^{14})^{\text{d}}$	–
H^{13}CO^+	$4.8(12) \times 10^{12}$	0.47	$5.2(12) \times 10^{12}$	0.25
HC^{18}O^+	$4.8(10) \times 10^{11}$	0.050	$5.7(11) \times 10^{11}$	0.029
DCO ⁺	$(1.5(3) \times 10^{13})^{\text{d}}$	–	$(1.8(4) \times 10^{13})^{\text{d}}$	–
D^{13}CO^+	$2.4(6) \times 10^{11}$	0.040	$3.0(7) \times 10^{11}$	0.023
HNC	$(10(2) \times 10^{13})^{\text{d}}$	–	$(1.2(3) \times 10^{14})^{\text{d}}$	–
HN^{13}C	$1.6(4) \times 10^{12}$	0.092	$1.9(5) \times 10^{12}$	0.052
H^{15}NC	$3.1(7) \times 10^{11}$	0.020	$3.7(8) \times 10^{11}$	0.012
DNC	$4.5(11) \times 10^{12}$	0.29	$5.2(11) \times 10^{12}$	0.16
HCN	$(5.5(11) \times 10^{13})^{\text{d}}$	–	$(6.5(12) \times 10^{13})^{\text{d}}$	–
H^{13}CN	$9.1(18) \times 10^{11}$	< 0.028	$1.1(2) \times 10^{12}$	< 0.016
HC^{15}N	$2.2(5) \times 10^{11}$	0.015	$2.6(5) \times 10^{11}$	0.009
DCN	$2.6(5) \times 10^{12}$	< 0.11	$3.1(6) \times 10^{12}$	< 0.061
N_2H^+	$5.8(3) \times 10^{12}$	< 0.20	$6.6(13) \times 10^{12}$	< 0.11
N_2D^+	$3.0(6) \times 10^{11}$	< 0.010	$3.6(7) \times 10^{11}$	< 0.006
CCH ^e	$1.4(3) \times 10^{15}$	< 0.25	$1.5(3) \times 10^{15}$	< 0.14
^{13}CCH	$6.3(10) \times 10^{12}$	< 0.007	$7.5(15) \times 10^{12}$	< 0.004
C^{13}CH	$9.4(19) \times 10^{12}$	< 0.009	$1.1(2) \times 10^{13}$	< 0.005
CCD	$4.7(3) \times 10^{13}$	< 0.092	$5.6(11) \times 10^{13}$	< 0.053

Table 3.4 (continued)

Molecule	$T_{\text{rot}} = 10 \text{ K}$		$T_{\text{rot}} = 15 \text{ K}$	
	$N \text{ (cm}^{-2}\text{)}$	$\tau \text{ range}$	$N \text{ (cm}^{-2}\text{)}$	$\tau \text{ range}$
HCS ⁺	$3.8(8) \times 10^{11}$	0.008	$4.3(9) \times 10^{11}$	0.005
HCO	$5.3(11) \times 10^{12}$	< 0.023	$7.2(14) \times 10^{12}$	< 0.013
c-H ₂ C ₃ O	$5.4(16) \times 10^{11}$	< 0.009	$4.5(11) \times 10^{11}$	< 0.005
H ₂ CO	$(1.2(3) \times 10^{14})^{\text{d,f}}$	–	$(1.6(4) \times 10^{14})^{\text{d,f}}$	–
H ₂ ¹³ CO	$2.0(5) \times 10^{12}$	0.025	$2.6(7) \times 10^{12}$	0.015
D ₂ CO	$1.8(7) \times 10^{12}$	< 0.046	$2.2(8) \times 10^{12}$	< 0.026
CH ₃ CHO	$1.6(3) \times 10^{12}$	< 0.009	$1.6(4) \times 10^{12}$	< 0.005
H ₂ CS	$2.7(5) \times 10^{12}$	< 0.023	$2.8(5) \times 10^{12}$	< 0.013
HDCS	$6.3(18) \times 10^{11}$	0.008	$8(2) \times 10^{11}$	0.004
HCCNC	$5.2(16) \times 10^{11}$	0.005	$3.1(9) \times 10^{11}$	0.003
HNCO	$2.6(5) \times 10^{12}$	< 0.036	$2.6(3) \times 10^{12}$	< 0.023
NH ₂ D	$1.9(17) \times 10^{12}$	0.007	$1.5(14) \times 10^{12}$	0.004
OCS	< 2.3×10^{12}	–	< 1.9×10^{12}	–
HCOOCH ₃	< 1.3×10^{13}	–	< 9.7×10^{12}	–
(CH ₃) ₂ O	< 4.1×10^{12}	–	< 5.0×10^{12}	–

Note. — The numbers in parentheses represent the errors in units of the last significant digits.

^aThe spectral lines of C¹⁸O are used for evaluation of the column density, where the ¹⁶O/¹⁸O ratio is assumed to be 560 (Wilson & Rood 1994).

^bThe spectral lines of ¹³C¹⁸O are used for evaluation of the column density, where the ¹⁶O/¹⁸O ratio is assumed to be 560 (Wilson & Rood 1994).

^cThe spectral lines of the ³⁴S species are used for evaluation of the column density, where the ³²S/³⁴S ratio is assumed to be 22 (Chin *et al.* 1996).

^dThe spectral lines of the ¹³C species are used for evaluation of the column density, where the ¹²C/¹³C ratio is assumed to be 60 (Lucas & Liszt 1998).

^eTwo optically-thin hyperfine components are used for evaluation of the column density.

^fNo lines are observed in this survey.

Table 3.5. Fractional abundance relative to H₂, calculated from Tables 3.3 and 3.4.

Molecule	X	Molecule	X
CO	$(4.8(16) \times 10^{-5})^a$	c-C ₃ H ₂	$5.3(12) \times 10^{-10}$
¹³ CO	$(7(2) \times 10^{-7})^b$	c- ¹³ CCCH ₂	$2.6(6) \times 10^{-12}$
C ¹⁸ O	$9(3) \times 10^{-8}$	c-CC ¹³ CH ₂	$1.3(3) \times 10^{-11}$
¹³ C ¹⁸ O	$1.3(4) \times 10^{-9}$	c-C ₃ HD	$2.4(5) \times 10^{-11}$
CS	$(4.2(12) \times 10^{-10})^c$	c-C ₃ D ₂	$2.7(11) \times 10^{-12}$
C ³⁴ S	$1.9(5) \times 10^{-11}$	l-C ₃ H ₂	$1.5(3) \times 10^{-11}$
C ³³ S	$2.8(10) \times 10^{-12}$	C ₄ H	$2.8(6) \times 10^{-9}$
CN	$3.2(9) \times 10^{-9}$	C ₄ H ₂	$2.4(5) \times 10^{-11}$
¹³ CN	$5.2(14) \times 10^{-11}$	C ₅ H	$6.4(18) \times 10^{-12}$
C ¹⁵ N	$1.4(4) \times 10^{-11}$	HC ₃ N	$1.5(3) \times 10^{-10}$
SO	$1.3(11) \times 10^{-10}$	H ¹³ CCCN	$1.8(6) \times 10^{-12}$
HCO ⁺	$(3.8(11) \times 10^{-9})^d$	HC ¹³ CCN	$2.9(7) \times 10^{-12}$
H ¹³ CO ⁺	$6.3(19) \times 10^{-11}$	HCC ¹³ CN	$3.0(11) \times 10^{-12}$
HC ¹⁸ O ⁺	$6.9(19) \times 10^{-12}$	DC ₃ N	$5.7(18) \times 10^{-12}$
DCO ⁺	$(2.2(7) \times 10^{-10})^d$	HC ₅ N	$3(2) \times 10^{-11}$
D ¹³ CO ⁺	$3.6(11) \times 10^{-12}$	c-H ₂ C ₃ O	$5.5(17) \times 10^{-12}$
HNC	$(1.4(4) \times 10^{-9})^d$	H ₂ CO	$(1.9(6) \times 10^{-9})^{d,f}$
HN ¹³ C	$2.3(7) \times 10^{-11}$	H ₂ ¹³ CO	$3.1(10) \times 10^{-11}$
H ¹⁵ NC	$4.5(13) \times 10^{-12}$	D ₂ CO	$2.7(11) \times 10^{-11}$
DNC	$6.3(19) \times 10^{-11}$	H ₂ CS	$3.5(9) \times 10^{-11}$
HCN	$(8(2) \times 10^{-10})^d$	HDCS	$10(3) \times 10^{-12}$
H ¹³ CN	$1.3(4) \times 10^{-11}$	NH ₂ D	$1.8(17) \times 10^{-11}$
HC ¹⁵ N	$3.1(9) \times 10^{-12}$	HCCNC	$3.8(14) \times 10^{-12}$
DCN	$3.8(11) \times 10^{-11}$	HNCO	$3.2(7) \times 10^{-11}$
N ₂ H ⁺	$8(2) \times 10^{-11}$	CH ₃ CHO	$2.0(7) \times 10^{-11}$
N ₂ D ⁺	$4.4(12) \times 10^{-12}$	CH ₃ CCH	$8.5(18) \times 10^{-10}$
CCH ^e	$1.9(5) \times 10^{-8}$	CH ₂ DCCH	$1.2(2) \times 10^{-10}$
¹³ CCH	$9(3) \times 10^{-11}$	CH ₃ OH	$2.8(13) \times 10^{-10}$
C ¹³ CH	$1.4(4) \times 10^{-10}$	CH ₃ CN	$3.1(6) \times 10^{-12}$
CCD	$6.9(19) \times 10^{-10}$	CH ₂ CN	$2.6(7) \times 10^{-11}$
HCS ⁺	$5.2(15) \times 10^{-12}$	CH ₂ CO	$9(4) \times 10^{-11}$

Table 3.5 (continued)

Molecule	X	Molecule	X
HCO	$9(2) \times 10^{-11}$	HCCCHO	$3.0(7) \times 10^{-11}$
CCS	$7(3) \times 10^{-11}$	OCS	$< 2.3 \times 10^{-11}$
C ₃ O	$2.2(14) \times 10^{-12}$	HCOOCH ₃	$< 1.2 \times 10^{-10}$
l-C ₃ H	$4.3(9) \times 10^{-11}$	(CH ₃) ₂ O	$< 6.1 \times 10^{-11}$
c-C ₃ H	$1.7(7) \times 10^{-10}$		

Note. — The numbers in parentheses represent the errors in units of the last significant digits. The column density of H₂ is evaluated from that of C¹⁷O to be $(8.2 \pm 1.6) \times 10^{22} \text{ cm}^{-2}$. For molecules listed in Table 3.4, the column density derived with $T_{\text{rot}} = 15 \text{ K}$ is assumed.

^{a,b,c,d,e,f}See the footnotes in Table 3.4

3.4. Isotopic ratios

3.4.1. Deuterated species

Since we detect 12 deuterated species with reasonably good S/N ratios, we here derive their abundance ratios relative to the normal species, as summarized in Table 3.6. For the isotopic species, we adopt the same rotational temperatures as those for the normal species. For molecules for which the rotational temperatures are not derived by the fit, the ratios are derived by assuming the excitation temperature of 15 K. Note that the results do not change within the error limits, even if we adopt the excitation temperature of 10 K. The D/H ratio (i.e., what fraction of the hydrogen atom is replaced by the deuterium atom in the species of interest) is not the same as the abundance ratio, when the molecular species contains multiple equivalent H or D atoms. The D/H ratios translated from the derived abundance ratios are also shown in Table 3.6.

The abundance ratios derived in this study are consistent with the previous reports, as shown in Table 3.6. Carbon-chain molecules (CCH and HC₃N) and standard species (HCN, HCO⁺, N₂H⁺, and HNC) show moderate D/H ratios of ~ 0.04 – 0.05 . Note that the D/H ratios of HCO⁺ and HNC can be regarded as an upper limit and lower limit, respectively. The H¹³CO⁺ and DNC lines could be optically thick, if we adopt the excitation temperature lower than 10 K. For overcoming this situation, using the double isotope species such as DN¹³C to evaluate the D/H ratio would be preferable. CH₂DCCH is statistically favored by a factor of 3, because there are three equivalent hydrogen atoms in the methyl group to be deuterated. Thus, the [CH₂DCCH]/[CH₃CCH] ratio of 0.141 means a similar level of deuterium fractionation to the other carbon-chain species, when the statistical weight is considered.

The moderate D/H ratio observed in this study is consistent with the interpretation reported by Sakai *et al.* (2009b) and Sakai & Yamamoto (2013). In the WCCC sources, the prestellar-core phase would be shorter than the chemical timescale of the C-to-CO conversion ($\sim 10^6$ yr). The prestellar-core phase is not long enough for deuterium transfer reactions and CO depletion onto dust grains to occur. Thus, the D/H ratios should be relatively low in the WCCC sources (Sakai *et al.* 2009b). This is in contrast to the hot corino sources, and is thought to be a consequence of a longer cold prestellar-core phase with high degree of CO depletion. In fact, the [CCD]/[CCH] ratio is reported to be 0.18 in the hot core source IRAS 16293-2422 (van Dishoeck *et al.* 1995), which is much higher than that in L1527 (0.037).

On the other hand, the D/H ratios of c-C₃D₂, D₂CO, and HDCS are found to be high in comparison with those of other species. This trend is seen in other low-mass star-forming

regions, as described below. The $[\text{HDCS}]/[\text{H}_2\text{CS}]$ ratio is 0.29, which is much higher than the abundance ratios of the other species. The D/H ratio is still as high as 0.14, in which the statistical weight of 2 due to the two equivalent hydrogen atoms is taken into account. The high $[\text{HDCS}]/[\text{H}_2\text{CS}]$ ratio (0.29) is previously reported in the evolved prestellar core, Barnard 1, which is higher than the D/H ratios of the other molecules observed in this source (Marcelino *et al.* 2005). Marcelino *et al.* (2005) reproduced the high abundance ratio of HDCS in their steady-state gas-phase chemical model.

The derived $[\text{D}_2\text{CO}]/[\text{H}_2\text{CO}]$ ratio of 0.014 is also high, because the D/H ratio (i.e., the square root of $[\text{D}_2\text{CO}]/[\text{H}_2\text{CO}]$) is as high as 0.12. The high $[\text{D}_2\text{CO}]/[\text{H}_2\text{CO}]$ ratio is often revealed in many low-mass star-forming regions including L1527 (e.g., Roberts & Millar 2007; Parise *et al.* 2006). Parise *et al.* (2006) reported the high $[\text{D}_2\text{CO}]/[\text{H}_2\text{CO}]$ ratio in L1527 (0.44), while Roberts & Millar (2007) reported the $[\text{D}_2\text{CO}]/[\text{H}_2\text{CO}]$ ratio of 0.016. Our result is close to the result by Roberts & Millar (2007). Several mechanisms both in the gas-phase and the solid-phase are proposed to account for the high D_2CO abundance. Taquet, Ceccarelli, & Kahane (2012) modeled the high D/H ratio, considering the abstraction and substitution of H by D atom on ice surface (e.g., $\text{H}_2\text{CO} + \text{D} \rightarrow \text{HD}\text{CO} + \text{H}$; $\text{HD}\text{CO} + \text{D} \rightarrow \text{D}_2\text{CO} + \text{H}$). Roueff *et al.* (2007) suggested that the D/H ratio of formaldehyde is related to the deuterium fractionation through CH_3^+ (i.e., $\text{CH}_3^+ + \text{HD} \rightarrow \text{CH}_2\text{D}^+ + \text{H}_2 + 390 \text{ K}$) in their steady-state gas-phase model, because CH_3 produced from CH_3^+ reacts with O atoms to form formaldehyde.

The derived $[\text{c-C}_3\text{D}_2]/[\text{c-C}_3\text{HD}]$ ratio of 0.11 in L1527 is higher than the $[\text{c-C}_3\text{HD}]/[\text{c-C}_3\text{H}_2]$ ratio (0.044). The $[\text{c-C}_3\text{HD}]/[\text{c-C}_3\text{H}_2]$ ratio of 0.044 is even lower than those of other molecules, when the equivalent two H atoms in $\text{c-C}_3\text{H}_2$ are considered. Since the abundance ratio of a doubly deuterated species, $[\text{XD}_2]/[\text{XHD}]$, should be statistically 4 times lower than that of the singly deuterated one, $[\text{XHD}]/[\text{XH}_2]$, this result means that $\text{c-C}_3\text{HD}$ is more readily deuterated than $\text{c-C}_3\text{H}_2$. On the other hand, Spezzano *et al.* (2013) reported that the $[\text{c-C}_3\text{D}_2]/[\text{c-C}_3\text{HD}]$ ratio is comparable to the $[\text{c-C}_3\text{HD}]/[\text{c-C}_3\text{H}_2]$ ratio in the prestellar cores L1544 and TMC-1C, although the errors of the ratios are large. They concluded that the observed D/H ratios can be explained by simple gas-phase reactions (e.g., the successive deuteration of $\text{c-C}_3\text{H}_2$ by the reaction with H_2D^+ , D_2H^+ , and D_3^+). However, the situation can be different in L1527, because the overabundance of $\text{c-C}_3\text{D}_2$ relative to $\text{c-C}_3\text{HD}$ cannot be explained by considering only a single formation pathway. Hence, the result is puzzling, and chemical models may need to be revisited.

It should be noted that the anomalous D/H ratios may also be related to the large beam

size of the single-dish telescope, as discussed in Chapter 4.3. The D/H ratios derived from the single-dish observations may suffer from systematic errors caused by the simplified assumption of the same emitting region and the same excitation temperature. Thus, observations with high spatial resolution are needed to solve the origin of the high D/H ratios of some molecules in this source.

3.4.2. ^{13}C -substituted species

In this survey, the ^{13}C species of CO, C^{18}O , CN, HCO^+ , DCO^+ , HNC, HCN, CCH, $c\text{-C}_3\text{H}_2$, HC_3N , and H_2CO are detected. Among them, we derive the $^{12}\text{C}/^{13}\text{C}$ ratios for the cases that the column densities of the corresponding normal species are reasonably determined without suffering from the high optical depth problem. The ratios for C^{18}O , CN, CCH, HC_3N , and $c\text{-C}_3\text{H}_2$ are summarized in Table 3.7. For molecules for which the rotational temperatures are not derived by the fit, the ratios are derived by assuming the excitation temperature of 15 K. The results do not change within the error limits, even if the excitation temperature of 10 K is adopted.

As described in Chapter 1, recent studies revealed that the high $^{12}\text{C}/^{13}\text{C}$ ratios of molecules are produced from C^+ . In L1527, CCH and HC_3N show dilution of ^{13}C species except for HCC^{13}CN (Table 3.7; Sakai *et al.* 2010b; Araki *et al.* 2016; Taniguchi, Saito, & Ozeki 2016). For CCH, the dilution is confirmed in this survey, where the column density of the normal species is derived from the optically-thin hyperfine components ($J = 3/2-1/2$, $F = 1-1$; $\tau = 0.14$, and $J = 3/2-1/2$, $F = 1-0$; $\tau = 0.13$). In addition, the high $^{12}\text{C}/^{13}\text{C}$ ratios of $c\text{-C}_3\text{H}_2$ are confirmed. Note that the $^{12}\text{C}/^{13}\text{C}$ ratios of $c\text{-C}_3\text{H}_2$ are even higher in the detailed analysis in Section 4.1. On the other hand, the derived $^{12}\text{C}/^{13}\text{C}$ ratios of HC_3N are much less accurate than the reported values, because the sensitivity of this survey is not as good as the previous work (Araki *et al.* 2016).

Such a dilution process can occur even in the protostellar envelope of L1527, whose gas kinetic temperature is 25 K (Sakai *et al.* 2010b). In order to verify this interpretation, we consider the following relation under the steady-state approximation:

$$\frac{[^{13}\text{C}^+]}{[^{12}\text{C}^+]} = \frac{k_b[^{13}\text{CO}]}{k_f[^{12}\text{CO}]}, \quad (3.3)$$

where k_f and k_b are the rate coefficients of the forward and backward reactions of (1.10), respectively, and $[X]$ denotes the abundance of X . These rate coefficients fulfill the following

Table 3.6. D/H ratios.

Ratios	This work		Previous works
	Abundance ratio	D/H ratio ^a	Abundance ratio
D ¹³ CO ⁺ /H ¹³ CO ⁺	0.057(19)		0.048 ^b
N ₂ D ⁺ /N ₂ H ⁺	0.054(15)		0.06(1) ^c
DCN/HCN	0.048(13) ^d		0.037(8) ^{d,e}
DNC/HNC	0.045(14) ^d		0.046(4) ^{d,f}
CCD/CCH	0.037(10)		—
DC ₃ N/HC ₃ N	0.039(10)		0.0370(7) ^g
c-C ₃ HD/c-C ₃ H ₂	0.044(7)	0.022(4)	0.071(23) ^h
c-C ₃ D ₂ /c-C ₃ H ₂	0.0050(18)	0.071(13)	—
c-C ₃ D ₂ /c-C ₃ HD	0.11(4)	0.23(8)	—
CH ₂ DCCH/CH ₃ CCH	0.141(12)	0.047(4)	—
HDCS/H ₂ CS	0.29(10)	0.14(5)	—
D ₂ CO/H ₂ CO	0.014(6) ^d	0.12(3)	0.016(5) ^{c,d} ; 0.44 ^{+0.60} _{-0.29} ⁱ

Note. — The numbers in parentheses represent the errors in units of the last significant digits.

^aThe D/H ratio means the abundance ratio for the single deuteration, which is corrected for the statistical weight caused by molecular symmetry (Persson *et al.* 2018).

^bThe [DCO⁺]/[HCO⁺] ratio reported by Jørgensen, Schöier & van Dishoeck (2004), where the column density of HCO⁺ is derived from the H¹³CO⁺ lines by assuming the ¹²C/¹³C ratio of 60.

^cRoberts & Millar (2007)

^dThe column density of the normal species is derived from the ¹³C species, where the ¹²C/¹³C ratio is assumed to be 60.

^eRoberts *et al.* (2002)

^fHirota, Ikeda & Yamamoto (2001)

^gAraki *et al.* (2016)

^hSakai *et al.* (2009b)

ⁱParise *et al.* (2006)

relation:

$$k_b = k_f \exp\left(-\frac{\Delta G}{kT}\right), \quad (3.4)$$

where ΔG represents the free energy difference between the right and left hand sides of the reaction (1.10). Since k_b/k_f is evaluated to be 0.2 at 25 K, the dilution process of $^{13}\text{C}^+$ is barely possible in the warm region of L1527.

L1527 is a warm-carbon-chain-chemistry source, where CH_4 evaporated from dust grains in the warm ($\gtrsim 25$ K) and dense part near the protostar triggers efficient production of carbon-chain molecules including *c*- C_3H_2 . CH_4 is thought to be formed by hydrogenation from the neutral carbon atoms depleted onto dust grains in the cold prestellar core phase and/or the less dense phase. The $^{12}\text{C}/^{13}\text{C}$ ratio of the carbon atom is also expected to be higher than the elemental ratio as the $^{12}\text{C}^+ / ^{13}\text{C}^+$ ratio, because the neutral carbon atom (C) is formed from electron recombination of the carbon ion (C^+). Hence, the $^{12}\text{C}/^{13}\text{C}$ ratio of CH_4 formed on dust grains would also be higher. This may also contribute to the dilution of the ^{13}C species of the carbon-chain molecules.

The ^{13}C atom is fractionated in molecules into two groups by the reaction (1.10). While the molecules produced from C^+ show the high $^{12}\text{C}/^{13}\text{C}$ ratios, molecules produced directly from CO are expected to have the normal $^{12}\text{C}/^{13}\text{C}$ ratio of 60–70, because ^{13}CO is the main reservoir of ^{13}C . This fractionation is already confirmed in the cold prestellar core TMC-1: various carbon-chain molecules show the dilution of ^{13}C (Sakai *et al.* 2007, 2010b, 2013), while CH_3OH , which is formed through successive hydrogenation of CO on dust grains (Watanabe & Kouchi 2002), shows the normal $^{12}\text{C}/^{13}\text{C}$ ratio (Soma *et al.* 2015). Since the derived $[\text{C}^{18}\text{O}]/[^{13}\text{C}^{18}\text{O}]$ ratio in L1527 is consistent with the elemental ratio within the error, our study further confirms the fractionation of ^{13}C species of carbon-chain molecules in the protostellar core, L1527.

The above situation is different from a high $[\text{C}^{18}\text{O}]/[^{13}\text{C}^{18}\text{O}]$ ratio caused by the isotope selective photodissociation (e.g., Visser, van Dishoeck, & Black 2009). This mechanism enhances the $^{13}\text{C}^+$ abundance, and subsequently decreases the $^{12}\text{C}/^{13}\text{C}$ ratio in various molecules formed from $^{13}\text{C}^+$ (enrichment of the ^{13}C species). This is opposite to our observational trend. Thus, this mechanism seems unimportant in this source. It is also suggested that a high $[\text{C}^{18}\text{O}]/[^{13}\text{C}^{18}\text{O}]$ ratio in the gas phase is caused by the difference of the binding energy between ^{13}CO and ^{12}CO (Smith *et al.* 2015; Jørgensen *et al.* 2018). This can cause the lower abundance of $^{13}\text{C}^+$ relative to $^{12}\text{C}^+$, resulting in lower abundances of the ^{13}C species of various molecules. However, the dilution of the ^{13}C species is widely found even in cold clouds, and this mechanism seems less important than the mechanism mentioned in the above paragraph.

The derived $[\text{CN}]/[^{13}\text{CN}]$ ratio (61 ± 17) is also comparable to the elemental ratio. In diffuse clouds, dilution of $^{13}\text{C}^+$ is not significant due to high temperature. If CN produced in such an earlier phase of molecular cloud evolution still remains, the $^{12}\text{C}/^{13}\text{C}$ ratio of CN is close to 60–70. The derived $^{12}\text{C}/^{13}\text{C}$ ratio of CN is consistent with the possible formation pathway of HC_3N : $\text{C}_2\text{H}_2 + \text{CN} \rightarrow \text{HC}_3\text{N} + \text{H}$ (Fukuzawa & Osamura 1996; Woon & Herbst 1996, 1997; Takano *et al.* 1998). In the formation reaction of HC_3N , the C-N bond in CN is considered to be preserved. Thus, the $[\text{HC}_3\text{N}]/[\text{HCC}^{13}\text{CN}]$ ratio would be similar to the $[\text{CN}]/[^{13}\text{CN}]$ ratio of 61. This expectation is now verified in L1527 by the $[\text{HC}_3\text{N}]/[\text{HCC}^{13}\text{CN}]$ ratio of 49 ± 15 (this study) and 64.2 ± 1.1 (Araki *et al.* 2016).

3.4.3. ^{15}N -substituted species

The ^{15}N species of CN, HCN, and HNC are detected in this survey. The $^{14}\text{N}/^{15}\text{N}$ ratios of the three species are consistent with one another within the error, as shown in Table 3.8. Sources where the $^{14}\text{N}/^{15}\text{N}$ ratios of CN, HCN, and HNC are derived are limited to Barnard 1 and the protocluster OMC-2 FIR4. In both sources, the $^{14}\text{N}/^{15}\text{N}$ ratios of the above three species are comparable to one another (Daniel *et al.* 2013; Kahane *et al.* 2018), and the ratios are similar to those derived in L1527 (Table 3.8). This result is consistent with the astrochemical models, which predict that the molecules bearing the nitrile functional group (-CN) have a common fractionation process (e.g., Rodgers & Charnley 2008). On the other hand, the $^{14}\text{N}/^{15}\text{N}$ ratio of CN is reported to be significantly higher than that of HCN in the prestellar core L1544 (Hily-Blant *et al.* 2013a,b). This report contradicts with our result in L1527. Further observations are thus needed to solve this discrepancy.

Araki *et al.* (2016) reported that the $^{14}\text{N}/^{15}\text{N}$ ratio of HC_3N is 338 ± 12 in L1527. If HC_3N is produced from the reaction mentioned above ($\text{C}_2\text{H}_2 + \text{CN} \rightarrow \text{HC}_3\text{N} + \text{H}$), the $^{14}\text{N}/^{15}\text{N}$ ratios of HC_3N and CN should be similar. On the other hand, the $^{14}\text{N}/^{15}\text{N}$ ratio of CN (230 ± 80) is derived to be lower than that of HC_3N . However, the error of this study is large, and this discrepancy is also a target for future observations.

3.5. Comparison with other sources

3.5.1. TMC-1

In Figure 3.4, the column densities of molecules derived in this study in L1527 are compared with those reported for TMC-1, which is the representative carbon-chain rich prestellar core.

Table 3.7. $^{12}\text{C}/^{13}\text{C}$ ratios.

Ratios	This work	Previous works
$[\text{C}^{18}\text{O}]/[\text{C}^{13}\text{C}^{18}\text{O}]$	70(20)	–
$[\text{CN}]/[\text{C}^{13}\text{CN}]$	61(17)	–
$[\text{CCH}]/[\text{C}^{13}\text{CCH}]$	210(60)	$> 135^{\text{a}}$
$[\text{CCH}]/[\text{C}^{13}\text{CH}]$	140(40)	$> 80^{\text{a}}$
$[\text{HC}_3\text{N}]/[\text{H}^{13}\text{CCCN}]$	85(22)	$86.4(16)^{\text{b}}, 100(20)^{\text{c}}$
$[\text{HC}_3\text{N}]/[\text{HC}^{13}\text{CCN}]$	51(7)	$85.4(17)^{\text{b}}, 90(15)^{\text{c}}$
$[\text{HC}_3\text{N}]/[\text{HCC}^{13}\text{CN}]$	49(15)	$64.2(11)^{\text{b}}, 79(12)^{\text{c}}$
$[\text{c-C}_3\text{H}_2]/[\text{c-}^{13}\text{CCCH}_2]$	200(30)	–
$[\text{c-C}_3\text{H}_2]/[\text{c-CC}^{13}\text{CH}_2]$	41(8)	–

Note. — The numbers in parentheses represent the errors in units of the last significant digits.

^aSakai *et al.* (2010b)

^bAraki *et al.* (2016)

^cTaniguchi, Saito, & Ozeki (2016). The temperature of 9.7 K is assumed.

Table 3.8. $^{14}\text{N}/^{15}\text{N}$ ratios.

Ratios	L1527 ^a	B1 ^b	OMC-2 FIR4 ^c
$[\text{CN}]/[\text{C}^{15}\text{N}]$	230(80)	290_{-80}^{+160}	270(60)
$[\text{HCN}]/[\text{HC}^{15}\text{N}]$	250(80) ^d	330_{-50}^{+60}	270(50)
$[\text{HNC}]/[\text{H}^{15}\text{NC}]$	300(100) ^d	225_{-45}^{+75}	290(50)

Note. — The numbers in parentheses represent the errors in units of the last significant digits.

^aThis work

^bDaniel *et al.* (2013)

^cKahane *et al.* (2018)

^dThe column densities of the normal species are derived from the ^{13}C species, where the $^{12}\text{C}/^{13}\text{C}$ ratio is assumed to be 60.

Basically, the column densities are well correlated between the two sources. We note the following trends.

1. The column density ratios ($N_{\text{TMC-1}}/N_{\text{L1527}}$) of the nitrogen-bearing species (e.g., HC_3N and HC_5N) and the sulfur-bearing species (e.g., CCS and H_2CS) are higher than those of the hydrocarbons.
2. For C_nH , longer chain molecules have relatively low $N_{\text{TMC-1}}/N_{\text{L1527}}$ ratios. For instance, the column densities of CCH and $c/l\text{-C}_3\text{H}$ are higher than those in TMC-1, while the column densities of C_4H and C_5H are lower. This trend is more significant in longer chains as reported by Sakai *et al.* (2008b). Note that Araki *et al.* (2017) reported that C_7H and C_6H_2 are the exception: relative abundances of C_7H and C_6H_2 in L1527 compared to TMC-1 are higher than those of C_6H and C_4H_2 , respectively.

The characteristics of WCCC, which are originally suggested by Sakai *et al.* (2008b), are further confirmed. In WCCC, carbon-chain molecules are efficiently regenerated from CH_4 , which is sublimated from the ice mantles after the onset of star formation. Longer chains tend to be deficient in comparison with TMC-1, because they are produced more slowly than shorter chains. The formation timescale of N-bearing chains can also be long due to slow neutral-neutral reactions, suppressing the abundances of HC_nN and other N-bearing species in WCCC sources relative to the carbon-chain molecules. S-bearing species can remain deficient, if S-bearing species are still depleted on dust grains due to their higher desorption temperatures than that of CH_4 .

As for COMs, the column density ratios relative to CH_3OH in L1527 and TMC-1 are compared in Table 3.9. The column densities in TMC-1 are taken from Soma *et al.* (2018). The column density ratios in L1527 are almost comparable to those in TMC-1, suggesting that, unlike the hot corino case, the formation of COMs is inefficient. This is consistent with the WCCC mechanism described in Chapter 1 (Sakai & Yamamoto 2013).

3.5.2. IRAS 16293-2422

Figure 3.5 shows the correlation plot of the column densities derived in L1527 and those in IRAS 16293-2422. This source is known to be a binary source, and the chemistry of each component has been studied by interferometric observations as introduced in Chapter 1 (e.g., Jørgensen *et al.* 2016). However, we here discuss the beam averaged column densities at the protostellar core scale (a few 1000 au) for a fair comparison with our line survey result for

L1527 at a similar size scale. The beam-averaged column densities (beam size $\sim 11''$ – $28''$) of CH_3CHO , HCOOCH_3 , and $(\text{CH}_3)_2\text{O}$ in IRAS 16293-2422 are derived from the data reported by Cazaux *et al.* (2003) by using a least-squares method, under the assumption of the LTE condition. For other species, the beam-averaged column densities are derived from the spectral line survey observation in 0.9–3-mm bands (TIMASSS; Caux *et al.* 2011) with the same method as for L1527 described in Section 3. We note the following trends.

1. The column density ratios (N_{16293}/N_{L1527}) of the carbon-chain related molecules, CCH, C_4H , HC_3N , and *c*- C_3H_2 , are around 0.1–1.
2. On the other hand, the column density ratios (N_{16293}/N_{L1527}) of the CH_3OH , H_2CO , and CH_3CHO are higher than ~ 10 . Complex organic molecules such as HCOOCH_3 and $(\text{CH}_3)_2\text{O}$, which are characteristic species to hot corino sources, are not detected in L1527. The upper limits of HCOOCH_3 and $(\text{CH}_3)_2\text{O}$ in L1527 suggest that these species are significantly less abundant than in IRAS 16293-2422 by two orders of magnitude or more. Table 3.9 shows the column density ratios of COMs *relative to* CH_3OH in L1527 and IRAS 16293-2422. The high abundance of H_2CO relative to CH_3OH in L1527 is consistent with the fast contraction scenario in WCCC, because the timescale for the formation of CH_3OH on dust grains is longer than that of H_2CO (Taquet, Ceccarelli, & Kahane 2012). On the other hand, CH_3CHO shows the similar ratio among the 3 sources shown in Table 3.9. This result implies that CH_3CHO may not be enhanced by the hot corino chemistry.
3. The column density ratios of the S-bearing species are around 10–100 except for CCS. CCS is efficiently produced during chemically young cold-core phase (Suzuki *et al.* 1992), and is not enhanced by the activity of the central protostar (Hirota, Sakai & Yamamoto 2010). The faster contraction timescale in L1527 may result in the relatively higher abundance of ‘remnant’ CCS in comparison with other S-bearing species.

As shown in Figure 3.5, the N_{16293}/N_{L1527} ratios range from 10^2 – 10^3 (COMs) to 0.1 (carbon-chain molecules). Chemical difference with such a high dynamic range of the column density ratio ($\gtrsim 3$ orders of magnitude) is noteworthy. For instance, Watanabe *et al.* (2012) conducted a spectral line survey toward the Class 0–I protostar R CrA IRS7B, revealing a higher abundance of CCH and lower abundances of CH_3OH and SO_2 in comparison with IRAS 16293-2422. The dynamic range of the column density ratios is 2–3 orders of magnitude, and is lower than the case between L1527 and IRAS 16293-2422. Watanabe *et al.* (2012) concluded that R CrA IRS7B is

a source with a mixture of hot corino chemistry and WCCC or a source under a strong influence of the external UV radiation. The higher dynamic range of the column density ratios shown in Figure 3.5 further confirms that the hot corinos such as IRAS 16293-2422 and the WCCC sources such as L1527 are the two distinct cases in chemical composition.

The full chemical composition of sources can be characterized without any preconception only by an unbiased spectral line survey with high sensitivity that can detect not only the major species but also the minor species such as the COMs and carbon-chain molecules. Since unbiased spectral line survey observations toward low-mass star-forming regions have been carried out only toward a few representative sources such as IRAS 16293-2422, R CrA IRS7B, and L1527, those toward other low-mass star-forming regions are of particular importance to reveal the complete picture of the chemical diversity.

Table 3.9. Column density ratios of organic species relative to CH₃OH.

Species	L1527	TMC-1 (CP ^a)	TMC-1 (MP ^b)	IRAS16293-2422
H ₂ CO	7(3)	–	–	1.1(8)
CH ₃ CHO	0.08(5)	0.046(16) ^c	0.09(4) ^c	0.06(3)
CH ₂ CO	0.31(19)	0.20(7)	0.09(4)	–
c-H ₂ C ₃ O	0.020(10)	0.011(2)	–	–
HCOOCH ₃	< 0.42 (3σ)	–	0.026(11) ^c	1.2(4)
(CH ₃) ₂ O	< 0.22 (3σ)	< 0.13 ^c	0.031(17) ^c	11(6)

Note. — The numbers in parentheses represent the errors in units of the last significant digits. The column densities are taken from Soma *et al.* (2018) for TMC-1. The beam-averaged column densities of CH₃OH and other COMs (CH₃CHO, HCOOCH₃, and (CH₃)₂O) in IRAS16293-2422 are evaluated by the least-squares fit of the observation data reported by Caux *et al.* (2011) and Cazaux *et al.* (2003), respectively, under the assumption of the LTE condition.

^aCyanopolyne Peak

^bMethanol Peak

^cThe column density is the sum of two velocity components.

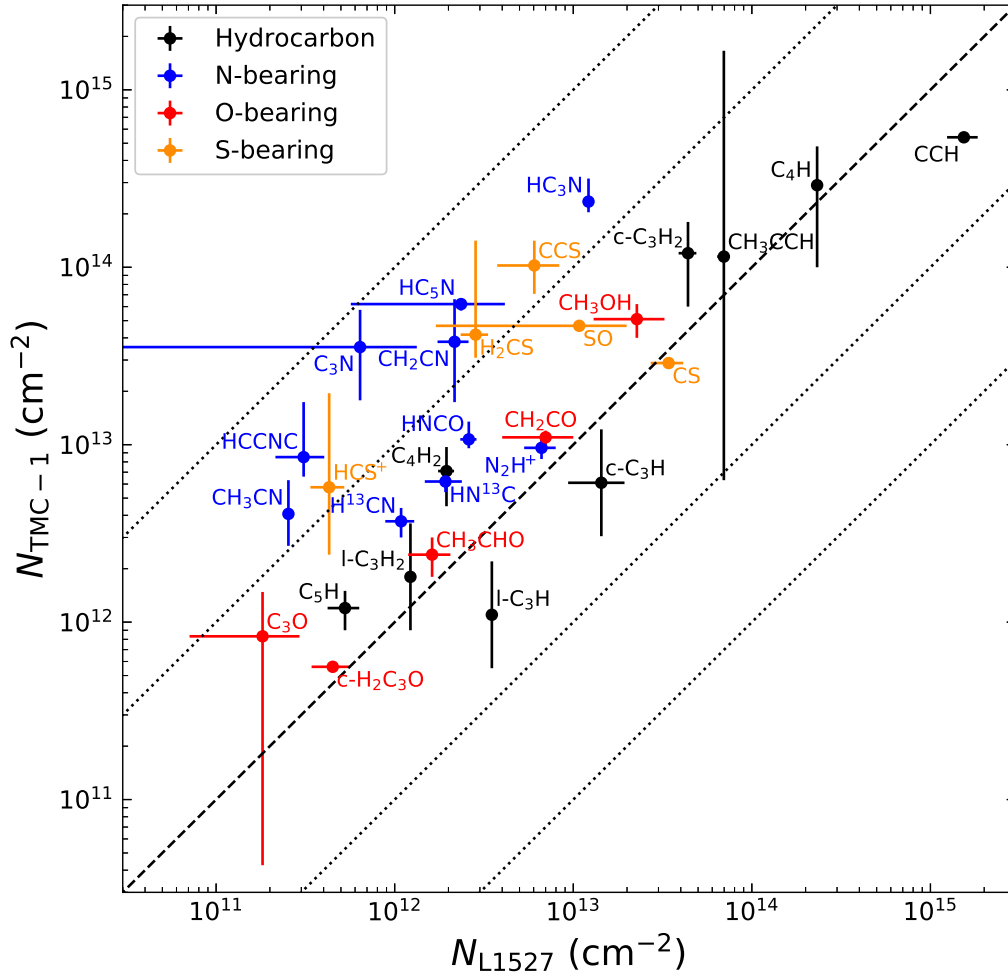


Figure 3.4: The correlation plot of the column densities in L1527 (N_{L1527}) and in TMC-1 (N_{TMC-1}). The dashed line represents $N_{L1527} = N_{TMC-1}$. The four dotted lines show the column density ratio of 100, 10, 0.1, and 0.01. Column densities in TMC-1 are taken from the following references: Loison *et al.* (2017, $c\text{-C}_3\text{H}$, $l\text{-C}_3\text{H}$, $c\text{-C}_3\text{H}_2$, and $l\text{-C}_3\text{H}_2$), Sakai (2008, C_4H , C_4H_2 , and C_5H), Sakai *et al.* (2008b, C_4H , C_4H_2 , and C_5H), Sakai *et al.* (2010b, CCH), Gratier *et al.* (2016, CH_3CCH , HC_3N , HCCNC , CH_2CN , CH_3CN , HNCO , C_3N , CH_2CN , C_3O , SO , CS , CCS , H_2CS , and HCS^+), Taniguchi *et al.* (2016, HC_5N), Soma *et al.* (2015, CH_3OH), Soma *et al.* (2018, CH_2CO and $c\text{-H}_2\text{C}_3\text{O}$), Crapsi *et al.* (2005, N_2H^+), and Hirota *et al.* (1998, HN^{13}C and H^{13}CN).

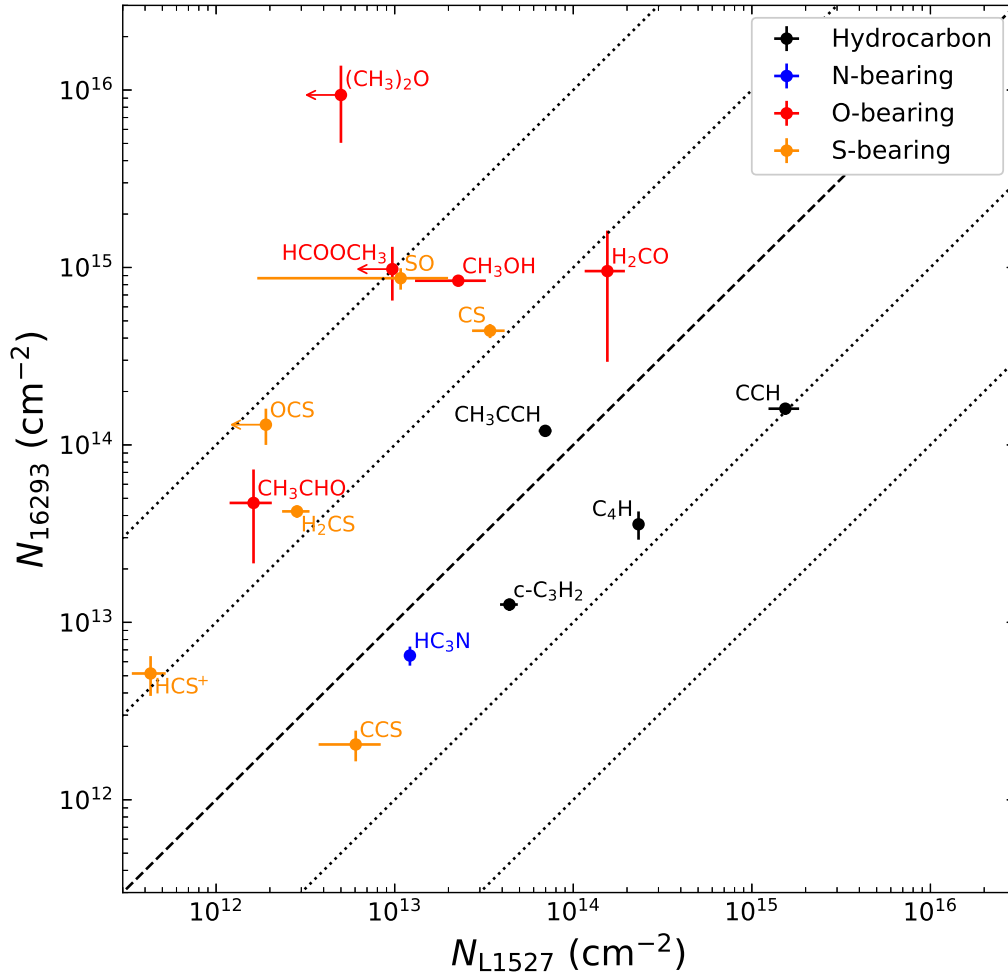


Figure 3.5: The correlation plot of the column densities of carbon-chain molecules, COMs, and S-bearing molecules in L1527 (N_{L1527}) and in IRAS 16293-2422 (N_{16293}). The dashed line represents $N_{L1527} = N_{16293}$. The four dotted lines show the column density ratio of 100, 10, 0.1, and 0.01. The beam-averaged column densities in IRAS 16293-2422 are derived from Cazaux *et al.* (2003) for CH_3CHO , HCOOCH_3 , and $(\text{CH}_3)_2\text{O}$. The column densities of other species are derived from Caux *et al.* (2011).

CHAPTER 4

COMPLEMENTARY STUDY OF THE ^{13}C ANOMALY

In the last chapter, we revealed the ^{13}C anomaly in L1527 for most of the basic C-bearing species. In this chapter, we describe the complementary observations of the two molecules, $c\text{-C}_3\text{H}_2$ and H_2CO , by the single-dish telescopes, and discuss their ^{13}C anomaly that could not be investigated only by the line survey with the 3-mm band. In the next section, we analyze $c\text{-C}_3\text{H}_2$, for which many spectral lines lie in the higher frequency range that the line survey of NRO 45 m could not cover. Then, we analyze the simplest COM, formaldehyde (H_2CO), whose minor isotopologues are not detected in the line survey due to the lack of sensitivity. The content of section 4.1 is a part of the master thesis of the author (Yoshida 2016).

4.1. $c\text{-C}_3\text{H}_2$

$c\text{-C}_3\text{H}_2$ is a carbon-chain related molecule, and is known to exist widely in interstellar clouds (e.g., Madden *et al.* 1989; Cox *et al.* 1989). It has two kinds of ^{13}C isotopic species, as shown in Figure 4.1. The off-axis ^{13}C species (referred to hereafter as $c\text{-CC}^{13}\text{CH}_2$) is statistically favored by a factor of 2 in comparison with the on-axis ^{13}C species (referred to as $c\text{-}^{13}\text{CCCH}_2$), because there are two equivalent carbon atoms in $c\text{-C}_3\text{H}_2$ for ^{13}C substitution for this species. It was detected in TMC-1 and other sources (Madden *et al.* 1986; Gómez-González *et al.* 1986; Spezzano *et al.* 2012). During the spectral line surveys of L1527 with IRAM 30 m telescope (the IRAM large program ASAI) as well as NRO 45 m, we detected many spectral lines of the off-axis and on-axis ^{13}C isotopic species as well as those of the main isotopologue. On the basis of these extensive datasets, we explore the ^{13}C abundance anomaly of $c\text{-C}_3\text{H}_2$ in L1527.

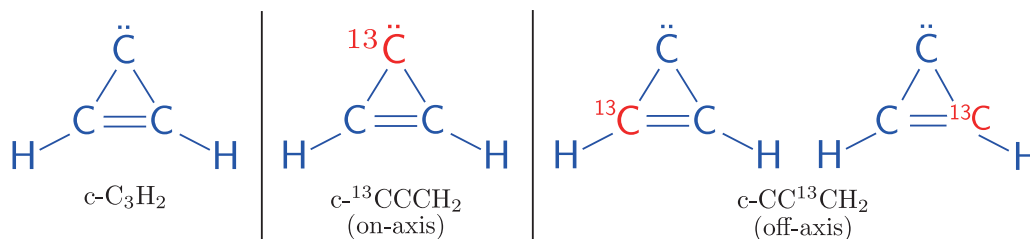


Figure 4.1: Molecular geometry of $c\text{-C}_3\text{H}_2$ and its ^{13}C species.

4.1.1. Observations

In the analysis of $c\text{-C}_3\text{H}_2$, the spectral line survey observation with IRAM 30 m is used in addition to that with NRO 45 m. This section summarizes the observation with IRAM 30 m. See Section 3.2 for NRO 45 m. Observations with IRAM 30 m telescope were performed in several runs between 2012 and 2013, as part of the ASAI (Astrochemical Surveys at IRAM) Large Program. The survey covers the spectral bands at 3 mm (80–112 GHz), 2 mm (130–173 GHz), and 1.3 mm (200–276 GHz). The beam size is $29''$, $17''$, and $12''$ at 86, 145, and 210 GHz, respectively, as reported in the IRAM website¹. The wobbler switching mode was employed with a beam throw of $180''$. This amount of the beam throw is enough, because most of the emission comes from the $15''$ – $20''$ diameter area around the protostar according to the interferometer observations combined with single-dish observations (Sakai *et al.* 2010b). The frontends were the broad-band EMIR receivers, and the back-ends were the fast Fourier transform spectrometers (FTS) in their 195-kHz resolution mode, corresponding to the velocity resolutions of 0.21–0.73 km s⁻¹ at the 1–3-mm bands. The antenna temperature (T_{A}^*) was converted to the main-beam brightness temperature (T_{mb}) by dividing by $B_{\text{eff}}/F_{\text{eff}}$. Here, B_{eff} and F_{eff} are beam efficiency and forward efficiency, respectively. The $B_{\text{eff}}/F_{\text{eff}}$ value is 0.85, 0.80, and 0.67 at 86, 145, and 210 GHz, respectively.

4.1.2. Overall results

In the Nobeyama observations, we detected 7 lines of $c\text{-C}_3\text{H}_2$ in the 3-mm band (Table 4.4). Later, we further detected 8, 9, and 17 lines in the 3-mm, 2-mm, and 1.3-mm bands in the ASAI observations. Examples of the observed spectra are shown in Figure 4.2, along with the best Gaussian fit to their profiles. In total, 41 lines of $c\text{-C}_3\text{H}_2$ were detected, among which 7 transitions were observed both in the Nobeyama and ASAI observations. Even high excitation lines of $8_{1,8}\text{--}8_{0,8}$ and $8_{2,7}\text{--}8_{1,8}$, whose upper state energies are as high as 77 K (53 cm^{-1}), were detected. The detected lines are summarized in Tables 4.1 and 4.4, and are also shown in the energy level diagram (Figure 4.3). Since $c\text{-C}_3\text{H}_2$ has a pair of equivalent H nuclei, the rotational levels are classified into the ortho and para species. Radiative and collisional interconversions between the ortho and the para species are strongly forbidden, and hence, the ortho and the para species behave as different molecular species. In our observations, 19 and 18 lines were detected for the ortho and para species, respectively, while the remaining 4 lines detected in

¹<http://www.iram.es/IRAMES/mainWiki/Iram30mEfficiencies>

the 1.3-mm band are blended lines of the ortho and para species.

In addition to the lines of normal species, we also detected the lines of the ^{13}C isotopic species. The line parameters of $c\text{-CC}^{13}\text{CH}_2$ and $c\text{-}^{13}\text{CCCH}_2$ species (Figure 4.1) are summarized in Tables 4.2 and 4.3, respectively. For $c\text{-CC}^{13}\text{CH}_2$, we detected 6 lines in the 3-mm band in the Nobeyama observations, and 2, 4, and 7 lines in the 3-mm, 2-mm, 1.3-mm bands, respectively, in the ASAI observations. In total, we detected 19 lines for $c\text{-CC}^{13}\text{CH}_2$, as summarized in Tables 4.2 and 4.4. In contrast to the normal species, $c\text{-CC}^{13}\text{CH}_2$ does not have the ortho and para classification, because the two hydrogen nuclei are no longer equivalent. For $c\text{-}^{13}\text{CCCH}_2$, we detected 3 lines in the 3-mm band in the Nobeyama observations, and 2, 1, and 3 lines in the 3-mm, 2-mm, 1.3-mm bands, respectively, in the ASAI observations, as summarized in Tables 4.3 and 4.4. Hence, $c\text{-}^{13}\text{CCCH}_2$ is definitively detected, as shown in Figure 4.2. This species has the ortho and para states as in the case of the normal species.

4.1.3. LTE analysis for $c\text{-C}_3\text{H}_2$

Assuming the local thermodynamic equilibrium (LTE) condition, we determine the rotational temperatures and the beam-averaged column densities of $c\text{-C}_3\text{H}_2$ and its ^{13}C species by using the least-squares analysis with the equations (3.1) and (3.2). The partition function is numerically calculated from energies and degeneracies of the rotational levels, which are taken from the spectroscopy database, CDMS (See also original spectroscopy references: Bogey *et al.* 1986; Vrtilik *et al.* 1987; Bogey *et al.* 1987; Spezzano *et al.* 2012).

Because the size of the emitting region is comparable to or smaller than the telescope beam size, the effect of beam dilution has to be taken into account. This correction for the beam dilution is particularly important in this analysis, because the 1-, 2- and 3-mm data, which result in different beam sizes, are used simultaneously. Furthermore, the correction is also necessary for the 3-mm data taken with the two different telescopes. The correction for the beam dilution is made by dividing the observed intensity by the beam dilution factor $\eta = \theta_s^2 / (\theta_s^2 + \theta_b^2)$, where θ_s and θ_b denote the source diameter and the antenna beam width (FWHM), respectively. This correction factor assumes a Gaussian beam and a Gaussian distribution of the source emission. The FWHM beam widths are assumed to be $1.7 \times 10^3 / \nu(\text{GHz})$ and $2.4 \times 10^3 / \nu(\text{GHz})$ in arcseconds for NRO 45 m and IRAM 30 m, respectively, on the basis of the beam sizes mentioned in Sections 3.2 and 4.1.1. Sakai *et al.* (2010b) reported that $c\text{-C}_3\text{H}_2$ is distributed within a diameter of 2000–3000 au from the protostar, which corresponds to the size of $15''$ – $20''$. Thus, the size of the emitting region is assumed to be $20''$. The intensities of the high

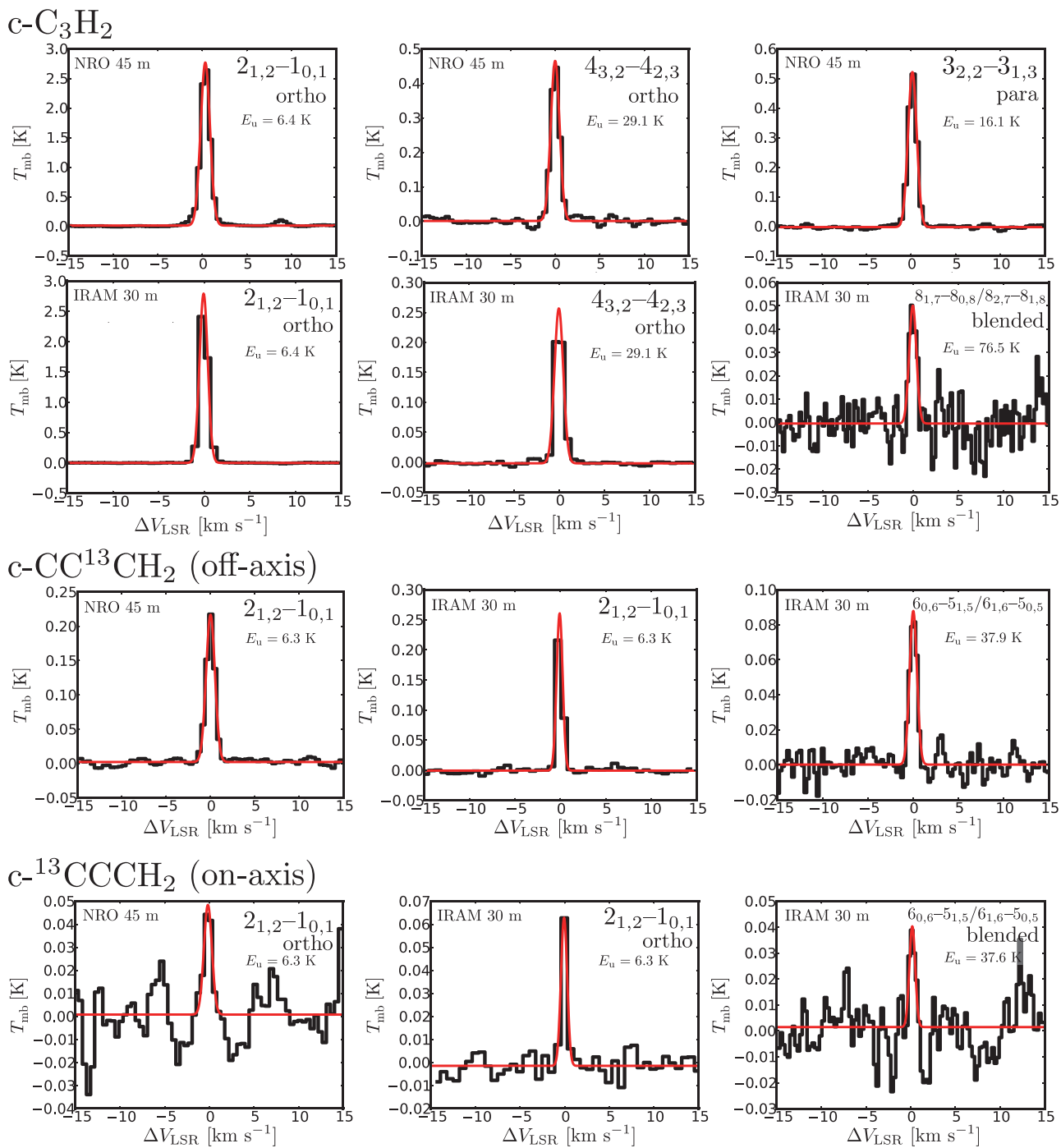


Figure 4.2: Observed line profiles of $c\text{-C}_3\text{H}_2$ and its ^{13}C species in L1527. The results of Gaussian fitting are also shown in red.

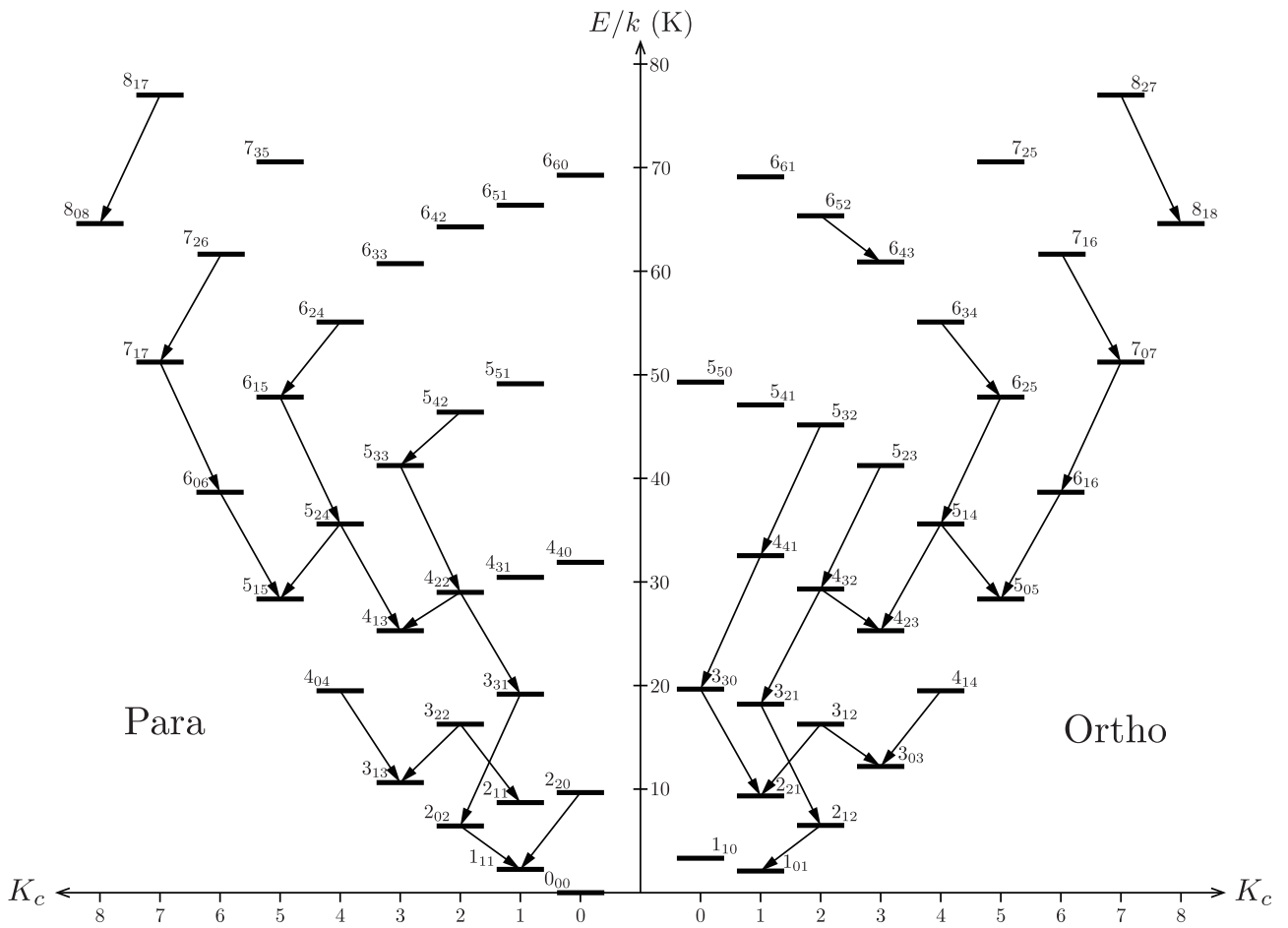


Figure 4.3: The energy level diagram of c-C₃H₂. The transitions observed in L1527 are shown by downward arrows.

excitation lines ($E_u \gtrsim 30$ K) in the 3-mm band observed with NRO 45 m are brighter by a factor of 1.3–2.4 than those observed with IRAM 30 m, which further supports such a compact distribution. In the least-squares analysis, the ortho and para species are treated as different molecules, and the ortho-to-para ratio is taken as a fitting parameter. This analysis is possible owing to the large dataset of the observed line intensities. Relative weights of the data in the least-square analysis are determined by the errors of the line parameters including the uncertainty of the intensity calibration (20%). The total (ortho plus para) column density is derived to be $(1.08 \pm 0.16) \times 10^{14}$ cm $^{-2}$. The ortho-to-para ratio is evaluated to be 3.1 ± 0.4 , which is comparable to the statistical weight of 3. This ratio is consistent with the previous report by Takakuwa *et al.* (2001) (2.5 ± 0.5). The rotational temperature is (8.3 ± 0.3) K, which is lower than that reported for C $_4$ H $_2$ in L1527 of 12.3 K (Sakai *et al.* 2008b). The errors denote the standard deviation of the fit.

We also estimate the column densities of the two ^{13}C species, $c\text{-}^{13}\text{CCCH}_2$ and $c\text{-CC}^{13}\text{CH}_2$, by assuming LTE condition. The column density and the rotational temperature of $c\text{-}^{13}\text{CCCH}_2$ are evaluated to be $(3.5 \pm 0.7) \times 10^{11}$ cm $^{-2}$ and (8.6 ± 1.5) K, respectively, by assuming the same ortho-to-para ratio as the normal species. On the other hand, the column density and the excitation temperature of $c\text{-CC}^{13}\text{CH}_2$ are determined to be $(1.79 \pm 0.19) \times 10^{12}$ cm $^{-2}$ and (7.3 ± 0.4) K, respectively. The abundance ratio of $[c\text{-C}_3\text{H}_2]/[c\text{-}^{13}\text{CCCH}_2]$ is thus determined to be 310 ± 80 , whereas that of $[c\text{-C}_3\text{H}_2]/[c\text{-CC}^{13}\text{CH}_2]$ is 61 ± 11 . Here, $[c\text{-CC}^{13}\text{CH}_2]$ represents the total abundance of the $c\text{-CC}^{13}\text{CH}_2$ species without any correction for the statistical factor of 2 (Figure 4.1; Section 4.1.2). These results are higher than the ratios expected for the condition that ^{13}C is randomly distributed among the three carbon atoms and the elemental abundance ratio of $^{12}\text{C}/^{13}\text{C}$ is 60–70, as shown in Table 4.5.

Figure 4.4 shows the residuals in the least-squares fit divided by the uncertainty δT of each line, $(T_{\text{obs}} - T_{\text{fit}})/\delta T$, where T_{obs} and T_{fit} are the observed intensity and the best-fit value, respectively. The uncertainty of the intensity δT for each line is estimated by taking into account the Gaussian fitting error of the line profile and the calibration uncertainty. Figure 4.4 shows slight systematic residuals in the fit. Intensities of the lines with high and low upper state energies systematically show positive residuals, while those of the lines with moderate upper state energies tend to have negative residuals. Such a systematic trend can also be seen, even if the different source sizes of 15'' and 30'' are assumed. This may indicate that the source includes two components having different rotational temperatures. The physical structure of the source (i.e., the gradient in the density and the temperature) may also play a role. However, the systematic residuals are eliminated by a non-LTE analysis described below,

and we therefore consider that the systematic residuals mainly originate from imperfection of the LTE assumption.

4.1.4. LVG analysis for *c*-C₃H₂

We employ a large velocity gradient (LVG) analysis based on the non-LTE radiative transfer code RADEX (van der Tak *et al.* 2007) for the analysis of the normal species. If the gas kinetic temperature is assumed to be 25 K (Sakai *et al.* 2010b), the H₂ density and the total column density of *c*-C₃H₂ are determined to be $(2.9 \pm 0.5) \times 10^5 \text{ cm}^{-3}$ and $(8.8 \pm 1.1) \times 10^{13} \text{ cm}^{-2}$, respectively. Even if the gas kinetic temperature is assumed to be 10 K for reference, the total column density of *c*-C₃H₂ does not change very much ($(1.18 \pm 0.11) \times 10^{14} \text{ cm}^{-2}$). Figure 4.5 shows the residuals of the fit for the gas kinetic temperature of 25 K, calculated in the same way as in Figure 4.4. The systematic errors seen in Figure 4.4 are now eliminated in Figure 4.5. Although the non-LTE analysis is favorable as seen here, the collisional cross sections are not reported for the ¹³C isotopic species. Hence, we cannot determine the abundance ratios of the ¹³C isotopic species relative to the normal species by using the non-LTE analysis. Since the total column density derived from the non-LTE analysis differs from that derived from the LTE analysis only by 20%, we employ the LTE results for discussions of the ¹²C/¹³C ratio of *c*-C₃H₂.

4.1.5. Discussion

The ¹²C/¹³C ratios of *c*-C₃H₂ derived from the column densities are summarized in Table 4.5. The averaged ¹²C/¹³C ratio of *c*-C₃H₂ is calculated as

$$R_{\text{av}} = \frac{3[\textit{c}\text{-C}_3\text{H}_2]}{[\textit{c}\text{-}^{13}\text{CCCH}_2] + [\textit{c}\text{-CC}^{13}\text{CH}_2]}. \quad (4.1)$$

The numerical factor 3 is introduced because three carbon atoms are available for the ¹³C substitution. The R_{av} value is evaluated to be 150 ± 30 under the LTE condition. As shown in Table 4.5, the ¹²C/¹³C ratios of *c*-C₃H₂ are thus found to be higher than those expected from the interstellar elemental abundance ratio of 60–70 (Lucas & Liszt 1998; Milam *et al.* 2005).

The derived ¹²C/¹³C ratios of *c*-C₃H₂ are 1.5 times higher than that derived from the NRO 45 m data only (Section 3). This discrepancy would originate from the limited numbers of detected lines. In this analysis, 41 lines including optically thin lines in 1.3–3 mm-bands are used to derive the column density of the normal species, while only 7 lines are detected in

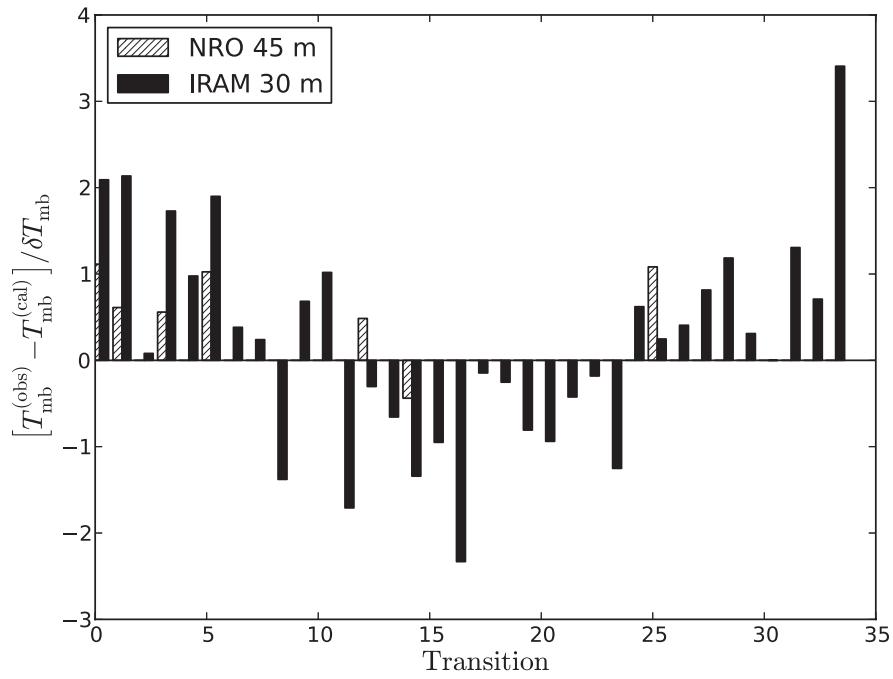


Figure 4.4: Residuals of the LTE fit for the normal species divided by uncertainty of each line, arranged in ascending order of the upper-state energy.

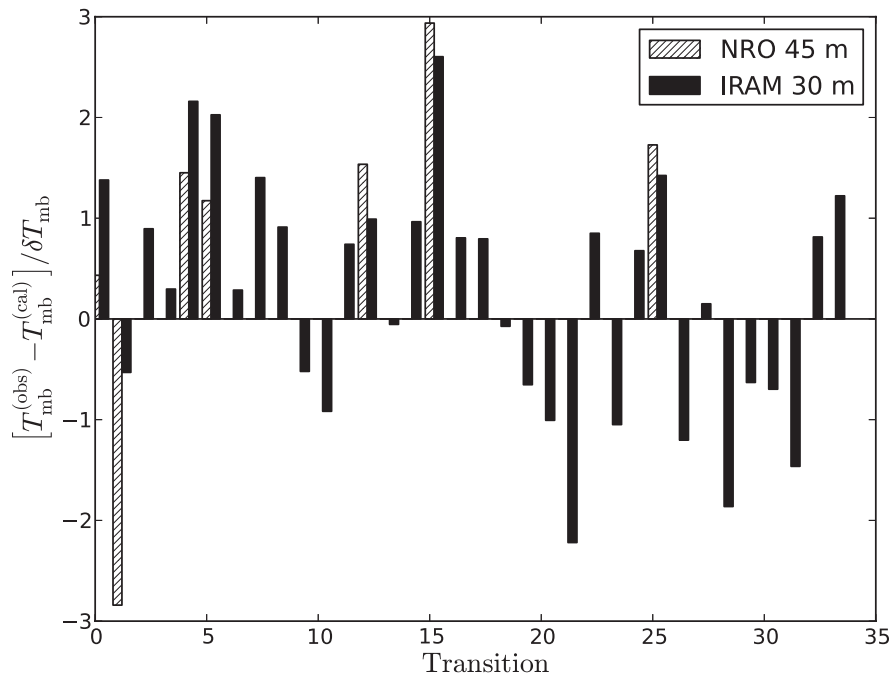


Figure 4.5: The same as Figure 4.4, but obtained by assuming the LVG condition.

the line survey observation with NRO 45 m, some of which are relatively optically thick. The optically-thick lines suppress the column density of the normal species, which would make the $^{12}\text{C}/^{13}\text{C}$ ratio lower.

As described in the Introduction, it is reported that several carbon-chain molecules show the abundance anomaly of the ^{13}C species. For CCH, CCS, C_3S , C_4H , and HC_3N , the ^{13}C abundances for different carbon atoms in a single molecular species are different from one another. In order to compare the abundance of the two ^{13}C species (Section 4.1.2), we calculate the $[\text{c-}^{13}\text{CCCH}_2]/[\text{c-CC}^{13}\text{CH}_2]$ ratio to be 0.20 ± 0.05 . If ^{13}C were randomly substituted for the three carbon atoms, the $[\text{c-}^{13}\text{CCCH}_2]/[\text{c-CC}^{13}\text{CH}_2]$ ratio would be 0.5. Hence, the observed ratio indicates that $\text{c-CC}^{13}\text{CH}_2$ exists more favorably than $\text{c-}^{13}\text{CCCH}_2$. It has been thought that the main production pathway for $\text{c-C}_3\text{H}_2$ is the electron recombination of C_3H_3^+ . This is because the cyclopropenyl cation C_3H_3^+ is a major ionic species, which is produced by the gas-phase reactions starting from CH_4 (Sakai & Yamamoto 2013). Since C_3H_3^+ has three equivalent carbon atoms, $\text{c-C}_3\text{H}_2$ produced from C_3H_3^+ cannot contribute to the abundance anomaly of ^{13}C species. Hence, other reactions have to be considered as the dominant production pathway (e.g., $\text{C}_2\text{H}_2 + \text{CH} \rightarrow \text{C}_3\text{H}_2 + \text{H}$).

Another possible reason for the abundance anomaly of the two ^{13}C species is the exchange reaction between $\text{c-}^{13}\text{CCCH}_2$ and $\text{c-CC}^{13}\text{CH}_2$, although it is uncertain whether this reaction happens for the closed shell molecule, $\text{c-C}_3\text{H}_2$. The zero-point vibrational energies of $\text{c-}^{13}\text{CCCH}_2$ and $\text{c-CC}^{13}\text{CH}_2$ are evaluated to be lower than the normal species by 8.74 K and 53.2 K, respectively, by using the molecular constants by Dateo & Lee (1997). Hence, it would be possible that $\text{c-CC}^{13}\text{CH}_2$ is enhanced relative to $\text{c-}^{13}\text{CCCH}_2$, if the exchange reaction is possible. In case of ^{13}CCH and C^{13}CH , the reaction such as



is proposed (Sakai *et al.* 2010a). It is thus interesting to explore whether a similar process is possible for $\text{c-C}_3\text{H}_2$. It should be noted that the isotopologue with the lowest zero-point vibrational energy tends to have higher abundances for CCH, CCS, and C_3S , although this trend is uncertain for C_4H (Sakai *et al.* 2007, 2010a, 2013). This fact may suggest possible contribution of the position exchange reactions (Sakai *et al.* 2010a; Furuya *et al.* 2011). More detailed studies of these reactions as well as chemical model calculations for the ^{13}C species in molecular clouds are awaited.

Table 4.1. Observed line parameters of c-C₃H₂ toward L1527

Frequency (GHz)	Transition	o/p	E_u (K)	$\langle S\mu^2 \rangle$ (Debye ²)	ΔV_{LSR}^a (km s ⁻¹)	Δv^a (km s ⁻¹)	rms (mK)	T_{mb}^a (K)	$f T_{\text{mb}} dv$ (K km s ⁻¹)	σ_{LTE}^b	σ_{LVG}^c	telescope
80.723180	4 _{2,2} -4 _{1,3}	p	28.8	19.5	-0.07(4)	1.72(9)	5.8	0.12(3)	0.25(5)	0.48	1.54	NRO
					-0.09(6)	0.81(10)	5.9	0.14(3)	0.11(2)	-0.30	0.99	IRAM
82.093544	20 ₂ -1 _{1,1}	p	6.4	14.6	-0.15(13)	1.40(3)	34.3	1.5(3)	2.5(5)	1.11	0.43	NRO
					-0.030(4)	0.820(11)	3.9	1.8(4)	1.6(3)	2.09	1.38	IRAM
82.966200	3 _{1,2} -3 _{0,3}	o	16.0	31.3	-0.101(7)	1.255(17)	15.2	1.1(2)	1.6(3)	0.56	1.45	NRO
					-0.063(4)	0.788(5)	3.5	1.4(3)	1.2(2)	1.73	2.16	IRAM
84.727688	3 _{2,2} -3 _{1,3}	p	16.1	10.3	0.150(5)	1.154(12)	5.5	0.52(11)	0.67(13)	1.02	1.17	NRO
					-0.037(5)	1.196(10)	2.7	0.42(8)	0.54(11)	1.90	2.03	IRAM
85.338894	2 _{1,2} -1 _{0,1}	o	6.4	48.1	0.340(6)	1.239(14)	21.1	2.8(6)	3.8(8)	0.61	-2.84	NRO
					-0.070(5)	1.065(16)	2.9	2.8(6)	3.3(7)	2.14	-0.53	IRAM
85.656431	4 _{3,2} -4 _{2,3}	o	29.1	56.2	-0.010(9)	1.16(2)	7.4	0.46(9)	0.57(11)	-0.44	2.94	NRO
					-0.060(9)	1.15(3)	2.1	0.26(5)	0.33(7)	-1.34	2.60	IRAM
87.435318	5 _{4,2} -5 _{3,3}	p	45.3	26.2	-0.2(2)	2.0(5)	10.5	0.032(9)	0.045(19)	1.08	1.73	NRO
					0.00(11)	1.9(3)	1.8	0.016(4)	0.036(8)	0.25	1.42	IRAM
90.344082	6 _{5,2} -6 _{4,3}	o	64.7	98.3	-0.16(19)	1.2(5)	3.8	0.014(5)	0.017(7)	0.71	0.81	IRAM
145.089606	3 _{1,2} -2 _{2,1}	o	16.0	40.0	0.004(2)	0.727(5)	12.8	3.0(6)	2.3(5)	0.98	0.30	IRAM
150.436555	2 _{2,0} -1 _{1,1}	p	9.7	6.8	-0.136(2)	0.634(8)	8.8	1.7(3)	1.2(2)	0.80	0.89	IRAM
150.820665	4 _{0,4} -3 _{1,3}	p	19.3	36.9	-0.162(4)	0.779(10)	8.2	2.3(5)	1.9(4)	0.68	-0.52	IRAM
150.851908	4 _{1,4} -3 _{0,3}	o	19.3	110.7	-0.201(13)	0.92(3)	8.3	3.3(7)	3.2(6)	1.02	-0.92	IRAM
150.954691	6 _{2,4} -6 _{1,5}	p	54.7	20.3	-0.23(8)	0.6(3)	9.3	0.05(2)	0.025(9)	0.31	-0.63	IRAM
151.039173	6 _{3,4} -6 _{2,5}	o	54.7	60.8	-0.10(4)	0.71(9)	8.8	0.10(2)	0.085(20)	-0.010	-0.70	IRAM
151.343878	5 _{1,4} -5 _{0,5}	o	35.4	32.4	-0.065(8)	0.811(17)	6.7	0.43(9)	0.37(8)	-0.15	0.79	IRAM
151.361105	5 _{2,4} -5 _{1,5}	p	35.4	10.8	0.00(2)	0.75(5)	6.4	0.14(3)	0.11(2)	-0.94	-0.65	IRAM
155.518303	3 _{2,2} -2 _{1,1}	p	16.1	17.8	0.005(2)	0.687(5)	8.2	2.0(4)	1.5(3)	0.38	0.29	IRAM
204.788926	4 _{2,2} -3 _{3,1}	p	28.8	11.2	-0.036(7)	0.761(16)	7.4	0.52(10)	0.44(9)	-0.66	-0.054	IRAM
216.278756	3 _{3,0} -2 _{2,1}	o	19.5	45.6	-0.128(7)	0.892(15)	5.2	2.0(4)	1.9(4)	-1.71	0.74	IRAM
217.822148	6 _{0,6} -5 _{1,5} , 6 _{1,6} -5 _{0,5}	p/o	38.6	58.3	-0.092(3)	0.922(8)	4.4	2.5(5)	2.5(5)	-0.42	-2.22	IRAM
217.940046	5 _{1,4} -4 _{2,3}	o	35.4	110.3	-0.057(2)	0.863(5)	5.5	1.8(4)	1.7(3)	-0.25	-0.073	IRAM
218.160456	5 _{2,4} -4 _{1,3}	p	35.4	36.8	-0.022(4)	0.815(11)	6.5	0.73(15)	0.63(13)	-0.81	-1.01	IRAM
218.732732	7 _{2,6} -7 _{1,7} , 7 _{1,6} -7 _{0,7}	p/o	61.2	11.0	0.05(3)	0.92(8)	4.4	0.071(15)	0.084(18)	1.31	-1.46	IRAM
227.169138	4 _{3,2} -3 _{2,1}	o	29.1	61.6	-0.093(4)	0.827(9)	8.4	1.8(4)	1.6(3)	-0.95	0.96	IRAM
244.222150	3 _{2,1} -2 _{1,2}	o	18.2	7.3	-0.047(3)	0.761(6)	6.0	1.5(3)	1.2(2)	0.24	1.40	IRAM
249.054368	5 _{2,3} -4 _{3,2}	o	41.0	76.3	-0.050(4)	0.791(10)	5.1	1.0(2)	0.89(18)	-0.18	0.85	IRAM
251.314367	7 _{1,7} -6 _{0,6} , 7 _{0,7} -6 _{1,6}	p/o	50.7	69.0	-0.014(3)	0.830(8)	5.7	1.6(3)	1.5(3)	1.19	-1.86	IRAM
251.508709	6 _{1,5} -5 _{1,4}	p	47.5	47.4	0.029(9)	0.74(2)	6.0	0.41(8)	0.35(7)	0.41	-1.20	IRAM
251.527311	6 _{2,5} -5 _{1,4}	o	47.5	142.2	-0.005(4)	0.791(10)	6.4	1.1(2)	1.0(2)	0.81	0.15	IRAM
252.409837	8 _{1,7} -8 _{0,8} , 8 _{2,7} -8 _{1,8}	p/o	76.5	11.1	-0.05(6)	0.94(14)	5.3	0.051(12)	0.038(10)	3.41	1.22	IRAM
254.987652	5 _{3,3} -4 _{2,2}	p	41.1	26.8	0.048(8)	0.752(18)	5.6	0.36(7)	0.30(6)	-1.25	-1.04	IRAM
260.479746	5 _{3,2} -4 _{4,1}	o	44.7	25.8	0.00(11)	0.83(3)	6.8	0.32(6)	0.31(6)	0.62	0.68	IRAM
261.831811	3 _{3,1} -2 _{0,2}	p	19.0	1.4	0.02(3)	0.68(6)	18.4	0.30(6)	0.19(4)	-1.38	0.91	IRAM
265.759481	4 _{4,1} -3 _{3,0}	o	32.2	89.8	-0.076(5)	0.879(13)	8.2	1.4(3)	1.4(3)	-2.33	0.80	IRAM

Note. — The numbers in parentheses represent the errors in unit of the last significant digits.

^aObtained by a Gaussian fit.

^bThe residual divided by the intensity error, shown in Figure 4.4.

^cThe same as σ_{LTE} , but shown in Figure 4.5.

Table 4.2. Observed line parameters of $c\text{-CC}^{13}\text{CH}_2$ toward L1527

Frequency (GHz)	Transition	E_u (K)	$(S\mu^2)$ (Debye ²)	ΔV_{LSR}^a (km s^{-1})	Δv^a (km s^{-1})	rms (mK)	T_{mb}^a (K)	$\int T_{\text{mb}} dv$ (K km s^{-1})	σ_{LTE}^b	telescope
80.047537	20,2-11,1	6.3	27.8	-0.07(2)	1.25(5)	7.5	0.16(3)	0.23(5)	1.68	NRO
80.775347	31,2-30,3	15.7	21.0	0.19(16)	1.5(4)	6.4	0.021(6)	0.036(11)	0.29	NRO
83.474137	32,2-31,3	15.9	20.5	-0.00(16)	1.5(4)	6.8	0.022(7)	0.033(12)	0.35	NRO
84.185635	21,2-10,1	6.3	31.3	0.015(10)	1.18(2)	4.3	0.21(4)	0.28(6)	0.053	IRAM
114.897371	30,3-21,2	11.8	50.5	0.00(4)	0.90(6)	19.6	0.32(7)	0.30(6)	2.29	IRAM
115.524356	31,3-20,2	11.8	50.7	-0.00(6)	0.78(7)	22.3	0.31(7)	0.32(7)	0.80	NRO
140.432881	31,2-22,1	15.7	23.9	-0.13(3)	0.53(10)	7.3	0.15(4)	0.081(18)	-0.052	NRO
147.702239	22,0-11,1	9.6	13.9	-0.18(3)	0.65(5)	9.4	0.17(4)	0.10(2)	0.25	IRAM
148.114191	41,4-30,3	19.0	71.6	-0.161(18)	0.78(4)	6.9	0.18(4)	0.14(3)	-0.40	IRAM
153.894626	32,2-21,1	15.9	34.8	-0.10(2)	0.63(6)	9.2	0.16(4)	0.13(3)	-0.83	IRAM
212.457672	33,0-22,1	19.2	31.7	-0.02(5)	0.94(11)	7.3	0.081(18)	0.083(19)	-3.06	IRAM
213.843018	61,6-50,5, 60,6-51,5	37.9	113.5	0.02(3)	0.96(6)	4.4	0.088(18)	0.085(18)	0.66	IRAM
213.872779	51,4-42,3	34.8	70.7	0.06(5)	0.79(11)	4.4	0.045(10)	0.029(7)	0.11	IRAM
214.313034	52,4-41,3	34.8	70.8	-0.07(5)	0.82(11)	4.2	0.052(12)	0.060(13)	0.78	IRAM
225.435934	43,2-32,1	28.6	40.3	0.02(9)	1.00(2)	7.9	0.051(14)	0.044(14)	-0.027	IRAM
237.998109	32,1-21,2	17.8	5.1	-0.08(6)	0.71(14)	4.3	0.037(10)	0.019(6)	-0.53	IRAM
246.723236	71,7-60,6, 70,7-61,6	49.7	134.3	0.21(6)	0.70(14)	5.6	0.044(12)	0.040(10)	1.25	IRAM

Note. — The numbers in parentheses represent the errors in unit of the last significant digits.

^aObtained by a Gaussian fit.

^bResiduals of the LTE fit divided by the uncertainty of each line.

Table 4.3. Observed line parameters of $c\text{-}^{13}\text{CCCH}_2$ toward L1527

Frequency (GHz)	Transition	o/p	E_u (K)	$(S\mu^2)$ (Debye ²)	ΔV_{LSR}^a (km s ⁻¹)	Δv^a (km s ⁻¹)	rms (mK)	T_{mb}^a (K)	$\int T_{\text{mb}} dv$ (K km s ⁻¹)	σ_{LTE}^b	telescope
81.150881	$2_{0,2}-1_{1,1}$	p	6.3	31.0	0.10(18)	1.3(4)	5.5	0.016(5)	0.021(8)	0.84	NRO
					-0.00(3)	0.9(3)	4.1	0.018(6)	0.026(8)	1.17	IRAM
82.303747	$2_{1,2}-1_{0,1}$	o	6.3	96.2	-0.17(12)	1.1(3)	12.6	0.048(14)	0.049(16)	0.22	NRO
					-0.08(7)	0.83(8)	3.9	0.064(14)	0.060(13)	2.07	IRAM
114.381212	$3_{0,3}-2_{1,2}$	o	11.8	159.0	-0.15(11)	1.1(2)	14.8	0.08(2)	0.07(3)	0.30	NRO
145.353129	$3_{1,2}-2_{2,1}$	o	15.7	96.1	0.10(11)	0.6(2)	10.3	0.044(16)	0.033(13)	-0.80	IRAM
211.613800	$3_{3,0}-2_{2,1}$	o	18.9	75.0	0.02(7)	0.69(17)	4.9	0.033(10)	0.024(7)	-2.15	IRAM
212.387110	$6_{0,6}-5_{1,5}, 6_{1,6}-5_{0,5}$	p/o	37.6	117.2	0.18(9)	0.8(2)	6.5	0.039(12)	0.026(8)	0.39	IRAM
245.044421	$7_{1,7}-6_{0,6}, 7_{0,7}-6_{1,6}$	p/o	49.4	138.6	-0.04(10)	1.2(2)	4.8	0.029(8)	0.033(10)	2.72	IRAM

Note. — The numbers in parentheses represent the errors in unit of the last significant digits.

^aObtained by a Gaussian fit.

^bResiduals of the LTE fit divided by the uncertainty of each line.

Table 4.4. Number of detected lines.

Species	NRO 45 m		IRAM 30 m		Total
	3 mm	3 mm	2 mm	1.3 mm	
c-C ₃ H ₂	7 ^a	8	9	17	41
c-CC ¹³ CH ₂	6	2 ^b	4	7	19
c- ¹³ CCCH ₂	3	2 ^b	1	3	9

^aAll the transitions are also detected with IRAM 30 m.

^bAll the transitions are also detected with NRO 45 m.

Table 4.5. The observed ¹²C/¹³C ratios of c-C₃H₂.

Ratio	Observed ^a	Expected ^b
[c-C ₃ H ₂]/[c-CC ¹³ CH ₂]	61 ± 11	30–35
[c-C ₃ H ₂]/[c- ¹³ CCCH ₂]	310 ± 80	60–70
3[c-C ₃ H ₂]/([c-CC ¹³ CH ₂]+[c- ¹³ CCCH ₂])	150 ± 30	60–70
[c- ¹³ CCCH ₂]/[c-CC ¹³ CH ₂]	0.20 ± 0.05	0.5

Note. — The errors represent the standard deviation.

^aRatios directly derived from the column densities of c-C₃H₂, c-¹³CCCH₂, and c-CC¹³CH₂.

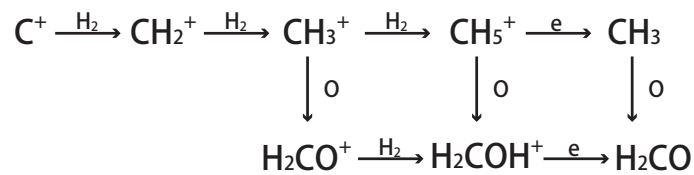
^bRatios expected for the condition that ¹³C is randomly distributed among the three carbon atoms and the elemental abundance ratio of ¹²C/¹³C is 60–70.

4.2. H₂CO

Formaldehyde (H₂CO) is an important parent species in interstellar production of complex organic molecules (COMs). In the gas phase, it is formed through a series of ion-molecule reactions starting from C⁺ (Figure 4.6a). It can also be formed on dust grains through hydrogenation of CO (Figure 4.6b). However, the relative contributions of these two mechanisms are still controversial. They would be different from source to source, and their characterization is of fundamental importance in understanding the production mechanism of COMs in each source. In this section, we investigate the formation mechanism of formaldehyde in low-mass star-forming regions by focusing on its ¹³C species.

As mentioned in Chapter 1, various carbon-chain molecules produced from C⁺ at low temperature show a ¹²C/¹³C ratio higher than the elemental ¹²C/¹³C ratio of 60–70 (dilution of ¹³C). On the other hand, the [¹²CO]/[¹³CO] ratio remains almost constant (60–70), because ¹³CO is the main reservoir of ¹³C. It is therefore expected that molecules formed directly from CO have the ¹²C/¹³C ratio of 60–70. Therefore, the molecular ¹²C/¹³C ratio can be used to explore the relative contribution of the gas-phase and the solid-phase productions of molecules. We apply this method to H₂CO in order to investigate its formation process. The main difficulty for determination of the ¹²C/¹³C ratio of formaldehyde is the high optical depth of the normal species lines. Hence, we observe the lines of H₂¹³CO and H₂C¹⁸O, which are optically thin. Since a significant anomaly of ¹⁶O/¹⁸O ratio is not known in dense molecular clouds, the use of H₂C¹⁸O for determination of the [H₂CO]/[H₂¹³CO] ratio under the fixed ¹⁶O/¹⁸O abundance is reasonable.

a) Gas phase reactions



b) Hydrogenation on grain surface

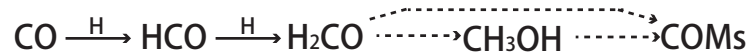


Figure 4.6: Possible formation pathways of formaldehyde

4.2.1. Observation

Although the spectral lines of H_2^{13}CO and $\text{H}_2\text{C}^{18}\text{O}$ at the 2-mm band ($J = 2-1$) are covered in the ASAI survey, the sensitivity of the survey is not good enough to detect the $\text{H}_2\text{C}^{18}\text{O}$ lines toward L1527. We therefore carried out the supplemental observation to improve the sensitivity. Additional observation with IRAM 30 m was conducted on January 2017, which only covered the spectral band at 2 mm to observe $J = 2-1$ lines of H_2^{13}CO and $\text{H}_2\text{C}^{18}\text{O}$. The frequency switching mode was employed, because the typical linewidth is much narrower ($\lesssim 1.0 \text{ km s}^{-1}$) than the period of the baseline ripples. The frontends were the broad-band EMIR receivers, and the back-ends were the FTS spectrometers in their 195 kHz resolution mode, which corresponds to the velocity resolution of 0.41 km s^{-1} at 140 GHz. The obtained data are concatenated with the ASAI data.

4.2.2. Results

The observed line parameters are summarized in Table 4.6. As shown in Figure 4.7, the $2_{12-1_{11}}$ and $2_{02-1_{01}}$ lines of H_2^{13}CO are clearly detected. The $2_{02-1_{01}}$ line of $\text{H}_2\text{C}^{18}\text{O}$ is tentatively detected with the S/N ratio lower than 3σ , while the $2_{12-1_{11}}$ line is clearly detected with the S/N ratio above 10σ . We evaluate the $[\text{H}_2^{13}\text{CO}]/[\text{H}_2\text{C}^{18}\text{O}]$ ratio by deriving the column densities under the assumption of the LTE condition. The excitation temperature is assumed to be 5–15 K. The column densities are derived by using only the $2_{12-1_{11}}$ line for both of the species, because the $2_{02-1_{01}}$ line of $\text{H}_2\text{C}^{18}\text{O}$ is detected with the S/N ratio lower than 3σ . The $[\text{H}_2^{13}\text{CO}]/[\text{H}_2\text{C}^{18}\text{O}]$ ratio is evaluated to be 9 ± 3 , yielding the $^{12}\text{C}/^{13}\text{C}$ ratio of 65 ± 19 under the assumption of the elemental $^{16}\text{O}/^{18}\text{O}$ ratio of 560 (Wilson & Rood 1994).

The derived $[\text{H}_2\text{CO}]/[\text{H}_2^{13}\text{CO}]$ ratio is close to the elemental $^{12}\text{C}/^{13}\text{C}$ ratio. This result likely indicates that formaldehyde inherits the $^{12}\text{C}/^{13}\text{C}$ ratio of CO. According to the interferometric observations discussed in Chapter 5.6, the emission of formaldehyde comes from innermost region near the protostar where the thermal desorption efficiently occurs. Maret *et al.* (2004) also revealed the significant contribution from the thermal desorption of formaldehyde in the vicinity of the protostar on the basis of their single-dish observations, although their observations cover a larger region which encompasses not only the warm region around the protostar but also the outer cold envelope. Hence, the $[\text{H}_2\text{CO}]/[\text{H}_2^{13}\text{CO}]$ ratio obtained in this study seems consistent with the picture of the formation of H_2CO via hydrogenation of CO on the dust grains. Note that this result does not completely deny the contribution from the gas-phase formation pathway. We can just say that the contribution from the grain surface

reactions would overwhelm that from the gas-phase reactions.

4.2.3. Observation toward the prestellar core L1544

Because the efficient thermal desorption from dust grain does not occur in low temperature conditions of prestellar cores, the gas-phase reactions may have a non-negligible contribution to the production of formaldehyde in comparison with the case of protostellar cores. With this in mind, we supplementarily observed the prototypical prestellar core, L1544, in Taurus, as a reference. The observation toward L1544 was conducted with IRAM 30 m at the same period as that for L1527. We observed the 2_{12} – 1_{11} line of H_2^{13}CO and $\text{H}_2\text{C}^{18}\text{O}$. The ^{13}C species was clearly detected, while the ^{18}O species was tentatively detected (Figure 4.8). The 3σ upper limit to the column density of $\text{H}_2\text{C}^{18}\text{O}$ is therefore derived on the assumption of the same line width as that of H_2^{13}CO (the FWHM line width of $\Delta v = 0.58 \text{ km s}^{-1}$). The lower limit to the $[\text{H}_2^{13}\text{CO}]/[\text{H}_2\text{C}^{18}\text{O}]$ ratio is evaluated to be 12, when the temperature is assumed to be 5–15 K. This ratio corresponds to the upper limit of the $^{12}\text{C}/^{13}\text{C}$ ratio of 50.

On the basis of the above result, it is likely that the dilution of ^{13}C species in formaldehyde does not occur in L1544. However, an apparent caveat is that the line of ^{18}O species is not clearly detected. Hence, further confirmation is needed. In L1544, the emission of CH_3OH , which is thought to be formed only on dust grains, has been detected (Vastel *et al.* 2014; Bizzocchi *et al.* 2014). The observed intensity of the CH_3OH emission is reasonable in view of the recent gas-grain chemical model considering nonthermal sublimation processes from dust grains (Vasyunin *et al.* 2017). Moreover, the recent mapping observations revealed that H_2CO follows the CH_3OH distribution in L1544 (Chac3n-Tanarro *et al.* 2018). These results indicate that formaldehyde is liberated from dust grains as well as methanol in L1544 by nonthermal processes (Section 1.2.1). Hence, the solid-phase formation by hydrogenation of CO may mainly

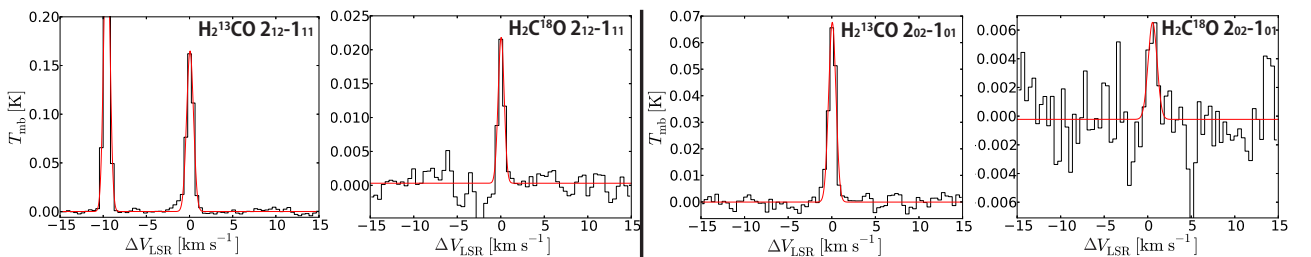


Figure 4.7: The observed spectral lines of the ^{13}C and ^{18}O species of H_2CO in L1527. ΔV_{LSR} denotes the velocity shift from the V_{LSR} of 5.85 km s^{-1} of L1527. The results of Gaussian fitting are also shown in red.

contribute to the derived $^{12}\text{C}/^{13}\text{C}$ ratio, resulting in the ratio close to the canonical value.

4.3. Concluding remarks on the carbon fractionation

In this thesis, we have determined the $^{12}\text{C}/^{13}\text{C}$ ratios of CO, CN, CCH, HC_3N , $c\text{-C}_3\text{H}_2$, and H_2CO on the basis of the extensive data of the line survey observation. We have found a significant dilution of the ^{13}C species for the carbon-chain related molecule $c\text{-C}_3\text{H}_2$. This further confirms that the ^{13}C anomaly is an important phenomenon in astrochemistry. Other carbon-chain molecules such as C_nH_m , C_nN , and C_nS are therefore expected to show the dilution of ^{13}C species in prestellar- and protostellar-cores, because they are mainly produced by the gas-phase reactions from C^+ . On the other hand, the $^{12}\text{C}/^{13}\text{C}$ ratio of H_2CO has been found to show a similar value to that of CO, indicating that it is mainly produced on dust grains through the hydrogenation reactions of CO. Thus, COMs such as HCOOH , HCOOCH_3 , and CH_3OCH_3 , which are thought to be produced similarly, are expected to have similar ratios to that of CO.

On the other hand, it remains unclear whether the ^{13}C dilution of carbon-chain species can be used as the tracer for the chemical evolution. For CCH and HC_3N , the $^{12}\text{C}/^{13}\text{C}$ ratios have been examined in several prestellar cores. The lower limits of the $[\text{C}^{13}\text{CCH}]/[\text{CCH}]$ and $[\text{C}^{13}\text{CH}]/[\text{CCH}]$ ratio are derived to be 250 and 170, respectively, in TMC-1 (CP) (Sakai *et al.* 2010b). The $^{12}\text{C}/^{13}\text{C}$ ratios of HC_3N are derived in three prestellar cores, L1521B, L134N, and TMC-1 (Takano *et al.* 1998; Taniguchi, Ozeki, & Saito 2017). The averaged $^{12}\text{C}/^{13}\text{C}$ ratios over the three ^{13}C isotopologues of HC_3N are evaluated to be 95 ± 8 , 67 ± 10 , and 70 ± 5 in L1521B, L134N, and TMC-1, respectively. The derived $^{12}\text{C}/^{13}\text{C}$ ratios in these prestellar cores are comparable to or even lower than the $^{12}\text{C}/^{13}\text{C}$ ratios in L1527. This indicates that the

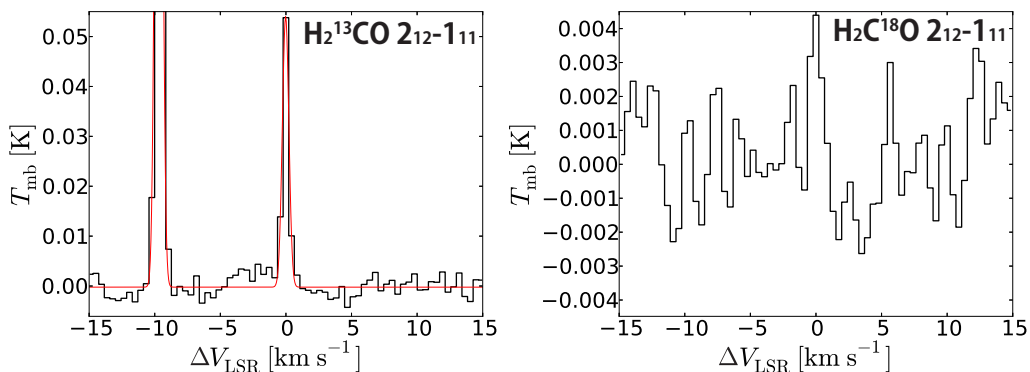


Figure 4.8: The observed spectral lines of the ^{13}C and ^{18}O species of H_2CO in L1544. ΔV_{LSR} denotes the velocity shift from the V_{LSR} of 7.2 km s^{-1} of L1544. The results of Gaussian fitting are also shown in red.

evolutionary trend from prestellar cores to protostellar cores is not seen. However, the number of sources studied is still small, and hence, more extensive observations toward other sources are needed to examine the evolutionary trend in a statistical way.

It should be noted that determination of the $^{12}\text{C}/^{13}\text{C}$ ratio requires accurate determination of the column density of the normal species. This was indeed possible by conducting line survey observations in the present study, where a large number of lines were used to conduct a fine analysis. However, such an analysis is not always possible for a statistical study. On the other hand, the anomaly in the $^{12}\text{C}/^{13}\text{C}$ ratio among different carbon atoms in a single molecule can be studied only by observations of the ^{13}C species, which usually emit optically thin lines. Once the cause of the $^{12}\text{C}/^{13}\text{C}$ anomaly in a single molecule is established by more observational studies, it could be a new tracer to understand chemical processes and physical conditions of molecular clouds.

Table 4.6. List of observed lines in L1527

Species	Transition	Frequency (GHz)	E_u (K)	$S\mu^2$ (D ²)	ΔV_{LSR}^a (km s ⁻¹)	T_{mb} (K)	Δv (km s ⁻¹)	$\int T_{\text{mb}} dv$ (K km s ⁻¹)	rms (mK)
H ₂ ¹³ CO	2 ₁₂ -1 ₁₁	137.4499503	21.7	24.5	0.061(9)	0.165(3)	0.94(2)	0.173(2)	2.0
H ₂ ¹³ CO	2 ₀₂ -1 ₀₁	141.9837404	10.2	10.9	0.059(15)	0.068(2)	0.99(4)	0.0702(13)	2.1
H ₂ C ¹⁸ O	2 ₁₂ -1 ₁₁	134.4359203	21.5	24.5	0.047(4)	0.0215(19)	0.81(8)	0.0174(13)	1.6
H ₂ C ¹⁸ O	2 ₀₂ -1 ₀₁	138.7708610	10.0	10.9	0.56(17)	0.0068(19)	1.2(4)	0.0083(17)	2.4

Note. — The numbers in parentheses represent the errors in units of the last significant digits.

^aVelocity shift from the V_{LSR} of 5.85 km s⁻¹

CHAPTER 5

MAPPING OBSERVATION OF DEUTERATED SPECIES WITH ALMA

5.1. Introduction

The deuterium fractionation is known to proceed in dense and cold conditions during the prestellar-core phase (e.g., Hirota, Ikeda & Yamamoto 2001; Bacmann *et al.* 2003; Crapsi *et al.* 2005; Parise *et al.* 2006; Hirota *et al.* 2011). It is expected to decrease after the onset of star formation, when the central protostar starts to heat the parent core (e.g., Emprechtinger *et al.* 2009; Friesen *et al.* 2013; Imai *et al.* 2018). Although this temporal variation of the deuterium fractionation has extensively been examined by observations toward prestellar- and protostellar-cores, most of the previous studies are conducted by single-dish telescopes. In these observations, small-scale structures in protostellar cores associated with star formation are not resolved, and hence, the obtained deuterium fractionation is one averaged over a few 1000-au-scale area. A limited angular resolution in single-dish observations thus hinders the study of the evolution of deuterium fractionation from the parent core to the disk-forming region around the protostar. However, such high-resolution and high-sensitivity observations of deuterated species are now feasible thanks to the Atacama Large Millimeter/submillimeter Array (ALMA).

Murillo *et al.* (2015) observed the DCO⁺ ($J = 3-2$) line with ALMA toward the low-mass star-forming region harboring the Class 0 protostar, VLA1623. They found that the distribution of the DCO⁺ emission has a ring structure with a 1000-au scale which probably traces the disk-envelope interface. Although the distribution of DCO⁺ is revealed in their work, the spatial variation of the deuterium fractionation is not investigated. Persson *et al.* (2018) recently conducted the observations of formaldehyde (H₂CO) and its minor isotopologues including D, ¹³C, ¹⁸O, and ¹⁷O toward the Class 0 protostellar binary IRAS 16293-2422. They only focus on the deuterium fractionation in the closest vicinity of the protostar, where H₂CO efficiently sublimates from dust grains due to protostellar heating. Therefore, it is still unclear how the deuterium fractionation evolves from the outer cold envelope at a few 1000-au scale to the disk-forming region around the protostar at a 100-au scale. This is of particular importance in exploring the origin of the deuterium fractionation found in small Solar-System bodies

(Ceccarelli *et al.* 2014).

In this Chapter, we tackle this problem through observations of H₂CO and CCH and their deuterated species toward the low-mass protostellar source L1527, which is a prototypical warm carbon-chain chemistry (WCCC) source (Section 1.2.2 and Chapter 3). H₂CO is a fundamental organic molecule, which is ubiquitously found in various interstellar sources. It is thought to be formed by hydrogenation reactions of CO on dust grains as well as gas-phase reactions (e.g., Taquet, Ceccarelli, & Kahane 2012; Soma *et al.* 2018). Parise *et al.* (2006) reported that the [HDCO]/[H₂CO] ratio is extraordinarily high in L1527 (1.7) in comparison with other Class 0 sources, while Roberts & Millar (2007) reported a similar ratio to others (0.06). These results are based on the single-dish observations, and hence, the high-resolution observations with ALMA will be able to resolve this contradiction. On the other hand, CCH is one of the fundamental carbon-chain molecules. It is proposed to be enhanced in the WCCC sources through evaporation of CH₄ in a lukewarm region around the protostar and subsequent chemical reactions in the gas phase. Since CCH is characteristic to the WCCC source, we also study this species in addition to H₂CO.

In order to delineate the spatial variation of the deuterium fractionation from a few 1000-au scale to a 100-au scale, we employ the Atacama Compact Array (ACA) of ALMA in combination with the main array to fill the short spacing data. By including the ACA data, we will be able to achieve a maximum recoverable size of around 20'', which corresponds to a linear scale of around 3000 au. High sensitivity of ALMA will allow us to detect the weak emissions of deuterated species with an S/N ratio high enough for the purpose of this study.

5.2. Observation

The L1527 data analyzed here were observed during several Cycles of ALMA. Details of the ALMA observations are summarized in Table 5.1. The field center is $(\alpha_{2000}, \delta_{2000}) = (04^{\text{h}}39^{\text{m}}53^{\text{s}}.89, 26^{\circ}03'9''.8)$. We observed the H₂CO ($5_{15}-4_{14}$), D₂CO ($4_{04}-3_{03}$ and $4_{23}-3_{22}$), CCH ($N = 3-2$), and CCD ($N = 3-2$) lines with the 12-m array and ACA, as well as the HDCO ($4_{13}-3_{12}$) and H₂CO ($5_{05}-4_{04}$) lines only with ACA. Parameters of the observed line emissions are summarized in Table 5.2. The native frequency resolution is 122 kHz for the observation of CCH and H₂CO with the 12-m array, which correspond to 0.15 km s⁻¹ and 0.10 km s⁻¹, respectively, while it is 61 kHz for the other observations. The velocity channels are rebinned to the resolution with 0.15 km s⁻¹ and 0.085 km s⁻¹, for the 12-m data and the ACA data, respectively, to compare the data observed with the different velocity resolutions.

The uncertainty of the absolute flux calibration is 10%. A structure extended over $19''$ or larger is subject to the resolving-out effect according to (ALMA Partnership *et al.* 2016, See Section 2.2.2). This is derived from the minimum baseline (8.8 m) of the ACA Band 7 observation, whose maximum recoverable scale is smallest in all the ACA observations that we conducted. The data were imaged and CLEANed with Common Astronomy Software Applications (CASA), by using Briggs weighting with a robustness parameter of 0.5 (Section 2.2.2). Self-calibration is not applied for simplicity. The primary beam correction is done for all the images.

5.3. H₂CO

5.3.1. Distributions

Figures 5.1 (a)–(d) show the integrated intensity maps of the H₂CO ($5_{15}-4_{14}$), D₂CO ($4_{04}-3_{03}$ and $4_{23}-3_{22}$) and HDCO ($4_{13}-3_{12}$) lines observed with ACA. Although the spatial resolution of the H₂CO line ($5''.19 \times 3''.21$ with the position angle (P.A.) of 57°) is better than other species due to the difference in observing frequencies, the image of the H₂CO line is smoothed to the similar resolution to those of the deuterated species ($(6''.6 \times 5''.5)$, P.A. = -76°) for a fair comparison. The H₂CO line emission is peaked at the protostar position, and is concentrated in the vicinity of the protostar ($r \sim 5''$). In contrast, the D₂CO and HDCO line emissions have rather extended distributions ($\sim 10''$), where peak positions are shifted from the protostar position. Figures 5.1 (e)–(f) shows the position-velocity (PV) diagrams of the three species along the disk/envelope direction (P.A. = 180°). The H₂CO line shows a high velocity component of $\sim 1-2 \text{ km s}^{-1}$ shifted from the systemic velocity (5.8 km s^{-1}), whereas the deuterated species does not.

In order to delineate the different spatial distributions between the normal and deuterated species in detail, we combined the 12-m array data to the ACA data. Figure 5.2 shows the integrated intensity maps and the PV diagrams along the envelope direction for the H₂CO ($5_{15}-4_{14}$) and D₂CO ($4_{04}-3_{03}$ and $4_{23}-3_{22}$) lines. Although the H₂CO ($5_{15}-4_{14}$) line and the D₂CO ($4_{04}-3_{03}$) line have better spatial resolutions ($\sim 0''.9$) than that of the D₂CO ($4_{23}-3_{22}$) line, the outer taper of $1''.1$ is applied for imaging the above two lines so as to have the similar spatial resolution to that of the D₂CO ($4_{23}-3_{22}$) line. The difference between the normal and deuterated species is clearly seen in the combined images. It is further confirmed that the distribution of the normal species is concentrated around the protostar, while that of the deuterated species extends over $\sim 10''$. In the PV diagram, the H₂CO emission shows a spin-up feature to the

Table 5.1. Properties of the ALMA observations.

Obs. ID	Date (UTC)	Band	Array	Baseline (m)	Num. of antennas	T_{sys} (K)	Calibrator		$\theta_{\text{PB}}^{\text{a}}$ (arcsec)	
							Flux	Phase		
2011.0.00604.S	2012 Aug. 10, 26	6	12-m	18.0-381	22-24	70-120	J0432-013	Callisto	J0510+1800	23
2011.0.00604.S	2012 Aug. 29	7	12-m	12.1-314	26	100-200	J0432-013	Callisto	J0510+1800	17
2012.1.00647.S	2014 Jul. 20	6	12-m	17.4-648	35	70-170	J0510+1800	J0432-013, J0510+1800	J0510+1800	26
2013.1.01331.S	2015 Jan. 2	6	12-m	19.8-245	38	70-120	J0423-0120	Uranus	J0510+1800	26
2016.2.00117.S	2017 Aug. 31, Sep. 1, 2, 15, 16, 17	6	7-m	7.0-42.4	10-12	50-170	J0510+1800	Uranus, J0522-3627	J0510+1800	45
2016.2.00117.S	2017 Aug. 3, 16	7	7-m	8.8-33.4	9	100-330	J0522-3627	Uranus, J0522-3627	J0438+3004	29
2017.1.01375.S	2018 May 3	6	7-m	8.5-38.4	12	60-90	J0522-3627	J0522-3627	J0510+1800	42

^aThe primary beam size (half-power beam width)

Table 5.2. List of observed lines.

Species	Transition	Frequency (GHz)	E_u (K)	$S\mu^2$ (D^2)	Synthesized beam ^a	
					7 m-array	Combined ^b
H ₂ CO	5 ₁₅ -4 ₁₄	351.768645	62.5	26.1	5''.19 × 3''.21 (56°.7) ^c	1''.19 × 1''.10 (-10°.9)
H ₂ CO	5 ₀₅ -4 ₀₄	362.736048	52.3	27.2	5''.45 × 3''.15 (61°.8) ^c	-
HDCO	4 ₁₃ -3 ₁₂	246.9246	37.6	37.6	6''.20 × 5''.27 (-76°.6)	-
D ₂ CO	4 ₀₄ -3 ₀₃	231.410234	27.9	21.7	6''.61 × 5''.61 (-75°.4)	1''.29 × 1''.23, (-12°.7)
D ₂ CO	4 ₂₃ -3 ₂₂	233.650441	49.6	16.3	6''.53 × 5''.57 (-76°.5)	1''.68 × 1''.30 (-60°.1)
CCH	$N = 3-2, J = 5/2-3/2, F = 3-2$	262.064986	25.2	1.63	6''.79 × 4''.95 (-59°.2) ^d	1''.23 × 1''.11 (-47°.3)
CCH	$N = 3-2, J = 5/2-3/2, F = 2-1$	262.067469	25.2	1.07	6''.79 × 4''.95 (-59°.2) ^d	1''.23 × 1''.11 (-47°.3)
CCH	$N = 3-2, J = 5/2-3/2, F = 2-2$	262.0789347	25.2	0.14	6''.79 × 4''.95 (-59°.2) ^d	1''.23 × 1''.11 (-47°.3)
CCD	$N = 3-2, J = 7/2-5/2, F = 9/2-7/2$	216.37283	20.8	2.54	7''.42 × 6''.52 (-44°.1)	1''.67 × 1''.22 (63°.0)
CCD	$N = 3-2, J = 7/2-5/2, F = 7/2-5/2$ and $5/2-3/2$	216.37332	20.8	3.24	7''.42 × 6''.52 (-44°.1)	1''.67 × 1''.22 (63°.0)
CCD	$N = 3-2, J = 5/2-3/2, F = 7/2-5/2$ and $5/2-3/2$	216.42832	20.8	3.07	7''.44 × 6''.58 (-35°.9)	1''.67 × 1''.22 (63°.1)
CCD	$N = 3-2, J = 5/2-3/2, F = 3/2-1/2$	216.42876	20.8	0.71	7''.44 × 6''.58 (-35°.9)	1''.67 × 1''.22 (63°.1)

^aThe numbers in parentheses are the position angle.

^bThe 12-m array and ACA array data are combined.

^cOriginal resolution. It is smoothed to 6''.60 × 5''.50 (-75°.0) in the analysis.

^dOriginal resolution. It is smoothed to 7''.40 × 6''.60 (-40°.0) in the analysis.

protostar along the envelope direction at a $2''$ scale. Namely, the southern and northern sides of the protostar are blueshifted and redshifted, respectively. The maximum velocity shift from the systemic velocity is as high as about 2 km s^{-1} , as also seen in the ACA data. In addition, a weak feature of the counter velocity component (the redshifted component on the southern side and the blueshifted one on the northern side) can be seen (Figure 5.2). This feature suggests that H_2CO resides in the infalling-rotating envelope, as already reported with the same 12-m array data (Sakai *et al.* 2014a; Oya *et al.* 2015). On the other hand, the D_2CO emission does not show such a spin-up feature to the protostar. The maximum velocity shift from the systemic velocity is as low as about 0.5 km s^{-1} . This indicates that the deuterated species is deficient in the infalling-rotating envelope where the normal species is abundant.

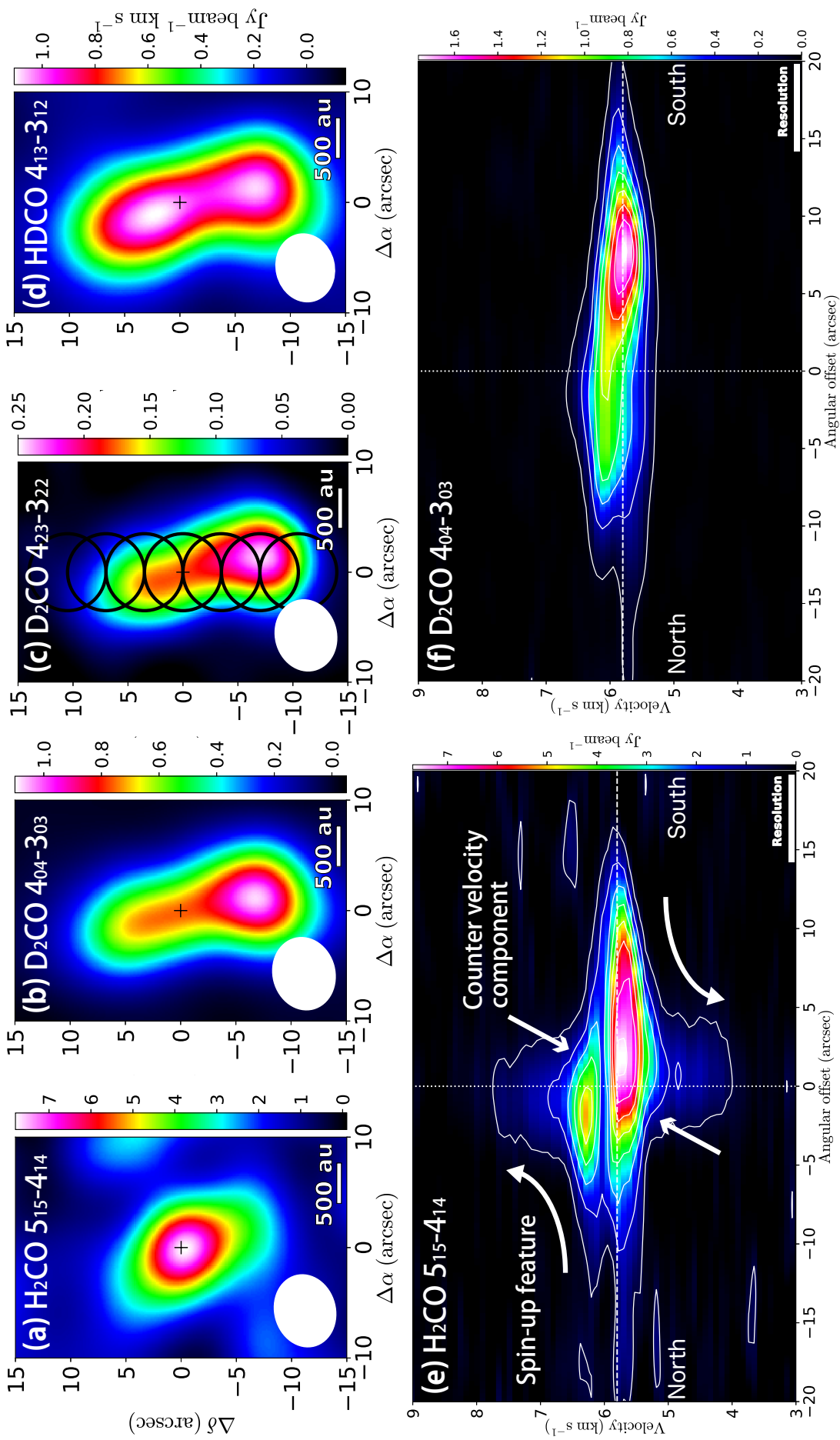


Figure 5.1: (a–d) The integrated intensity maps of the H_2CO , D_2CO , and HDCO lines obtained with ACA. The spatial resolution of the H_2CO line is smoothed to the similar resolution to those of the deuterated species for a fair comparison. The cross marks show the protostar position. The white circles show the synthesized beam size. The sampling areas (the black circles) for deriving the column density and temperature of D_2CO are superposed on the integrated intensity map of the $\text{D}_2\text{CO } 4_{23-3_{22}}$ line (c). (e–f) The PV diagrams of the $\text{H}_2\text{CO } (5_{15-4_{14}})$ and $\text{D}_2\text{CO } (4_{04-3_{03}})$ line along the envelope direction (P.A. = 180°). The white horizontal and vertical lines show the systemic velocity (5.8 km s^{-1}) and the protostar position, respectively. The lowest contour levels are at 10σ and 20σ for H_2CO and D_2CO , where $\sigma = 50$ and 6 mJy beam^{-1} , respectively.

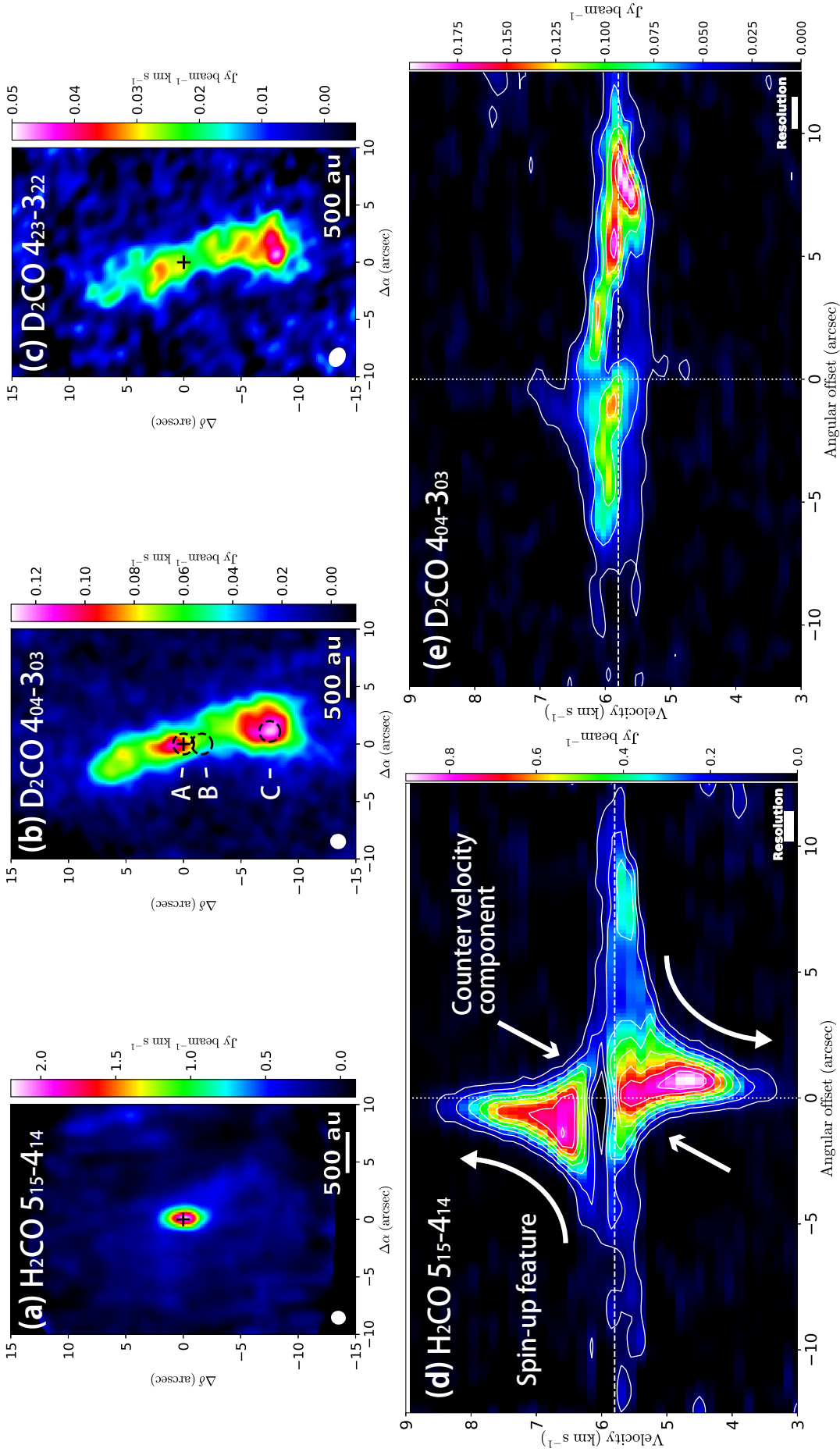


Figure 5.2: (a–c) The integrated intensity maps of the H_2CO and D_2CO lines, where the 12-m array data and the ACA data are combined. The cross marks show the protostar position. The white circles show the synthesized beam size. (d–e) The PV diagrams of the H_2CO ($5_{15}-4_{14}$) and D_2CO ($4_{04}-3_{03}$) line along the envelope direction (P.A. = 180°). The white horizontal and vertical lines show the systemic velocity (5.8 km s^{-1}) and the protostar position, respectively. The lowest contour levels are at 10σ and 3σ , and the level intervals are 10σ and 6σ for H_2CO and D_2CO , where $\sigma = 10$ and 6 mJy beam^{-1} , respectively.

5.3.2. Column density and temperature of D_2CO

To quantitatively reveal the radial dependence of the deuterium fractionation along the envelope direction, we here derive the column density of D_2CO and the gas kinetic temperature from the two D_2CO lines observed with ACA. The radiative transition between different K levels of D_2CO is very weak due to symmetry, and hence, the relative populations between the $K = 0$ and $K = 2$ levels are considered to be almost thermalized to the gas kinetic temperature. We prepare the spectrum for each circular area along the envelope direction (Figure 5.1 c), as shown in Figure 5.3. The diameter of the sampled areas ($7''.0$; ~ 1000 au) is comparable to the major axis of the synthesized beam of the ACA observations ($6''.6$), and the center is every $3''.5$ from the protostar position. The column densities and kinetic temperatures are derived from the integrated intensities of the two lines under the local-thermodynamical equilibrium (LTE) condition. The derived column densities and temperatures are shown in Figure 5.4. Here, the total (ortho and para) column density is shown, where the ortho-to-para ratio is assumed to be the statistical value of 2. The column density is the highest at the position $7''.0$ south to the protostar ($(2.3 \pm 0.2) \times 10^{12} \text{ cm}^{-2}$), where the integrated intensities are the highest of the seven areas. The gas kinetic temperature is the highest at the protostar position (20 ± 3 K), although it is almost constant throughout the envelope (17–20 K). The temperature at the protostar position is slightly lower than that of $c\text{-C}_3\text{H}_2$ averaged over the $1'' \times 1''$ region at the protostar (23–33 K) and significantly lower than that of SO averaged over the $1'' \times 2''$ region at the protostar (> 60 K) reported by Sakai *et al.* (2014b). This comparison suggests that the D_2CO lines mainly trace the outer cold envelope. The derived temperature is comparable to or lower than the desorption temperature of CO, and hence, the deuterium fractionation can be efficiently proceeded there.

Note that the D_2CO line emissions may suffer from an absorption by a foreground gas in the north part to the protostar, because the line profile shows a double-peak feature. The column density and temperature may therefore have large uncertainties at the north positions. In the following section, we discuss the D/H ratios in the southern side of the envelope.

5.3.3. D/H ratios obtained with the ACA data

Assuming the temperature of D_2CO derived from the ACA data, we first evaluate the D/H ratios in the southern envelope. Figure 5.5 shows the line profiles at the selected positions in the southern envelope. The top left panel and the bottom left panel show the spectra of the ACA data extracted from a circular region ($r = 3''.5$; ~ 500 au) centered at the protostar

position and the position where the integrated intensity of the D_2CO $4_{04}-3_{03}$ line is the highest, respectively. The characteristics of the spectra of H_2CO , HDCO , and D_2CO obtained with ACA are summarized as follows. The H_2CO and HDCO lines have absorption dips around the systemic velocity at the protostar position. The high velocity component ($\Delta v \sim 1-2 \text{ km s}^{-1}$) can be seen in the H_2CO emission. The HDCO line also has the high velocity-shift component near the protostar position, although it is weak compared to that of the normal species. Even in the position about 1000 au apart from the protostar, the peak velocities of the H_2CO and HDCO lines are slightly blueshifted from those of D_2CO , and hence, they may also be weakly affected by the self-absorption. Note that the H_2CO $5_{15}-4_{14}$ line is likely optically thin even in the outer cold envelope, because the line of para species ($5_{05}-4_{04}$) is detected with an intensity which is consistent with the statistical ortho-to-para ratio of 3. As an example, the spectra of the ortho and para lines at 1000 au south to the protostar ($(\Delta\alpha, \Delta\delta) = (0'', -7''.0)$) are shown in Figure 5.6.

We derive the D/H ratios at the protostar position, the D_2CO peak position, and the three positions south to the protostar with a separation of $3''.5$: $(\Delta\alpha, \Delta\delta) = (0'', 0'')$, $(1''.1, -6''.8)$, $(0'', -3''.5)$, $(0'', -7''.0)$, and $(0'', -10''.5)$. The spectra along the envelope are shown in Figure 5.7 (b). The integrated intensity in the blueshifted side from the systemic velocity ($5.0-5.6 \text{ km s}^{-1}$) is used, in order to avoid the effect of the absorption from the foreground gas and the high velocity component. We assume the LTE condition and the statistical ortho-to-para ratios of 3 and 2 for H_2CO and D_2CO , respectively. The temperature is assumed to be the same as that of D_2CO , which is derived from the total integrated intensities of the $K = 0$ and 2 lines. The derived abundance ratios are summarized in Table 5.3. The $[\text{D}_2\text{CO}]/[\text{HDCO}]$ ratio is almost constant throughout the envelope, while the $[\text{HDCO}]/[\text{H}_2\text{CO}]$ ratio decreases with decreasing distance from the protostar.

The gas kinetic temperature and the rotational temperature are not always the same: the former one is generally higher than the latter, because the radiation process contributes to decreasing the populations in the upper-state level. If we assume the rotational temperature as low as 10 K, the $[\text{HDCO}]/[\text{H}_2\text{CO}]$ ratios become about a half of that derived by assuming 20 K, probably because the transition used to evaluate the column density for the normal species has a higher upper state energy than those of the deuterated species. Nevertheless, we can conclude the decreasing trend of the deuterium fractionation along the envelope, even if the rotational temperature in the outer envelope ($> 1000 \text{ au}$) is as low as 10 K and that in the protostar position is 20 K.

We also derive the $[\text{HDCO}]/[\text{H}_2\text{CO}]$ ratio by using the high velocity component (2.0–5.0 km s^{-1}) at the protostar position and the $3''.5$ south position. The $[\text{HDCO}]/[\text{H}_2\text{CO}]$ ratio at the protostar position and the $3''.5$ south position are derived to be 0.13–0.23 and 0.08–0.13, respectively, where the rotational temperature is assumed to be 20–40 K. These values are lower than those derived for the 5.0–5.6 km s^{-1} components at all the positions (> 0.37).

5.3.4. D/H ratios with the combined data

The ACA observation does not fully resolve the distributions of H_2CO and D_2CO . In order to evaluate the D/H ratios at the intensity peak position of D_2CO and the protostar position, we also analyze the combined image of the 12-m array and ACA (Figure 5.2). We here focus on three positions: the protostar position which traces the disk component ($(\Delta\alpha, \Delta\delta) = (0'', 0'')$; position A in Figure 5.2 b), the infalling-rotating envelope (IRE) about 220 au south to the protostar ($(\Delta\alpha, \Delta\delta) = (0'', -1''.6)$; position B), and the southern peak where the integrated intensity of the $\text{D}_2\text{CO } 4_{04}\text{-}3_{03}$ line is the highest ($(\Delta\alpha, \Delta\delta) = (1''.1, -7''.5)$; position C). These regions are indicated in Figure 5.2 b in dashed circles. Although the integrated intensity of the $\text{D}_2\text{CO } 4_{04}\text{-}3_{03}$ line is also strong near the position $0''\text{-}3''$ north to the protostar, we exclude this position because the line profile of the D_2CO line shows a double-peak feature due to the absorption by a foreground gas.

The spectra are shown in Figure 5.5. They are prepared for the circular region with a radius comparable to the major axis of the synthesized beam ($0''.9$; ~ 125 au). The integrated intensities of the disk and IRE components (positions A and B, respectively) are evaluated for the velocity ranges of 2.0–4.0 km s^{-1} and 4.0–5.0 km s^{-1} , respectively, which are set to exclude the contamination from the other components: the velocity shifts of > 1.8 km s^{-1} and 0.8–1.8 km s^{-1} roughly correspond to $r < 100$ au and $r \sim 100\text{--}300$ au, respectively (Sakai *et al.* 2014b). Because the D_2CO emissions are not detected in these velocity ranges, the column densities of D_2CO are derived from the 3σ upper limits of the $4_{04}\text{-}3_{03}$ line spectrum:

$$\int T dv < 3\sigma(1 + \epsilon)\sqrt{v_{\text{ch}}\Delta v}, \quad (5.1)$$

where σ is the rms noise, ϵ the calibration uncertainty (0.1), v_{ch} the spectral resolution, and Δv the velocity width used for the evaluation of the integrated intensity. The assumed rotational temperature ranges are 30–90 K and 30–50 K for the disk and IRE components, respectively (Sakai *et al.* 2014a). In the D_2CO peak position, the emission lines of H_2CO and D_2CO are peaked almost on the same velocity, as shown in Figure 5.5, and hence, the total column

densities are derived from the total integrated intensities. The column density of D₂CO and the gas kinetic temperature are derived to be $(7.5 \pm 0.8) \times 10^{12} \text{ cm}^{-2}$ and $19 \pm 3 \text{ K}$, respectively. The column density of H₂CO is derived under the assumption of the same temperature as D₂CO. The derived [D₂CO]/[H₂CO] ratios and the D/H ratios (i.e., the square root of [D₂CO]/[H₂CO]) in the three positions are summarized in Table 5.4.

The derived [D₂CO]/[H₂CO] ratio is as high as 0.8 in the D₂CO peak (position C), while it is lower than 0.03–0.04 in the IRE (position B). Hence, the decrease of the deuterium fractionation along the envelope is further confirmed in the combined data. The upper limit of [D₂CO]/[H₂CO] ratio for the disk component (position A) is higher than that in the IRE, mainly because integrated intensity of the normal species in the disk ($V_{\text{LSR}} = 2.0\text{--}4.0 \text{ km s}^{-1}$) is weaker than that in the IRE ($V_{\text{LSR}} = 4.0\text{--}5.0 \text{ km s}^{-1}$).

5.4. CCH

5.4.1. Distributions

Figure 5.8 shows the integrated intensity maps of the two hyperfine components of the CCH and CCD ($N = 3\text{--}2$) lines observed with ACA. Although the original spatial resolution of the CCH lines ($6''.8 \times 5''.0$, P.A. = -59°) is better than that of the CCD lines, the images of CCH are smoothed to have the similar resolution to that of the deuterated species ($(7''.4 \times 6''.6)$, P.A. = -40°) for a fair comparison. The distributions of the two hyperfine component lines of CCH shown in Figure 5.8 look different from each other probably due to the poor S/N. The stronger hyperfine component ($F = 3\text{--}2$ and $2\text{--}1$) is centrally peaked, while the weaker one ($F = 2\text{--}2$) shows a rather elongated distribution along the envelope direction. The distributions of the two CCD lines are similar to those of the HDCO and D₂CO: the peaks are $\sim 10''$ south to the protostar.

Figure 5.9 shows the integrated intensity maps, where the 12-m array data are combined with the ACA data. The stronger hyperfine component shows a double-peak feature in the vicinity of the protostar (500 au). This component traces the infalling-rotating envelope, because the PV diagram along the envelope direction (Figure 5.10) shows the high velocity component and the counter velocity component as in the case of H₂CO. On the other hand, the double-peak feature is marginally seen in the weak hyperfine component of CCH (Figure 5.9 b). The CCD emissions are strong in the south-western and south-eastern parts of the protostar. The emissions in the south-western and south-eastern parts are also seen in the CCH lines, especially in the south-west side. These spatial components coincide with that of C¹⁸O ($J = 2\text{--}1$) line in

Table 5.3. Abundance ratios of H₂CO and CCH obtained with the ACA data.

$(\Delta\alpha, \Delta\delta)$	[D ₂ CO]/[HDCO]	[HDCO]/[H ₂ CO]	[D ₂ CO]/[H ₂ CO]	[CCD]/[CCH]
(0'', 0'')	0.20(3)	0.37(5)	0.076(10)	0.038(7)
(0'', -3''.5)	0.23(3)	0.37(5)	0.086(10)	0.036(6)
(0'', -7''.0)	0.25(3)	0.68(10)	0.168(19)	0.072(11) ^b
(0'', -10''.5)	0.23(3)	1.4(2)	0.34(6)	0.099(18) ^b
(1''.1, -6''.8) ^a	0.25(3)	0.66(9)	0.163(18)	0.070(10) ^b

Note. — The numbers in parentheses represent the errors in units of the last significant digits. The integrated intensity with the velocity between 5.0–5.6 km s⁻¹ is used, unless otherwise stated.

^aThe integrated intensity of the D₂CO 4₀₄–3₀₃ is the highest.

^bThe total integrated intensity is used.

Table 5.4. D/H ratios obtained with the combined data.

Region	Disk	IRE	D ₂ CO peak
Position	(0'', 0'')	(0'', -1''.6)	(1''.1, -7''.5)
Velocity range (km s ⁻¹)	2.0–4.0	4.0–5.0	4.5–7.1
Temperature (K)	30–90	30–50	19.3 ^a
[D ₂ CO]/[H ₂ CO]	< 0.14 – < 0.30	< 0.03 – < 0.04	0.81(12)
$\sqrt{[\text{D}_2\text{CO}]/[\text{H}_2\text{CO}]}$	< 0.37 – < 0.55	< 0.16 – < 0.20	0.90(7)
[CCD]/[CCH]	—	< 0.016	> 0.32

^aDerived from the D₂CO lines

the ALMA archival data (Figure 1.7 B; Ohashi *et al.* 2014), indicating that they originate from the cavity wall of outflow, where the UV radiation would enhance the production of CCH.

The PV diagram of CCD along the envelope direction (Figure 5.10 b) does not show the emission from high velocity component, suggesting that CCD is deficient in the infalling-rotating envelope, as in the case of D₂CO.

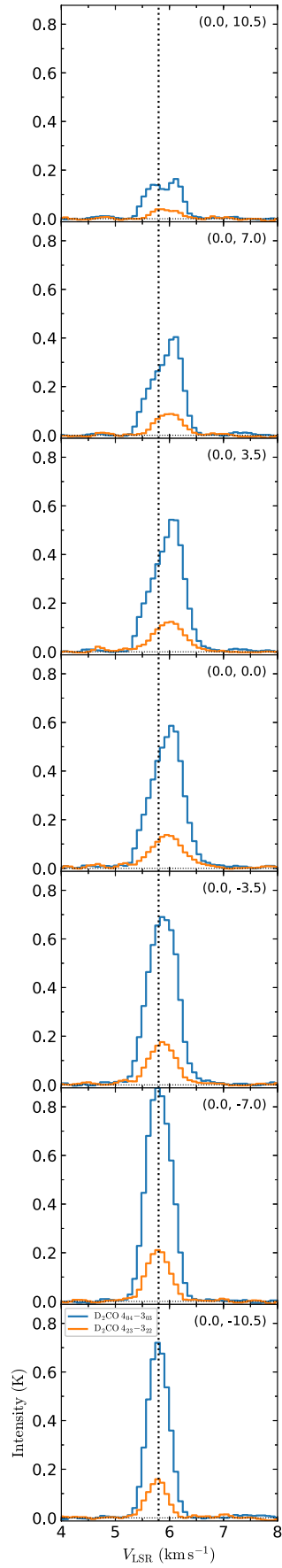


Figure 5.3: The spectra of the D_2CO $4_{04}-3_{03}$ and $4_{23}-3_{22}$ lines along the envelope, which are used for the derivation of the column density and the kinetic temperature. The each position is indicated in Figure 5.1 (c). The numbers in parentheses denote the relative coordinates to the protostar in arcsec.

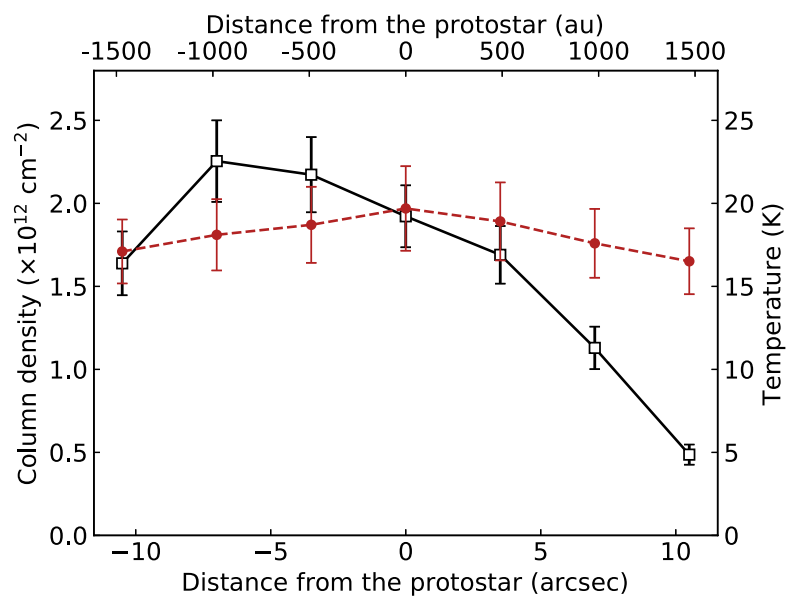


Figure 5.4: The column density of D_2CO and the gas kinetic temperature along the envelope, shown with the square mark and the circular mark, respectively.

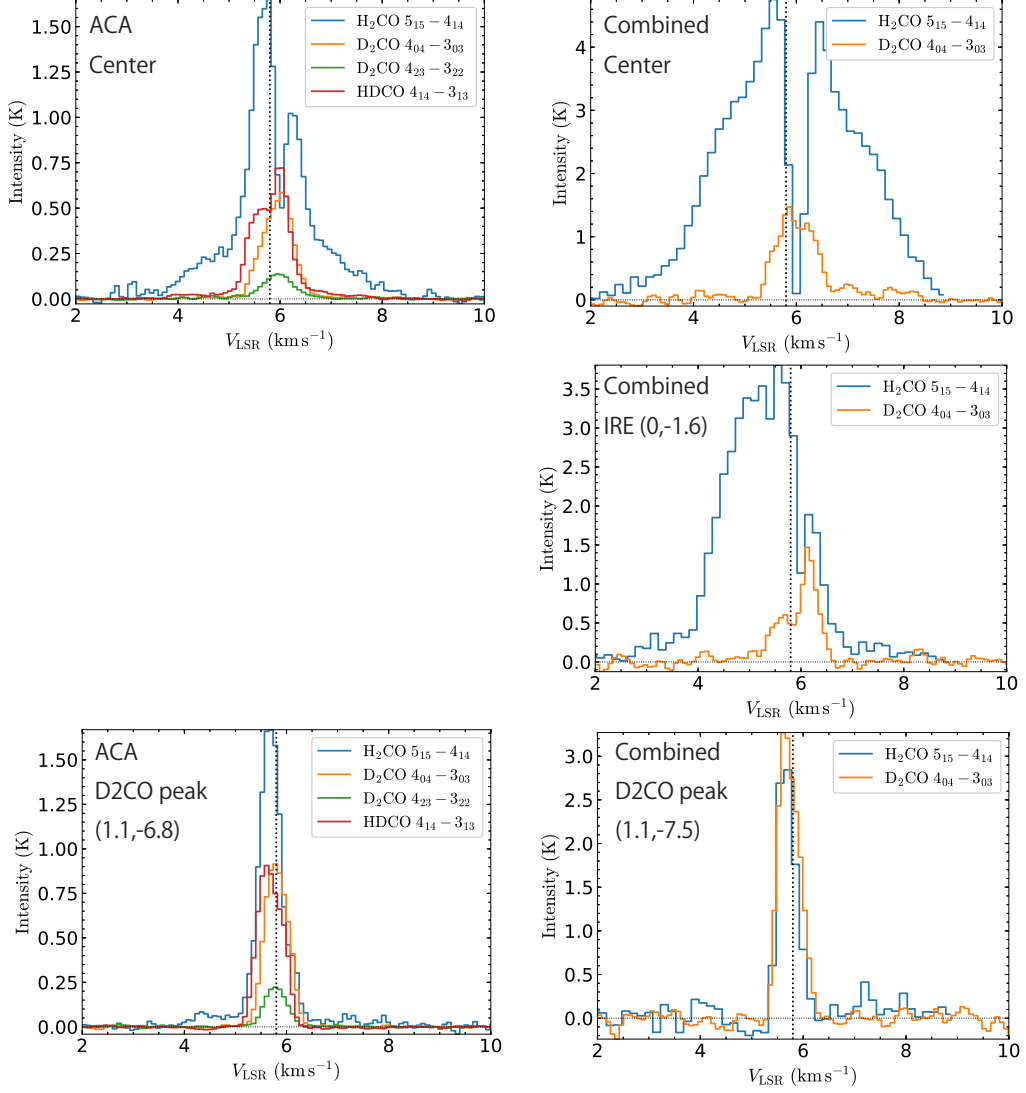


Figure 5.5: The spectra extracted from the protostar position (top panels), the position corresponds to the IRE ($(\Delta\alpha, \Delta\delta) = (0'', -1''.6)$; middle panel), and positions at which the integrated intensity of the D₂CO 4₀₄-3₀₃ line is the maximum ($(\Delta\alpha, \Delta\delta) = (1''.1, -6''.8)$ for the ACA data and $(\Delta\alpha, \Delta\delta) = (1''.1, -7''.5)$ for the combined data; bottom panels). The ACA data are shown in the left side, and the combined data in the right side. The spectra are extracted within the circular area with the radius of 3''.5 and 0''.9 for the ACA and combined data, respectively. The vertical dashed lines show the systemic velocity (5.8 km s $^{-1}$).

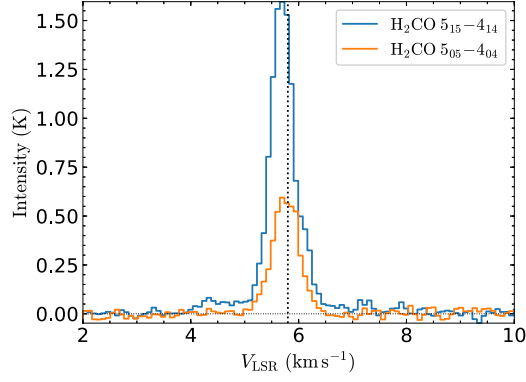


Figure 5.6: The spectra of the $5_{15}-4_{14}$ and $5_{05}-4_{04}$ transitions of H_2CO at 1000 au south to the protostar ($(\Delta\alpha, \Delta\delta) = (0'', -7''.0)$). The vertical dashed line indicates the systemic velocity.

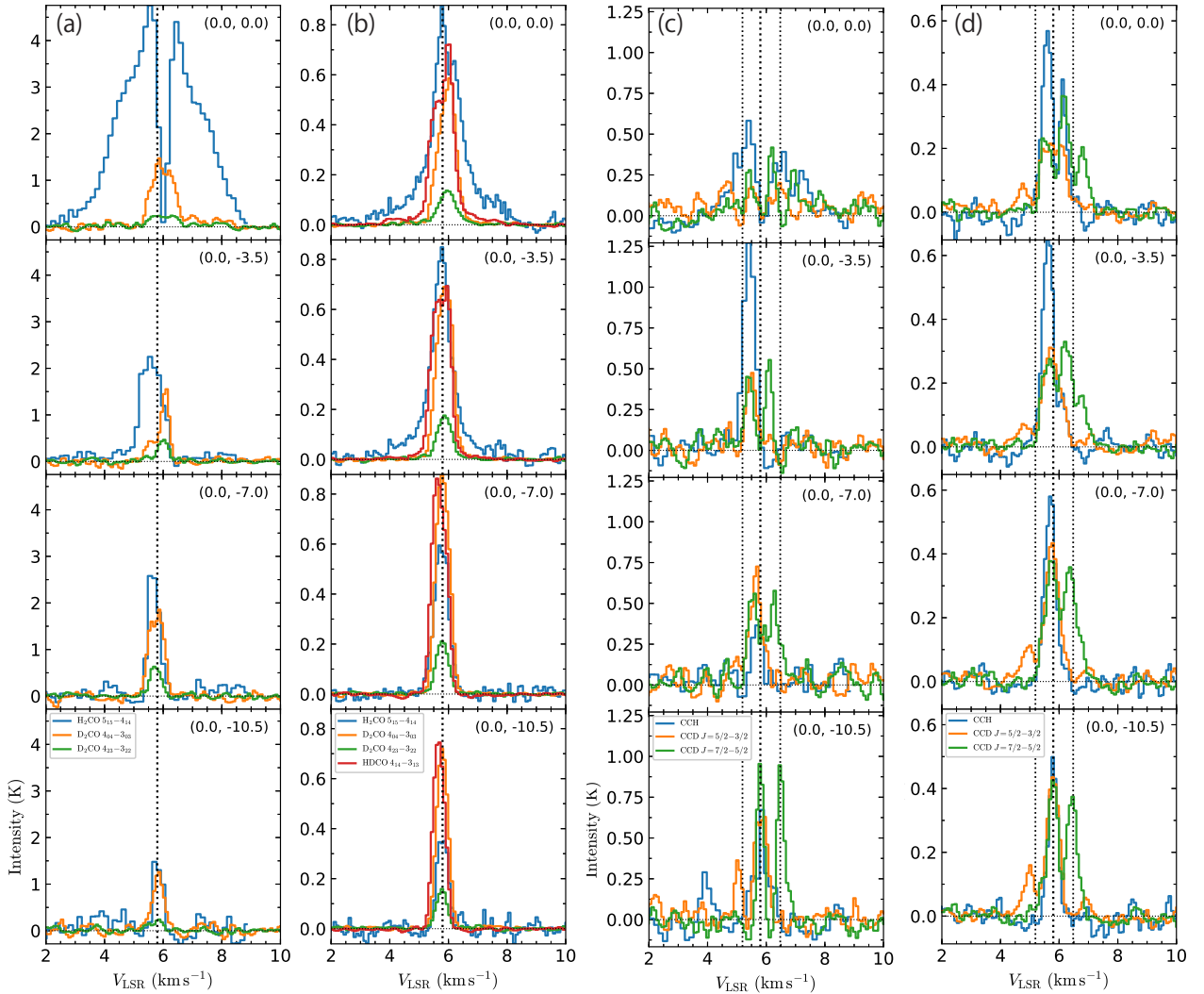


Figure 5.7: The spectrum along the protostellar envelope: (a) the formaldehyde lines obtained by the combined image, (b) those by the ACA data, (c) the CCH ($N = 3-2$, $J = 5/2-3/2$, $F = 2-2$) and CCD lines obtained by the combined image, (d) those by the ACA data. The vertical dashed lines show the systemic velocity (5.8 km s^{-1}). The corresponding velocities for the satellite lines of CCD are also shown in vertical lines. The spectra are prepared for the circular area with the radius of $3''.5$ and $0''.9$ for the ACA and combined data, respectively.

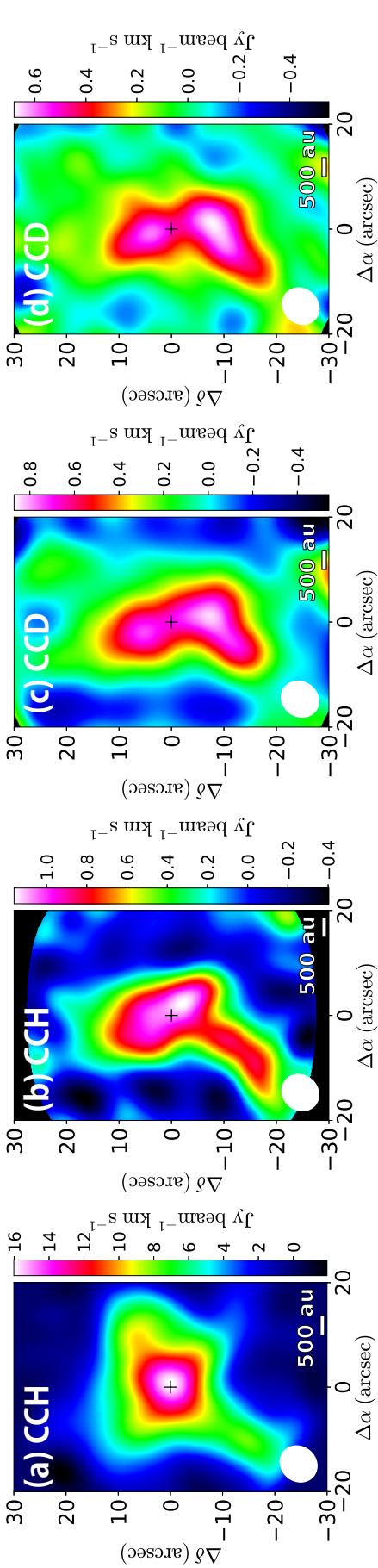


Figure 5.8: The integrated intensity maps of the hyperfine components of CCH and CCD obtained with ACA: (a) CCH $N = 3-2$, $J = 5/2-3/2$, $F = 2-1$, (b) CCH $N = 3-2$, $J = 5/2-3/2$, $F = 2-2$, (c) CCD $N = 3-2$, $J = 7/2-5/2$, $F = 9/2-7/2$, and $5/2-3/2$, (d) CCD $N = 3-2$, $J = 5/2-3/2$, $F = 7/2-5/2$, $5/2-3/2$, and $3/2-1/2$. The cross marks show the protostar position. The white circles show the synthesized beam size.

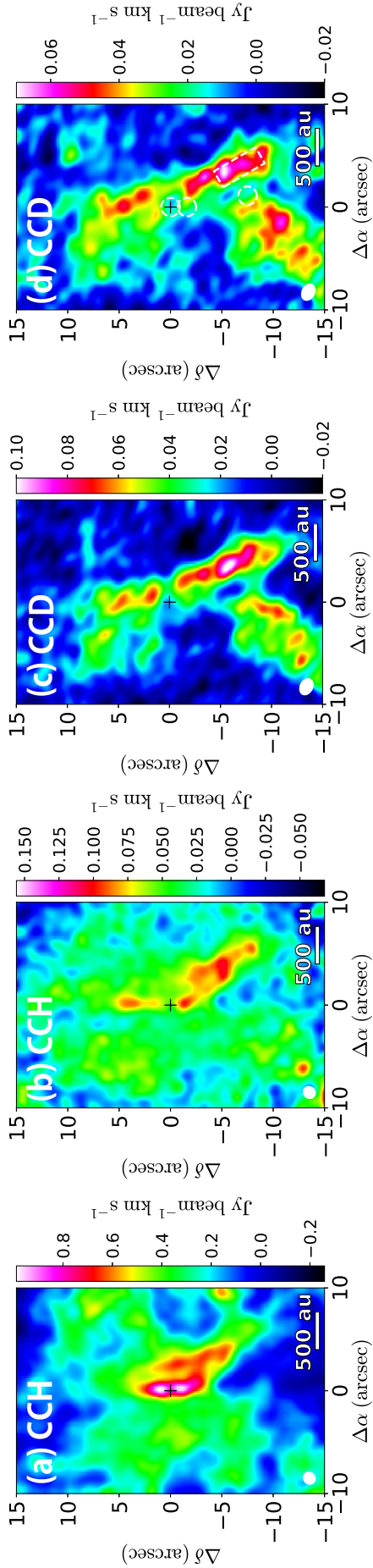


Figure 5.9: The same as Figure 5.8, but the 12-m array data are combined with the ACA data. The white areas in (d) are sampled to derive the $[CCD]/[CCH]$ ratio.

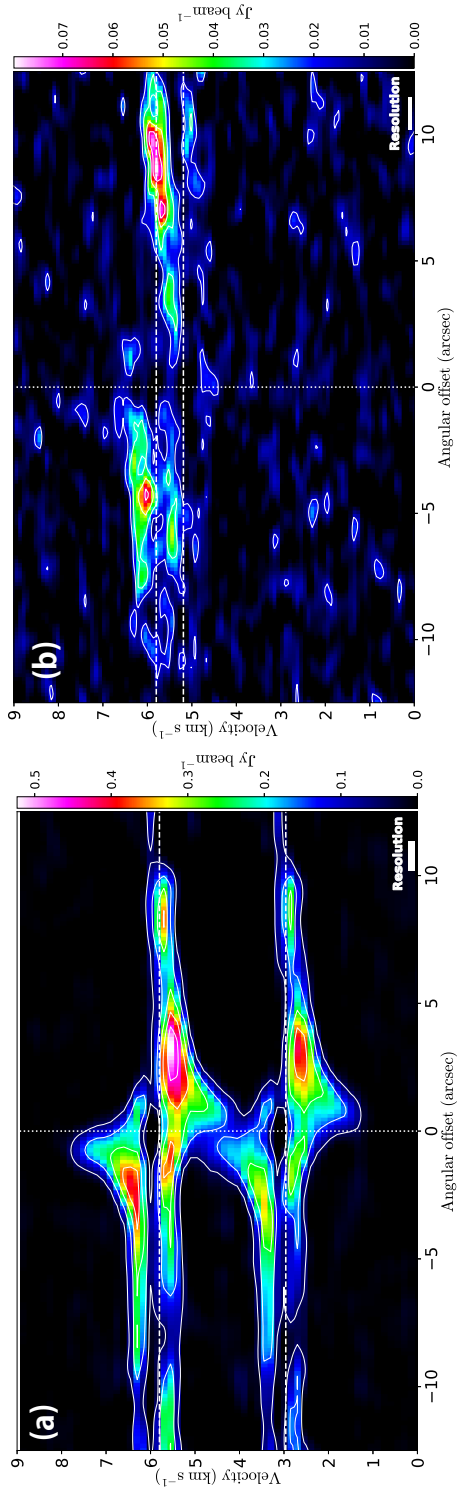


Figure 5.10: The PV diagrams of (a) CCH $N = 3-2$, $J = 5/2-3/2$, $F = 3-2$ and (b) CCD $N = 3-2$, $J = 5/2-3/2$, $F = 7/2-5/2$ and $5/2-3/2$ lines along the envelope direction (P.A. = 180°). The satellite lines ($F = 2-1$ for CCH and $F = 3/2-1/2$ for CCD) are also included. The white vertical lines show the protostar position. The horizontal lines indicate the systemic velocity (5.8 km s^{-1}) and the corresponding velocity for the satellite lines. The lowest contour levels are at 10σ and 3σ , and the level intervals are 20σ and 30σ for CCH and CCD, where $\sigma = 5$ and 6 mJy beam^{-1} , respectively.

5.4.2. D/H ratios

We estimate the D/H ratios in the southern envelope with the ACA data. Figure 5.11 shows the line profiles at the selected positions in the southern envelope. The lines of CCH and CCD are affected by the self-absorption at the protostar position. The CCD $N = 3-2$, $J = 7/2-5/2$ spectrum has three peaks, because this line is splitted into two components with similar intensities ($F = 9/2-7/2$ with $S\mu^2$ of 2.5 D^2 and $F = 5/2-3/2$ and $7/2-5/2$ with $S\mu^2$ of 3.2 D^2), both of which suffer from the self-absorption. On the other hand, the peak velocities almost correspond to the systemic velocity in the outer envelope ($r \gtrsim 1000 \text{ au}$), indicating that they are free from the self-absorption.

We derive the D/H ratios at the same four circular areas along the envelope direction as in the case of H_2CO . The diameter of the sampled areas ($7''.0$) is comparable to the resolution along the north-to-south direction, and the center is every $3''.5$ from the protostar position. The spectra are shown in Figure 5.7 (d).

The D/H ratio is derived in the following ways. In the positions near the protostar ($\Delta\delta = 0''$ and $-3''.5$), the integrated intensity in the blueshifted side from the systemic velocity ($5.0-5.6 \text{ km s}^{-1}$) is used. The $J = 7/2-5/2$, $F = 5/2-3/2$ and $7/2-5/2$ component is employed for the evaluation of the column density of CCD, in order to avoid the contamination from other satellite lines. The rotational temperature is assumed to be 30 K , and the LTE condition is assumed. In the outer regions ($\Delta\delta = -7''.0$ and $-10''.5$), we derive the D/H ratios by using the total integrated intensities. The rotational temperature is assumed to be 20 K . The derived abundance ratios are summarized in Table 5.3. The change in the rotation temperate by 10 K does not change the results within the error. The CCH line is likely optically thin, because the intensity ratio to the weaker hyperfine component ($J = 7/2-5/2$, $F = 3-3$; $S\mu^2 = 0.065 \text{ D}^2$) is almost comparable to the intrinsic intensity ratio of about a half.

In addition to the ACA observations, we also analyze the combined data with the 12-m array observations, as in the case of formaldehyde. The spectra at the three positions mentioned in Section 5.3.4 are shown in Figure 5.11. The derived $[\text{CCD}]/[\text{CCH}]$ ratios are summarized in Table 5.4. The D/H ratio is not evaluated at the protostar position, because CCH is deficient in the disk component inward of the centrifugal barrier (Sakai *et al.* 2014b), as can be seen in Figure 5.11. Because the CCD and CCH emissions are not detected in the IRE (position B) and the D_2CO peak (position C), respectively, the 3σ upper limits are estimated by the equation (5.1). The derived D/H ratios are summarized in Table 5.4. The D/H ratio exceeds 0.32 at the D_2CO peak, where the deuterium fractionation is thought to be efficiently proceeded, while it

is less than 0.016 in the IRE. Thus, the decrease in the D/H ratio along the envelope is seen also for the CCH case.

In addition, we evaluate the D/H ratio in the outflow cavity wall region (white square in Figure 5.9). In the outflow cavity wall, the [CCD]/[CCH] ratio is derived to be 0.06–0.07, which is almost independent of the assumption of the excitation temperature.

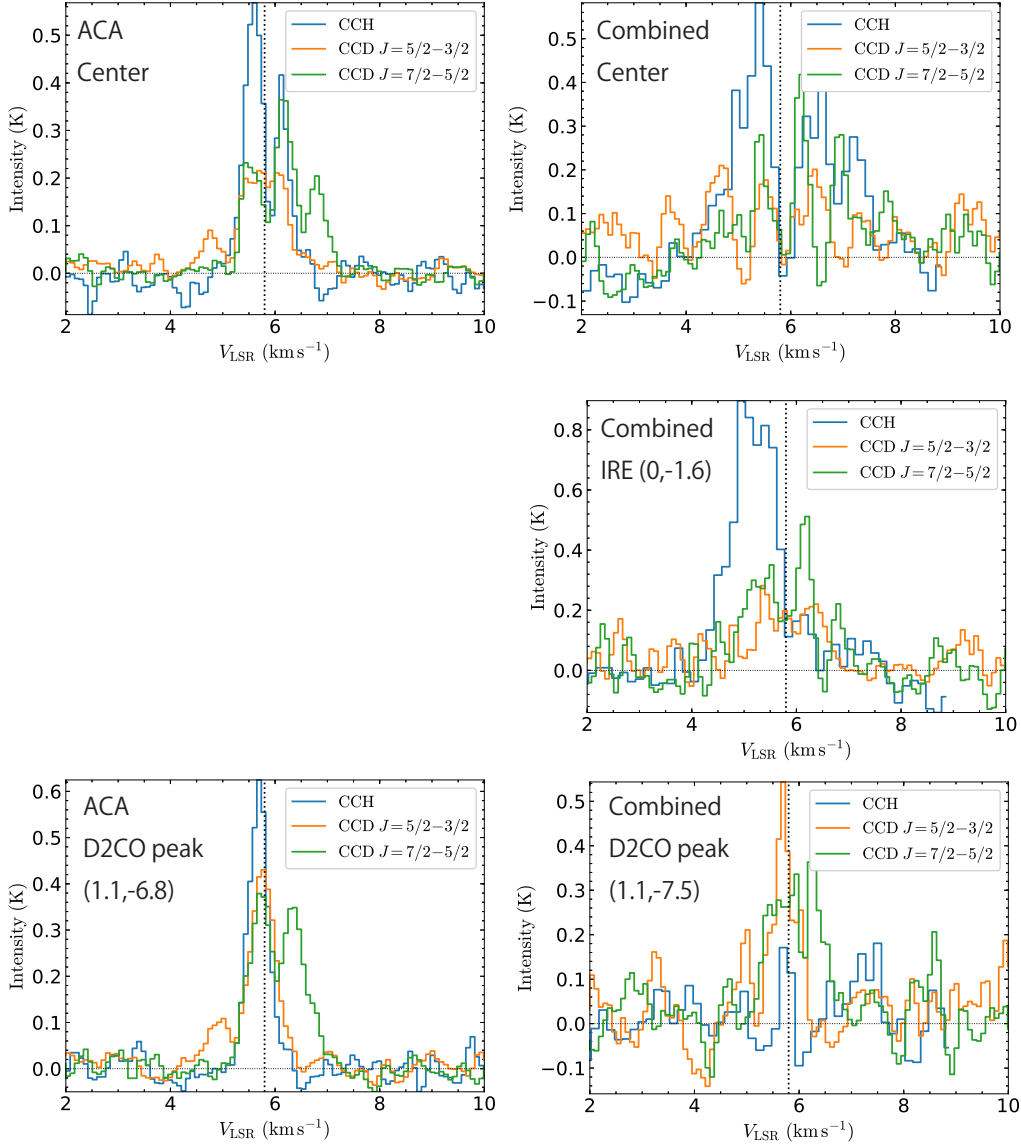


Figure 5.11: The same as Figure 5.5, but for the spectrum of CCH ($N = 3-2$, $J = 5/2-3/2$, $F = 2-2$) and CCD lines. The vertical dashed line shows the systemic velocity (5.8 km s^{-1}) and the corresponding velocity for the satellite lines.

5.5. Discussion

5.5.1. Origin of the different distributions and the radial change of the deuterium fractionation

The H_2CO emission concentrates in the vicinity of the protostar, where the HDCO and D_2CO emissions are weak. This indicates that the normal species is preferentially produced in the vicinity of the protostar, because the selective destruction of the deuterated species is unlikely to occur. In the inner envelope near the protostar, H_2CO is thought to be released into the gas phase from dust grains when the temperature becomes higher than the desorption temperature of about 40 K due to the protostellar heating. A possible reason for the deficiency of the deuterated species can therefore be the low deuterium fractionation in the ice mantle. This scenario is theoretically proposed by Furuya *et al.* (2016) to account for the low deuterium fractionation of water in the innermost region near the protostar (e.g., NGC1333 IRAS 2A; Coutens *et al.* 2014). Water is efficiently formed on dust grains via hydrogenation of the oxygen atom before the deuterium fractionation efficiently occurs, and hence, a large amount of the normal species is stored in the ice mantle (Section 1.2.1; Figure 1.2). This leads to the decrease in the $[\text{HDO}]/[\text{H}_2\text{O}]$ ratio inward of the water snowline. If a large amount of formaldehyde is formed and preserved in the ice mantle before the deuterium fractionation becomes efficient, the amount of the deuterated species on ice can be significantly less than that of the normal species. Note that Furuya (2017) reported methanol does not show the decrease in the D/H ratio by the gas-grain chemical model, because it is efficiently formed only on the surface layers of the ice mantle during the later stage of the ice formation. The present result shows that this picture cannot simply be applied for the H_2CO case.

As in the case of formaldehyde, the $[\text{CCD}]/[\text{CCH}]$ ratio is found to decrease with decreasing distance from the protostar, indicating that the normal species is preferably produced in the vicinity of the protostar. In L1527, carbon-chain molecules are efficiently produced from CH_4 sublimated from the dust grain (WCCC; Sakai & Yamamoto 2013). Because the desorption temperature of CH_4 is around 25 K, CCH in the IRE is considered to be produced by the WCCC mechanism. CH_4 is formed on the ice by the hydrogenation of the C atom, which is mainly depleted before its conversion to CO in the gas phase (Section 1.2.1). The D/H ratio of CH_4 can therefore be low in the ice mantle, resulting in the low $[\text{CCD}]/[\text{CCH}]$ ratio in the IRE.

In the outer envelope, the conditions necessary for the efficient deuterium fractionation are fulfilled. Namely, the temperature is low (< 20 K) and the density is high ($\gtrsim 10^5\text{--}10^6$ cm^{-3}). The deuterated formaldehyde is thought to be formed on the ice surfaces to explain the observed high D/H ratio. If this is the case, they are sublimated via non-thermal processes

such as reactive desorption (Garrod *et al.* 2006) and comic-ray-induced photodesorption (Prasad & Tarafdar 1983), because the derived temperature is significantly lower than the desorption temperature of 40 K.

The different processes of the deuterium fractionation between the inner and outer envelopes are likely responsible for the radial change in the D/H ratios. The [HDCO]/[H₂CO] ratio decreases with decreasing distance from the protostar, because HDCO is abundant in the outer envelope ($r \sim 1000$ au) while the normal species is abundant in the vicinity of the protostar. The [D₂CO]/[HDCO] ratio is almost constant throughout the envelope, because the sublimation of the deuterated species from dust grains can be negligible in comparison with those produced in the outer envelope.

5.5.2. Comparison with the single-dish observations

As mentioned in Section 5.1, the deuterium fractionations of H₂CO in L1527 are previously examined by Parise *et al.* (2006) and Roberts & Millar (2007), based on the single-dish observations. Parise *et al.* (2006) reported that the [D₂CO]/[HDCO] and [HDCO]/[H₂CO] ratios are $0.28^{+0.25}_{-0.16}$ and $1.7^{+2.6}_{-1.1}$, while Roberts & Millar (2007) reported 0.29 ± 0.05 and 0.066 ± 0.013 , respectively. The [D₂CO]/[HDCO] ratios obtained by the single-dish observations are consistent with that by our study (0.20–0.25). It is because the distributions of D₂CO and HDCO are similar, and the [D₂CO]/[HDCO] ratio is almost constant throughout the core. On the other hand, the [HDCO]/[H₂CO] ratios are not consistent with one another, likely because of the different spatial distributions between the normal and the deuterated species (HDCO). The normal species resides in the inner disk, the infalling-rotating envelope, and the outflow, while HDCO and D₂CO only resides in the outer envelope. The previous studies assume the same emitting region and the same rotational temperature between the normal and deuterated species, which seems too simplified. Since the single-dish observation encompasses the whole emitting region of H₂CO, the [HDCO]/[H₂CO] ratio would be low in single-dish observations, as in the case of Roberts & Millar (2007). The extremely high [HDCO]/[H₂CO] ratio of 1.7 by Parise *et al.* (2006) could originate from the underestimation of the column density of the normal species which is derived from some spectral lines strongly self-absorbed (Maret *et al.* 2004).

The lower limit of the [CCD]/[CCH] ratio of 0.3 is also significantly higher than that obtained by the line survey observation (0.037; Table 3.6), probably because the single-dish telescope encompasses the whole emitting region of the normal species, as in the case of formalde-

hyde. In the outflow cavity wall, the D/H ratio would be lower than that in the D₂CO peak, probably because the density is lower and the temperature is higher.

5.5.3. Comparison with chemical models

The formation and deuteration of formaldehyde and other complex organic molecules are studied through astrochemical modeling by Taquet, Charnley, & Sipilä (2014). They trace the deuterium fractionation during the early stage of the star formation from the prestellar to protostellar phases, taking into account the multilayered structure of the ice mantles (Section 1.2.1; Figure 1.2). According to their result, the radial abundance profile of formaldehyde in the protostellar phase consists of three regimes: the cold external envelope with the temperature lower than the desorption temperature T_d , the cold intermediate envelope where the temperature is higher than T_d of H₂CO but lower than that of water, and the warm inner envelope with the temperature higher than T_d of water (Figure 1.3). The abundance of formaldehyde rises abruptly in the intermediate envelope. The distribution of the observed H₂CO emission is roughly consistent with this picture, although the third regime could not be seen due to the lack of spatial resolution. The radial profile of the D/H ratios of formaldehyde can also be classified into the above three regimes, and does not contradict to our observation which reveals the difference of the deuterium fractionation between the outer envelope and the inner envelope. However, the observation and the model are not consistent with each other in some points. First, the [HDCO]/[H₂CO] ratio is as low as 0.1 in the cold envelope in the chemical model, while it is even above unity in this observation. Second, the [HDCO]/[H₂CO] ratio in the cold outer envelope and that in the cold intermediate envelope are similar in the model, while it is higher in the outer envelope in this observation. Hence, we would like to point out that some chemical mechanisms may be missing to account for the high deuterium fractionation in the outer cold envelope.

5.6. Summary and Conclusion

The deuterium fractionation is an important tool in understanding the chemical evolution from prestellar cores to protostellar cores. In this study, we have presented the high spatial resolution observation of H₂CO, CCH, and their deuterated species toward the low-mass protostellar core L1527.

- (1) The distributions of H₂CO and its deuterated counterparts are clearly different from

each other: the former is concentrated in the vicinity of the protostar, whereas the latter is extended more widely at a 1000 au. With a higher spatial resolution image combined with the 12-m array data, D₂CO is found to be absent in the inner envelope ($r \lesssim 250$ au) where the normal species is abundant. The same trend can be seen for CCH and CCD, although they are also abundant in the outflow cavity wall. The temperature derived from the two D₂CO lines is as low as 20 K in the outer envelope, indicating that the deuterated species of H₂CO are produced in the gas phase reactions and/or sublimated non-thermally from dust grains.

(2) The measured [HDCO]/[H₂CO] and [CCD]/[CCH] ratios along the protostellar envelope decrease with decreasing distance from the protostar. This is because the efficient sublimation/production of the normal species due to the temperature rise results in the low deuterium fractionation in the inner envelope. On the other hand, the [D₂CO]/[HDCO] ratio is constant. Since the deuterated species is absent in the vicinity of the protostar, the [D₂CO]/[HDCO] ratio mostly traces the ratio in the outer envelope. The decrease of the deuterium fractionation is also confirmed in the combined image.

(3) The [HDCO]/[H₂CO] is almost unity in the outer envelope. This ratio is higher than that predicted by the astrochemical gas-grain model including the multilayered structure of ice mantles, and hence, some chemical processes would be missing to explain the observed D/H ratio.

(4) The gas phase D/H ratios in the innermost warm regions are found to be comparable to or lower than the previous reports based on single dish observations, likely reflecting the D/H ratios preserved in the ice mantles, as is suggested in the case of organic molecules by the high spatial-resolution observation toward IRAS 16293-2422 (Persson *et al.* 2018; Jørgensen *et al.* 2018).

The striking difference of the D/H ratios between the inner and outer envelope originates from the difference of time scales between the deuterium fractionation and the evolution of ice mantles. Since deuterium fractionation starts from the reaction with H₃⁺, the time scale of deuterium fractionation is roughly given as $\tau \sim 1/k[\text{H}_3^+]$, where k denotes the rate coefficient of the reaction. The rate coefficients of ion-molecule reactions are usually comparable to the Langevin rate coefficient (2×10^{-9} cm³ s⁻¹). The H₃⁺ abundance is determined by the balance between its formation and destruction. H₃⁺ is formed from reactions (1.2) and (1.3), and is destroyed by abundant neutral species such as CO and O. Therefore, the following relation

holds for the balance of the H_3^+ abundance under the steady-state approximation:

$$\zeta[\text{H}_2] = k([\text{CO}] + [\text{O}])[\text{H}_3^+], \quad (5.2)$$

where ζ is the cosmic-ray ionization rate coefficient ($2 \times 10^{-17} \text{ s}^{-1}$). Because the sum of the CO and O abundances relative to H_2 can be assumed to be the oxygen abundance of 3.5×10^{-4} , the time scale of deuterium fractionation is $5 \times 10^5 \text{ yr}$, which is independent of the H_2 density. On the other hand, the adsorption time scale of gas-phase species onto dust grains is roughly given by $\tau \sim 10^5 / (10^4 \text{ cm}^{-3} / n_{\text{H}}) \text{ yr}$, when the dust size distribution is taken into account (e.g., Caselli *et al.* 1999). Hence, the time scale of adsorption onto dust grains is shorter than that of deuterium fractionation in typical prestellar cores ($n_{\text{H}} \gg 10^4 \text{ cm}^{-3}$). This means that molecules adsorb onto dust grains before the chemical equilibrium, resulting in low D/H ratios in the bulk of ice mantles. The D/H ratios of gas-phase molecules which originate from the thermal sublimation from dust grains and subsequent gas-phase reactions can therefore be altered in the vicinity of the protostar. This effect needs to be considered, when the evolution of the deuterium fractionation to the protoplanetary stage is explored.

CHAPTER 6

CONCLUSION

6.1. Summary of this thesis

During the last decade, molecular isotopic ratios, especially the molecular D/H ratios, have been used for the chemical diagnostics to study the evolutionary stages from prestellar cores to protostellar cores. However, several questions regarding the isotopic ratios remain to be addressed. First, the spatial distributions of the D/H ratios in protostellar cores are not well known. Although the decreasing trend in the D/H ratios along the protostellar evolution has been studied in a statistical manner, it is unclear whether this trend can be seen within a single protostellar core. It is awaited to resolve the structures of a protostellar core, such as disk, envelope, and outflow, and to reveal the distribution of the isotope ratios, in order to trace the evolution of the isotopic ratios from prestellar cores to protoplanetary systems. Second, isotopic fractionations other than deuterium are not well investigated in the context of the chemical evolution. For instance, the ^{13}C fractionation, which can be caused at low temperature by the isotopic exchange reaction like the deuterium fractionation, has been studied only for limited molecular species toward limited sources. Hence, comprehensive understanding of the ^{13}C fractionation by observing a variety of molecular species is needed.

One strategy to investigate the evolution of the isotopic ratios is to reveal statistical trends by observing many sources in different evolutionary stages. However, it is important to investigate one source as a testbed, because neither a full picture of the ^{13}C fractionation nor distribution of deuterium fractionation has been explored so far. We have therefore conducted extensive observations with high spatial resolution and high sensitivity toward the representative Class 0 low-mass protostellar source L1527, and have gained new insights into the chemical evolution of isotopic ratios.

6.1.1. Overall chemical composition of L1527

In order to reveal the chemical composition of this source without any preconception, we first conducted a sensitive spectral line survey observation in the 3 mm band toward L1527 with the Nobeyama 45 m telescope. In total, 69 molecular species are identified, among which

27 species are carbon-chain species and their isomers, including their minor isotopologues. To characterize the chemical composition of L1527, we compared it with those of the prototypical hot corino chemistry source IRAS 16293-2422 and the prestellar core TMC-1 (CP). The chemical composition of L1527 is found to show a clear WCCC characteristic: unsaturated organic species such as C_nH ($n = 3, 4, 5, \dots$) (carbon-chain molecules) are abundant, while saturated complex organic molecules such as $HCOOCH_3$ and $(CH_3)_2O$ are deficient in comparison with hot corino chemistry source such as IRAS 16293-2422. Although both prestellar cores and WCCC sources are characterized by rich carbon chain molecules, the longer carbon chains are relatively deficient in L1527 in comparison with the prestellar core TMC-1. This indicates that the carbon-chain molecules in L1527 are not just the remnants of those produced in the parent prestellar-core phase, but are produced in the protostellar-core phase, because the longer carbon-chain molecules take longer time to be formed.

6.1.2. *Molecular $^{12}C/^{13}C$ ratios at a 1000 au scale*

We presented a first comprehensive study to determine the $^{12}C/^{13}C$ ratios of various species in a protostellar core. Based on the line survey observation and the supplementary observations, we evaluated the $^{12}C/^{13}C$ ratios of CO, CN, CCH, HC_3N , $c-C_3H_2$, and H_2CO . The $^{12}C/^{13}C$ ratios of CO, CN, and H_2CO are comparable to the elemental $^{12}C/^{13}C$ ratio of 60–70, while those derived for CCH, HC_3N and $c-C_3H_2$ show higher $^{12}C/^{13}C$ ratios than the elemental ratio. Our result further confirms the possible mechanism of the ^{13}C dilution: the molecules produced from the C^+ ion suffer from the ^{13}C dilution, whereas the molecules produced from CO or those produced before the ^{13}C dilution occurs show the normal $^{12}C/^{13}C$ ratio close to the elemental ratio. On the other hand, it remains unclear whether the ^{13}C dilution of carbon-chain species can be used as the tracer for the chemical evolution, because the ^{13}C dilution is examined only for a few sources so far.

6.1.3. *Molecular D/H ratios at a 1000 au scale*

In the line survey in the 3 mm band as well as the supplemental observations in the 4 mm band with NRO 45 m, we detected 11 deuterated species. The derived molecular D/H ratios are a few percent regardless of molecular species with some exception, which is consistent with previous studies. The molecular D/H ratios averaged over the 1000 au scale is relatively lower in L1527 than those reported for hot corino sources. This feature would originate from the relatively shorter timescale of the prestellar-core phase for the WCCC source L1527.

6.1.4. Distributions of deuterated species within 1000 au

To reveal the spatial distributions of the deuterium fractionation in L1527, we conducted the ALMA observation of CCH and H₂CO and their deuterated counterparts. The distributions of H₂CO and its deuterated isotopologues are found to be clearly different from each other. The emission of H₂CO is concentrated in the vicinity of the protostar ($r < 250$ au), indicating the efficient evaporation from dust grains. On the other hand, the deuterated species mainly reside in the outer envelope ($r \sim 1000$ au), and do not show the emission in the vicinity of the protostar. The deuterium fractionation in the outer envelope is derived to be high ($[\text{D}_2\text{CO}]/[\text{H}_2\text{CO}] \sim 0.8$). On the other hand, it is found to be lower in the vicinity of the protostar ($[\text{D}_2\text{CO}]/[\text{H}_2\text{CO}] \lesssim 0.04$). The similar trend can also be seen for the $[\text{CCD}]/[\text{CCH}]$ case. Hence, the degree of the deuterium fractionation in the protostellar envelope most likely decreases with decreasing distance from the protostar within a 1000 au scale. A shorter timescale of ice evolution relative to that of deuterium fractionation makes the D/H ratios in the inner layers of the ice mantles low, likely leading to the observed low D/H ratios in the vicinity of the protostar. This means that the high deuterium fractionation caused in the cold protostellar envelope would not be inherited to the protoplanetary-disk phase as it is.

6.2. Future prospects

As described above, we successfully revealed the striking difference in the spatial distributions between the main isotopologue and its deuterated counterparts in the low-mass protostar L1527. This result indicates that the protostellar activities and the associated structural changes provide a substantial influence on the isotopic ratios. Moreover, the deuterium fractionation obtained with ALMA is found to be significantly different from those derived based on the single-dish telescopes, probably because observations with the unresolved large beam of the single-dish telescopes have a large uncertainty. Hence, it is indispensable to investigate protostellar cores by high spatial-resolution observations with ALMA to bridge the isotopic ratio reported in prestellar cores and that in protoplanetary disks, although the single-dish observations are also important to reveal the chemical characteristic averaged over a whole area of a target source. Open questions to be addressed by the high spatial-resolution observations are briefly described as follows.

6.2.1. Deuterated species

It is still unclear whether other protostellar sources show a similar evolutionary behavior in deuterium fractionation to that observed for L1527 case. Because the physical parameters of the protostar such as the luminosity and the elapsed time after its birth would have an influence on environmental conditions and chemical compositions in the outer envelope, observations toward other protostellar cores would reveal the difference in the deuterium fractionation among protostellar cores. For instance, the only Class 0 source in which the deuterium fractionation is extensively studied with ALMA, IRAS 16293-2422, does not show the different distributions between the normal and deuterated species of formaldehyde at a 1000 au scale, unlike the L1527 case (Persson *et al.* 2018). This difference between L1527 and IRAS 16293-2422 may originate from the difference in the physical and chemical environment in the protostellar cores. On the other hand, Ceccarelli *et al.* (2001) reported D₂CO peaks 1200 au south to the protostar by a wider mapping observation toward IRAS 16293-2422. In addition, the measured D/H ratios in the close vicinity of the protostar in IRAS 16293-2422 with ALMA (e.g., Jørgensen *et al.* 2018; Persson *et al.* 2018) are systematically lower than those reported with the single-dish telescopes (e.g., van Dishoeck *et al.* 1995). This indicates that a large scale structure that could be resolved out even with the ACA observations may exist, and hence, short-spacing observations with the total power array of ALMA would provide us with new information on the large-scale distribution of deuterated species in this source. Since few observations have been conducted to study the radial dependence of the deuterium fractionation in protostellar cores, future high resolution interferometric observations including the shorter baseline toward other sources could shed light on any possible dependence on the physical and chemical environment in protostellar cores.

The high spatial-resolution observations can also be used to study the formation mechanism of deuterated species. To understand the formation (and deuteration) pathways of H₂CO, it is worth investigating the distributions and the deuterium fractionation of other organic species which are formed on the ice mantles, such as CH₃OH. In L1527, D₂CO is found to be abundant in the outer envelope (1000 au apart from the protostar). If CH₃OH and its deuterated species are similarly distributed, it is likely that H₂CO is also formed on the ice mantle, because CH₃OH is formed only on the ice mantles. If the deuterium fractionation of CH₃OH in the outer envelope differs from that of H₂CO, the deuteration mechanisms are different between H₂CO and CH₃OH: the difference may indicate that the deuteration of H₂CO is proceeded mainly in the gas phase. Since the previous single-dish observation reported a slightly lower deuterium fractionation of CH₃OH ($[\text{CH}_2\text{DOH}]/[\text{CH}_3\text{OH}] \lesssim 0.03$) than that of H₂CO (Sakai

et al. 2009b), it is interesting to confirm whether this difference can also be seen by high spatial-resolution observations.

6.2.2. ^{13}C species

It is interesting to see whether the ^{13}C anomaly found for carbon-chain molecules can be seen at a 100 au scale. The ratio may decrease to the standard value (60–70) near the protostar, if destruction and reproduction of the carbon-chain molecules is active in the warm condition where the mechanism of the dilution does not work well. On the other hand, Jørgensen *et al.* (2018) recently reported that the $^{12}\text{C}/^{13}\text{C}$ ratio of CH_3OCH_3 is two times *lower* than the standard ratio in IRAS 16293-2422, when the statistical weight of 2 for the ^{13}C substitution of CH_3OCH_3 is taken into account. They suggested that ^{12}CO can be desorbed more easily than ^{13}CO due to the difference of the binding energy between the two (Smith *et al.* 2015), resulting in the low $^{12}\text{CO}/^{13}\text{CO}$ ratio in the ice surface in the region where the dust temperature is just around the CO sublimation. Because CH_3OCH_3 is thought to be formed on the ice surface in the warming-up phase of protostellar cores, the $^{12}\text{C}/^{13}\text{C}$ ratio of CH_3OCH_3 can also be low. The difference of the ^{13}C fractionation between carbon-chain molecules (dilution) and molecules formed from CO on the ice (enrichment), if exists, will be transferred into carbonaceous compounds formed on dust grains. Hence, the ^{13}C anomaly in the vicinity of the protostar provides us with a possible link to the anomaly found in meteorites. In particular, carbon-chain molecules are generally non-volatile species, and hence, they are adsorbed onto dust grains in the closest vicinity of the protostar. Therefore, carbon-chain molecules can be delivered into the disk in the solid phase: probably they will be polymerized to form carbonaceous compounds, which would be a source of pre-solar organic materials. Hence, it is important to examine whether the $^{12}\text{C}/^{13}\text{C}$ anomaly can be seen around the centrifugal barrier ($r \sim 100$ au).

We can also investigate whether the different $^{12}\text{C}/^{13}\text{C}$ ratio between two ^{13}C isotopologues (e.g., ^{13}CCH vs C^{13}CH and *c*- $^{13}\text{CCCH}_2$ vs *c*- $\text{CC}^{13}\text{CH}_2$) is also observed at a 100 au scale. Previous studies on the ^{13}C anomaly revealed that the most stable ^{13}C species tends to be the most abundant among all the ^{13}C isotopologues of a molecular species, implying that the exchange reaction between ^{13}C species plays a role. If the exchange reaction such as equation (4.2) actually happens, the difference in abundances between two ^{13}C species could be eliminated toward the protostar due to the temperature rise. Hence, the distributions of the ^{13}C species would contain novel information on the basic chemical process occurring in molecular clouds, although detailed experimental and theoretical studies on related chemical reactions are also needed.

ACKNOWLEDGEMENTS

Special thanks are due to my thesis supervisor Professor Satoshi Yamamoto for his invaluable support during my PhD course. The author also gives my special thanks to Prof. Nami Sakai for giving me the opportunities for studying at RIKEN, as well as her helpful suggestions. They have spent a great amount of time working with me and have helped me improve the contents of this thesis.

I would like to thank Prof. Cecilia Ceccarelli and Prof. Bertrand Lefloch for valuable discussions, particularly for communication of the ASAI data prior to publication. I am grateful to the members of Yamamoto group: Dr. Yoko Oya, Mr. Yuji Ebisawa, Mr. Muneaki Imai, Mr. Masaki Takegahara, Ms. Yuki Okoda, Mr. Takanori Fujita, and Ms. Miki Ueda, and the alumni: Dr. Yoshimasa Watanabe, Dr. Daiki Shibata, Dr. Tatsuya Soma, Dr. Yuri Nishimura, Dr. Ana López Sepulcre, Dr. Akihumi Asahara, Mr. Yutaro Chiba, and Mr. Osamu Oguchi. I am also grateful to the members of the star and planet formation laboratory in RIKEN: Dr. Aya E. Higuchi, Dr. Satoshi Ohashi, Dr. Yichen Chang, Dr. Hideki Umehata, Ms. Ritsuko Matsumoto, and Ms. Naoko Seiji. The author has been encouraged through discussions with them. The author also thanks to the NRO 45 m and IRAM 30 m team for supporting me the common use observations. Finally, the author would like to thank my family for their support.

This study is financially supported by the RIKEN Junior Research Associate Program and the JSPS fellowship.

REFERENCES

- Adams, F. C., Lada, C. J., & Shu, F. H. 1987, *ApJ*, 312, 788
- Aikawa, Y., Wakelam, V., Garrod, T., & Herbst, E. *ApJ*, 2008, 674, 884
- Alves, J. F., Lada, C. J., & Lada, E. A. *Nature* 2001, 409, 159
- ALMA Partnership, Asayama, S., Biggs, A., *et al.* 2016, ALMA Cycle 4 Technical Handbook, <https://almascience.org/documentsand-tools/cycle4/alma-technical-handbook>, 978-3-923524-66-2.
- André, P., Ward-Thompson, D., & Barsony, M. 1993, *ApJ*, 406, 122
- Araki, M., Takano, S., Sakai, N., Yamamoto, S., Oyama, T., Kuze, N., & Tsukiyama, K. 2016, *ApJ*, 833, 291
- Araki, M., Takano, S., Sakai, N., Yamamoto, S., Oyama, T., Kuze, N., & Tsukiyama, K. 2017, *ApJ*, 847, 51
- Asvany, O., Schlemmer, S., & Gerlich, D. 2004, *ApJ*, 617, 685
- Bachiller, R. 1996, *ARA&A*, 34, 111
- Bacmann, A., Lefloch, B., Ceccarelli, C., Castets, A., Steinacker, J., & Loinard, L. 2002, *A&A*, 389, L6
- Bacmann, A., Lefloch, B., Ceccarelli, C., Steinacker, J., Castets, A., & Loinard, L. 2003, *ApJ*, 585, 55
- Balucani, N., Ceccarelli, C., & Taquet, V. 2015, *MNRAS*, 449, L16
- Beichman, C. A., Myers, P. C., Emerson, J. P., *et al.* 1986, *ApJ*, 307, 337
- Benson, P. J., & Myers, P. C. 1989, *ApJS*, 71, 89
- Bergin, E. A., Alves, J., Huard, T., Lada, C. J. 2002, *ApJ*, 570, 101
- Bergin, E. A., Tafalla, M. *ARA&A*, 2007, 45, 339
- Bizzocchi, L., Caselli, P., Spezzano, S., & Leonardo, E. 2014, *A&A*, 569, 27
- Bogey, M., Demuynck, C., & Destombes, J. L. 1986, *Chem. Phys. Lett.*, 125, 383
- Bogey, M., Demuynck, C., Destombes, J. L., & Dubus, H. 1987, *J. Mol. Spectrosc.*, 122, 313

- Bogey, M., Demuynck, C., Destombes, J. L. 1985, A&A, 144, 15
- Bonnor, W. B. 1956, MNRAS, 116, 351
- Bontemps, S., Andre, P., Terebey, S., & Cabrit, S. 1996, A&A, 311, 858
- Bottinelli, S., *et al.* 2004, ApJ, 617, L69
- Briggs, D. S. 1995, BAAS, 27, 1444
- Busemann, H., Nguyen, A. N., Cody, G. D., *et al.* 2009, Earth and Planetary Science Letters, 288, 44
- Caselli, P., Walmsley, C. M., Tafalla, Dore, M. L. & Myers, P. C. 1999, ApJ, 523, L165
- Caux, E., *et al.* 2011, A&A, 532, A23
- Cazaux, S., *et al.* 2003, ApJ, 593, L51
- Ceccarelli C., Caselli P., Bockelée-Morvan, D., *et al.* 2015, Protostars and Planets VI, ed. H. Beuther, R. Klessen, C. Dullemond, & Th. Henning (Tucson, University of Arizona Press), 859
- Ceccarelli, C., Loinard, L., Castets, A., Tielens, A. G. G. M., Caux, E., Lefloch, B., & Vastel, C. 2001, A&A, 372, 998
- Chácon-Tanarro, A., Caselli, P., Bizzocchi, L., *et al.* 2018, A&A, in press
- Cheung, A. C., Rank, D. M., Townes, C. H., Thornton, D. D., & Welch, W. J. 1968, Physical Review Letters, 21, 1705
- Chin, Y.-N., Henkel, C., Whiteoak, J. B., Langer, N., Churchwell, E. B., 1996, A&A, 305, 960
- Codella, C., *et al.* 2016, A&A, 586, L3
- Collings, M. P., Anderson, M. A., Chen, R., *et al.* 2004, MNRAS, 354, 1133
- Coutens, A., Jørgensen, J. K., Persson, M. V., van Dishoeck, E. F., Vastel, C., & Taquet, V. 2014, ApJ, 792, L5
- Coutens, A., Vastel, C., Cabrit, S., *et al.* 2013, A&A, 560, 39
- Cox, P., Walmsley, C. M., & Güsten, R. 1989, A&A, 209, 382

- Crapsi, A., Caselli, P., Walmsley, C. M., Myers, P. C., Tafalla, M., Lee, C. W., Bourke, T. L., 2005, *ApJ*, 619, 379
- Daniel, F., *et al.* 2013, *A&A*, 560, A3
- Dateo, C. E., & Lee, T. J. 1997, *Spectrochim. Acta*, A53, 1065.
- Emprechtinger, M., Caselli, P., Volgenau, N. H., Stutzki, J., & Wiedner, M. C. 2009, *A&A*, 493, 89
- Favre, C., Jørgensen, J. K., David, F., Christian, B., Bisschop, S. E., Bourke, T. L., Hogerheijde, M. R., & Frieswijk, W. W. F. 2014, *ApJ*, 790, 55
- Floss, C., Stadermann, F. J., Bradley, J. P., *et al.* 2006, *Geochimica et Cosmochimica Acta*, 70, 2371
- Flower, D. R. 1999, *MNRAS*, 305, 651
- Frerking, M. A., Langer, W. D., & Wilson, R. W. 1982, *ApJ*, 262, 590
- Friesen, R. K., Kirk, H. M., & Shirley, Y. L. 2013, *ApJ*, 765, 59
- Fukuzawa, K., & Osamura, Y., 1996, Abstract of IAU symposium 178, *Molecules in Astrophysics: Probes & Processes*, ed. D. J. Jansen, M. R. Hogerheijde, and E. F. van Dishoeck (Sterrewacht Leiden), p. 186.
- Furuya, K., Aikawa, Y., Sakai, N., & Yamamoto, S. 2011, *ApJ*, 731, 38
- Furuya, K., van Dishoeck, E. F., & Aikawa, Y., 2016, *A&A*, 586, 127
- Furuya, K., in *Proceedings of the IAU symposium No. 332, Astrochemistry VII Through the Cosmos from Galaxies to Planets*, Cunningham, M., Millar, T., & Aikawa, Y., eds., 2017
- Gerin, M., Wootten, H. A., Combes, F. *et al.* 1987, *A&A*, 173, L1
- Garrod, R. T., & Herbst, E. 2006, *A&A*, 457, 927
- Garrod, R., Park, I. H., Caselli, P., & Herbst, E. 2006, *Faraday Discuss.*, 133, 51
- Gerlich, D., Herbst, E., & Roueff, E. 2002, *Planet. Space Sci.*, 50, 1275
- Gibb, E. L., Whittet, D. C. B., Boogert, A. C. A., & Tielens, A. G. G. M. 2004, *ApJS*, 151, 35
- Godfrey, P. D., Brown, R. D., Gunn, H. L., Blackman, G. L., & Storey, J. W. V. 1977, *MNRAS*, 180, 83

- Gratier, P., Majumdar, L., Ohishi, M., Roueff, E., Loison, J. C., Hickson, K. M., & Wakelam, V. 2016, ApJ, 225, 25
- Green, S., & Thaddeus, P. 1974, ApJ, 191, 653
- Gómez-González, J., Guélin, M., Cernicharo, J., Kahane, C., & Bogey, M. 1986, A&A, 168, L11
- Hasegawa, T. I., Herbst, E., Leung, C. M. 1992, ApJS, 82, 167
- Hassel, G. E., Herbst, E., & Garrod, R. T. 2008, ApJ, 681, 1385
- Hayashi, C. 1961, PASJ, 13, 450
- Herbst, E., Adams, N. G., Smith, D., & Defrees, D. J. 1987, ApJ, 312, 351
- Herbst, E. & Klemperer, W. 1973, ApJ, 185, 505
- Hogerheijde, M. R., van Dishoeck, E. F., Blake, G. A., & van Langevelde, H. J. 1998, ApJ, 502, 315
- Howe, D. A., Millar, T. J., Schilke, P., & Walmsley, C. M. 1994, MNRAS, 267, 59
- Huntress, W. T. 1977, ApJS, 33, 495
- Higuchi, A. E., Sakai, N., Watanabe, Y., *et al.* 2018, ApJS, 236, 52
- Hily-Blant, P., Bonal, L., Faure, A., & Quirico, E. 2013, iracus, 223, 582
- Hily-Blant, P., Pineau des Forêts, G., Faure, A., Le Gal, R., & Padovani, M. 2013, A&A, 557, A65
- Hirota, T., Yamamoto, S., Mikami, H., & Ohishi, M. 1998, ApJ, 503, 717
- Hirota, T., Ikeda, M., & Yamamoto, S. 2001, ApJ, 547, 814
- Hirota, T., Sakai, N., & Yamamoto, S. 2010, ApJ, 720, 1370
- Hirota, T., Sakai, N., Sakai, N., & Yamamoto, S. 2011, ApJ, 736, 4
- Högbom, J. A. 1974, A&AS, 15, 417
- Hollis, J. M., Snyder, L. E., Lovas, F. J., & Buhl, D. 1976, ApJ, 209, L83
- Imai, M., Sakai, N., López-Sepulcre, A., *et al.* 2018, ApJ, 869, 51

- Jørgensen, J. K., Favre, C., Bisschop, S. E., Bourke, T. L., van Dishoeck, E. F., & Schmalzl, M. 2012, *ApJ*, 757, L4
- Jørgensen, J. K., *et al.* 2016, *A&A*, 595, A117
- Jørgensen, J. K., Müller, H. S. P., Calcutt, H., *et al.* 2018, *A&A*, 620, A170
- Jørgensen, J. K., Schöier, F. L., & van Dishoeck, E. F. 2002, *A&A*, 389, 908
- Jørgensen, J. K., Schöier, F. L., & van Dishoeck, E. F. 2004, *A&A*, 416, 603
- Kahane, C., Cernicharo, J., Gómez-González, J., & Guélin, M. 1992, *A&A*, 256, 235
- Kahane, C., Al-Edhari, A. J., Ceccarelli, C., López-Sepulcre, A., Fontani, F., & Kama, M. 2018, *ApJ*, 852, 130
- Kaifu, N., *et al.* 2004, *PASJ*, 56, 69
- Kuan, Y.-J., *et al.* 2004, *ApJ*, 616, L27
- Lada, C. J., & Wilking, B. A. 1984, *ApJ*, 287, 610
- Langer, W. D., Graedel, T. E., Frerking, M. A., & Armentrout, P. B. 1984, *ApJ*, 277, 581
- Larson, R. B. 1969, *MNRAS*, 145, 271
- Ligterink, N. F. W., *et al.* 2017, *MNRAS*, 469, 2
- Linsky, J. L. 2003, *Space Science Reviews*, 106, 49
- Lique, F., Spielfiedel, A., & Cernicharo, J. 2006, *A&A*, 451, 1125
- Lis, D. C., Roueff, E., Gerin, M., *et al.* 2002, *ApJ*, 571, L55
- Liszt, H. S. & Ziurys, L. M. 2012, *ApJ*, 747, 55
- Lefloch, B. *et al.* 2018, *MNRAS*, 477, 4792
- Loison, J. C., *et al.* 2017, *MNRAS*, 470, 4075
- Lovas, F. J., Luts, H., & Dreizler, H. 1979, *J. Phys. Chem. Ref. Data*, 8, 1051
- Lucas, R., & Liszt, H. 1998, *A&A*, 337, 246
- Madden, S. C., Irvine, W. M., & Matthews, H. E. 1986, *ApJ*, 311, L27

- Madden, S. C., Irvine, W. M., Matthews, H. E., Friberg, P., & Swade D. A. 1989, AJ, 97, 1403
- Marcelino, N., Cernicharo, J., Roueff, E., Gerin, M. & Mauersberger, R. ApJ, 2005, 620, 308
- Marcelino, N., Cernicharo, J., Tercero, B., & Roueff, E. ApJ, 2009, 690, L27
- Maret, S., Ceccarelli, C., Caux, E., *et al.* 2004, A&A, 416, 57
- Masunaga, H., Initsuka, S. 2000, ApJ, 531, 350
- McGuire, B. A. 2018, ApJS, in press
- Milam, S. N., Savage, C., Brewster, M. A., Ziurys, L. M., & Wyckoff, S. 2005, ApJ, 634, 1126
- Milam, S. N., Woolf, N. J., & Ziurys, L. M. 2009, ApJ, 690, 837
- Motte, F., & André, P. 2001, A&A, 365, 440
- Müller, H. S. P., Thorwirth, S., Roth, D. A. & Winnewisser, G. 2001, A&A, 370, L49
- Müller, H. S. P., Schlöder, F., Stutzki, J., & Winnewisser, G. 2005, JMoSt, 742, 215
- Mumma, M. J., & Charnley, S. B. 2011, ARA&A, 49, 471
- Murillo, N. M., Bruderer, S., van Dishoeck, E. F., *et al.* 2015, A&A, 579, A114
- Nakajima, T., Sakai, T., Asayama, S., *et al.* 2008, PASJ, 60, 435
- Öberg, K., van der Marel, N., Kristensen, L. E., & van Dishoeck, E. F. 2011, ApJ, 740, 14
- Ohashi, N., Hayashi, M., Ho, P. T. P., & Momose, M. 1997, ApJ, 475, 211
- Ohashi, N., Saigo, K., Aso, Y., *et al.* 2014, ApJ, 796, 131
- Oya, Y., Sakai, N., Sakai, T., *et al.* 2014, ApJ, 795, 152
- Oya, Y., Sakai, N., Lefloch, B., *et al.* 2015, ApJ, 812, 59
- Oya, Y., Sakai, N., López-Sepulcre, A., Watanabe, Y., Ceccarelli, C., Lefloch, B., Favre, C., & Yamamoto, S. 2016, ApJ, 824, 88
- Oya, Y., *et al.* 2018, ApJ, 854, 96
- Penzias, A. A., Wannier, P. G., Wilson, R. W., & Linke, R. A. 1977, ApJ, 211, 108
- Parise, B., Castets, A., Herbst, E., *et al.* 2004, A&A, 416, 159

- Parise, B., Ceccarelli, C., Tielens, A. G. G. M., Castets, A., Caux, E., Lefloch, B., & Maret, S. 2006, *A&A*, 453, 949
- Persson, M. V. *et al.* 2018, *A&A*, 610, 54
- Pickett, H. M., Poynter, R. L., Cohen, E. A., Delitsky, M. L., Pearson, J. C., & Müller, H. S. P. 1998, *J. Quant. Spectrosc. & Rad. Transfer*, 60, 883
- Prasad, S. S., & Tarafdar, S. P. 1983, *ApJ*, 267, 603
- Rabli, D., & Flower, D. R. 2010, *MNRAS*, 406, 95
- Roberts, H., Fullar, G. A., Millar, T. J., Hatchell, J., Buckle, J. V. 2002, *A&A*, 381, 1026
- Roberts, H., Herbst, E., & Millar, T. J. 2003, *ApJ*, 591, 41
- Roberts, H. & Millar, T. J. 2007, *A&A*, 471, 849
- Rodgers, S. D., & Charnley, S. B. 2002, *Planet. Space Sci.*, 50, 1125
- Rodgers, S. D., & Charnley, S. B. 2008, *ApJ*, 689, 1448
- Roueff, E., Parise, B., & Herbst, E. 2007, *A&A*, 464, 245
- Roueff, E., Loison, J. C., & Hickson, K. M. 2015, *A&A*, 576, 18
- Ryle, M., Neville, A. C. 1962, *MNRAS*, 125, 39
- Saito, S., Ozeki, H., Ohishi, M., & Yamamoto, S. 2000, *ApJ*, 535, 227
- Sakai, N, Sakai, T., & Yamamoto, S. 2006, *PASJ*, 58, L15
- Sakai, N, Sakai, T., Osamura, Y., & Yamamoto, S. 2007, *ApJ*, 667, L65
- Sakai, N, Sakai, T., & Yamamoto, S. 2008, *Ap&SS*, 313, 153
- Sakai, N, Sakai, T., Hirota, T., & Yamamoto, S. 2008, *ApJ*, 672, 371
- Sakai, N, Sakai, T., Aikawa, Y., & Yamamoto, S. 2008, *ApJ*, 675, L89
- Sakai, N. 2008, PhD thesis, The University of Tokyo
- Sakai, N, Sakai, T., Hirota, T., Burton, M., & Yamamoto, S. 2009, *ApJ*, 697,769
- Sakai, N, Sakai, T., Hirota, T., & Yamamoto, S. 2009, *ApJ*, 702, 1025

- Sakai, N., Saruwatari, O., Sakai, T., Takano, S., & Yamamoto, S. 2010a, *A&A*, 512, A31
- Sakai, N., Sakai, T., Hitora, T., & Yamamoto, S. 2010, *ApJ*, 722, 1633
- Sakai, N., Takano, S., Sakai, T., Shiba, S., Sumiyoshi, S., Endo, Y., & Yamamoto, S. 2013, *JPC*, 117, 9831
- Sakai, N., & Yamamoto, S. 2013, *Chemical Review*, 113, 8981
- Sakai, N., Oya, Y., Sakai, T., *et al.* 2014a, *ApJ*, 791, L38
- Sakai, N., Sakai, T., Hirota, T., *et al.* 2014b, *Nature*, 507, 78
- Schöier, F. L., Jørgensen, J. K., van Dishoeck, E. F., & Blake, G. A.
- Schilke, P., Walmsley, C. M., Pineau des Forêts, G., Roueff, E., Flower, D. R., & Guilloteau, S. 1992, *A&A*, 256, 595
- Shu, F. H., Adams, F. C., & Lizano, S. 1986, *ARA&A*, 25, 23
- Smith, R. L., Pontoppidan, K. M., Young, E. D., & Morris, M. R. 2015, *ApJ*, 813, 120
- Snell, R. L. & Wootten, A. 1979, *ApJ*, 228, 748
- Snyder, L. E., Hollis, J. M., Buhl, D., & Watson, W. D. 1977, *ApJ*, 218, L61
- Soma, T., Sakai, N., Watanabe, Y., & Yamamoto, S. 2015, *ApJ*, 802, 74
- Soma, T., Sakai, N., Watanabe, Y., & Yamamoto, S. 2018, *ApJ*, 854, 116
- Spezzano, S., Tamassia, F., Thorwirth, S., Thaddeus, P., Gottlieb, C. A., & McCarthy, M. C. 2012, *ApJS*, 200, 1
- Spezzano, S., *et al.* 2013, *ApJ*, 769, L19
- Spielfiedel, A., Feautrier, N., Najar, F., Ben Abdallah, D., Dayou, F., Senent, M. L., & Lique, F. 2012, *MNRAS*, 421, 1891
- Sugimura, M., *et al.* 2011, *PASJ*, 63, 459
- Suzuki, H., Yamamoto, S., Ohishi, M., Kaifu, N., Ishikawa, S., Hirahara, Y., & Takano, S. 1994, *ApJ*, 392, 551
- Stahler, S. W., Shu, F. H., & Taam, R. E. 1980, *ApJ*, 241, 637

- Takakuwa, S., Kawaguchi, K., Mikami, H., & Saito, M. 2001, PASJ, 53, 251
- Takano, S., Masuda, A., Hirahara, Y., *et al.* 1998, A&A, 329, 1156
- Taniguchi, K., Ozeki, H., Saito, M., Sakai, N., Nakamura, F., Kamenno, S., Takano, S., & Yamamoto, S. 2016, ApJ, 817, 147
- Taniguchi, K., Saito, M., & Ozeki, H. 2016, ApJ, 830, 106
- Taniguchi, K., Ozeki, H., & Saito, M. 2017, ApJ, 846, 46
- Taquet, V., Ceccarelli, C., & Kahane, C. 2012, A&A, 538, A42
- Taquet, V., Charnley, S., & Sipilä, O. 2014, ApJ, 791, 120
- Taquet, V., López-Sepulcre, A., Ceccarelli, C., Neri, R., Kahane, C., & Charnley, S. 2015, ApJ, 804, 81
- Tielens, A. G. G. M. 2005, Phys. Chem. Interstellar Medium (Cambridge University Press)
- Tobin, J. J., Hartmann, L., Calvet, N., & D'Alessio, P. 2008, ApJ, 679, 1364
- Tobin, J. J., Hartmann, L., Chiang, H. -F., *et al.* 2012, Nature, 492, 83
- Tomkin, J., Luck, R. E., & Lambert, D. L. 1976, ApJ, 210, 694
- Torres, R. M., Loinard, L., Mioduszewski, A. J., & Rodríguez, L. F. 2007, ApJ, 671, 1813
- Turner, B. E., Zuckerman, B., Morris, M., & Palmer, P. 1978, ApJ, 219, L43
- Ulich, B. L. & Haars, R. W. 1976, ApJS, 30, 247
- Vastel, C., Caselli, P., Ceccarelli, C., *et al.* 2004, ApJ, 645, 1198
- Vastel, C., Ceccarelli, C., Lefloch, B., & Bachiller, R. 2014, ApJ, 795, L2
- van der Tak, F. F. S., Black, J. H., Schöier, F. L., Jansen, D. J., & van Dishoeck, E. F. 2007, A&A, 468, 627
- van Dishoeck, E. F., & Black, J. H. 1989, ApJ, 340, 273
- van Dishoeck, E. F., Blake, G. A., Jansen, D. J., & Groesbeck, T. D. 1995, ApJ, 447, 760
- van't Hoff, M. L. R., Tobin, J. H., Harsono, D., & van Dishoeck, E. F. 2018, A&A, 615, 83
- Vasyunin, A. I., & Herbst, E. 2012, ApJ, 769, 34

- Vasyunin, A. I., Caselli, P., Dulieu, F., & Jiménez-Serra, I. 2017, *ApJ*, 842, 33
- Visser, R., van Dishoeck, E. F., & Black, J. H. 2009, *A&A*, 503, 323
- Vrtilek, J. M., Gottlieb, C. A., Langer, W. D., Thaddeus, P., & Wilson, R. W. 1985, *ApJ*, 296, 35
- Vrtilek, J. M., Gottlieb, C. A., & Thaddeus, P. 1987, *ApJ*, 314, 716
- Wampfler, S. F., Jørgensen, J. K., Bizzarro, M., & Bisschop, S. E. 2014, *A&A*, 572, 24
- Watanabe, N., & Kouchi, A. 2002, *ApJ*, 571, L173
- Watanabe, Y., Sakai, N., Lindberg, J. E., Jørgensen, J. K., Bisschop, S. E. & Yamamoto, S. 2012, *ApJ*, 745, 126
- Watson, W. D., Anicich, V. G., & Huntress, W. T., Jr. 1976, *ApJ*, 205, L165
- Wilner, D. J. & Welch, W. J. 1994, *ApJ*, 427, 898
- Wilson, T. L., Mauersberger, R., Gensheimer, P. D., Muders, D., & Bieging, J. H. 1999, *ApJ*, 525, 343
- Wilson, T. L., & Rood, R. T. 1994, *ARA&A*, 32, 191
- Woods, P. M., & Willacy, K. 2009, *ApJ*, 693, 1360
- Woon, D. E., & Herbst, E. 1996, in IAU symposium 178, *Molecules in Astrophysics: Probes & Processes*, (Sterrewacht Leiden), Poster B33
- Woon, D. E., & Herbst, E. 1997, *ApJ*, 477, 204
- Yamaguchi, T., *et al.* 2012, *PASJ*, 64, 105
- Yang, B., Stancil, P. C., Balakrishnan, N., & Forrey, R. C. 2010, *ApJ*, 718, 1062
- Yen, H. W., Takakuwa, S., Ohashi, N., & Ho, P. T. P. 2013, *ApJ*, 772, 22
- Yoshida, K. 2016, Master thesis, The University of Tokyo
- Zhou, S., Evans, II, N. J., & Wang, Y. 1996, *ApJ*, 466, 296

APPENDIX A. Data of the line survey observation with NRO 45 m

Table A.1. Line parameters observed in the 3-mm band.

Frequency (GHz)	Molecule	Transition	E_u (cm^{-1})	ΔV_{LSR}^a (km s^{-1})	T_{mb}^a (K)	Δv^a (km s^{-1})	$\int T_{\text{mb}} dv$ (K km s^{-1})	rms (mK)
79.812333	c-C ₃ HD	2 _{1,2} -1 _{0,1}	4.1	-0.059(7)	0.477(6)	1.164(18)	0.600(9)	6.7
79.876710	HC ₅ N	30-29	41.3	-0.04(2)	0.118(5)	1.25(6)	0.170(5)	4.8
80.046678	C ₄ H ₂	9 _{1,9} -8 _{1,8}	22.7	-0.10(3)	0.145(6)	1.40(7)	0.239(9)	6.4
80.047537	c-CC ¹³ CH ₂	2 _{0,2} -1 _{1,1}	4.4	-0.07(2)	0.164(6)	1.26(5)	0.229(8)	7.4
80.076652	CH ₂ CO	4 _{1,4} -3 _{1,3}	15.7	0.02(5)	0.088(7)	1.36(11)	0.140(11)	8.2
80.383887	C ₄ H ₂	9 _{0,9} -8 _{0,8}	13.4	-0.22(2)	0.101(4)	1.19(5)	0.135(5)	4.2
80.412848	l-C ₃ H	2 ² Π _{1/2} , $J = 7/2-5/2$, $F = 3-2$, f	19.4	0.0(2)	0.015(4) ^b	1.6(5)	0.029(9)	6.1
80.420646	l-C ₃ H	2 ² Π _{1/2} , $J = 7/2-5/2$, $F = 4-3$, f	19.4	-0.1(2)	0.014(4) ^b	1.6(5)	0.030(6)	5.0
80.422052	l-C ₃ H	2 ² Π _{1/2} , $J = 7/2-5/2$, $F = 3-2$, f	19.4	0.4(3)	0.013(5) ^b	1.7(7)	0.043(7)	5.7
80.480188	CH ₂ CN	4 _{0,4} -3 _{0,3} , $J = 9/2-7/2$, $F_1 = 7/2-5/2$, $F = 9/2-7/2$	6.7	0.03(4)	0.0222(12)	1.50(9)	0.026(7)	5.0
80.480411	CH ₂ CN	4 _{0,4} -3 _{0,3} , $J = 9/2-7/2$, $F_1 = 9/2-7/2$, $F = 11/2-9/2$	6.7	0.03(4)	0.0267(15)	1.50(9)	0.029(7)	5.0
80.480454	CH ₂ CN	4 _{0,4} -3 _{0,3} , $J = 9/2-7/2$, $F_1 = 11/2-9/2$, $F = 13/2-11/2$	6.7	0.03(4)	0.0322(18)	1.50(9)	0.037(7)	5.0
80.481639	CH ₂ CN	4 _{0,4} -3 _{0,3} , $J = 9/2-7/2$, $F_1 = 7/2-5/2$, $F = 7/2-5/2$	6.7	0.03(4)	0.0161(9) ^c	1.50(9)	0.003(7)	5.0
80.482217	CH ₂ CN	4 _{0,4} -3 _{0,3} , $J = 9/2-7/2$, $F_1 = 9/2-7/2$, $F = 9/2-7/2$	6.7	0.03(4)	0.0202(11)	1.50(9)	0.004(7)	5.0
80.483158	CH ₂ CN	4 _{0,4} -3 _{0,3} , $J = 9/2-7/2$, $F_1 = 11/2-9/2$, $F = 11/2-9/2$	6.7	0.03(4)	0.0252(14)	1.50(9)	0.020(7)	5.0
80.484890	CH ₂ CN	4 _{0,4} -3 _{0,3} , $J = 9/2-5/2$, $F_1 = 11/2-7/2$, $F = 9/2-7/2$	6.7	0.03(4)	0.0195(11) ^c	1.50(9)	0.005(7)	5.0
80.487232	CH ₂ CN	4 _{0,4} -3 _{0,3} , $J = 7/2-7/2$, $F_1 = 9/2-9/2$, $F = 9/2-7/2$	6.7	0.03(4)	0.0218(12)	1.50(9)	0.039(7)	5.0
80.488519	CH ₂ CN	4 _{0,4} -3 _{0,3} , $J = 7/2-5/2$, $F_1 = 7/2-5/2$, $F = 7/2-5/2$	6.7	0.03(4)	0.0160(9) ^c	1.50(9)	0.022(7)	5.0
80.490250	CH ₂ CN	4 _{0,4} -3 _{0,3} , $J = 7/2-5/2$, $F_1 = 9/2-7/2$, $F = 11/2-9/2$	6.7	0.03(4)	0.0274(15)	1.50(9)	0.079(7)	5.0
80.490706	CH ₂ CN	4 _{0,4} -3 _{0,3} , $J = 7/2-5/2$, $F_1 = 7/2-5/2$, $F = 9/2-7/2$	6.7	0.03(4)	0.0218(12)	1.50(9)	0.071(7)	5.0

Table A.1 (continued)

Frequency (GHz)	Molecule	Transition	E_u (cm^{-1})	ΔV_{LSR}^a (km s^{-1})	T_{mb}^a (K)	Δv^a (km s^{-1})	$\int T_{\text{mb}} dv$ (K km s^{-1})	rms (mK)
80.491239	CH ₂ CN	$4_{0,4}-3_{0,3}, J=7/2-5/2, F_1=5/2-3/2, F=7/2-5/2$	6.7	0.03(4)	0.0171(9) ^c	1.50(9)	0.049(7)	5.0
80.577159	CH ₂ DCCH	$5_{1,5}-4_{1,4}$	11.9	0.26(12)	0.017(5) ^c	0.8(2)	0.014(4)	4.7
80.718829	C ₄ H ₂	$9_{1,8}-8_{1,7}$	22.9	-0.03(3)	0.140(8)	1.15(7)	0.164(11)	8.8
80.723180	c-C ₃ H ₂	$4_{2,2}-4_{1,3}$	20.0	-0.07(4)	0.124(5)	1.72(9)	0.253(9)	5.8
80.775347	c-CC ¹³ CH ₂	$3_{1,2}-3_{0,3}$	10.9	0.19(16)	0.021(5) ^c	1.5(4)	0.036(9)	6.2
80.832117	CH ₂ CO	$4_{0,4}-3_{0,3}$	6.7	0.04(6)	0.045(4)	1.26(14)	0.069(7)	5.3
80.902226	CH ₂ DCCH	$5_{0,5}-4_{0,4}$	8.1	0.02(6)	0.048(5)	1.16(14)	0.061(6)	6.1
80.928180	C ₃ S	$14-13$	20.2	-0.6(2)	0.019(5) ^c	1.5(5)	0.020(7)	6.2
81.150881	c- ¹³ CCCH ₂	$2_{0,2}-1_{1,1}$	4.4	0.09(18)	0.016(4) ^b	1.3(4)	0.021(7)	5.5
81.228145	CH ₂ DCCH	$5_{1,4}-4_{1,3}$	11.9	0.30(13)	0.043(12) ^c	0.9(3)	0.030(12)	13.0
81.505170	CCS	$N=6-5, J=7-6$	10.7	0.05(4)	0.207(11)	1.53(9)	0.384(17)	11.7
81.534111	HC ¹³ CCN	$9-8$	13.6	0.18(7)	0.064(9)	1.01(17)	0.059(12)	10.3
81.541981	HCC ¹³ CN	$9-8$	13.6	0.08(5)	0.077(5)	1.53(12)	0.120(10)	6.9
81.586230	CH ₂ CO	$4_{1,3}-3_{1,2}$	15.9	0.09(5)	0.097(7)	1.34(12)	0.141(13)	9.3
81.777856	C ₆ H	$2^2\Pi_{3/2}, J=59/2-57/2, e$	41.4	-0.37(15)	0.049(12) ^c	1.3(4)	0.078(19)	14.5
81.801237	C ₆ H	$2^2\Pi_{3/2}, J=59/2-57/2, f$	41.4	-0.05(18)	0.041(7) ^c	2.0(4)	0.081(15)	11.4
81.881468	HC ₃ N	$9-8$	13.7	0.063(5)	2.163(18)	1.308(12)	3.121(14)	13.1
82.093544	c-C ₃ H ₂	$2_{0,2}-1_{1,1}$	4.5	-0.150(13)	1.52(3)	1.40(3)	2.48(5)	34.3
82.303747	c- ¹³ CCCH ₂	$2_{1,2}-1_{0,1}$	4.4	-0.17(12)	0.048(11) ^c	1.1(3)	0.049(13)	12.6
82.384050	C ₆ H	$2^2\Pi_{1/2}, J=59/2-57/2, f$	57.3	0.12(16)	0.030(14) ^b	0.8(4)	0.009(10)	11.4
82.395089	l-C ₃ H ₂	$4_{1,4}-3_{1,3}$	16.2	-0.02(3)	0.182(9)	1.26(7)	0.249(13)	9.6

Table A.1 (continued)

Frequency (GHz)	Molecule	Transition	E_u (cm^{-1})	ΔV_{LSR}^a (km s^{-1})	T_{mb}^a (K)	Δv^a (km s^{-1})	$\int T_{\text{mb}} dv$ (K km s^{-1})	rms (mK)
82.424912	HCCCHO	9 _{1,9} -8 _{1,8}	15.9	0.05(13)	0.040(6)	1.6(3)	0.075(13)	8.5
82.539039	HC ₅ N	31-30	44.1	-0.05(6)	0.089(6)	1.55(13)	0.127(10)	8.1
82.966200	c-C ₃ H ₂	3 _{1,2} -3 _{0,3}	11.2	-0.101(7)	1.131(14)	1.255(17)	1.596(20)	15.2
83.165345	l-C ₃ H ₂	4 _{0,4} -3 _{0,3}	6.9	-0.05(2)	0.139(6)	1.11(5)	0.154(8)	6.6
83.207505	C ₂ H ₃ CN	9 _{1,9} -8 _{1,8}	15.4	-0.10(16)	0.016(8) ^b	0.7(4)	0.009(5)	6.0
83.474137	c-CC ¹³ CH ₂	3 _{2,2} -3 _{1,3}	11.0	-0.02(16)	0.022(5) ^c	1.5(4)	0.033(10)	6.8
83.541399	C ₅ H	² Π _{1/2} , $J = 35/2-33/2$, e	25.7	-0.01(5)	0.056(5)	1.15(12)	0.070(6)	6.1
83.546917	C ₅ H	² Π _{1/2} , $J = 35/2-33/2$, f	25.7	0.17(7)	0.047(5)	1.37(17)	0.066(7)	6.7
83.775819	HCCCHO	9 _{0,9} -8 _{0,8}	14.0	0.08(5)	0.049(5)	1.13(12)	0.063(7)	5.3
83.933699	l-C ₃ H ₂	4 _{1,3} -3 _{1,2}	16.3	-0.001(12)	0.195(4)	1.15(3)	0.248(6)	5.0
84.119329	¹³ CCH	$N = 1-0$, $J = 3/2-1/2$, $F_1 = 2-1$, $F = 5/2-3/2$	2.8	-0.00(5) × 10 ⁻⁴	0.048(5)	0.97(12)	0.048(6)	5.4
84.124143	¹³ CCH	$N = 1-0$, $J = 3/2-1/2$, $F_1 = 2-1$, $F = 3/2-1/2$	2.8	0.06(6)	0.037(5)	0.99(15)	0.036(6)	5.5
84.151352	¹³ CCH	$N = 1-0$, $J = 3/2-1/2$, $F_1 = 1-0$, $F = 1/2-1/2$	2.8	-0.05(18)	0.019(3) ^c	2.1(4)	0.060(7)	5.1
84.153305	¹³ CCH	$N = 1-0$, $J = 3/2-1/2$, $F_1 = 1-0$, $F = 3/2-1/2$	2.8	0.04(8)	0.031(4)	1.27(20)	0.033(5)	4.9
84.185635	c-CC ¹³ CH ₂	2 _{1,2} -1 _{0,1}	4.4	0.015(10)	0.215(4)	1.18(2)	0.276(5)	4.3
84.192487	¹³ CCH	$N = 1-0$, $J = 1/2-1/2$, $F_1 = 1-1$, $F = 1/2-3/2$	2.8	-0.2(2)	0.010(6) ^b	0.9(6)	0.006(5)	5.9
84.206865	¹³ CCH	$N = 1-0$, $J = 1/2-1/2$, $F_1 = 1-1$, $F = 3/2-3/2$	2.8	0.14(10)	0.023(5)	1.0(2)	0.018(5)	5.2
84.429814	DC ₃ N	10-9	15.5	0.20(3)	0.113(5)	1.14(6)	0.145(7)	5.5
84.521169	CH ₃ OH	5 _{-1,5} -4 _{0,4} , E	28.1	0.12(14)	0.029(4)	2.2(3)	0.060(8)	6.0
84.727688	c-C ₃ H ₂	3 _{2,2} -3 _{1,3}	11.2	0.150(5)	0.525(5)	1.154(12)	0.668(7)	5.5
84.748625	c-C ₃ HD	6 _{3,3} -6 _{2,4}	36.9	0.6(2)	0.007(4) ^b	0.8(6)	0.001(3)	3.8

Table A.1 (continued)

Frequency (GHz)	Molecule	Transition	E_u (cm^{-1})	ΔV_{LSR}^a (km s^{-1})	T_{mb}^a (K)	Δv^a (km s^{-1})	$\int T_{\text{mb}} dv$ (K km s^{-1})	rms (mK)
84.946000	C ₂ H ₃ CN	9 _{0,9} -8 _{0,8}	14.2	0.32(18)	0.014(4) ^b	1.3(4)	0.013(6)	5.1
85.139103 ^d	OCS	7-6	11.4	—	—	—	—	6.7
85.162223	HC ¹⁸ O ⁺	1-0	2.8	0.332(10)	0.341(6)	1.15(2)	0.423(7)	5.5
85.201340	HC ₅ N	32-31	46.9	0.39(4)	0.075(6)	1.18(11)	0.114(6)	6.1
85.229335	C ¹³ CH	$N=1-0, J=3/2-1/2, F_1=2-1, F=5/2-3/2$	2.8	0.46(4)	0.074(5)	1.29(11)	0.128(7)	6.4
85.232805	C ¹³ CH	$N=1-0, J=3/2-1/2, F_1=2-1, F=3/2-1/2$	2.8	0.46(7)	0.053(6)	1.14(16)	0.057(8)	6.9
85.247728	C ¹³ CH	$N=1-0, J=3/2-1/2, F_1=1-0, F=1/2-1/2$	2.8	0.25(14)	0.018(5) ^c	0.9(3)	0.011(5)	5.6
85.256988	C ¹³ CH	$N=1-0, J=3/2-1/2, F_1=1-0, F=3/2-1/2$	2.8	0.49(6)	0.046(5)	1.10(14)	0.053(7)	5.8
85.272335	c-C ₃ H	$3_{1,2}-3_{1,3}, J=5/2-5/2, F=3-3, 2-2$	10.3	0.31(13)	0.032(3)	2.4(3)	0.069(8)	5.8
85.296727	CH ₂ DOH	$1_{1,0}-1_{0,1}$	4.3	-0.2(2)	0.013(5) ^b	1.2(5)	0.011(6)	5.7
85.303990	C ¹³ CH	$N=1-0, J=1/2-1/2, F_1=1-1, F=1/2-3/2$	2.9	0.37(9)	0.025(5)	1.0(2)	0.030(6)	5.1
85.307459	C ¹³ CH	$N=1-0, J=1/2-1/2, F_1=1-1, F=3/2-3/2$	2.9	0.54(9)	0.040(7)	1.0(2)	0.031(8)	8.5
85.314092	C ¹³ CH	$N=1-0, J=1/2-1/2, F_1=0-1, F=1/2-1/2$	2.9	0.17(17)	0.020(6) ^b	1.2(4)	0.014(7)	6.9
85.331926	CC ¹³ CCH	$N=9-8, J=19/2-17/2$	14.2	...	0.014 ^b	5.0
85.338894	c-C ₃ H ₂	$2_{1,2}-1_{0,1}$	4.5	0.340(6)	2.76(3)	1.239(14)	3.80(3)	21.1
85.347890	HCS ⁺	2-1	4.3	0.50(4)	0.057(4)	1.18(10)	0.077(5)	5.3
85.361195	HCCCCHO	$9_{1,8}-8_{1,7}$	16.4	0.45(7)	0.033(4)	1.26(17)	0.040(5)	4.8
85.370342	CC ¹³ CCH	$N=9-8, J=17/2-15/2$	14.2	0.45(15)	0.018(6) ^c	0.9(3)	0.021(5)	5.5
85.450766	CH ₃ CCH	$J_K=5_2-4_2$	28.6	0.04(9)	0.071(9)	1.5(2)	0.106(17)	12.2
85.455667	CH ₃ CCH	$J_K=5_1-4_1$	13.6	-0.07(3)	0.50(3)	1.07(7)	0.602(15)	12.7
85.457300	CH ₃ CCH	$J_K=5_0-4_0$	8.6	-0.08(3)	0.56(3)	1.21(6)	0.844(14)	13.6

Table A.1 (continued)

Frequency (GHz)	Molecule	Transition	E_u (cm^{-1})	ΔV_{LSR}^a (km s^{-1})	T_{mb}^a (K)	Δv^a (km s^{-1})	$\int T_{\text{mb}} dv$ (K km s^{-1})	rms (mK)
85.531512	HCO_2^+	$4_{0,4}-3_{0,3}$	7.1	0.87(15)	0.045(12) ^c	1.1(3)	0.039(13)	13.6
85.634010	C_4H	$N=9-8, J=19/2-17/2$	14.3	0.048(6)	1.198(12)	1.101(13)	1.454(14)	11.3
85.656431	$\text{c-C}_3\text{H}_2$	$4_{3,2}-4_{2,3}$	20.2	-0.010(9)	0.464(8)	1.16(2)	0.571(9)	7.4
85.672580	C_4H	$N=9-8, J=17/2-15/2$	14.3	-0.011(6)	1.016(10)	1.197(13)	1.324(14)	11.3
85.694978	$\text{c-C}_3\text{H}$	$3_{1,2}-3_{1,3}, J=7/2-7/2, F=3-3$	10.3	-1.0(2)	0.030(5) ^c	2.4(5)	0.093(14)	9.4
85.702495	$\text{c-C}_3\text{H}$	$3_{1,2}-3_{1,3}, J=7/2-7/2, F=4-4$	10.3	-0.08(14)	0.046(9)	1.6(3)	0.111(13)	11.0
85.926278	NH_2D	$1_{1,1}-1_{0,1}$	14.4	0.2(9)	0.05(4)	2(2)	0.136(12)	8.3
86.054966	HC^{15}N	1-0	2.9	0.14(2)	0.101(5)	1.07(6)	0.113(7)	5.5
86.093950	SO	$N=2-1, J=2-1$	13.4	0.22(9)	0.034(4)	1.5(2)	0.067(6)	5.2
86.181391	CCS	$N=7-6, J=6-5$	16.2	0.00(8)	0.041(5)	1.34(19)	0.074(6)	5.7
86.338733	H^{13}CN	$J=1-0, F=1-1$	2.9	0.07(3)	0.136(6)	1.31(7)	0.205(7)	6.4
86.340163	H^{13}CN	$J=1-0, F=2-1$	2.9	0.07(2)	0.168(5)	1.32(5)	0.247(5)	4.9
86.342251	H^{13}CN	$J=1-0, F=0-1$	2.9	-0.0(2)	0.06(2)	1.2(5)	0.069(5)	4.5
86.593678	C_3O	9-8	14.4	0.00(4)	0.121(10)	1.10(10)	0.125(14)	11.7
86.670760	HCO	$1_{0,1}-0_{0,0}, J=3/2-1/2, F=2-1$	2.9	0.28(4)	0.144(7)	1.41(8)	0.228(13)	9.5
86.708360 ^e	HCO	$1_{0,1}-0_{0,0}, J=3/2-1/2, F=1-0$	2.9	0.34(6)	0.090(8)	1.38(14)	0.129(13)	10.0
86.708379 ^e	C_3S	15-14	23.1	0.41(6)	0.090(8)	1.38(14)	0.130(13)	10.0
86.754288	H^{13}CO^+	1-0	2.9	-0.011(5)	2.60(2)	1.271(12)	3.764(15)	11.4
86.777460	HCO	$1_{0,1}-0_{0,0}, J=1/2-1/2, F=1-1$	2.9	0.21(5)	0.106(9)	1.23(12)	0.134(13)	10.6
86.805780	HCO	$1_{0,1}-0_{0,0}, J=1/2-1/2, F=0-1$	2.9	-0.21(13)	0.043(9)	1.4(3)	0.030(11)	10.4
87.090825	HN^{13}C	1-0	2.9	0.31(7)	0.61(7)	1.38(17)	0.91(11)	85.5

Table A.1 (continued)

Frequency (GHz)	Molecule	Transition	E_u (cm^{-1})	ΔV_{LSR}^a (km s^{-1})	T_{mb}^a (K)	Δv^a (km s^{-1})	$\int T_{\text{mb}} dv$ (K km s^{-1})	rms (mK)
87.284105	CCH	$N=1-0, J=3/2-1/2, F=1-1$	2.9	0.025(5)	1.506(19)	1.154(12)	1.458(9)	8.4
87.312812	$\text{C}_2\text{H}_3\text{CN}$	$9_{1,8}-8_{1,7}$	16.1	...	0.030 ^c	7.9
87.316898	CCH	$N=1-0, J=3/2-1/2, F=2-1$	2.9	-0.050(6)	4.18(4)	1.271(14)	5.971(13)	10.4
87.328585	CCH	$N=1-0, J=3/2-1/2, F=1-0$	2.9	-0.056(5)	2.95(2)	1.244(11)	4.091(10)	8.1
87.347994	C_6H	${}^2\Pi_{3/2}, J=63/2-61/2, f$	47.2	0.2(5)	0.016(5) ^b	2.8(11)	0.046(15)	9.5
87.401989	CCH	$N=1-0, J=1/2-1/2, F=1-1$	2.9	-0.031(6)	2.86(3)	1.315(15)	4.213(17)	13.4
87.407165	CCH	$N=1-0, J=1/2-1/2, F=0-1$	2.9	0.018(6)	2.24(2)	1.135(14)	2.866(15)	12.4
87.435318	$\text{c-C}_3\text{H}_2$	$5_{4,2}-5_{3,3}$	31.5	-0.2(2)	0.032(7) ^c	2.0(5)	0.057(14)	10.4
87.446470	CCH	$N=1-0, J=1/2-1/2, F=1-0$	2.9	-0.002(6)	1.435(15)	1.224(15)	1.990(12)	9.9
87.863630	HC_5N	$33-32$	49.8	0.16(7)	0.057(7)	1.12(17)	0.063(9)	8.9
87.925237	HNCO	$4_{0,4}-3_{0,3}$	7.3	0.217(12)	0.196(5)	0.90(3)	0.187(6)	5.4
87.967595	C_6H	${}^2\Pi_{1/2}, J=63/2-61/2, f$	63.1	0.22(13)	0.019(6) ^c	0.9(3)	0.021(6)	5.8
88.166832	H^{13}CCCN	$10-9$	16.2	0.39(9)	0.030(6)	0.9(2)	0.018(5)	6.3
88.308034	C_4D	$N=10-9, J=21/2-19/2$	16.2	...	0.010 ^b	6.5
88.315148	C_5H	${}^2\Pi_{1/2}, J=37/2-35/2, e$	28.7	0.09(13)	0.028(9) ^c	0.8(3)	0.011(7)	8.9
88.318557	$1-\text{C}_3\text{D}$	${}^2\Pi_{1/2}, J=9/2-7/2, e$	7.9	0.5(3)	0.019(6) ^b	1.9(7)	0.032(15)	9.5
88.320879	C_5H	${}^2\Pi_{1/2}, J=37/2-35/2, f$	28.7	0.24(16)	0.028(6) ^c	1.6(4)	0.036(10)	8.5
88.344000	C_4D	$N=10-9, J=19/2-17/2$	16.2	-0.20(13)	0.025(7) ^c	1.0(3)	0.021(7)	7.3
88.345803	$1-\text{C}_3\text{D}$	${}^2\Pi_{1/2}, J=9/2-7/2, f$	7.9	-0.0(3)	0.013(6) ^b	1.0(6)	0.016(7)	7.5
88.630416	HCN	$J=1-0, F=1-1$	3.0	-0.19(4)	0.75(3)	2.00(10)	1.787(14)	9.0
88.631848	HCN	$J=1-0, F=2-1$	3.0	-0.23(3)	1.14(3)	2.00(7)	2.705(14)	9.1

Table A.1 (continued)

Frequency (GHz)	Molecule	Transition	E_u (cm^{-1})	ΔV_{LSR}^a (km s^{-1})	T_{mb}^a (K)	Δv^a (km s^{-1})	$\int T_{\text{mb}} dv$ (K km s^{-1})	rms (mK)
88.633936	HCN	$J = 1-0, F = 0-1$	3.0	-0.00(4)	0.72(4)	1.51(10)	1.403(16)	11.4
88.865690	H^{15}NC	1-0	3.0	0.00(3)	0.139(7)	0.96(6)	0.122(7)	7.4
88.940236	C_4H_2	$10_{1,10}-9_{1,9}$	25.7	-0.12(3)	0.113(5)	1.24(6)	0.163(6)	5.9
89.045583	C_3N	$N = 9-8, J = 19/2-17/2$	14.9	0.02(9)	0.030(10)	0.7(3)	0.017(5)	6.3
89.064347	C_3N	$N = 9-8, J = 17/2-15/2$	14.9	...	0.010 ^b	8.1
89.188525	HCO^+	1-0	3.0	-0.23(3)	2.27(5)	2.68(7)	6.73(5)	27.9
89.307563	C_4H_2	$10_{2,8}-9_{2,7}$	54.0	-0.45(18)	0.017(5) ^b	1.2(4)	0.016(6)	6.0
89.314548	C_4H_2	$10_{0,10}-9_{0,9}$	16.4	-0.15(3)	0.081(4)	1.24(8)	0.121(6)	5.2
89.407817	CH_2DOH	$2_{0,2}-1_{0,1}$	4.5	-0.33(11)	0.019(8) ^c	0.7(3)	0.012(5)	6.1
89.419300	HCCNC	9-8	14.9	0.04(14)	0.022(6) ^c	1.0(3)	0.014(6)	6.8
89.687047	C_4H_2	$10_{1,9}-9_{1,8}$	25.9	-0.051(19)	0.135(5)	1.17(5)	0.171(7)	5.6
90.525890	HC_5N	34-33	52.8	0.04(7)	0.049(6)	1.01(16)	0.068(6)	6.6
90.593059	HC^{13}CCN	10-9	16.6	...	0.017 ^b	8.9
90.601777	HCC^{13}CN	10-9	16.6	0.00(14)	0.034(8) ^c	1.2(3)	0.048(12)	9.9
90.663568	HNC	1-0	3.0	0.222(7)	2.286(19)	1.654(16)	4.133(12)	8.3
90.686381	CCS	$N = 7-6, J = 7-6$	18.2	0.30(10)	0.047(6)	1.4(2)	0.060(9)	8.6
90.979023	HC_3N	10-9	16.7	0.192(5)	2.44(3)	1.059(13)	2.850(6)	6.4
91.494349	c- C_3H	$2_{1,2}-1_{1,1}, J = 5/2-3/2, F = 3-2$	3.1	0.093(8)	0.404(6)	1.077(20)	0.491(5)	5.8
91.497608	c- C_3H	$2_{1,2}-1_{1,1}, J = 5/2-3/2, F = 2-1$	3.1	0.183(14)	0.247(6)	1.14(3)	0.306(6)	5.8
91.512969	c- C_3H	$2_{1,2}-1_{1,1}, J = 5/2-3/2, F = 2-2$	3.1	0.15(10)	0.025(6)	0.9(2)	0.018(5)	6.1
91.572516	HCCCHO	$10_{1,10}-9_{1,9}$	18.9	-0.22(16)	0.019(5) ^b	1.2(4)	0.020(6)	6.3

Table A.1 (continued)

Frequency (GHz)	Molecule	Transition	E_u (cm^{-1})	ΔV_{LSR}^a (km s^{-1})	T_{mb}^a (K)	Δv^a (km s^{-1})	$\int T_{\text{mb}} dv$ (K km s^{-1})	rms (mK)
91.681696	c-C ₃ H	2 _{1,2} -1 _{1,1} , $J = 3/2-1/2$, $F = 1-1$	3.1	0.03(6)	0.033(4)	0.90(14)	0.032(4)	4.7
91.692752	c-C ₃ H	2 _{1,2} -1 _{1,1} , $J = 3/2-1/2$, $F = 1-0$	3.1	-0.05(3)	0.093(4)	1.25(6)	0.137(5)	4.6
91.699471	c-C ₃ H	2 _{1,2} -1 _{1,1} , $J = 3/2-1/2$, $F = 2-1$	3.1	0.061(12)	0.226(5)	1.19(3)	0.299(5)	5.3
91.747372	c-C ₃ H	2 _{1,2} -1 _{1,1} , $J = 3/2-3/2$, $F = 1-1$	3.1	0.14(6)	0.043(5)	0.99(14)	0.045(5)	5.7
91.751320	HCNO	4-3	7.7	0.13(15)	0.015(4) ^c	1.1(3)	0.023(6)	5.0
91.780518	c-C ₃ H	2 _{1,2} -1 _{1,1} , $J = 3/2-3/2$, $F = 2-2$	3.1	0.12(9)	0.039(4)	1.8(2)	0.091(7)	6.0
91.985314	CH ₃ CN	$J_K = 5_1-4_1$	14.2	0.15(8)	0.035(5)	1.10(19)	0.029(6)	6.4
91.987088	CH ₃ CN	$J_K = 5_0-4_0$	9.2	0.06(8)	0.044(6)	1.21(19)	0.050(9)	7.8
92.227853	C ₂ O	$N = 4-3$, $J = 5-4$	7.7	0.24(14)	0.021(5) ^c	1.2(3)	0.031(6)	6.2
92.363286	C ₂ O	$N = 4-3$, $J = 4-3$	8.0	-0.09(18)	0.025(9) ^b	0.9(4)	0.017(9)	10.4
92.426250	C ₂ H ₃ CN	10 _{1,10} -9 _{1,9}	18.5	-0.05(15)	0.041(14) ^b	0.9(4)	0.023(13)	15.3
92.517433	c-H ₂ C ₃ O	7 _{1,7} -6 _{1,6}	13.2	...	0.038 ^b	13.6
92.872375	DC ₃ N	11-10	18.6	0.14(6)	0.130(13)	1.14(13)	0.162(15)	15.6
92.894848	C ₆ H	${}^2\Pi_{3/2}$, $J = 67/2-65/2$, f	53.3	...	0.035 ^b	20.2
92.981601	HDCS	${}^3_{0,3}-2_{0,2}$	6.2	0.27(8)	0.053(11)	0.78(17)	0.048(11)	11.2
93.088901	C ₅ H	${}^2\Pi_{1/2}$, $J = 39/2-37/2$, e	31.8	0.18(11)	0.043(9)	1.0(3)	0.061(10)	10.4
93.094854	C ₅ H	${}^2\Pi_{1/2}$, $J = 39/2-37/2$, f	31.8	-0.3(3)	0.028(8) ^b	1.8(6)	0.043(16)	12.8
93.171925	N ₂ H ⁺	$J = 1-0$, $F_1 = 1-1$	3.1	-0.00(4)	1.17(8)	1.02(9)	1.440(19)	12.4
93.173763	N ₂ H ⁺	$J = 1-0$, $F_1 = 2-1$	3.1	0.30(4)	1.22(5)	1.79(9)	2.26(2)	10.3
93.176254	N ₂ H ⁺	$J = 1-0$, $F_1 = 0-1$	3.1	0.18(8)	0.57(9)	0.92(16)	0.544(15)	10.4
93.188123	HC ₅ N	35-34	56.0	0.04(11)	0.077(12)	1.23(20)	0.124(17)	12.0

Table A.1 (continued)

Frequency (GHz)	Molecule	Transition	E_u (cm^{-1})	ΔV_{LSR}^a (km s^{-1})	T_{mb}^a (K)	Δv^a (km s^{-1})	$\int T_{\text{mb}} dv$ (K km s^{-1})	rms (mK)
93.580859	CH ₃ CHO	5 _{1,5} -4 _{1,4} , A ⁺	10.9	...	0.019 ^b	13.0
93.595276	CH ₃ CHO	5 _{-1,5} -4 _{-1,4} , E	11.0	0.3(4)	0.028(14) ^b	1.5(9)	0.06(2)	14.7
93.870107	CCS	N = 7-6, J = 8-7	13.8	-0.00(4)	0.231(9)	0.97(5)	0.257(10)	8.4
94.088936	CHDCO	5 _{0,5} -4 _{0,4}	9.4	...	0.038	9.1
94.276636	C ₂ H ₃ CN	10 _{0,10} -9 _{0,9}	17.3	...	0.021 ^b	8.4
94.371354	c-C ₃ D ₂	3 _{0,3} -2 _{1,2}	6.8	0.0(2)	0.035(9) ^c	1.1(3)	0.028(12)	9.2
94.833681	HCCCHO	10 _{1,9} -9 _{1,8}	19.5	0.21(18)	0.044(18)	1.0(5)	0.048(12)	7.9
95.150393	C ₄ H	N = 10-9, J = 21/2-19/2	17.5	0.132(6)	0.93(2)	1.08(3)	1.057(11)	7.3
95.188947	C ₄ H	N = 10-9, J = 19/2-17/2	17.5	0.135(7)	0.87(3)	1.07(4)	1.001(16)	10.0
95.850335	HC ₅ N	36-35	59.2	0.03(7)	0.068(11)	1.2(3)	0.094(11)	8.0
95.947340	CH ₃ CHO	5 _{0,5} -4 _{0,4} , E	9.7	-0.1(2)	0.024(7) ^c	1.5(5)	0.029(11)	7.2
95.963380	CH ₃ CHO	5 _{0,5} -4 _{0,4} , A ⁺	9.6	0.0(2)	0.023(18) ^c	1.0(10)	0.013(9)	7.4
95.994082	c-C ₃ HD	2 _{1,1} -1 _{1,0}	5.3	0.09(4)	0.131(7)	0.99(6)	0.142(9)	6.1
96.214619	C ₃ O	10-9	17.7	...	0.091	6.2
96.412949	C ³⁴ S	2-1	4.8	-0.02(4)	0.169(8)	1.76(10)	0.353(13)	6.3
96.691587	CH ₂ DCCH	6 _{1,6} -5 _{1,5}	15.1	...	0.039	7.9
96.739362	CH ₃ OH	2 _{-1,2} -1 _{-1,1} , E	8.7	0.088(10)	0.496(19)	1.09(5)	0.595(13)	8.2
96.741375	CH ₃ OH	2 _{0,2} -1 _{0,1} , A ⁺	4.8	-0.021(12)	0.827(11)	0.912(16)	0.838(13)	8.8
96.744550	CH ₃ OH	2 _{0,2} -1 _{0,1} , E	14.0	-0.05(10)	0.082(10)	1.03(14)	0.090(13)	8.4
96.983001	H ¹³ CCCN	11-10	19.4	0.16(15)	0.043(14)	1.1(4)	0.066(14)	8.7
97.080728	CH ₂ DCCH	6 _{0,6} -5 _{0,5}	11.3	...	0.093	6.4

Table A.1 (continued)

Frequency (GHz)	Molecule	Transition	E_u (cm^{-1})	ΔV_{LSR}^a (km s^{-1})	T_{mb}^a (K)	Δv^a (km s^{-1})	$\int T_{\text{mb}} dv$ (K km s^{-1})	rms (mK)
97.172064	C ³³ S	2-1	4.9	0.64(15)	0.044(9)	1.0(2)	0.040(14)	8.9
97.175928	C ₄ D	$N=11-10, J=21/2-19/2$	19.5	-0.0(3)	0.027(14) ^b	1.0(7)	0.031(16)	10.2
97.472736	CH ₂ DCCH	6 _{1,5} -5 _{1,4}	15.2	...	0.028 ^b	18.4
97.761978	c-C ₃ D ₂	3 _{1,3} -2 _{0,2}	6.9	...	0.042	8.8
97.833632	C ₄ H ₂	11 _{1,11} -10 _{1,10}	29.0	0.07(5)	0.132(9)	1.05(9)	0.132(13)	8.5
97.862577	C ₅ H	$^2\Pi_{1/2}, J=41/2-39/2, e$	35.0	-0.1(3)	0.017(6) ^b	1.9(8)	0.040(12)	7.1
97.868769	C ₅ H	$^2\Pi_{1/2}, J=41/2-39/2, f$	35.0	...	0.037	6.8
97.980953	CS	2-1	4.9	0.05(2)	1.34(2)	2.58(5)	3.67(2)	9.1
97.995166	l-C ₃ H	$^2\Pi_{1/2}, J=9/2-7/2, F=5-4, e$	8.7	...	0.480	26.0
97.995913	l-C ₃ H	$^2\Pi_{1/2}, J=9/2-7/2, F=4-3, e$	8.7	0.07(16)	0.19(9)	1.1(7)	0.34(3)	26.4
98.011611	l-C ₃ H	$^2\Pi_{1/2}, J=9/2-7/2, F=5-4, f$	8.7	0.04(12)	0.28(6)	0.9(2)	0.273(10)	8.1
98.012524	l-C ₃ H	$^2\Pi_{1/2}, J=9/2-7/2, F=4-3, f$	8.7	...	0.253	7.8
98.244930	C ₄ H ₂	11 _{0,11} -10 _{0,10}	19.7	-0.00(7)	0.064(6)	1.06(17)	0.075(9)	6.1
98.512524	HC ₅ N	37-36	62.4	0.14(9)	0.050(7)	1.10(16)	0.077(7)	5.6
98.655094	C ₄ H ₂	11 _{1,10} -10 _{1,9}	29.1	$-0.00(5) \times 10^{-4}$	0.162(12)	0.83(8)	0.161(7)	6.0
98.863328	CH ₃ CHO	5 _{1,4} -4 _{1,3} , E	11.5	...	0.023	5.7
98.900948	CH ₃ CHO	5 _{1,4} -4 _{1,3} , A ⁻	11.5	0.00(15)	0.028(6)	1.0(2)	0.028(7)	5.8
98.940009	C ₃ N	$N=10-9, J=21/2-19/2$	18.2	0.00(17)	0.033(7)	1.0(2)	0.033(8)	6.7
98.958770	C ₃ N	$N=10-9, J=19/2-17/2$	18.2	0.13(14)	0.034(12)	0.9(4)	0.028(7)	6.0
99.299870	SO	$N=2-1, J=3-2$	6.4	-0.00(2)	0.58(2)	1.26(5)	0.884(11)	6.7
99.325217 ^d	(CH ₃) ₂ O	4 _{1,4} -3 _{0,3} , EE	7.1	-	-	-	-	6.1

Table A.1 (continued)

Frequency (GHz)	Molecule	Transition	E_u (cm^{-1})	ΔV_{LSR}^a (km s^{-1})	T_{mb}^a (K)	Δv^a (km s^{-1})	$\int T_{\text{mb}} dv$ (K km s $^{-1}$)	rms (mK)
99.354250	HCCNC	10-9	18.2	0.07(13)	0.031(7)	1.3(4)	0.040(8)	6.0
99.461077	c-H ₂ C ₃ O	7 _{3,4} -6 _{3,3}	20.7	...	0.018 ^b	6.4
99.651849	HC ¹³ CCN	11-10	19.9	0.05(10)	0.055(10)	1.0(2)	0.061(9)	6.0
99.661467	HCC ¹³ CN	11-10	19.9	-0.05(10)	0.050(8)	0.91(19)	0.052(8)	5.4
99.866521	CCS	$N = 8-7, J = 7-6$	19.6	0.03(17)	0.033(5)	2.0(4)	0.062(11)	6.5
100.076392	HC ₃ N	11-10	20.0	-0.057(5)	3.140(16)	0.849(6)	2.942(7)	6.3
100.094514	CH ₂ CO	5 _{1,5} -4 _{1,4}	19.1	0.08(3)	0.165(7)	0.87(5)	0.159(8)	6.1
100.598231	CH ₂ CN	5 _{0,5} -4 _{0,4} , $J = 11/2-9/2, F_1 = 9/2-7/2, F = 11/2-9/2$	10.1	-0.00(3)	0.0381(19)	0.84(5)	0.033(11)	6.6
100.598399	CH ₂ CN	5 _{0,5} -4 _{0,4} , $J = 11/2-9/2, F_1 = 11/2-9/2, F = 13/2-11/2$	10.1	-0.00(3)	0.045(2)	0.84(5)	0.047(11)	6.6
100.598421	CH ₂ CN	5 _{0,5} -4 _{0,4} , $J = 11/2-9/2, F_1 = 13/2-11/2, F = 15/2-13/2$	10.1	-0.00(3)	0.052(3)	0.84(5)	0.055(11)	6.6
100.599454	CH ₂ CN	5 _{0,5} -4 _{0,4} , $J = 11/2-9/2, F_1 = 9/2-7/2, F = 9/2-7/2$	10.1	-0.00(3)	0.0299(15)	0.84(5)	0.050(11)	6.6
100.599932	CH ₂ CN	5 _{0,5} -4 _{0,4} , $J = 11/2-9/2, F_1 = 11/2-9/2, F = 11/2-9/2$	10.1	-0.00(3)	0.0359(18)	0.84(5)	0.059(11)	6.6
100.600535	CH ₂ CN	5 _{0,5} -4 _{0,4} , $J = 11/2-9/2, F_1 = 9/2-7/2, F = 7/2-5/2$	10.1	-0.00(3)	0.0228(11) ^c	0.84(5)	0.039(12)	6.6
100.600607	CH ₂ CN	5 _{0,5} -4 _{0,4} , $J = 11/2-9/2, F_1 = 13/2-11/2, F = 13/2-11/2$	10.1	-0.00(3)	0.043(2)	0.84(5)	0.042(11)	6.6
100.601342	CH ₂ CN	5 _{0,5} -4 _{0,4} , $J = 11/2-9/2, F_1 = 11/2-9/2, F = 9/2-7/2$	10.1	-0.00(3)	0.0286(14)	0.84(5)	0.025(11)	6.6
100.602444	CH ₂ CN	5 _{0,5} -4 _{0,4} , $J = 11/2-9/2, F_1 = 13/2-11/2, F = 11/2-9/2$	10.1	-0.00(3)	0.0355(18)	0.84(5)	0.010(12)	6.6
100.606261	CH ₂ CN	5 _{0,5} -4 _{0,4} , $J = 9/2-7/2, F_1 = 11/2-9/2, F = 11/2-9/2$	10.1	-0.00(3)	0.0377(19)	0.84(5)	0.031(11)	6.6
100.607363	CH ₂ CN	5 _{0,5} -4 _{0,4} , $J = 9/2-7/2, F_1 = 9/2-7/2, F = 9/2-7/2$	10.1	-0.00(3)	0.0298(15)	0.84(5)	0.026(12)	6.6
100.608262	CH ₂ CN	5 _{0,5} -4 _{0,4} , $J = 9/2-7/2, F_1 = 7/2-5/2, F = 7/2-5/2$	10.1	-0.00(3)	0.0235(12) ^c	0.84(5)	0.027(11)	6.6
100.608813	CH ₂ CN	5 _{0,5} -4 _{0,4} , $J = 9/2-7/2, F_1 = 11/2-9/2, F = 13/2-11/2$	10.1	-0.00(3)	0.045(2)	0.84(5)	0.036(12)	6.6
100.609199	CH ₂ CN	5 _{0,5} -4 _{0,4} , $J = 9/2-7/2, F_1 = 9/2-7/2, F = 11/2-9/2$	10.1	-0.00(3)	0.0376(19)	0.84(5)	0.034(11)	6.6

Table A.1 (continued)

Frequency (GHz)	Molecule	Transition	E_u (cm^{-1})	ΔV_{LSR}^a (km s^{-1})	T_{mb}^a (K)	Δv^a (km s^{-1})	$\int T_{\text{mb}} dv$ (K km s^{-1})	rms (mK)
100.609626	CH ₂ CN	$5_{0,5-4_{0,4}}, J=9/2-7/2, F_1=7/2-5/2, F=9/2-7/2$	10.1	-0.00(3)	0.0311(16)	0.84(5)	0.021(11)	6.6
100.609662	CH ₂ CN	$5_{0,5-4_{0,4}}, J=9/2-7/2, F_1=9/2-7/2, F=7/2-5/2$	10.1	-0.00(3)	0.0216(11) ^c	0.84(5)	0.012(11)	6.6
100.610072	CH ₂ CN	$5_{0,5-4_{0,4}}, J=9/2-7/2, F_1=11/2-9/2, F=9/2-7/2$	10.1	-0.00(3)	0.0292(15)	0.84(5)	0.013(12)	6.6
100.683368 ^d	HCOOCH ₃	$9_{0,9-8_{0,8}}, A$	17.3	-	-	-	-	5.5
100.807872	c-C ₃ D	$2_{1,1-1_{1,0}}, J=5/2-3/2$	3.7	...	0.052	8.6
101.036630	CH ₂ CO	$5_{0,5-4_{0,4}}$	10.1	0.0(8)	0.051(12)	2.3(20)	0.071(18)	10.1
101.174677	HC ₃ N	38-37	65.8	0.0(2)	0.029(10) ^b	1.4(6)	0.036(15)	10.2
101.314818	DC ₃ N	12-11	22.0	...	0.081	10.7
101.477810	H ₂ CS	$3_{1,3-2_{1,2}}$	15.9	0.03(7)	0.128(9)	0.82(9)	0.090(12)	8.9
101.981429	CH ₂ CO	$5_{1,4-4_{1,3}}$	19.3	0.18(5)	0.137(17)	1.16(19)	0.142(19)	11.8
102.298030	HCCCHO	$11_{0,11-10_{0,10}}$	20.5	...	0.025 ^b	12.4
102.423019	c-C ₃ HD	$4_{1,3-4_{0,4}}$	15.5	0.19(13)	0.051(9)	0.91(18)	0.030(11)	7.9
102.540145	CH ₃ CCH	$J_K=6_2-5_2$	32.1	-0.00(5)	0.111(7)	0.92(7)	0.108(10)	7.2
102.546024	CH ₃ CCH	$J_K=6_1-5_1$	17.0	0.012(16)	0.585(10)	0.77(2)	0.498(10)	7.6
102.547984	CH ₃ CCH	$J_K=6_0-5_0$	12.0	0.048(14)	0.658(9)	0.789(16)	0.589(10)	7.7
102.636255	C ₅ H	$^2\Pi_{1/2}, J=43/2-41/2, e$	38.5	-0.01(13)	0.041(7)	1.6(3)	0.063(11)	7.3
102.642695	C ₅ H	$^2\Pi_{1/2}, J=43/2-41/2, f$	38.5	...	0.043	6.9
102.992379	l-C ₃ H ₂	$5_{1,5-4_{1,4}}$	19.6	0.03(6)	0.29(3)	0.75(10)	0.240(13)	10.4
103.040452	H ₂ CS	$3_{0,3-2_{0,2}}$	6.9	0.08(5)	0.153(9)	0.87(6)	0.162(9)	8.3
103.069925	c-H ₂ C ₃ O	$7_{1,6-6_{1,5}}$	14.7	0.10(15)	0.043(17)	0.9(4)	0.042(10)	7.1
103.319276	l-C ₃ H	$^2\Pi_{3/2}, J=9/2-7/2, F=5-4, f$	22.9	0.3(5)	0.029(7) ^c	4.2(11)	0.11(3)	8.4

Table A.1 (continued)

Frequency (GHz)	Molecule	Transition	E_u (cm^{-1})	ΔV_{LSR}^a (km s^{-1})	T_{mb}^a (K)	Δv^a (km s^{-1})	$\int T_{\text{mb}} dv$ (K km s^{-1})	rms (mK)
103.319786	l-C ₃ H	${}^2\Pi_{3/2}, J=9/2-7/2, F=4-3, f$	22.9	1.7(5)	0.027(7) ^b	3.9(12)	0.08(3)	11.6
103.372483	l-C ₃ H	${}^2\Pi_{3/2}, J=9/2-7/2, F=5-4, e$	22.9	...	0.038	9.0
103.373094	l-C ₃ H	${}^2\Pi_{3/2}, J=9/2-7/2, F=4-3, e$	22.9	-0.20(14)	0.042(9)	1.2(3)	0.077(8)	6.4
103.575395	C ₂ H ₃ CN	11 _{0,11} -10 _{0,10}	20.8	0.4(4)	0.017(6) ^b	2.3(9)	0.048(17)	7.8
103.640759	CCS	$N=8-7, J=8-7$	21.6	-0.08(14)	0.039(7)	0.86(20)	0.046(7)	6.2
103.836817	HC ₅ N	39-38	69.3	...	-1.765	7.3
103.952926	l-C ₃ H ₂	5 _{0,5} -4 _{0,4}	10.4	0.06(3)	0.179(14)	0.87(8)	0.169(9)	6.6
104.187126	c-C ₃ HD	3 _{0,3} -2 _{1,2}	7.5	0.092(14)	0.74(8)	0.79(8)	0.623(10)	8.1
104.297349	CC ¹³ CCCH	$N=11-10, J=23/2-21/2$	20.9	...	0.019 ^b	10.6
104.302170	HCCCHO	11 _{1,10} -10 _{1,9}	23.0	-0.3(2)	0.023(11) ^b	1.3(5)	0.021(11)	8.3
104.335725	CC ¹³ CCH	$N=11-10, J=21/2-19/2$	20.9	...	0.025 ^b	11.3
104.617040	H ₂ CS	3 _{1,2} -2 _{1,1}	16.1	0.14(5)	0.113(9)	1.19(10)	0.154(14)	8.7
104.666568	C ₄ H	$N=11-10, J=23/2-21/2$	20.9	0.136(8)	0.717(8)	1.158(14)	0.902(14)	8.8
104.705108	C ₄ H	$N=11-10, J=21/2-19/2$	21.0	0.086(9)	0.655(9)	1.216(19)	0.863(15)	9.4
104.711404	¹³ C ¹⁸ O	1-0	3.5	0.33(8)	0.076(11)	1.1(2)	0.083(11)	9.0
104.799707	c-C ₃ HD	3 _{1,3} -2 _{1,2}	7.6	...	0.100	9.5
104.915583	l-C ₃ H ₂	5 _{1,4} -4 _{1,3}	19.8	0.14(4)	0.213(19)	0.93(10)	0.193(15)	10.5
105.476475	c-H ₂ C ₃ O	8 _{1,8} -7 _{1,7}	16.7	-0.07(14)	0.040(7)	1.5(3)	0.064(11)	7.7
105.799113	H ¹³ CCCN	12-11	22.9	...	0.041 ^b	15.0
105.835363	C ₃ O	11-10	21.2	0.15(10)	0.088(18)	1.0(2)	0.090(15)	13.0
106.007682	C ₄ D	$N=12-11, J=23/2-21/2$	23.0	...	0.030 ^b	11.4

Table A.1 (continued)

Frequency (GHz)	Molecule	Transition	E_u (cm^{-1})	ΔV_{LSR}^a (km s^{-1})	T_{mb}^a (K)	Δv^a (km s^{-1})	$\int T_{\text{mb}} dv$ (K km s^{-1})	rms (mK)
106.256108	c-C ₃ HD	4 _{2,3} -4 _{1,4}	15.6	-0.06(7)	0.061(7)	1.10(13)	0.043(8)	6.5
106.347726	CCS	$N = 8-7, J = 9-8$	17.4	0.09(5)	0.098(6)	1.48(11)	0.166(10)	6.8
106.498910	HC ₅ N	40-39	72.8	-0.00(18) $\times 10^{-4}$	0.024(8) ^c	1.2(5)	0.032(9)	7.1
106.726849	C ₄ H ₂	12 _{1,12} -11 _{1,11}	32.5	0.03(5)	0.112(9)	1.03(9)	0.116(13)	8.8
106.811090	c-C ₃ HD	3 _{0,3} -2 _{0,2}	7.5	0.07(4)	0.125(7)	0.98(6)	0.132(9)	6.4
106.913563	HCO ₂ ⁺	5 _{0,5} -4 _{0,4}	10.7	...	0.015 ^b	6.5
107.013803	CH ₃ OH	3 _{1,3} -4 _{0,4} , A ⁺	19.7	-0.00(13)	-0.030(7)	1.2(3)	-0.029(8)	6.1
107.175007	C ₄ H ₂	12 _{0,12} -11 _{0,11}	23.2	-0.14(5)	0.084(17)	0.85(19)	0.078(7)	5.4
107.409891	C ₅ H	² $\Pi_{1/2}, J = 45/2-43/2, e$	42.0	...	0.018 ^b	8.3
107.416595	C ₅ H	² $\Pi_{1/2}, J = 45/2-43/2, f$	42.0	0.28(17)	0.026(8) ^c	1.2(5)	0.039(9)	7.1
107.423671	c-C ₃ HD	3 _{1,3} -2 _{0,2}	7.6	0.030(9)	0.589(8)	0.966(14)	0.625(10)	6.8
107.622954	C ₄ H ₂	12 _{1,11} -11 _{1,10}	32.7	0.09(7)	0.097(10)	1.13(12)	0.124(15)	9.8
107.971554	l-C ₃ D	² $\Pi_{1/2}, J = 11/2-9/2, f$	11.5	...	0.024 ^b	8.2
108.039986	l-C ₃ D	² $\Pi_{1/2}, J = 11/2-9/2, e$	11.5	-0.28(20)	0.027(7) ^c	1.6(5)	0.046(14)	7.5
108.426889	¹³ CN	$N = 1-0, J = 1/2-1/2, F_1 = 0-1, F = 1-2$	3.6	-0.0(3)	0.025(9) ^c	0.8(4)	0.006(6)	6.3
108.631121	¹³ CN	$N = 1-0, J = 1/2-1/2, F_1 = 1-0, F = 0-1$	3.6	...	0.025 ^b	8.5
108.636923	¹³ CN	$N = 1-0, J = 1/2-1/2, F_1 = 1-0, F = 1-1$	3.6	0.11(11)	0.052(9)	0.92(18)	0.054(9)	7.9
108.638212	¹³ CN	$N = 1-0, J = 3/2-1/2, F_1 = 1-1, F = 1-0$	3.6	0.29(13)	0.037(8)	1.1(3)	0.050(9)	7.6
108.644346	¹³ CN	$N = 1-0, J = 3/2-1/2, F_1 = 1-1, F = 0-1$	3.6	...	0.022 ^b	9.0
108.651297	¹³ CN	$N = 1-0, J = 1/2-1/2, F_1 = 1-0, F = 2-1$	3.6	...	0.064	9.1
108.657646	¹³ CN	$N = 1-0, J = 3/2-1/2, F_1 = 1-1, F = 2-2$	3.6	0.11(9)	0.071(12)	1.1(2)	0.091(16)	10.7

Table A.1 (continued)

Frequency (GHz)	Molecule	Transition	E_u (cm^{-1})	ΔV_{LSR}^a (km s^{-1})	T_{mb}^a (K)	Δv^a (km s^{-1})	$\int T_{\text{mb}} dv$ (K km s^{-1})	rms (mK)
108.710532	HC ¹³ CCN	12-11	23.6	...	0.017 ^b	10.0
108.720999	HCC ¹³ CN	12-11	23.6	0.01(11)	0.060(15)	1.1(3)	0.057(14)	11.6
108.780201	¹³ CN	$N=1-0, J=3/2-1/2, F_1=2-1, F=3-2$	3.6	0.04(5)	0.127(12)	0.99(11)	0.146(11)	9.8
108.782374	¹³ CN	$N=1-0, J=3/2-1/2, F_1=2-1, F=2-1$	3.6	-0.05(14)	0.069(17)	0.9(3)	0.051(12)	11.6
108.786982	¹³ CN	$N=1-0, J=3/2-1/2, F_1=2-1, F=1-0$	3.6	...	0.034 ^b	14.8
108.793753	¹³ CN	$N=1-0, J=3/2-1/2, F_1=2-1, F=1-1$	3.6	...	0.021 ^b	7.2
108.796400	¹³ CN	$N=1-0, J=3/2-1/2, F_1=2-1, F=2-2$	3.6	...	0.025 ^c	8.1
108.893963	CH ₃ OH	$0_{0,0}-1_{-1,1}, E$	9.1	0.07(5)	0.18(4)	0.77(17)	0.149(10)	8.0
109.029216	CH ₃ CCD	$J_K=7_1-6_1$	19.6	...	0.019 ^b	8.0
109.031214	CH ₃ CCD	$J_K=7_0-6_0$	14.5	...	0.027 ^c	7.6
109.173634	HC ₃ N	12-11	23.7	-0.008(4)	2.310(15)	1.212(9)	2.967(11)	8.6
109.252220	SO	$N=3-2, J=2-1$	14.6	0.39(12)	0.057(7)	2.0(3)	0.111(14)	7.2
109.289095	HCCNC	11-10	21.9	-0.0(3)	0.022(8) ^b	1.5(6)	0.046(13)	9.0
109.757133	DC ₃ N	13-12	25.6	-0.14(8)	0.06(2)	0.9(4)	0.046(10)	8.7
109.782173	C ¹⁸ O	1-0	3.7	-0.022(11)	4.41(9)	1.11(3)	5.582(12)	8.1
109.905749	HNCO	$5_{0,5}-4_{0,4}$	11.0	-0.05(2)	0.298(8)	0.81(3)	0.238(9)	7.4
110.024590	C ¹⁵ N	$N=1-0, J=3/2-1/2, F=2-1$	3.7	-0.23(14)	0.048(9)	1.5(3)	0.096(14)	10.0
110.153594	NH ₂ D	$1_{1,1}-1_{0,1}$	14.8	0.4(3)	0.027(8) ^b	1.7(6)	0.053(17)	9.3
110.201354	¹³ CO	1-0	3.7	0.240(12)	9.52(12)	1.96(3)	19.79(3)	14.5
110.381372	CH ₃ CN	$J_K=6_1-5_1$	17.9	-0.10(16)	0.033(8)	1.4(4)	0.042(11)	8.0
110.383500	CH ₃ CN	$J_K=6_0-5_0$	12.9	...	0.078	8.4

Table A.1 (continued)

Frequency (GHz)	Molecule	Transition	E_u (cm^{-1})	ΔV_{LSR}^a (km s^{-1})	T_{mb}^a (K)	Δv^a (km s^{-1})	$\int T_{\text{mb}} dv$ (K km s^{-1})	rms (mK)
110.837830	D ₂ CO	2 _{1,2} -1 _{1,1}	9.3	0.15(4)	0.162(11)	1.04(8)	0.184(14)	10.0
112.254524	CH ₃ CHO	6 _{-1,6} -5 _{-1,5} , E	14.7	...	0.037 ^c	12.2
112.358880	C ¹⁷ O	$J=1-0$, $F=3/2-5/2$, $7/2-5/2$	3.7	-0.060(16)	0.99(2)	1.25(3)	1.39(2)	17.2
112.360007	C ¹⁷ O	$J=1-0$, $F=5/2-5/2$	3.7	0.04(4)	0.51(3)	1.21(9)	0.62(12)	94.4
112.520200	U	0-0	3.8	-0.33(8)	0.198(11)	3.09(19)	0.62(4)	19.7
112.805469	CH ₂ DCCH	7 _{1,7} -6 _{1,6}	18.8	...	0.038 ^b	15.2
113.123370	CN	$N=1-0$, $J=1/2-1/2$, $F=1/2-1/2$	3.8	-0.13(2)	0.517(17)	0.84(3)	0.472(19)	15.1
113.144157	CN	$N=1-0$, $J=1/2-1/2$, $F=1/2-3/2$	3.8	-0.200(11)	0.786(14)	1.31(3)	1.141(18)	11.4
113.170491	CN	$N=1-0$, $J=1/2-1/2$, $F=3/2-1/2$	3.8	-0.280(14)	0.811(17)	1.32(3)	1.241(19)	12.1
113.191279	CN	$N=1-0$, $J=1/2-1/2$, $F=3/2-3/2$	3.8	-0.290(15)	0.843(18)	1.48(4)	1.40(3)	15.4
113.258171	CH ₂ DCCH	7 _{0,7} -6 _{0,6}	15.1	...	0.059	13.4
113.313910	U	0-0	3.8	...	0.075	12.0
113.410186	CCS	$N=9-8$, $J=8-7$	23.3	-0.3(3)	0.037(13) ^b	0.9(7)	0.058(14)	13.0
113.488120	CN	$N=1-0$, $J=3/2-1/2$, $F=3/2-1/2$	3.8	-0.17(3)	1.09(6)	1.35(8)	1.759(20)	12.2
113.490970	CN	$N=1-0$, $J=3/2-1/2$, $F=5/2-3/2$	3.8	-0.11(2)	1.62(5)	1.68(6)	3.22(3)	15.9
113.499644	CN	$N=1-0$, $J=3/2-1/2$, $F=1/2-1/2$	3.8	-0.119(16)	0.97(3)	1.23(4)	1.424(19)	12.3
113.508907	CN	$N=1-0$, $J=3/2-1/2$, $F=3/2-3/2$	3.8	-0.081(11)	1.19(2)	1.20(3)	1.63(2)	14.3
113.520432	CN	$N=1-0$, $J=3/2-1/2$, $F=1/2-3/2$	3.8	0.059(10)	0.60(2)	0.95(4)	0.614(16)	12.1
113.716762	CH ₂ DCCH	7 _{1,6} -6 _{1,5}	19.0	...	0.052	12.4
114.182515	C ₄ H	$N=12-11$, $J=25/2-23/2$	24.8	0.046(13)	0.770(18)	0.87(2)	0.783(18)	13.7
114.221041	C ₄ H	$N=12-11$, $J=23/2-21/2$	24.8	-0.013(14)	0.730(15)	0.856(20)	0.716(17)	13.4

Table A.1 (continued)

Frequency (GHz)	Molecule	Transition	E_u (cm^{-1})	ΔV_{LSR}^a (km s^{-1})	T_{mb}^a (K)	Δv^a (km s^{-1})	$\int T_{\text{mb}} dv$ (K km s^{-1})	rms (mK)
114.381212	c- ¹³ CCCH ₂	3 _{0,3} -2 _{1,2}	8.2	-0.15(11)	0.079(15)	1.1(2)	0.076(17)	14.5
114.614995	H ¹³ CCCN	13-12	26.8	0.47(17)	0.054(14) ^c	1.1(4)	0.06(2)	14.1
114.647951	c-C ₃ HD	3 _{1,2} -2 _{2,1}	9.8	0.21(7)	0.136(16)	1.25(16)	0.18(2)	14.7
114.897371	c-CC ¹³ CH ₂	3 _{0,3} -2 _{1,2}	8.2	0.00(4)	0.32(2)	0.90(6)	0.30(3)	19.6
114.940190	CH ₃ CHO	6 _{0,6} -5 _{0,5} , E	13.5	...	0.069	16.9
114.954995	c-CC ¹³ CH ₂	3 _{1,3} -2 _{1,2}	8.2	0.0(2)	0.11(3)	0.7(2)	0.10(3)	25.9
115.271202	CO	1-0	3.8	1.21(12)	8.8(7)	2.9(3)	32.28(13)	53.3
115.524356	c-CC ¹³ CH ₂	3 _{1,3} -2 _{0,2}	8.2	-0.00(6)	0.30(2)	0.78(7)	0.27(2)	22.0
115.619870	C ₄ H ₂	13 _{1,13} -12 _{1,12}	36.4	...	0.054 ^c	17.5
116.118107	CH ₃ CHO	6 _{2,4} -5 _{2,3} , A^+	19.8	0.0(4)	0.11(10) ^b	0.9(9)	0.09(7)	69.6
116.594779	CCS	$N = 9-8, J = 9-8$	25.5	...	0.071 ^b	37.4
116.688420	D ₂ CO	2 _{0,2} -1 _{0,1}	5.8	-0.04(11)	0.23(4)	1.4(3)	0.24(5)	37.4

Note. — The numbers in parentheses represent the errors in units of last significant digits.

^aObtained from the Gaussian fit. ΔV_{LSR} represents the velocity shift from V_{LSR} of 5.85 km s^{-1} . “...” shows that the fit was not successful due to the weak intensity or the insufficient resolution.

^bess than 3σ detection.

^cess than 4σ detection.

^dBlended.

^eThe line is not detected. The rms noise is used to derive the upper limit of the column density.

Table A.2. Line parameters of the supplementary observation in the 4-mm band.

Frequency (GHz)	Molecule	Transition	E_u (cm^{-1})	ΔV_{LSR}^a (km s^{-1})	T_{mb}^a (K)	Δv^a (km s^{-1})	$\int T_{\text{mb}} dv$ (K km s $^{-1}$)	rms (mK)
70.733206	D ¹³ CO+	1-0	2.4	0.12(3)	0.28(3)	0.53(7)	0.153(17)	32.4
71.024788	H ₂ ¹³ CO	1 _{0,1} -0 _{0,0}	2.4	0.13(5)	0.18(3)	0.63(11)	0.124(17)	30.2
72.039312	DCO ⁺	1-0	2.4	0.061(3)	3.31(3)	0.654(6)	2.308(17)	30.3
72.101715	CCD	$N=1-0, J=3/2-1/2, F=3/2-3/2$	2.4	-0.27(4)	0.20(3)	0.58(9)	0.147(16)	30.0
72.107700	CCD	$N=1-0, J=3/2-1/2, F=5/2-3/2$	2.4	-0.035(13)	0.61(3)	0.60(3)	0.395(16)	29.2
72.109114	CCD	$N=1-0, J=3/2-1/2, F=1/2-1/2$	2.4	0.40(3)	0.24(3)	0.43(6)	0.117(14)	29.8
72.112399	CCD	$N=1-0, J=3/2-1/2, F=3/2-1/2$	2.4	0.51(2)	0.33(3)	0.48(6)	0.144(15)	30.2
72.187704	CCD	$N=1-0, J=1/2-1/2, F=3/2-3/2$	2.4	-0.03(2)	0.36(3)	0.50(6)	0.165(20)	39.8
72.189505	CCD	$N=1-0, J=1/2-1/2, F=1/2-3/2$	2.4	-0.93(6)	0.19(3) ^c	0.76(14)	0.12(3)	53.1
72.198388	CCD	$N=1-0, J=1/2-1/2, F=3/2-1/2$	2.4	0.81(5)	0.18(3)	0.43(8)	0.065(16)	33.3
72.413504	DCN	$J=1-0, F=1-1$	2.4	0.019(20)	0.50(3)	0.67(5)	0.325(19)	32.2
72.414933	DCN	$J=1-0, F=2-1$	2.4	0.013(18)	0.63(3)	0.74(4)	0.53(2)	33.5
72.417028	DCN	$J=1-0, F=0-1$	2.4	0.09(4)	0.26(4)	0.51(10)	0.126(18)	36.0
76.117439	C ₄ H	$N=8-7, J=17/2-15/2$	11.4	0.08(2)	2.01(16)	0.60(5)	1.26(9)	171.0
76.156028	C ₄ H	$N=8-7, J=15/2-13/2$	11.4	0.090(7)	1.91(5)	0.575(18)	1.19(3)	54.5
76.198726	l-C ₃ H	$^2\Pi_{3/2}, J=7/2-5/2, F=4-3, e$	5.4	0.11(2)	0.56(4)	0.58(5)	0.36(2)	43.6
76.199928	l-C ₃ H	$^2\Pi_{3/2}, J=7/2-5/2, F=3-2, e$	5.4	0.13(2)	0.51(5)	0.47(5)	0.24(2)	42.5
76.204182	l-C ₃ H	$^2\Pi_{3/2}, J=7/2-5/2, F=4-3, f$	5.4	0.031(20)	0.59(4)	0.55(5)	0.31(2)	44.7
76.205103	l-C ₃ H	$^2\Pi_{3/2}, J=7/2-5/2, F=3-2, f$	5.4	0.08(3)	0.42(4)	0.60(7)	0.29(2)	43.0
76.305700	DNC	1-0	2.5	0.014(13)	1.75(5)	0.96(3)	1.84(4)	55.6
77.100041	c-C ₃ H ₂	5 _{3,2} -5 _{2,3}	31.1	0.18(2)	0.202(11)	0.78(5)	0.168(8)	13.9

Table A.2 (continued)

Frequency (GHz)	Molecule	Transition	E_u (cm^{-1})	ΔV_{LSR}^a (km s^{-1})	T_{mb}^a (K)	Δv^a (km s^{-1})	$\int T_{\text{mb}} dv$ (K km s^{-1})	rms (mK)
77.107760	N_2D^+	$N=1-0, J=1/2-1/2, F=2-2$	2.6	0.22(3)	0.038(4) ^b	0.58(7)	0.022(13)	13.1
77.109315	N_2D^+	$N=1-0, J=3/2-1/2, F=2-1$	2.6	0.22(3)	0.038(4) ^b	0.58(7)	0.046(13)	13.1
77.109612	N_2D^+	$N=1-0, J=3/2-1/2, F=3-2$	2.6	0.22(3)	0.071(8)	0.58(7)	0.035(13)	13.1
77.109811	N_2D^+	$N=1-0, J=3/2-1/2, F=1-0$	2.6	0.22(3)	0.0170(18) ^b	0.58(7)	0.006(13)	13.1
77.112106	N_2D^+	$N=1-0, J=1/2-1/2, F=1-2$	2.6	0.22(3)	0.0170(18) ^b	0.58(7)	0.020(12)	13.1
77.880542	CH_3CCD	$J_K=5_0-4_0$	7.8	0.05(9)	0.13(4) ^b	0.6(2)	0.13(2)	43.0
79.099313	CH_3CHO	$4_{1,3}-3_{1,2}, E$	8.2	-0.03(5)	0.079(15)	0.49(10)	0.014(7)	14.1
79.150166	CH_3CHO	$4_{1,3}-3_{1,2}, A^-$	8.2	0.13(7)	0.053(15) ^c	0.52(17)	0.037(8)	15.7
79.150993	C_3N	$N=8-7, J=17/2-15/2$	11.9	0.10(4)	0.098(14)	0.55(9)	0.056(8)	15.5

Note. — The numbers in parentheses represent the errors in units of last significant digits.

^aObtained from the Gaussian fit. ΔV_{LSR} represents the velocity shift from V_{LSR} of 5.85 km s^{-1} . “...” shows that the fit was not successful due to the weak intensity or the insufficient resolution.

^bess than 3σ detection.

^cess than 4σ detection.

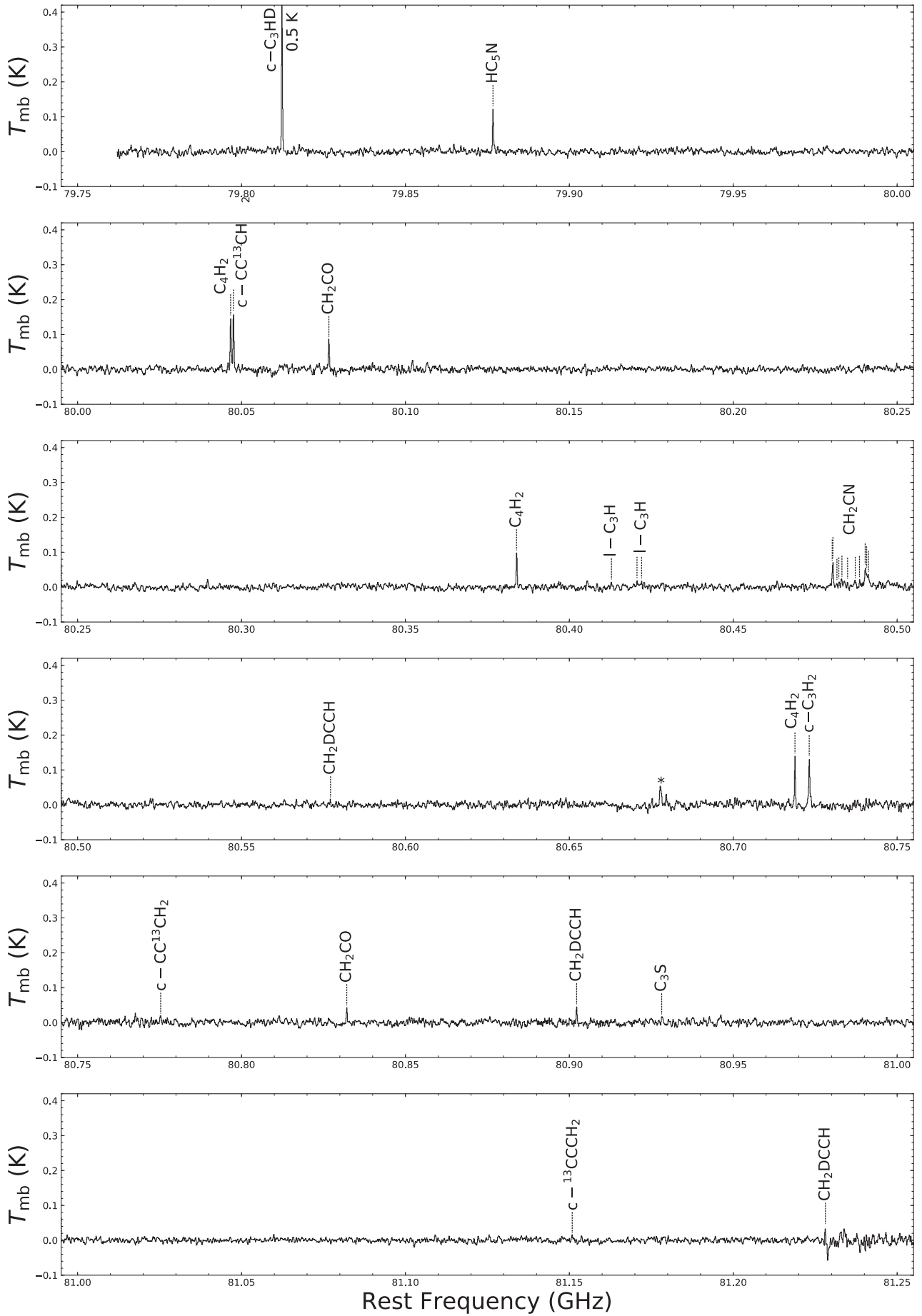


Figure A.1: Spectrum of L1527 in the 3 mm band. Spurious lines are indicated with asterisks.

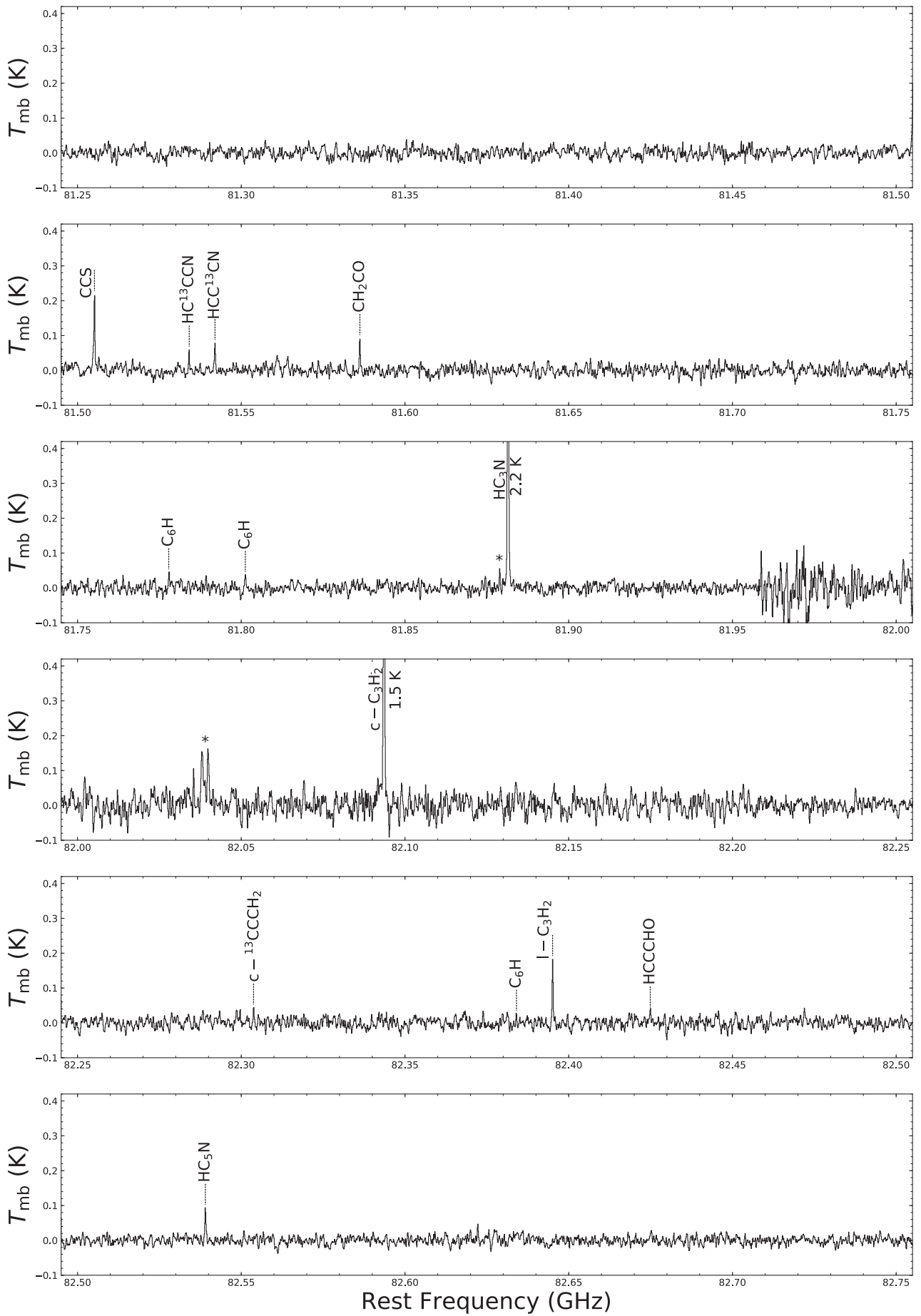


Figure A.1: (Continued.)

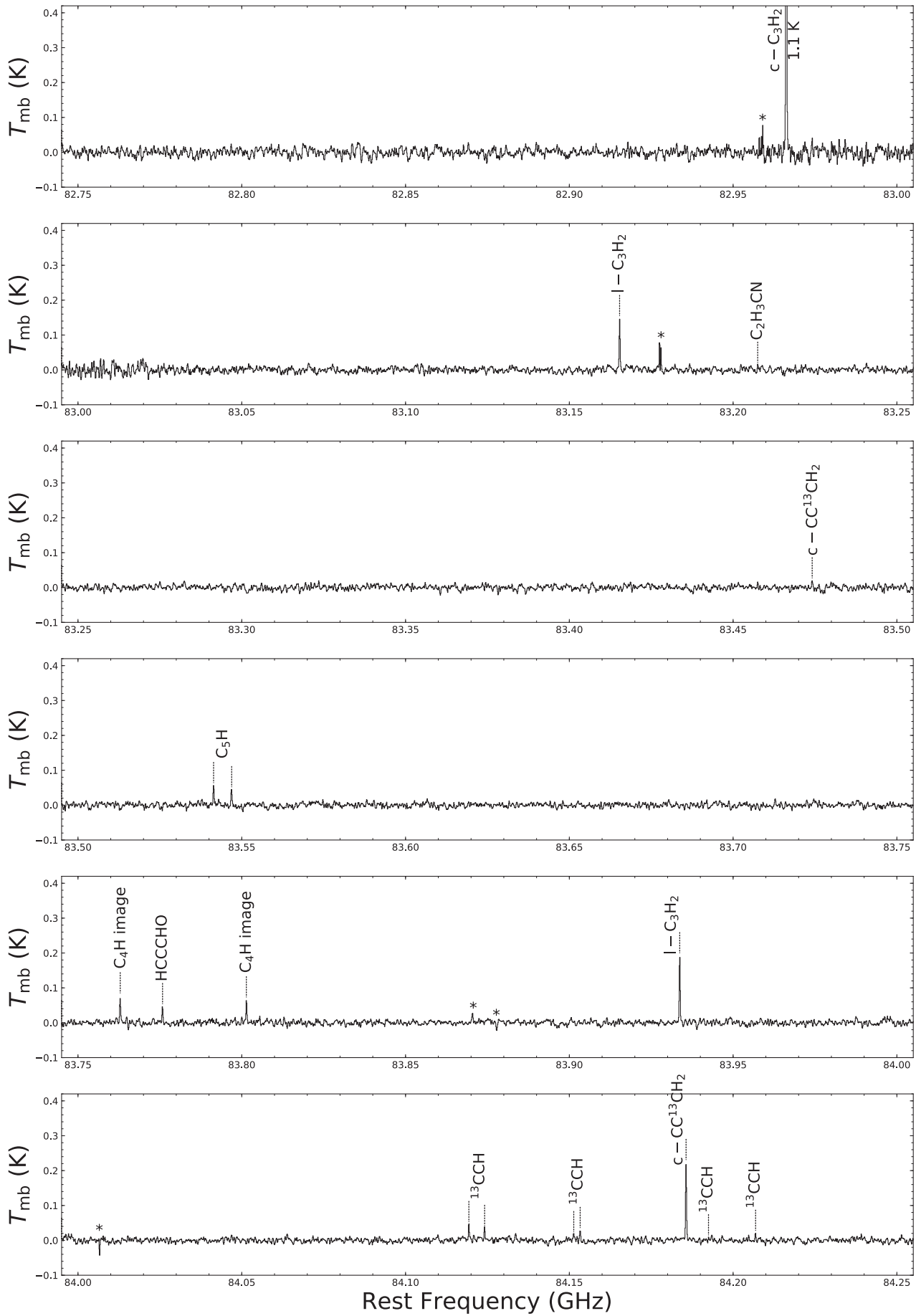


Figure A.1: (Continued.)

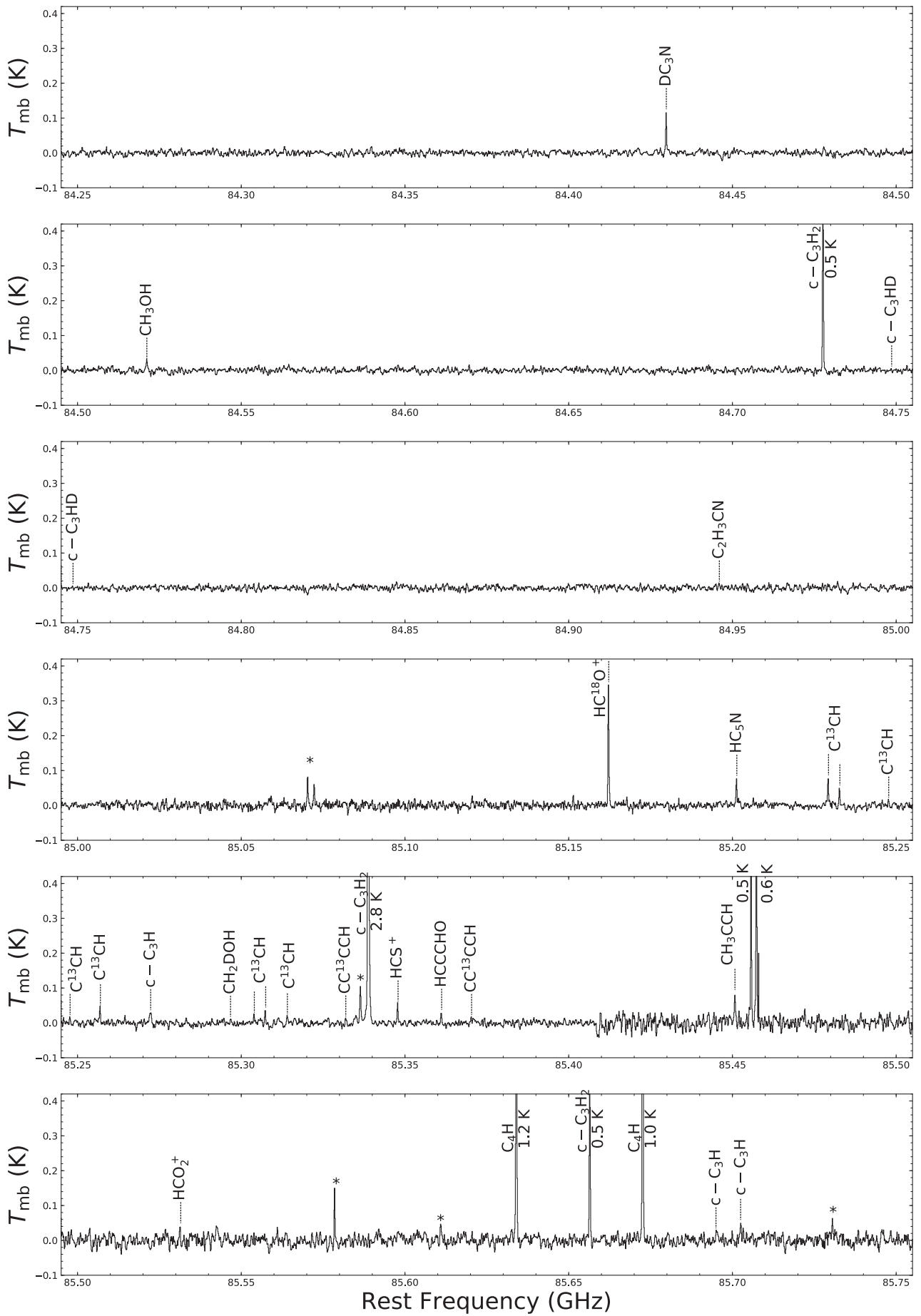


Figure A.1: (Continued.)

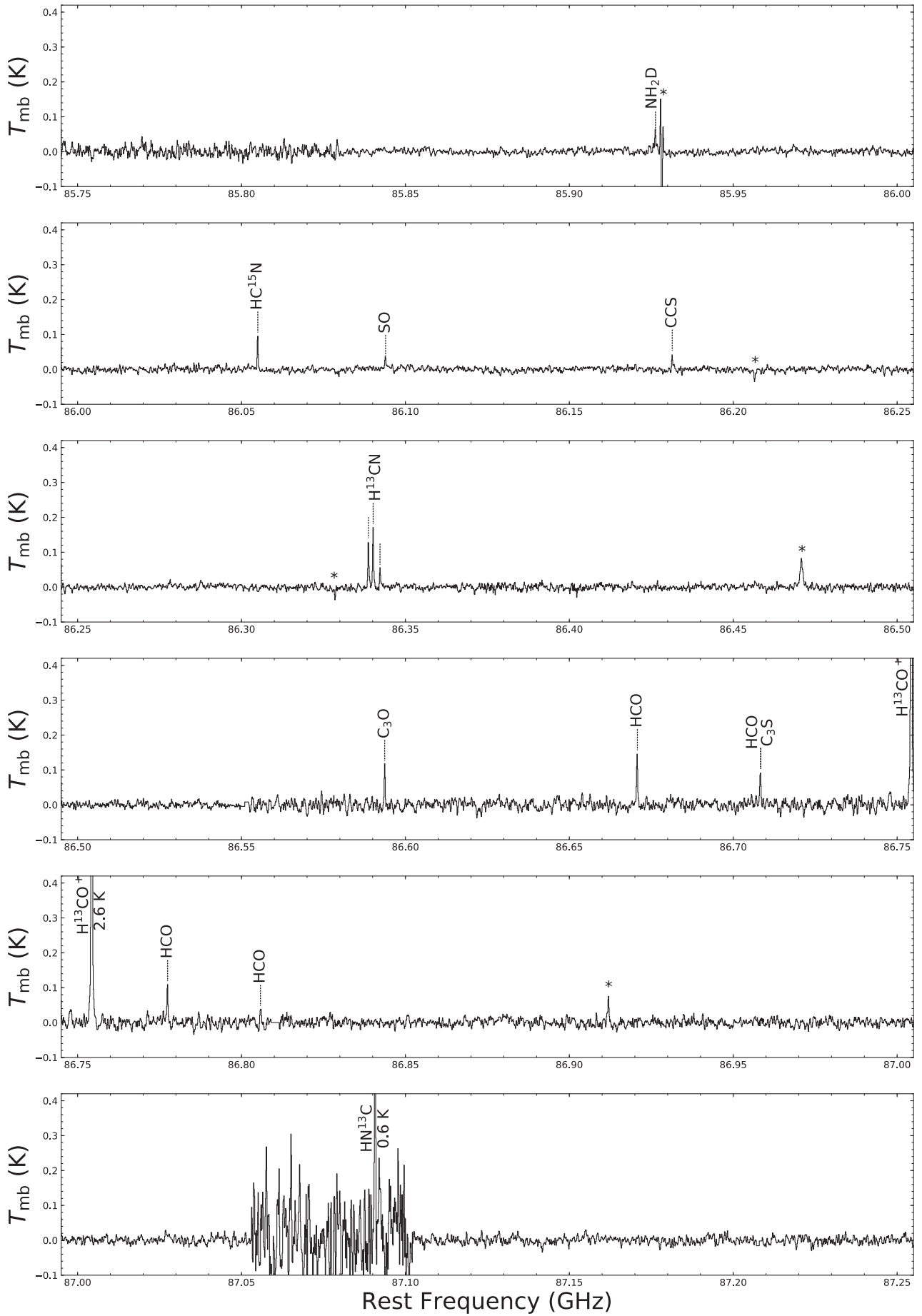


Figure A.1: (Continued.)

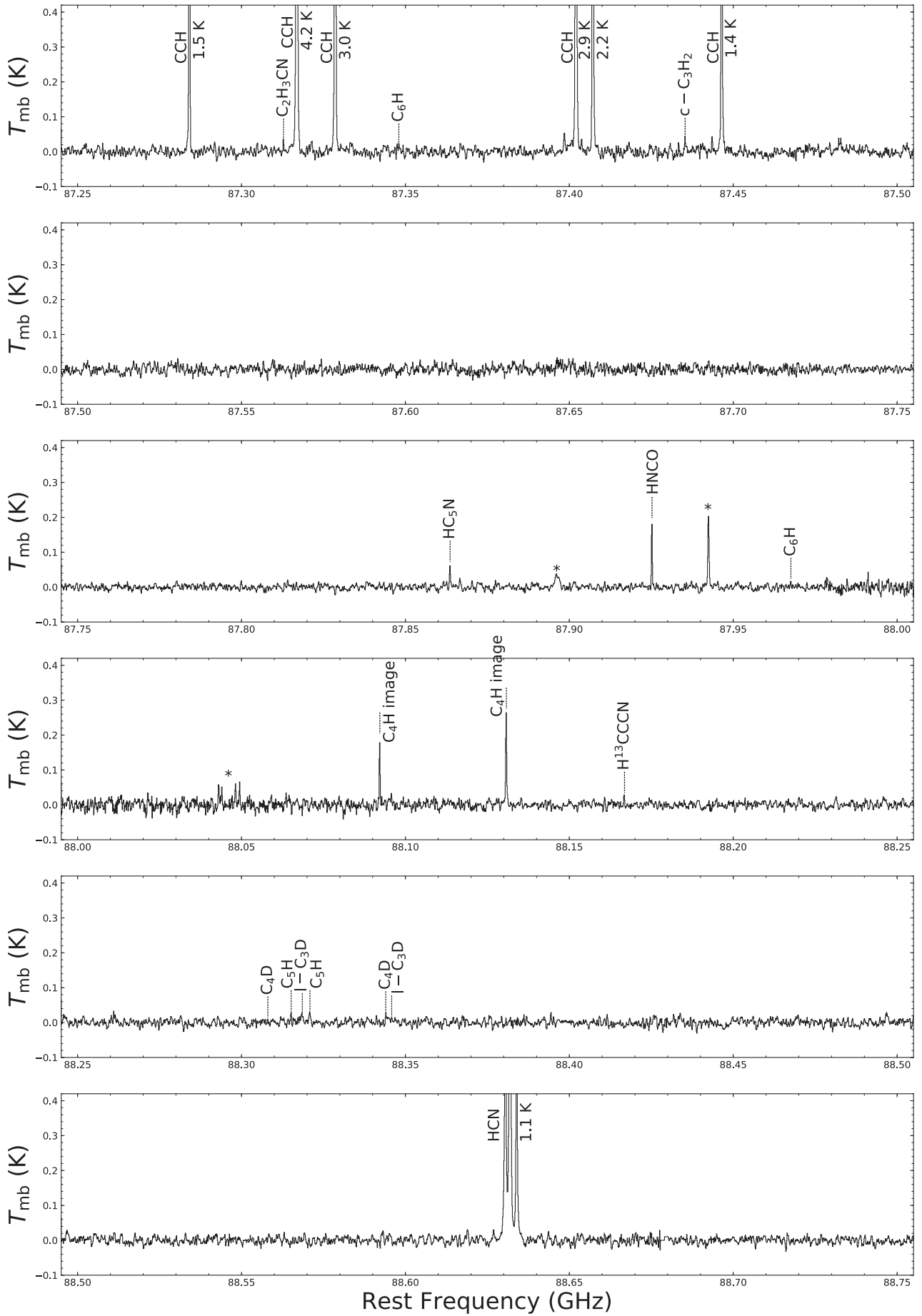


Figure A.1: (Continued.)
150

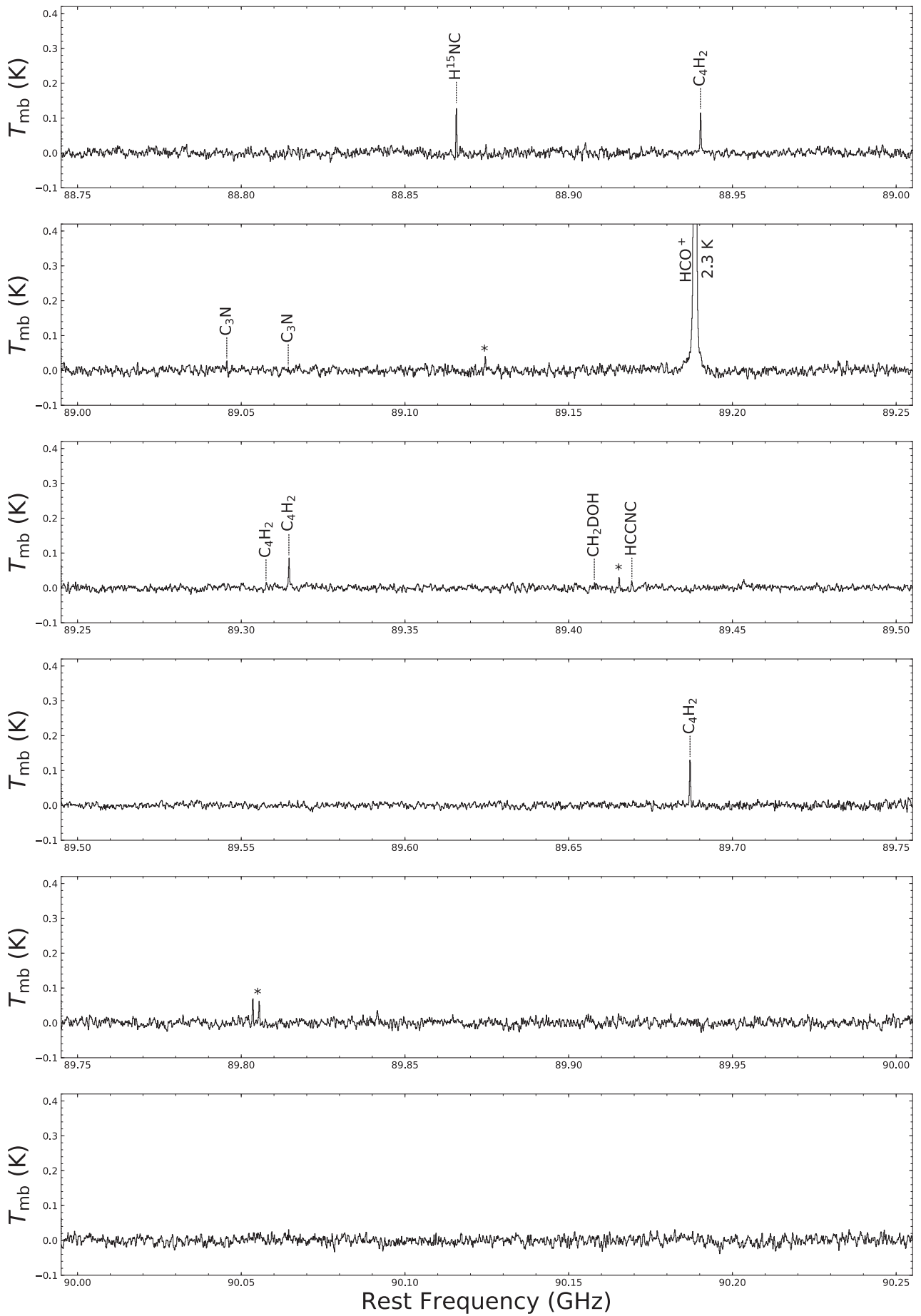


Figure A.1: (Continued.)

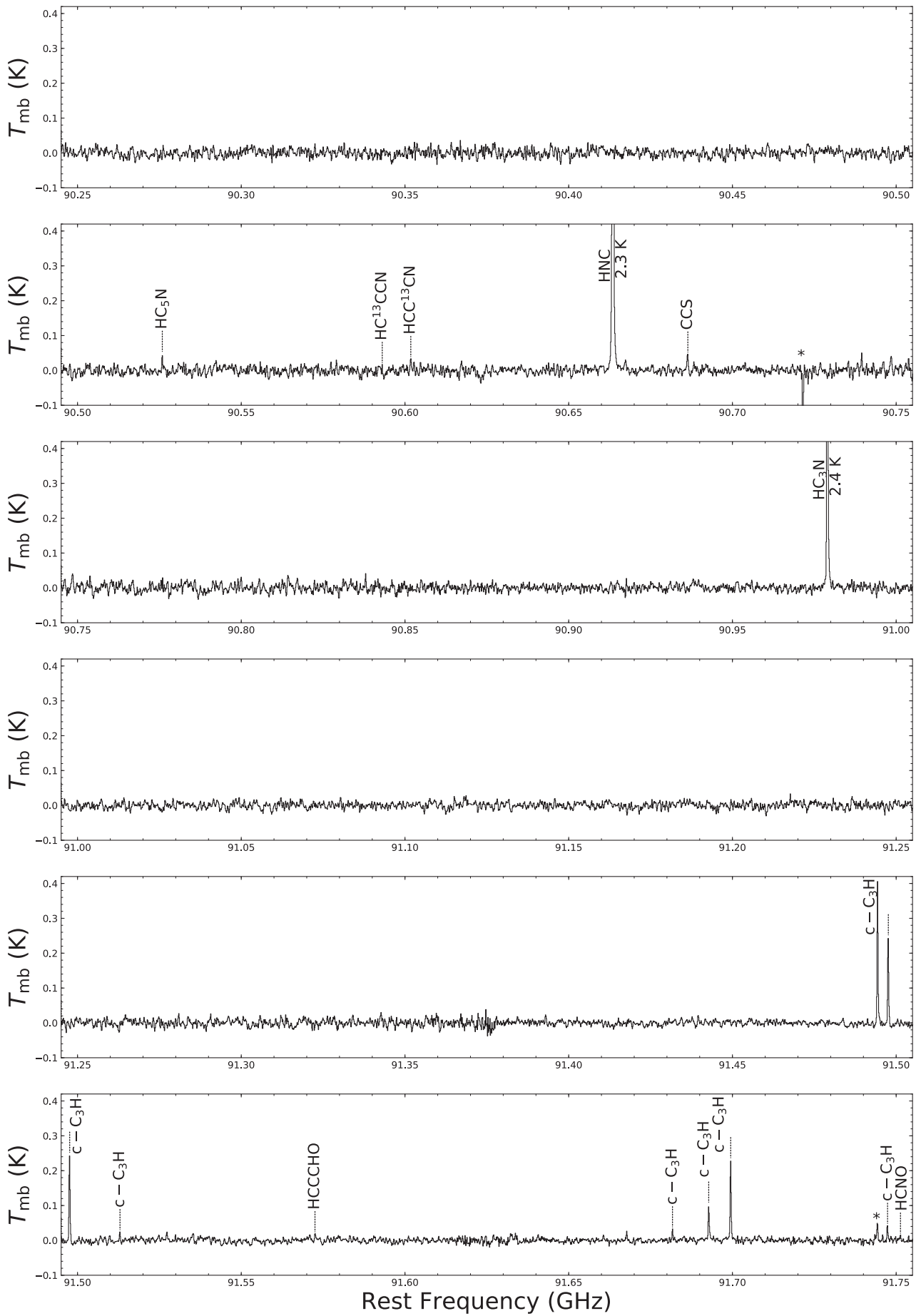


Figure A.1: (Continued.)

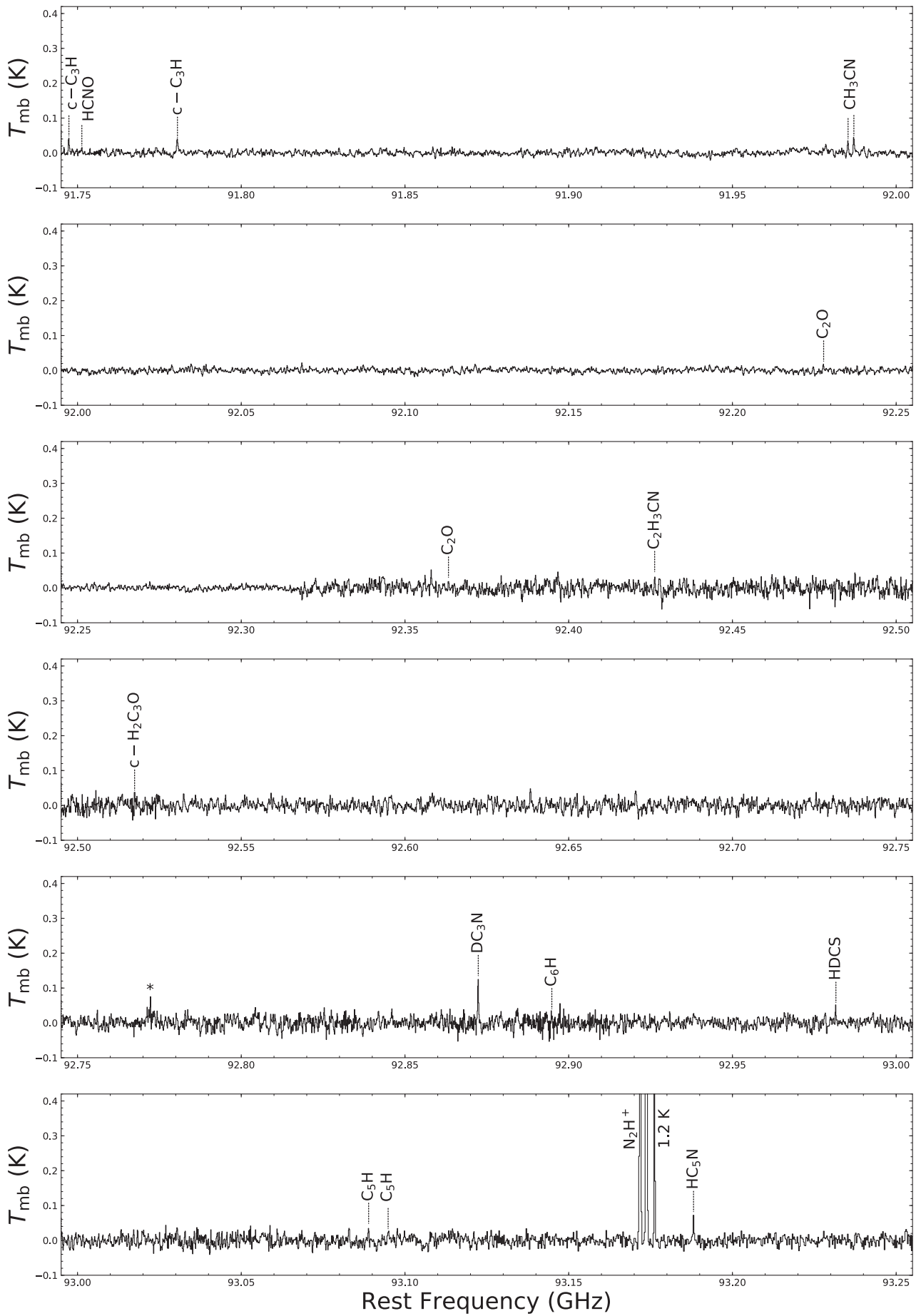


Figure A.1: (Continued.)

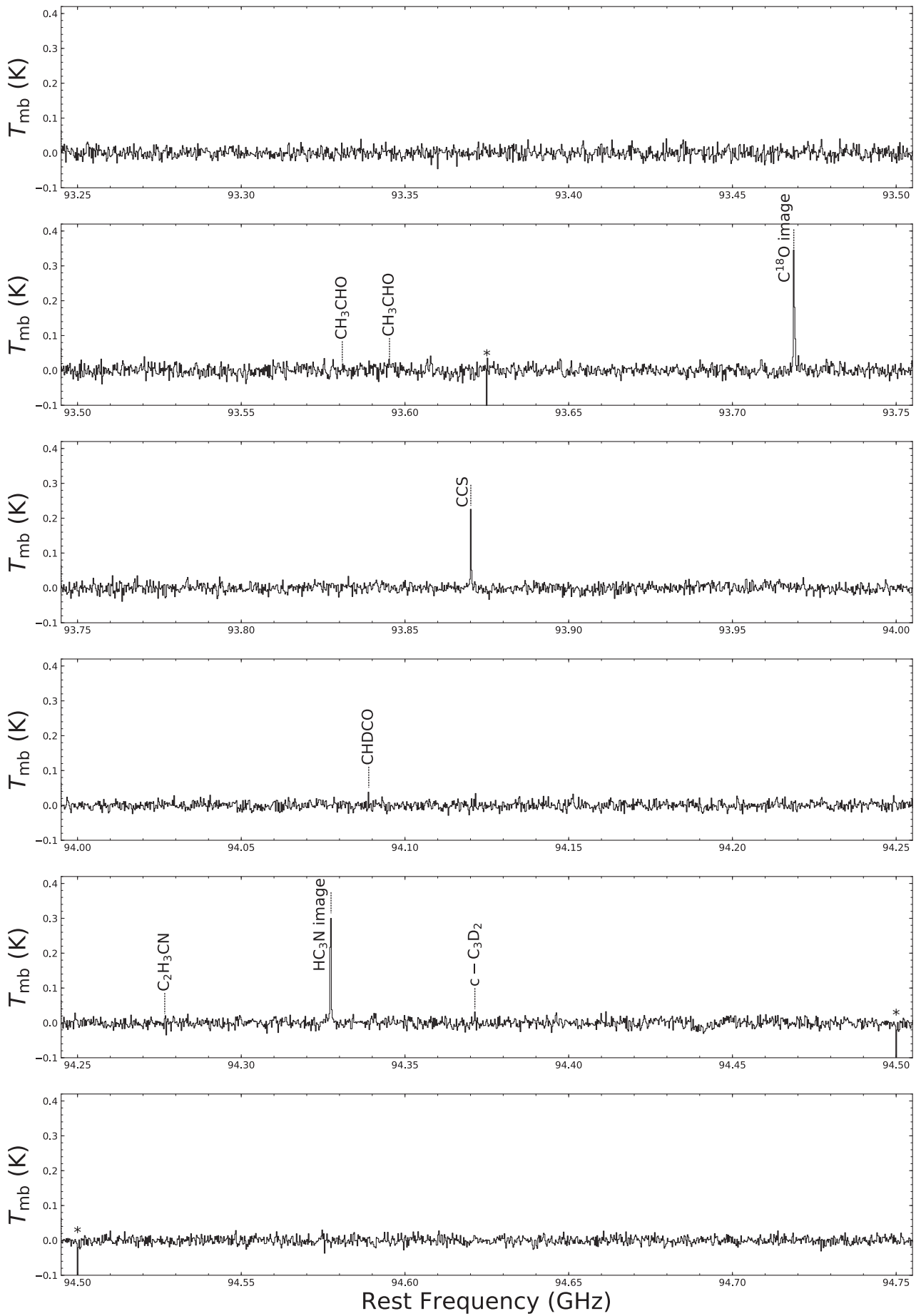


Figure A.1: (Continued.)

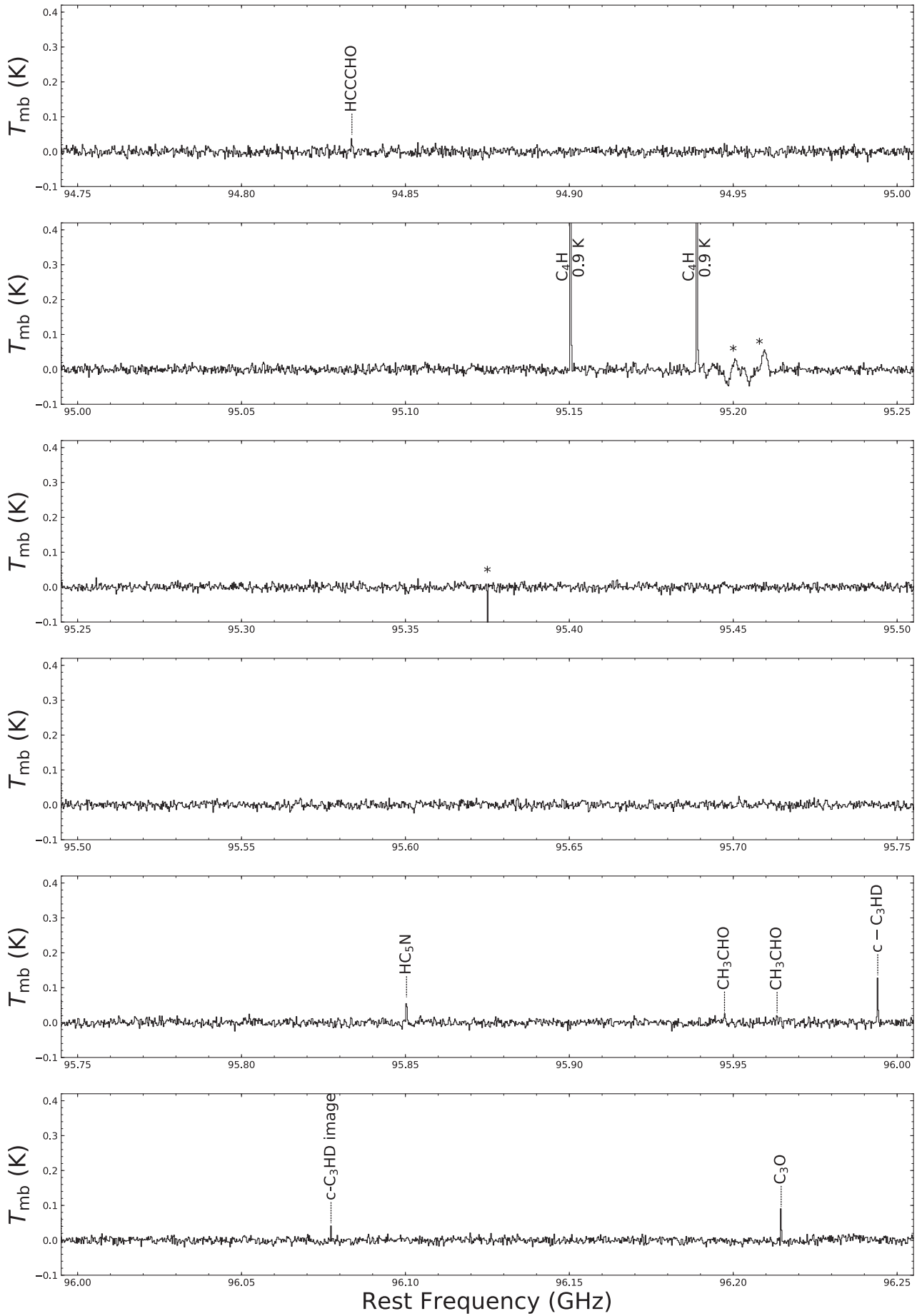


Figure A.1: (Continued.)
155

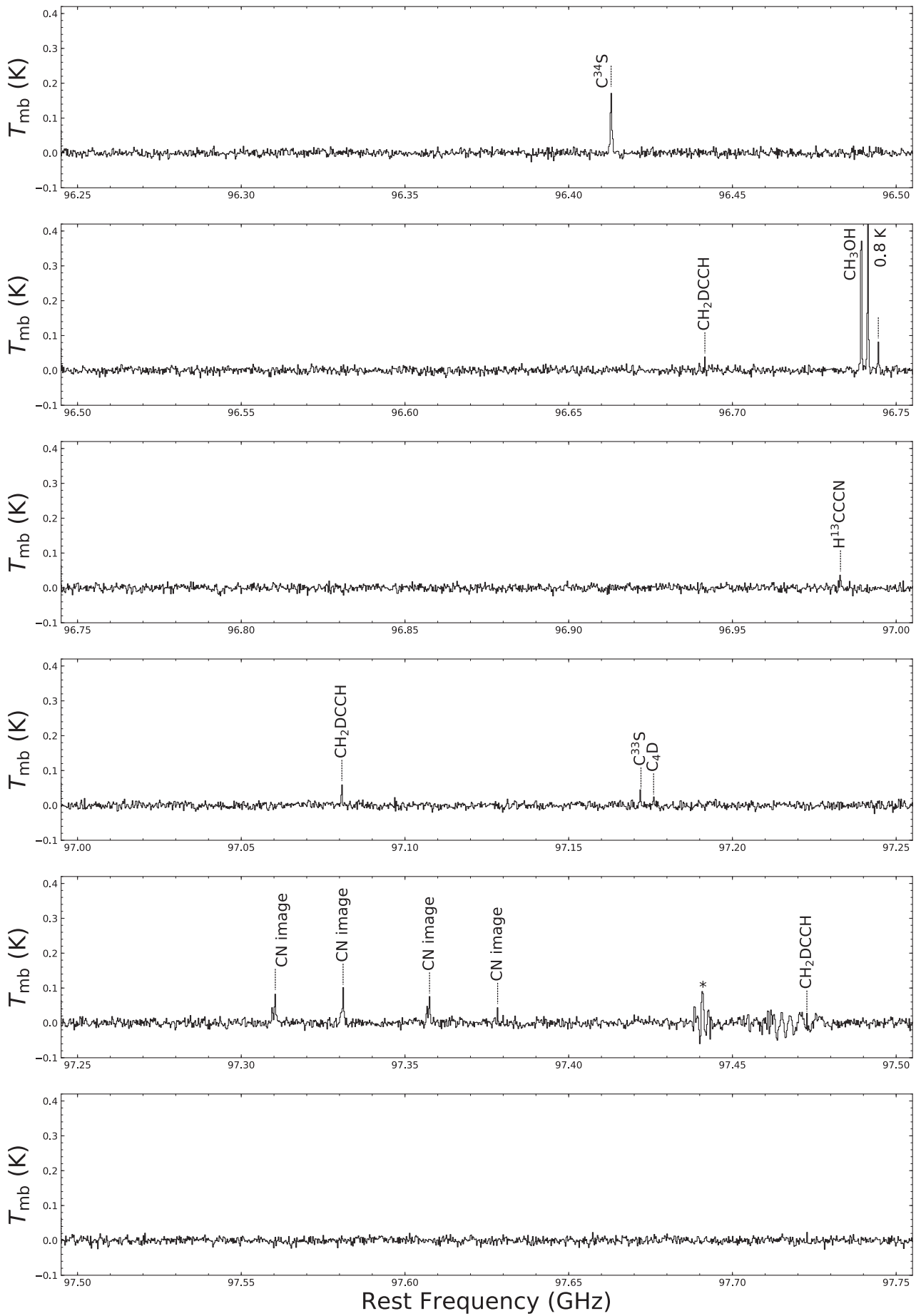


Figure A.1: (Continued.)
156

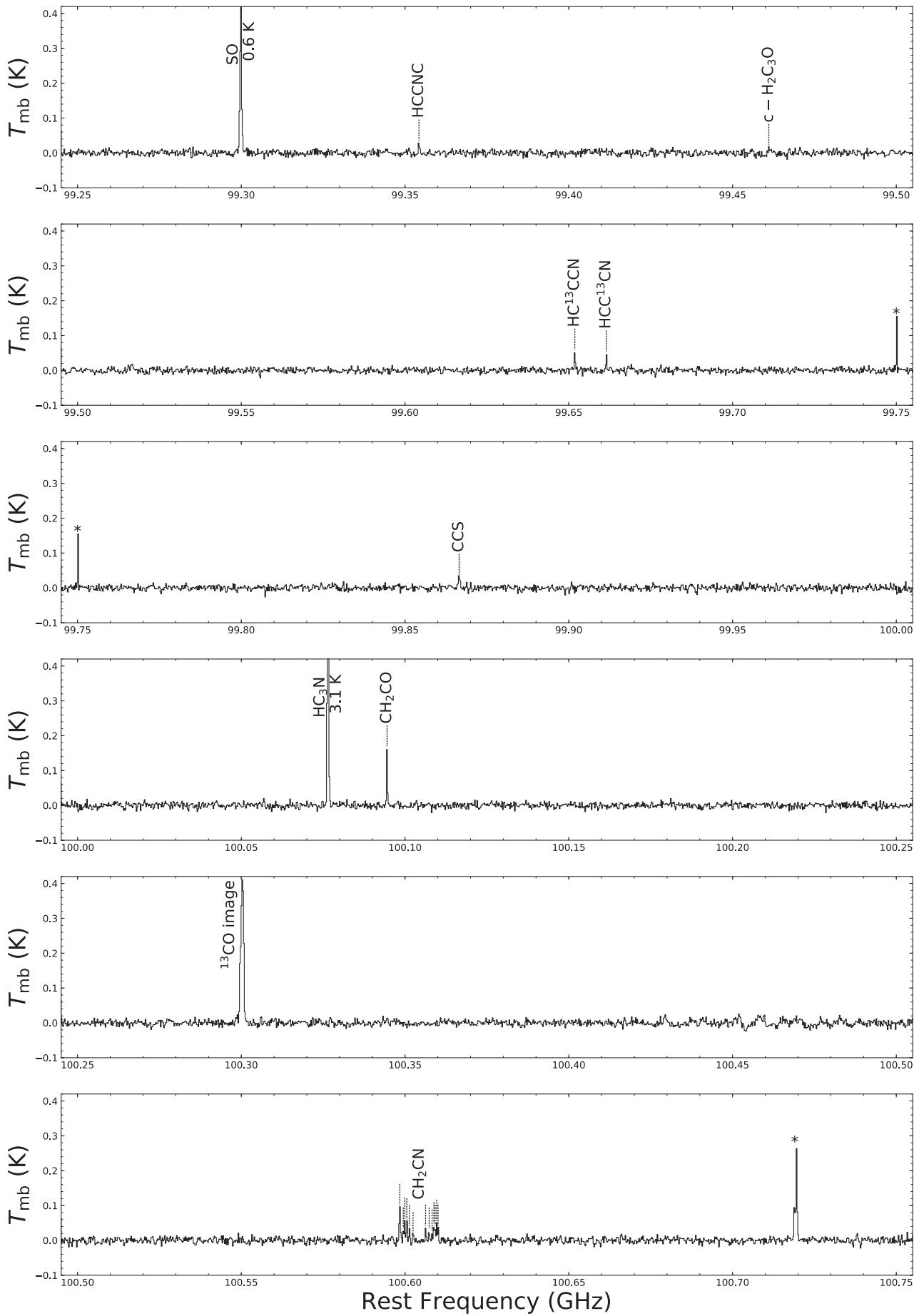


Figure A.1: (Continued.)

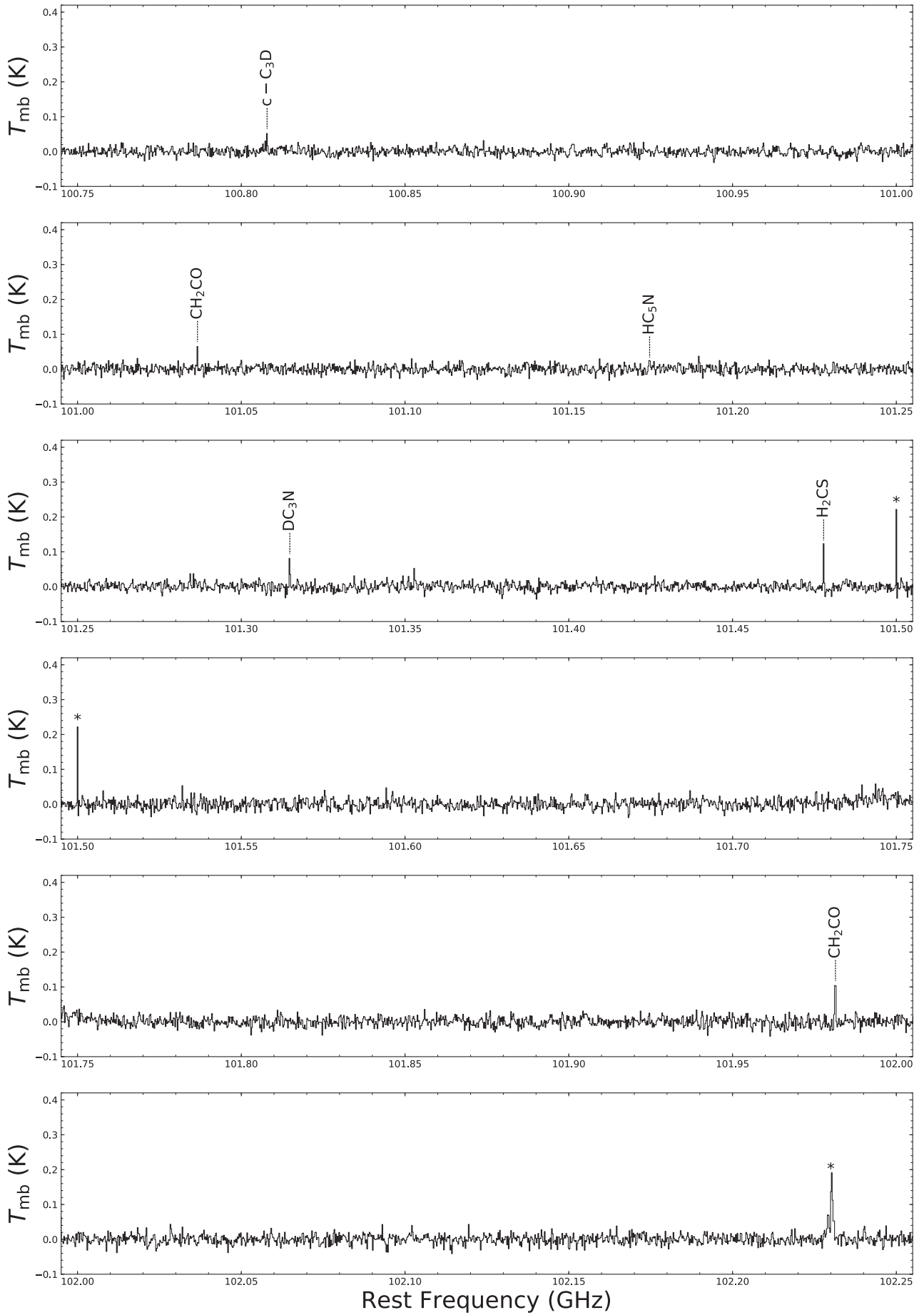


Figure A.1: (Continued.)

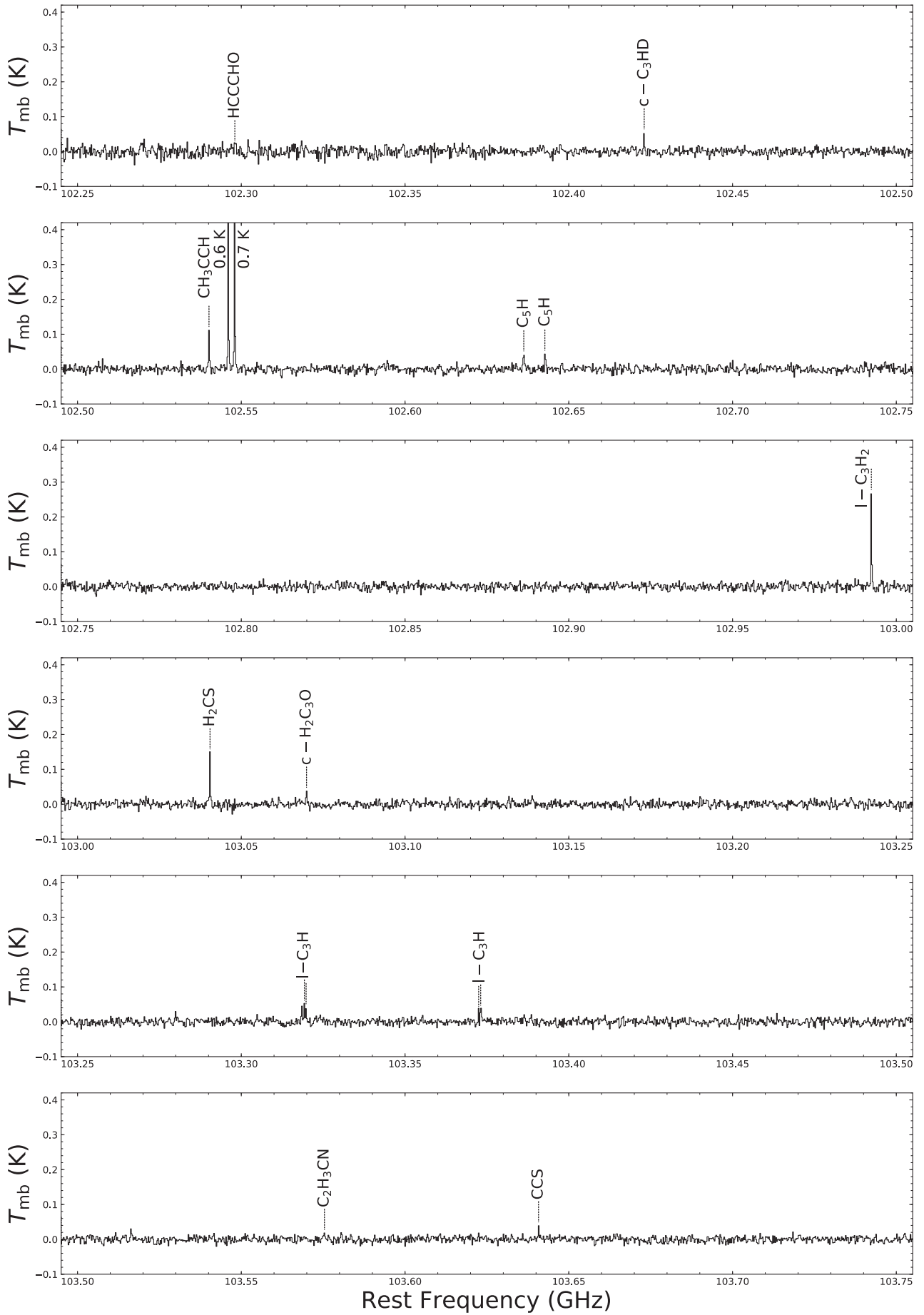


Figure A.1: (Continued.)

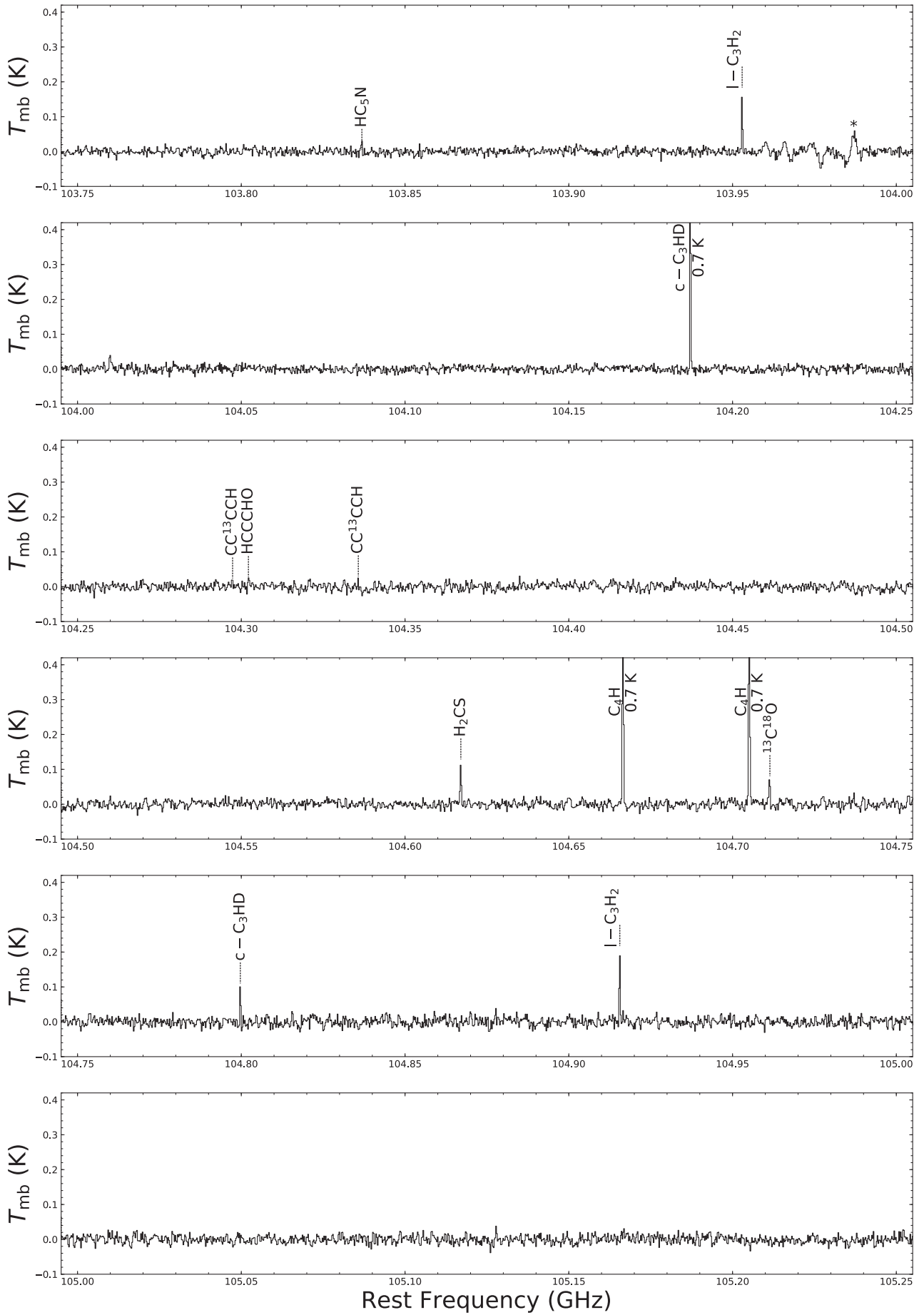


Figure A.1: (Continued.)

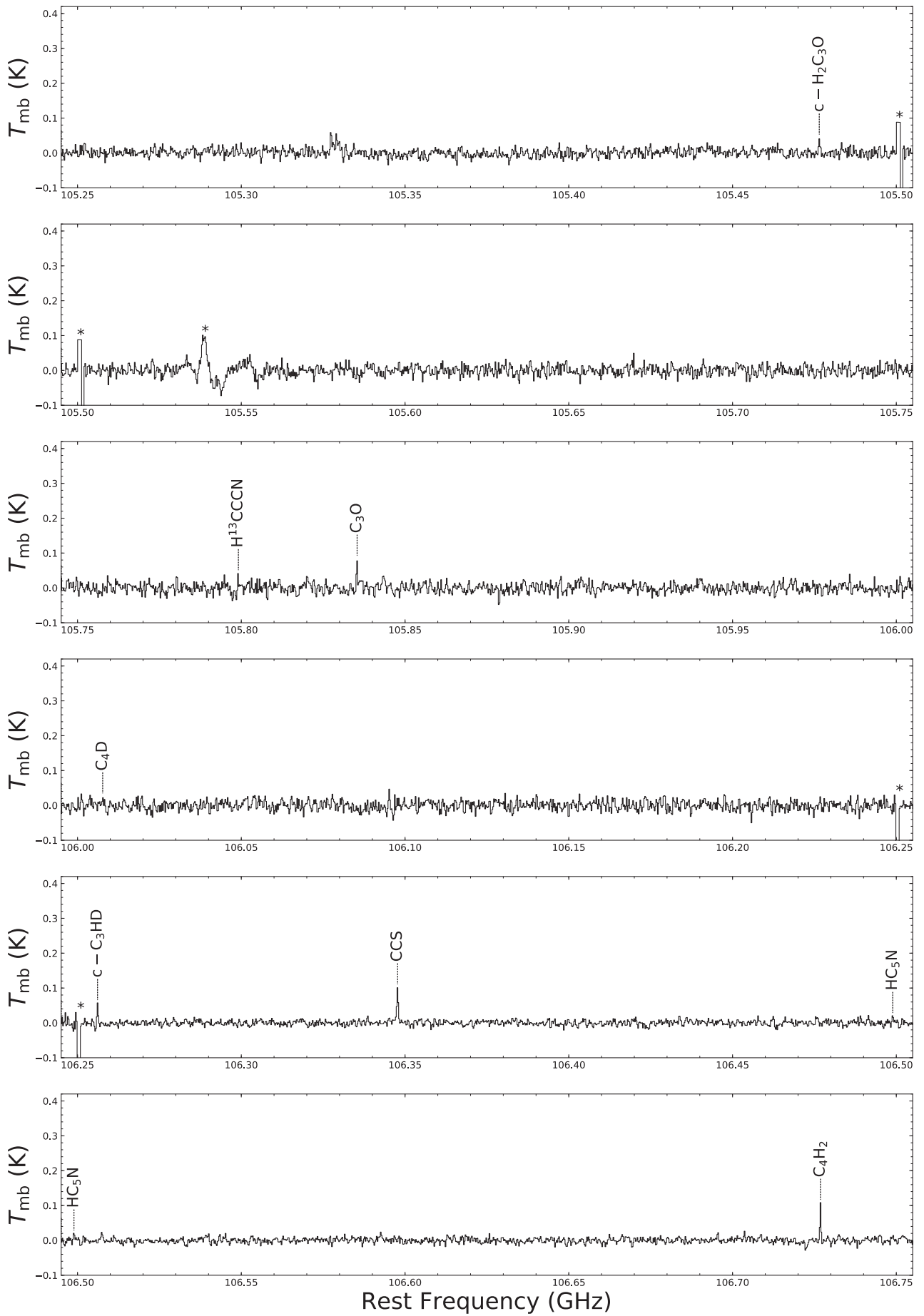


Figure A.1: (Continued.)

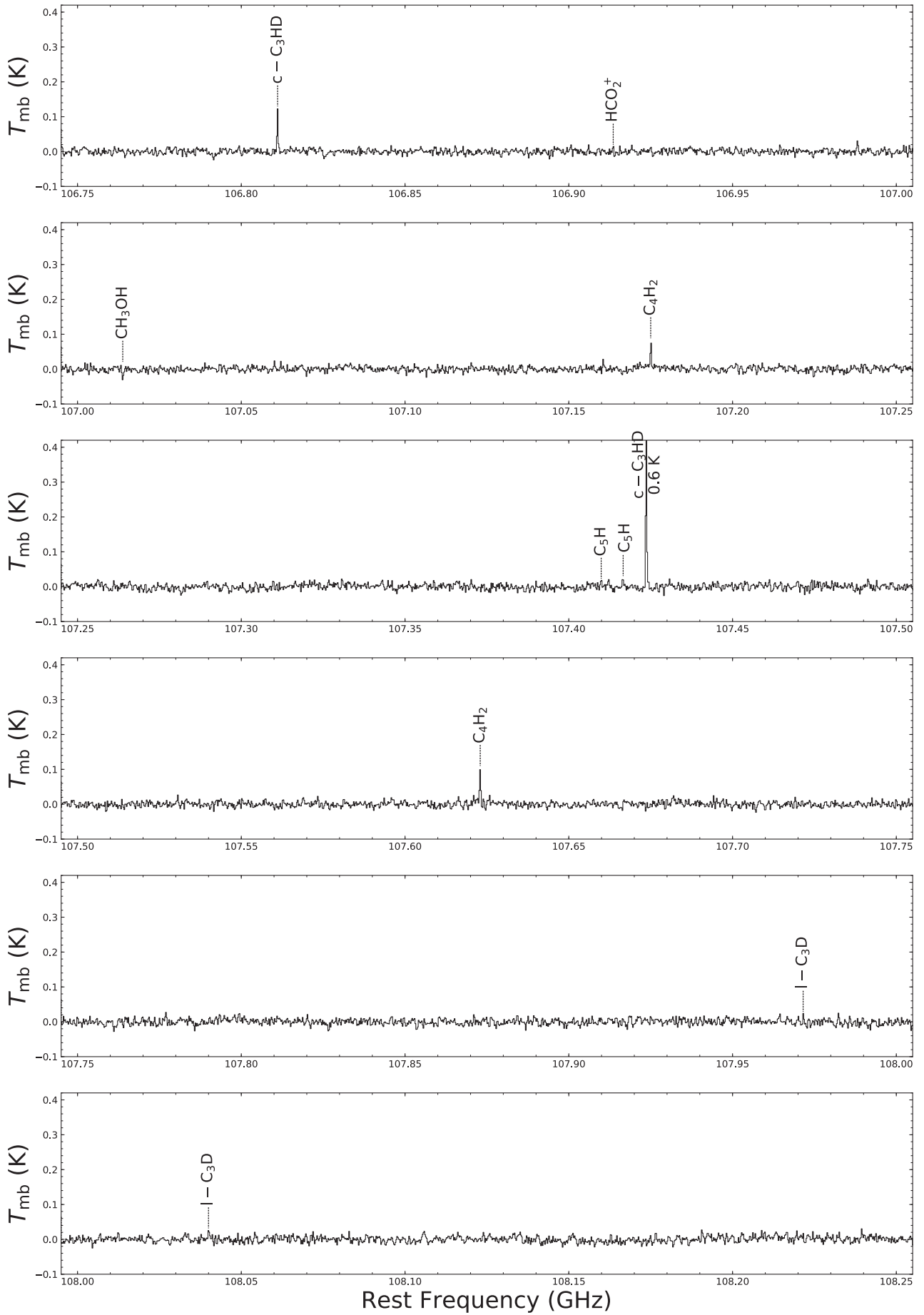


Figure A.1: (Continued.)

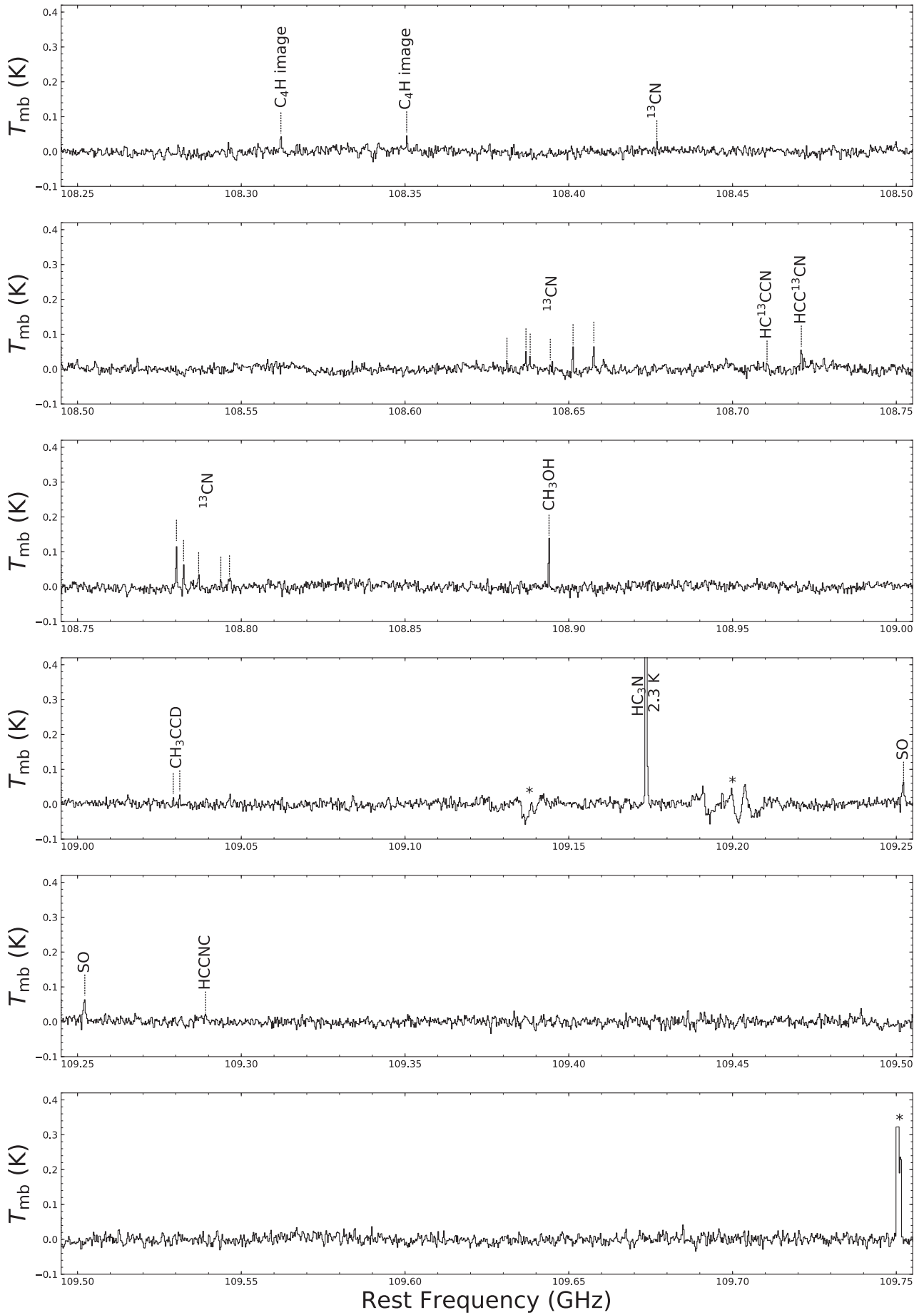


Figure A.1: (Continued.)

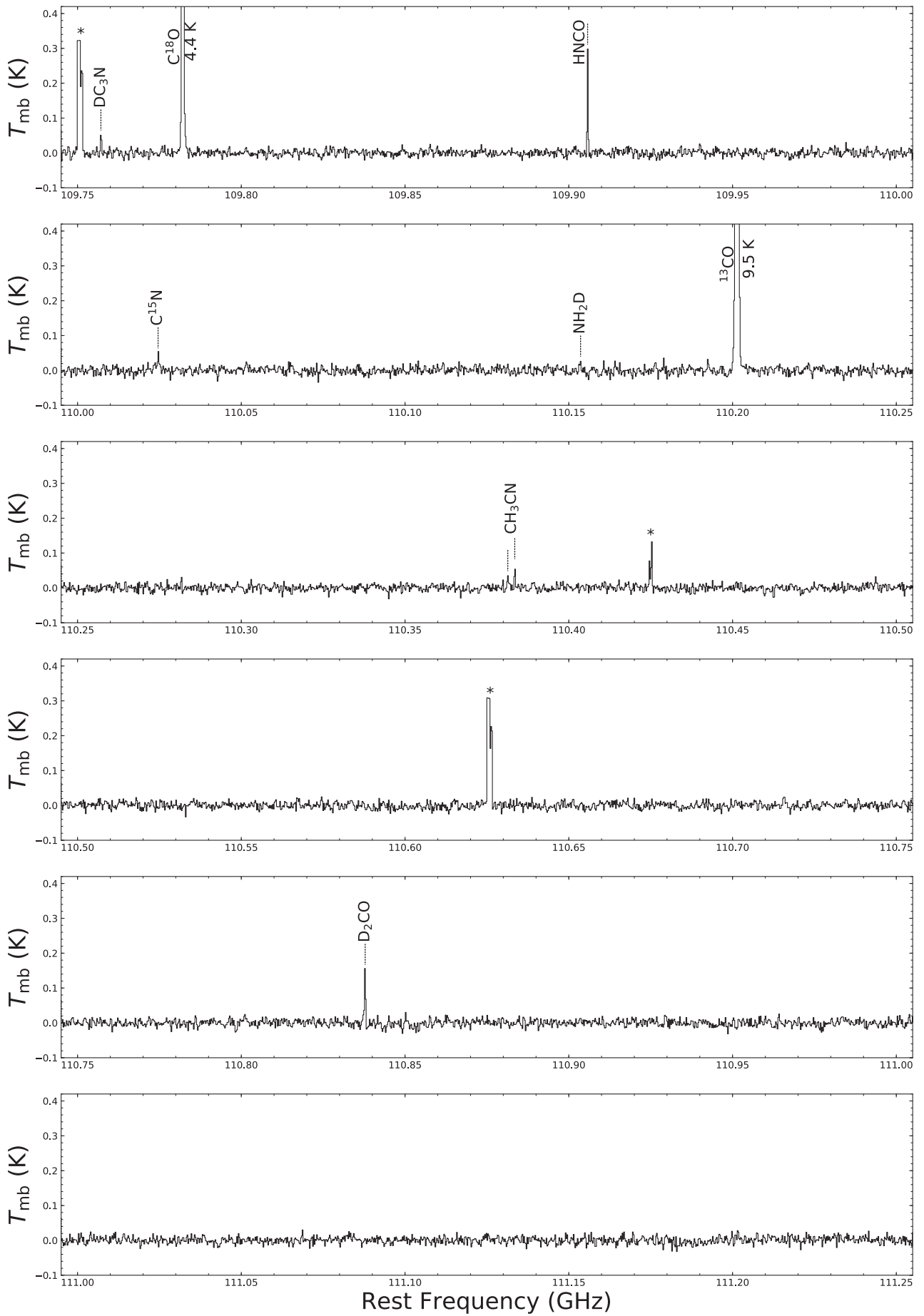


Figure A.1: (Continued.)
165

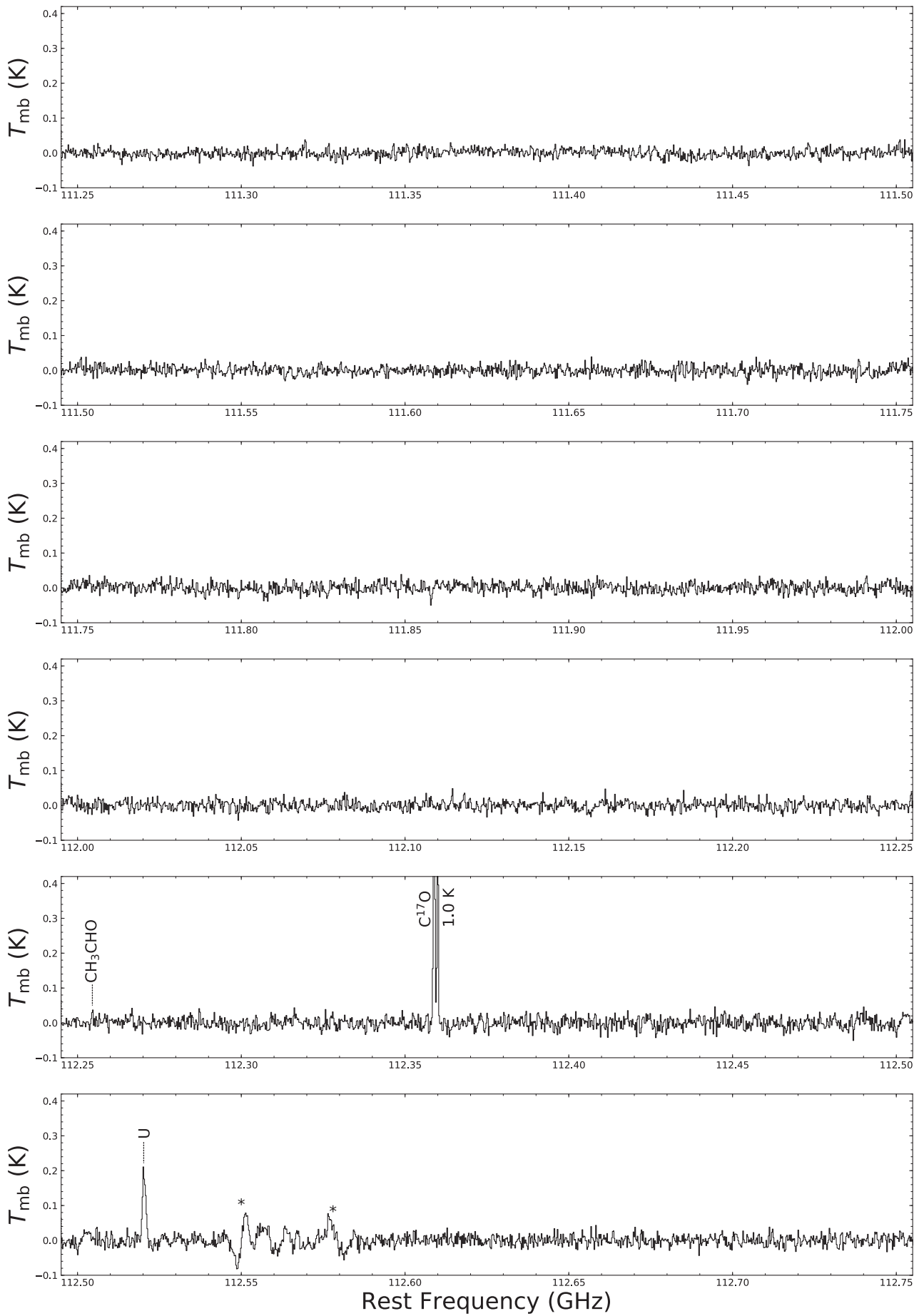


Figure A.1: (Continued.)

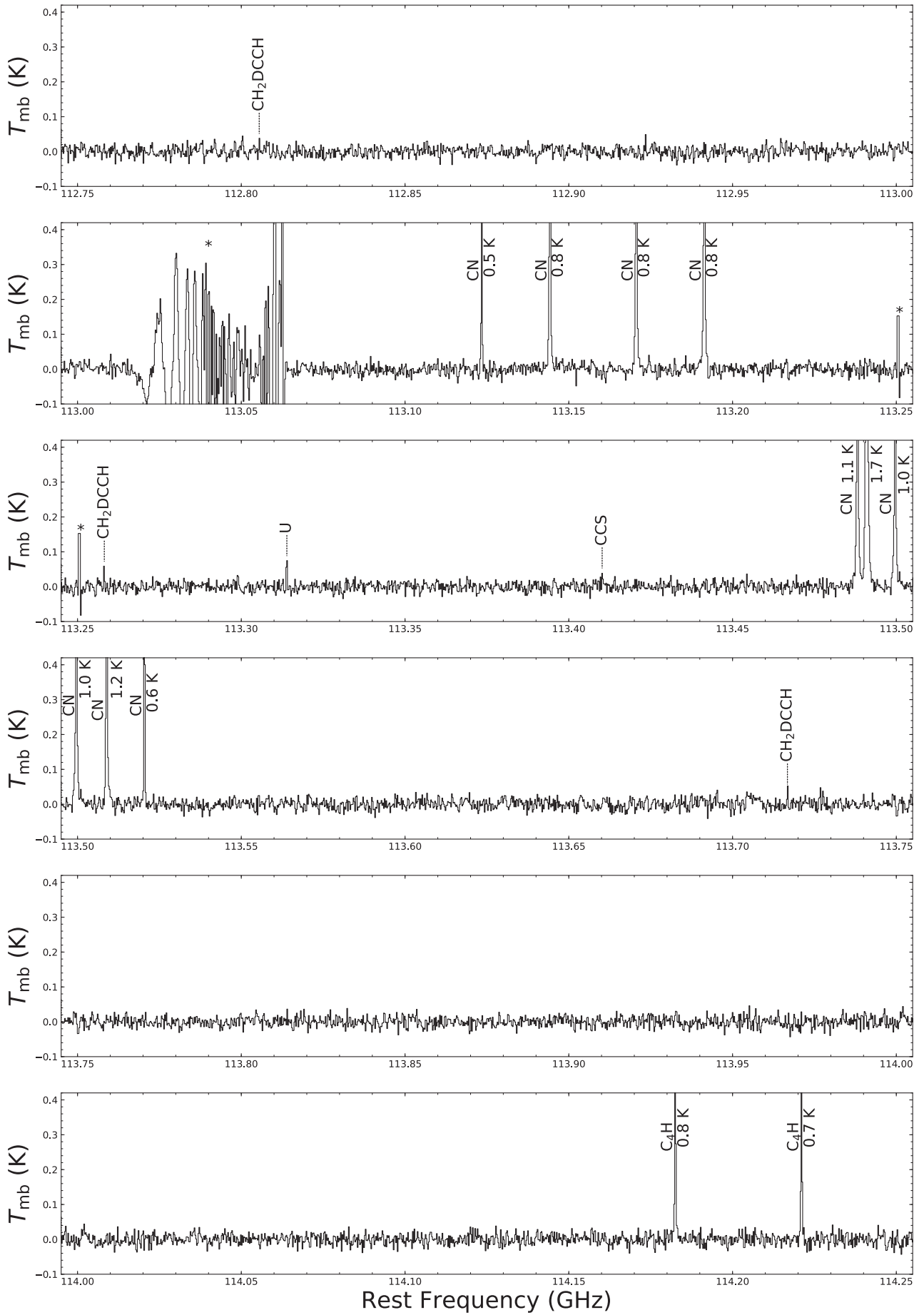


Figure A.1: (Continued.)

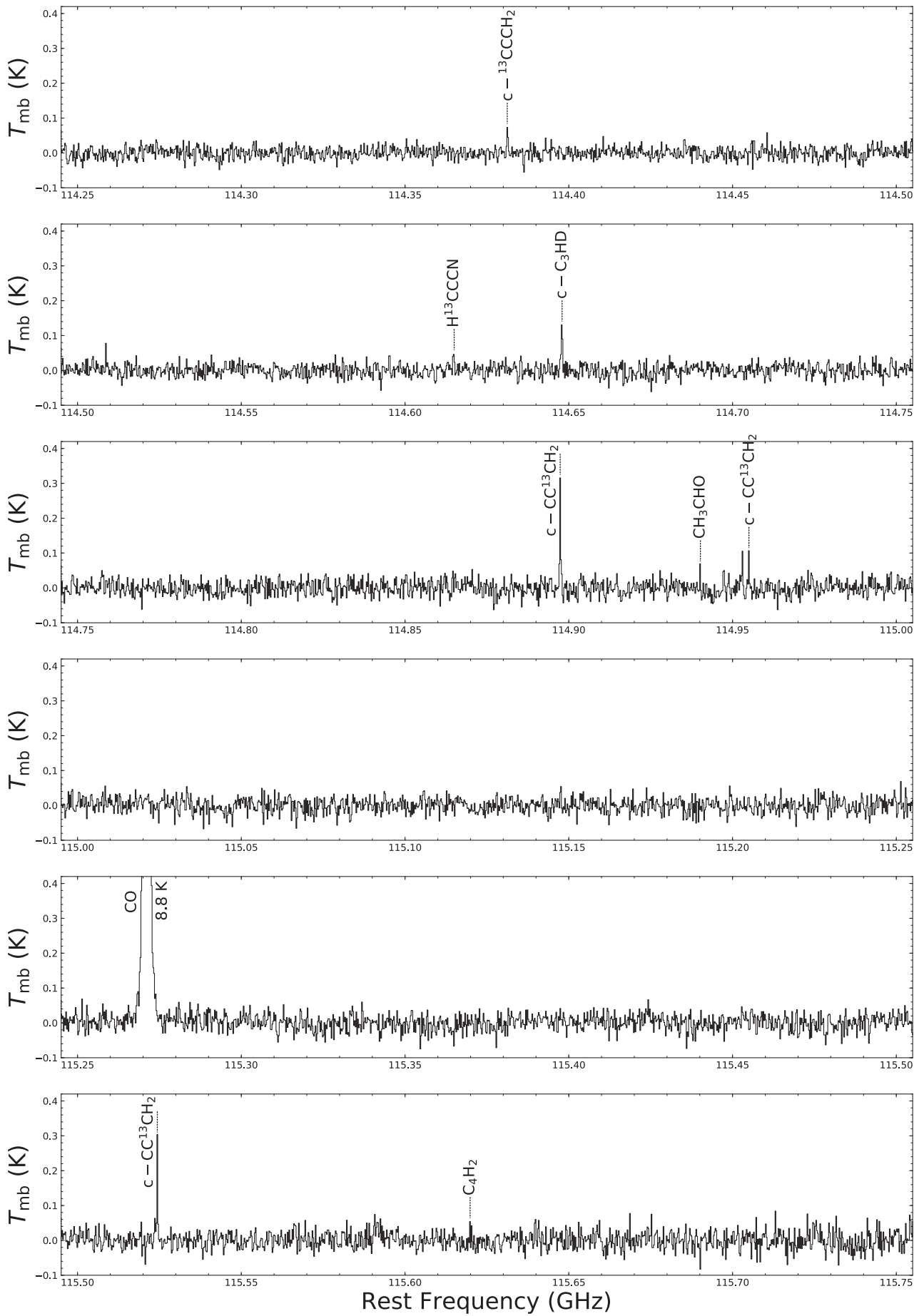
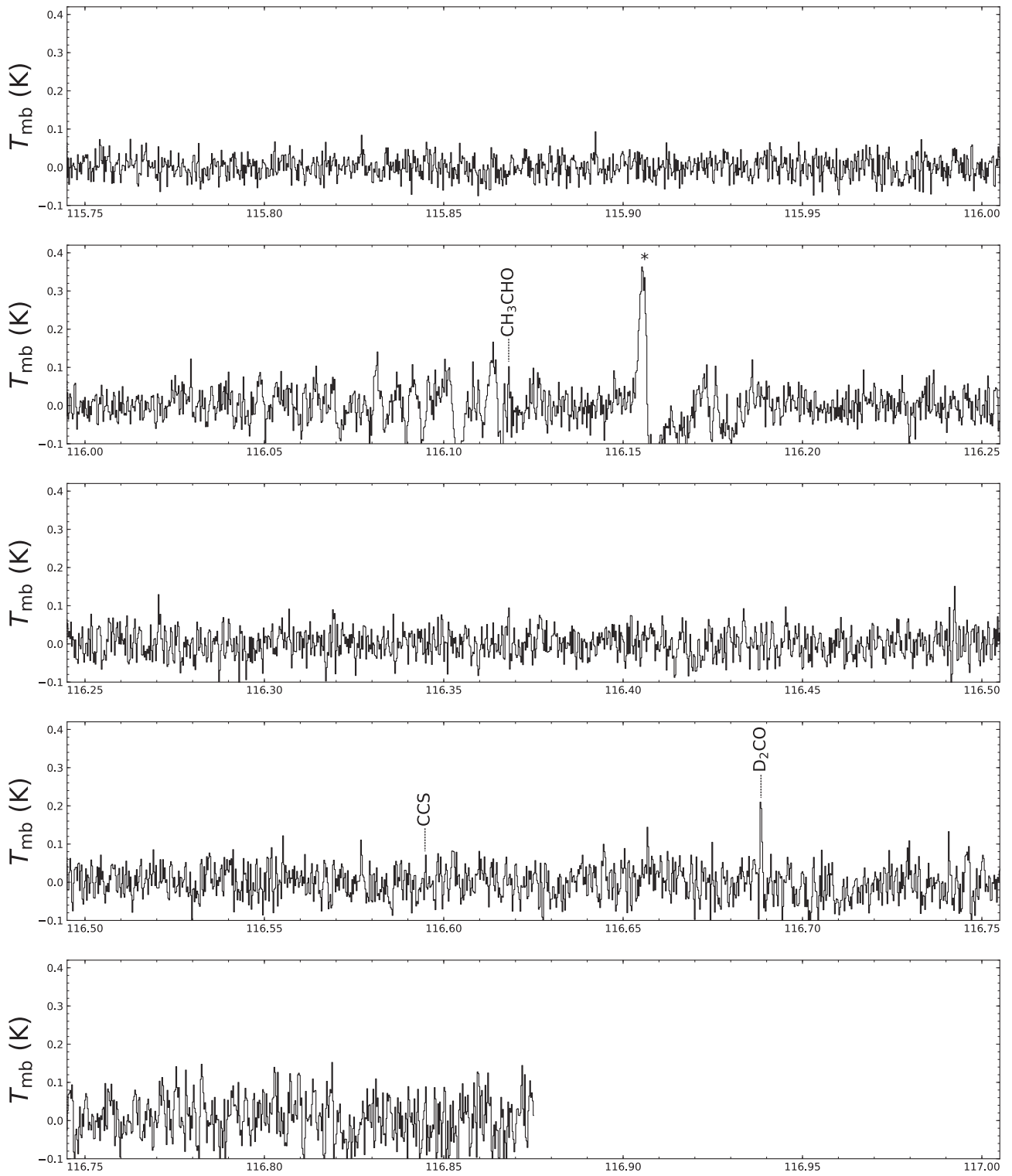


Figure A.1: (Continued.)
168



Rest Frequency (GHz)

Figure A.1: (Continued.)